Magnetic anisotropy studies of Kitaev model candidate materials

Dissertation

zur Erlangung des akademischen Grades

Dr. rer. nat.

eingereicht an der

Mathematisch-Naturwissenschaftlich-Technischen Fakultät

der Universität Augsburg

von

Ina-Marie Pietsch

Augsburg, Mai 2022

Erstgutachter:	Prof. Dr. Philipp Gegenwart
Zweitgutachter:	Prof. Dr. Manfred Albrecht

Tag der mündlichen Prüfung: 21.07.2022

„Man hat den Eindruck, dass die moderne Physik auf Annahmen beruht, die irgendwie dem Lächeln einer Katze gleichen, die gar nicht da ist.“

– Albert Einstein

Contents

1 | Introduction

The first encounter of humankind with magnetism lies back more than 2600 years from now. Nevertheless, the understanding of it has started only centuries ago and is still in progress. An old legend tells the story of Magnes, a Greek shephard, who was herding his sheep on Mount Ida. At one point the nails in his shoes and the metal tip of his staff stuck to the ground, on which he was standing. [1] The magnetic rocks, later known as lodestone, were naturally magnetized magnetite. This might have been the earliest discovery of a magnet. Since then, humans have learned to use magnetism for their purposes. In the beginning only for simple tasks such as the compass. Today they are used in numerous applications like in transformers, computers, speakers and electric motors, which we use everyday. Furthermore, magnetism is essential in medical applications like magnetic resonance imaging as well as for many experiments in research.

Since Maxwell we know that magnets can be created by moving electrical charges. It turned out that they cannot be seen separately, but are actually two sides of the same coin, called electromagnetism. A changing electric field produces a magnetic field and vice versa. Two of the pioneers to investigate magnetism in solids were Pierre Curie and Pierre Weiss. They developed the Curie-Weiss-Law, which describes the temperature dependence of a magnetic system. However, to explain the lodestone‘s magnetic properties, quantum mechanics had to be developed in the first half of the twentieth century. [2]

Nowadays research has moved away from simple magnets to materials that show exotic, more complex magnetism that is yet not fully understood. One big field is the topic of frustrated magnetism. Here, the temperature where the system orders is much lower than expected by the Curie-Weiss law. In 2006 Alexei Kitaev introduced the Kitaev honeycomb model [3], a purely theoretical spin model in two

dimensions. In this spin-1/2 model, the order in the system is completely suppressed due to very high frustration of the magnetic moments. The Kitaev model received a lot of attention, since it is one of the rare, more complex theoretical models, that is exactly solvable. It shows exotic properties as Majorana fermions and non-Abelian statistics with potential uses for quantum computing. It is therefore an ideal playground for researchers. At low temperatures, the model predicts a quantum spin liquid ground state of the spins, an exotic phase that is associated with no magnetic order, but strong correlations between the magnetic moments. The challenge for the experimental scientists was and still is to translate this model into the real world and find materials that exhibit the kind of interactions described here, henceforth called Kitaev interaction.

In 2009 Jackeli and Khaliullin proposed the now called Jackeli-Khaliullin-mechanism for strong spin-orbit Mott insulators [4]. Here, they proposed, a Kitaev interaction could be found in special d^5 systems due to the interplay of crystal field and spin-orbit coupling. One year later, they suggested together with Chaloupka the systems A_2IrO_3 (A=Li, Na) to be good candidates to fulfill all requirements and set up a Kitaev-Heisenberg model by adding a Heisenberg interaction to the Kitaev model [5]. Later α-$RuCl_3$ was added to the circle of 2d honeycomb candidates for realizing the Kitaev model [6]. All three systems show a magnetic transition at low temperatures, making the addition of at least one more exchange interaction necessary [7–9]. In the following years many groups found different models explaining the present magnetic orders, taking different interactions into account [10–17]. Today, experiments have already proven a dominant Kitaev exchange in Na_2IrO_3 and α-$RuCl_3$ [18–20]. Open questions are the actual importance of other types of interaction and a possible road to drive the materials into a Kitaev spin liquid state.

This thesis tries to do its part in shedding some light into the exotic physics of the spin-orbit Mott insulators Na_2IrO_3, α-$RuCl_3$ as well as $(Na_{1-x}Li_x)_2IrO_3$. This work was part of the E6 project of the collaborative research center TRR80 with the title: “Topological Quantum Phases in Correlated Electron Systems with Large Spin-Orbit Coupling”. The main task was the investigation of magnetization of the systems in different crystallographic field and measurement directions. The magnetic anisotropies are providing insights about the exchange interactions and the g-factors anisotropy in the materials. Four questions were the basis of this work. First, is it possible to enhance the size of the Na_2IrO_3 single crystals to enable a

broader range of measurements on them? Second, can we measure the transverse magnetization of α-$RuCl_3$ with the transverse option of the MPMS as it has been done by [21] and repeat the measurement on Na_2IrO_3 single crystals? Third, is there an in-plane anisotropy of Na_2IrO_3 single crystals? Fourth, how does the in-plane versus out-of-plane anisotropy in the longitudinal magnetization develop with the doping concentration for $(Na_{1-x}Li_x)_2IrO_3$? To answer these questions, the thesis is organized as follows:

Chapter 2 introduces basic concepts regarding strongly correlated materials and the magnetism we find in these materials. Furthermore, it gives an overview over important quantities that determine the magnetic moment and the magnetic interactions in d transition metal compounds, which is the material class the investigated compounds belong to.

Chapter 3 describes applied experimental methods to synthesize the samples, characterize them structurally and analyze their magnetic behavior.

In Chapter 4, a historical outline of the discovery of the Kitaev model candidates Na_2IrO_3, α-Li_2IrO_3 and α-$RuCl_3$ as well as an overview of the current knowledge about these materials is given regarding the synthesis procedures, the crystal structures as well as magnetic properties and doping experiments.

The results of this work are presented in Chapter 5. It is structured according to the material systems. Studies of the longitudinal and transverse susceptibility of α-$RuCl_3$, Na_2IrO_3 and $(Na_{1-x}Li_x)_2IrO_3$ in different crystallographic directions are combined with X-ray diffraction measurements. Additionally, factors of the synthesis of Na_2IrO_3 are investigated and the newly implemented transverse option of our MPMS thoroughly tested.

The last part, Chapter 6, summarizes and discusses the results of this work and provides ideas for further experiments.

Please note that all acronyms used in this work are listed in the appendix in section A.1.

2 | Strongly Correlated Materials

In typical insulators the electrons are localized to their atom and can be modeled without an interaction of the electrons on different atoms. For metals with freely moving electrons the interaction between those electrons can often be approximated by a mean-field, which is the same for all electrons. If both models fail to describe the observed physics, the electrons cannot be described by single-electron states and the electron system is called *correlated*. The electron-electron interaction depends strongly on the specific electronic environment the electrons are in and is found for most materials with incomplete d or f shell. Narrow bands enhance the effect of electron-electron correlations. If we now look at atoms in the order of 10^{23}, such problems can in general not be solved analytically. This requires the construction of models, which of course cover only a part of the physical realities. In the first section we want to look at some basic models for electron systems and introduce *Mott-insulators*, a class of materials which all compounds covered in this thesis belong to. The magnetism of insulators is governed by the local magnetic moments originating from the spin and orbital angular momentum of the electrons in each magnetic ion. This will be discussed in the second section, while introducing important concepts, which are needed later on. The last section will cover important parameters determining the electronic occupation and, therewith, the magnetic moment of the d transition metal compounds. The rich physics in correlated materials stems from the competition between charge, spin, orbital and lattice degrees of freedom, which can all have the same energy scale. This evokes new physical phenomena such as the Mott insulator, high-temperature superconductivity, topological insulators, semimetals and many more. [22–24]

2.1 Models of electron systems

The *free electron gas* is the simplest model of an electronic system. The electrons behave like a non-interacting gas, but must obey the Pauli principle. Therefore, only two electrons (spin up and spin down) can occupy the same energy state. The result for 3 dimensions for $T = 0\,\mathrm{K}$ is the Fermi sphere in k-space with electrons in the energetically highest states lying at the surface of the sphere with an energy E equal to the Fermi energy E_F. This model works well enough for metals, especially alkali metals. Here, only the delocalized s electrons are responsible for most physical properties. An electron can be seen as moving in an averaged potential produced by the other ions and electrons or as a quasiparticle, which behaves like an electron with an altered mass m^*.

If we now go from s electrons to electrons in d (or f) orbitals, they become more localized to their atom and the free electron gas model does not hold anymore. For these electrons we can start with the *tight-binding approximation*. In contrast to the free electron gas, the electrons are assumed to be restricted to the atoms. This approach still neglects the interaction between the electrons. Combining the orbitals of all isolated atoms leads to the formation of different bands, where the electrons reside. Materials with completely filled bands become insulators or semiconductors, depending on the size of their band gap and materials with partially filled bands form metals.

For many systems, this does not go far enough, because the interaction between the electrons is of great importance. Such systems are called *correlated electron systems*. They typically have an partially filled d or f shell with narrow bands. The most successful model describing electronic correlations is the *Hubbard model*. It can be viewed as the extension of the tight-binding model, adding the on-site electron-electron interaction. It is built by two quantities: The first one is the Coulomb energy U which is the energy that has to be overcome to put two electrons into the same orbital (obeying the Pauli principle). The second one is the hopping parameter t which describes the overlap of the orbital functions and is, therefore, a measure how easily the electrons can hop between different atoms. One can think of t as the kinetic energy and U as the potential energy. This simple model only includes an atom at each lattice site with one orbital, ignoring the

rest. Just by looking at the ratio U/t, we can describe many interesting effects. One example are the so-called *Mott insulators*. These systems are predicted to be metals by the tight-binding model, but become insulating when introducing U. In such a case, the energy cost to have two electrons on the same site (U) is higher than the energy gain won from allowing the electrons to hop. In other words, for $U/t \gg 1$ the model predicts an insulator, where the Coulomb energy opens up a gap in the band, as shown in Figure 2.1. Additionally, a Mott insulator will show an antiferromagnetic ordering, since there will be some hopping to the nearest neighbors, giving the need of antiparallel spins between neighbors. On the other hand, if $U/t \ll 1$ the system will favor to let the electrons move freely through the lattice and we will find a metal. In between is a metal-insulator transition. [2]

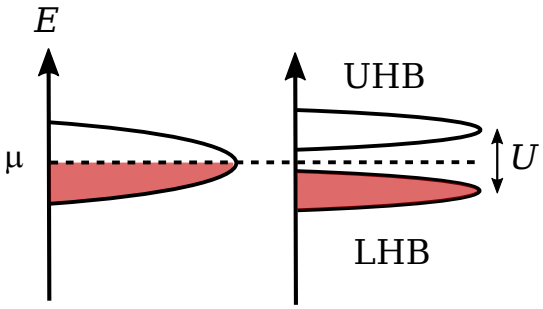

Figure 2.1.: A narrow half-filled band can be split into an upper Hubbard band (UHB) and a lower Hubbard band (LHB) due to a strong Coulomb repulsion, turning the system into a Mott insulator (figure inspired by [25]).

2.2 Magnetism of local moments

A large part of the research in solid state physics investigates the magnetism of local moments, which is caused by the spin and orbital motion of electrons localized to their atom. Here, the weaker magnetism caused by itinerant electrons as well as the atomic nuclei is neglected. Today we know many different forms magnetism can appear in. In the first part, we will look at the basic forms and will then, step by step, introduce important physical quantities and concepts. The second part will take a closer look at how the exchange interactions between the atomic moments arise, which are essential for most magnetic phenomena. At last, the field of frustrated magnetism is introduced and the concepts of a spin liquid explained. For this section [2] and [26] serve as references, except for the frustrated magnetism section, which is based to a large part on [27].

2.2.1 Fundamental forms

Diamagnetism

Diamagnetism is the weakest form of magnetism of local moments. All materials show a diamagnetic moment to some degree. It is characterized by a negative susceptibility. The magnetic susceptibility χ provides us with a quantity that states how the magnetization M (sum of magnetic moment per volume) of a system reacts to an external magnetic field H. It is defined as:

$$\chi = \frac{\partial M}{\partial H}. \tag{2.1}$$

A negative χ therefore corresponds to a magnetic system where the magnetization points in the opposite direction of the field, thereby weakening it. Diamagnetic materials show susceptibilities in the order of 10^{-4} to 10^{-6}(SI). Only superconductors in the Meissner phase are 'perfect' diamagnets with $\chi = -1$, which completely suppress the external field inside the magnet. The magnetization of diamagnets shows a linear behavior with field H and is constant with temperature T (Figure 2.2). M originates from the change of the orbital motion of the localized electrons by the magnetic field.

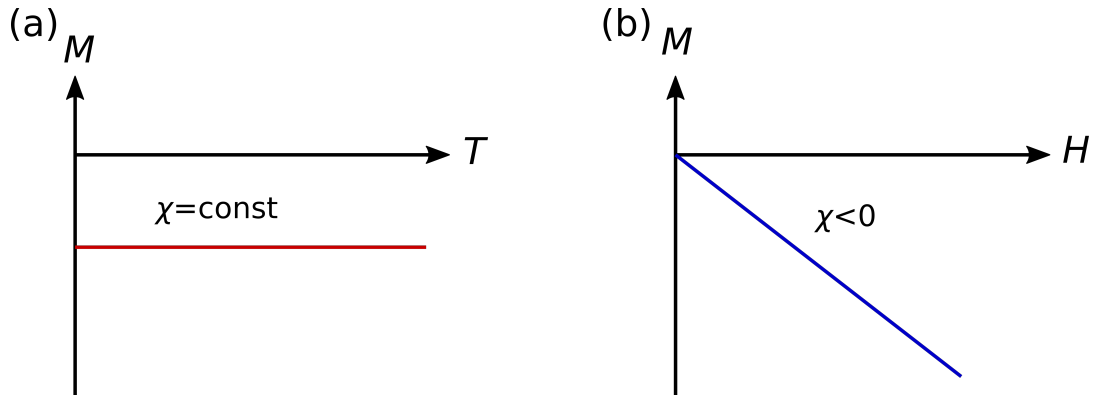

Figure 2.2.: Diamagnetic materials show a constant temperature dependence (a) and a linear field dependence (b). χ is always negative.

In this thesis diamagnetism will not play an important role. To receive more accurate data, it is sometimes necessary to subtract diamagnetic contributions. The

magnetism that we are interested in is the stronger magnetism that originates only from unpaired electrons of the ions, which will be discussed in the following.

Paramagnetism

Larger magnetic moments can be reached in paramagnetic materials. Paramagnetism (as well as all the following forms of magnetism) results from spin S and orbital momentum L of the localized electrons in the material.
For fully filled shells the quantum numbers L and S are 0. Therefore, only atoms with unpaired electrons can exhibit paramagnetism. The magnetic moments of the atoms align to an applied magnetic field H, which corresponds to a positive susceptibility ($\chi > 0$). If $H = 0$, the moments point randomly throughout the crystal. Interactions between the moments are weak and are overcome by the thermal energy. The value of the magnetization M depends on the ratio of the size of the Zeeman energy and the thermal energy, the two competing quantities in such a system:

$$x = \frac{E_{\text{Zeeman}}}{E_{\text{thermal}}} = \frac{g\mu_{\text{B}} J \cdot B}{k_{\text{B}} \cdot T} \tag{2.2}$$

with the total angular momentum J, which depends on S and L, and g as the Landé g-factor, which is defined as

$$g = 1 + \frac{J(J+1) + S(S+1) - L(L+1)}{2J(J+1)}.$$

The magnetization of a paramagnetic material is described by

$$M = ng\mu_{\text{B}} J\mathcal{B}(x), \tag{2.3}$$

where $ng\mu_{\text{B}}J$ describes the saturation magnetization M_{s}, n the number of magnetic atoms per volume and $\mathcal{B}(x)$ the Brillouin function:

$$\mathcal{B}(x) = \frac{2J+1}{2J} \coth\left(\frac{(2J+1)x}{2J}\right) - \frac{1}{2J} \coth\left(\frac{x}{2J}\right)$$

using the argument x from equation 2.2. For the limit of very large fields ($B \to \infty$) or very small temperatures ($T \to 0$) is $x = \infty$. In this regime, all moments are aligned with the field and $M = M_{\text{s}}$. On the opposite side for small fields and high

temperatures is $x \ll 1$ and the equation 2.3 can be simplified to

$$M \approx \frac{ng^2\mu_B^2 J(J+1)B}{3k_B T} = \frac{n\mu_{\text{eff}}^2 B}{3k_B T}, \tag{2.4}$$

introducing the effective moment $\mu_{\text{eff}} = g\mu_B\sqrt{J(J+1)}$. It can be used to quantify the paramagnetism in the system and is directly linked to the quantum number J. Using a second approximation, $B = \mu_0(H+M) \approx \mu_0 H$ as well as equation 2.1 and 2.4, we derive for the susceptibility:

$$\chi \approx \frac{n\mu_0\mu_{\text{eff}}^2}{3k_T} = \frac{C}{T}. \tag{2.5}$$

This is known as *Curie's law* with the Curie constant C, which is different for each material. For a paramagnetic system in the suitable regime, high enough T and low enough B, the inverse of the susceptibility χ^{-1} shows a linear behavior with temperature. Whatever is "high" or "low enough" depends on the specific system, the magnitude of its magnetic energy. Another prerequisite for Curies law is an unchanging distribution of the occupied orbitals, keeping the quantum numbers unchanged.

Magnetic order: ferro- and antiferromagnetism

Up to now we have assumed the influence of the magnetic moments of the neighboring ions is negligible. This is true if the temperature is sufficiently larger than the interaction, caused by electron-electron correlations, between them. In this parameter range, the moments look like a paramagnet (PM) and it is, therefore, called the paramagnetic phase. In most materials, though, there is a point in temperature when the kinetic energy is lower than the potential energy from their neighboring magnetic moments. If no field is applied, the moments will then order into fixed structures. This is called the ordered phase. The magnetic structure can be ferromagnetic (FM) – moments aligned parallel to their neigh-

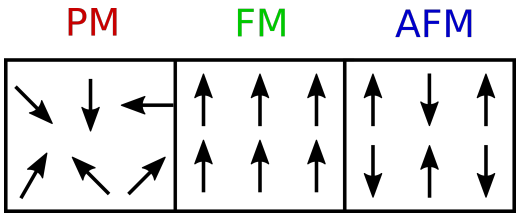

Figure 2.3.: Above the magnetic transition temperature the materials behave like a paramagnet (PM) with a random distribution of the moments. Below they order parallel (FM) or antiparallel (AFM).

bors –, antiferromagnetic (AFM) – moments aligned antiparallel to their neighbors – (see Figure 2.3) or any combination of the two. The ordering is accompanied by a phase transition and its transition temperature called Néel temperature T_N for antiferromagnets and Curie temperature T_C for ferromagnets. If a material shows an ordered phase, Curie's law needs to be altered and the Weiss temperature θ_W is introduced. This is the so-called *Curie-Weiss law*:

$$\chi = \frac{C}{T - \theta_W}. \tag{2.6}$$

Compared to a paramagnet is χ^{-1} of ferromagnets and antiferromagnets in the linear, paramagnetic phase shifted with θ_W being the x-intercept (see Figure 2.4).

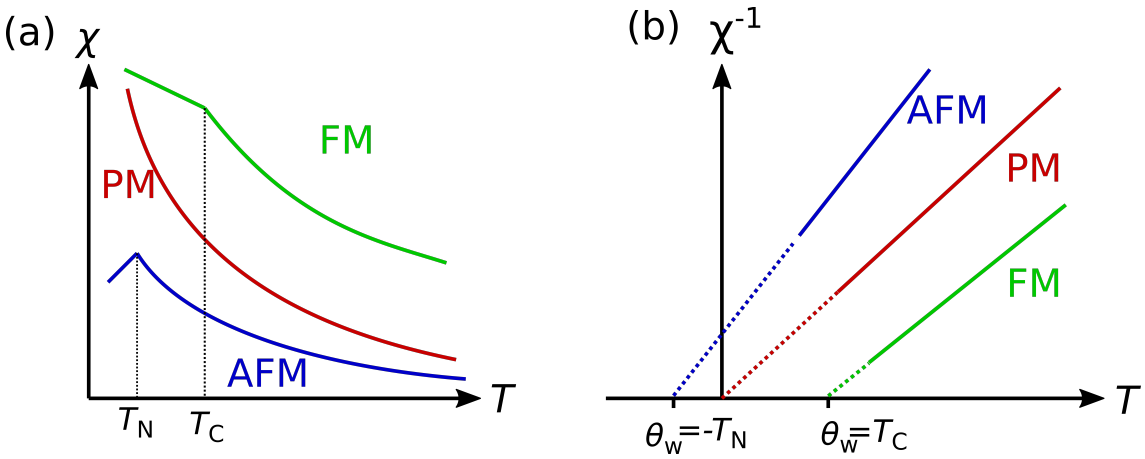

Figure 2.4.: Schematic comparison of $\chi(T)$ (a) and the $\chi^{-1}(T)$ (b) for a paramagnet (PM), a ferromagnet (FM) and an antiferromagnet (AFM) in a small magnetic field B. In the paramagnetic phase, χ^{-1} shows a linear behavior with different x-intercept θ_W. While χ decreases towards smaller temperatures in the ordered phase for an AFM, it increases for a PM and a FM.

Depending on the type of order, the Weiss temperature will be equal to the Néel temperature ($\theta_W = T_N$) (FM) or the negative of the Curie temperature ($\theta_W = -T_C$) (AFM). Just as Curie's law is only valid for a certain field and temperature regime, the same holds true for the extended Curie-Weiss law. At temperatures close to and lower than $T_{N,C}$ the inverse susceptibility χ^{-1} deviates from the linear behavior in T. At the ordering temperature the susceptibility $\chi(T)$ shows a maximum or kink.

The magnetization M and the susceptibility χ are suitable quantities to observe the magnetic order and gain basic information about the magnetic energy of the

system and the electronic occupation. The next section will give an introduction to exchange interactions, which determine the magnetic order.

2.2.2 Exchange interaction

Magnetic interactions are of purely quantum mechanical origin. They arise due to the overlap of wave functions and due to the fact that two identical particles (electrons in our case) must obey exchange symmetry.
When the wave functions of two identical particles $\psi_\mathrm{a}(\boldsymbol{r}_1)$ and $\psi_\mathrm{b}(\boldsymbol{r}_2)$ overlap, the joint wave function is the product of both states $\psi_\mathrm{a}(\boldsymbol{r}_1)\psi_\mathrm{b}(\boldsymbol{r}_2)$. When we now do an experiment, we will not be able to distinguish which of the two particles we have measured. This gives rise to the need that exchanging the two particle must leave the overall wave function unchanged. This is not fulfilled for the product state. Since electrons must have an antisymmetric wave function, the spin state can either be a symmetric triplet state χ_T (S=1) for an antisymmetric spatial state or antisymmetric singlet state χ_S (S=0) for a symmetric spatial state. The wave functions which fulfill both requirements are:

$$\Psi_\mathrm{S} = \frac{1}{\sqrt{2}}[\psi_\mathrm{a}(\boldsymbol{r}_1)\psi_\mathrm{b}(\boldsymbol{r}_2) + \psi_\mathrm{a}(\boldsymbol{r}_2)\psi_\mathrm{b}(\boldsymbol{r}_1)]\chi_\mathrm{S}$$
$$\Psi_\mathrm{T} = \frac{1}{\sqrt{2}}[\psi_\mathrm{a}(\boldsymbol{r}_1)\psi_\mathrm{b}(\boldsymbol{r}_2) - \psi_\mathrm{a}(\boldsymbol{r}_2)\psi_\mathrm{b}(\boldsymbol{r}_1)]\chi_\mathrm{T}$$

with the corresponding energies:

$$E_\mathrm{S} = \int \Psi_\mathrm{S}^* \hat{\mathcal{H}} \Psi_\mathrm{S} d\boldsymbol{r}_1 d\boldsymbol{r}_2 \qquad \text{and} \qquad E_\mathrm{T} = \int \Psi_\mathrm{T}^* \hat{\mathcal{H}} \Psi_\mathrm{T} d\boldsymbol{r}_1 d\boldsymbol{r}_2.$$

Assuming normalized χ_S and χ_T, the energy difference of both states is given by twice the *exchange integral* or *exchange constant* J:

$$E_\mathrm{S} - E_\mathrm{T} = 2J = 2\int \psi_\mathrm{a}^*(\boldsymbol{r}_1)\psi_\mathrm{b}^*(\boldsymbol{r}_2)\hat{\mathcal{H}}\psi_\mathrm{a}(\boldsymbol{r}_2)\psi_\mathrm{b}(\boldsymbol{r}_1)d\boldsymbol{r}_1 d\boldsymbol{r}_2$$

As a consequence, a positive J will favor a triplet state (S=1) and a negative J the singlet state (S=0). One can now construct a spin-dependent term of an effective

Hamiltonian (for more information see [2, p.75]) of the form:

$$\hat{\mathcal{H}}_{\text{spin}} = -2J\boldsymbol{S}_1 \cdot \boldsymbol{S}_2.$$

In the *Heisenberg model* one assumes such an interaction between each neighboring atom, simply adding up over all individual interactions between site i and j.

$$\hat{\mathcal{H}}_{\text{Heis}} = -\sum_{i,j} J_{ij}\boldsymbol{S_i} \cdot \boldsymbol{S}_j.$$

The factor 2 disappears due to the double counting as a consequence of summarizing over i and j. In this model, one can even use the approximation of a constant $J_{i,j} = J$ for all sites as well as adding interactions of the same form between next nearest neighbors or next next nearest neighbors. The same argument as above gives rise to ferromagnetic ordering for $J > 0$ and an antiferromagnetic one for $J < 0$.

The exchange interaction between the atoms can be due to the direct overlap of the wave functions or (most of the time) indirect. In the *superexchange* the overlap is produced via another non-magnetic ion, placed in between the magnetic ones. The *RKKY interaction*, on the other hand, uses the conduction electrons to mediate the exchange, which is why it is only found in metals. All interactions mentioned up to here either lead to parallel or antiparallel order of the magnetic moments. Completely different in this regard behaves the *Dzyaloshinskii-Moriya interaction*. This exchange can be found as a second-order perturbation of spin-orbit coupling in a superexchange and leads to canting of otherwise (anti)parallel aligned moments. Accordingly, it cannot be described by a Heisenberg term, but possesses the form:

$$\hat{\mathcal{H}}_{\text{DM}} = \boldsymbol{D}_{ij} \cdot \boldsymbol{S}_i \times \boldsymbol{S}_j.$$

Of course there are many more types of interactions possible and often more than one are competing with each other. For the specific materials studied in this thesis, we also find the bond-directional *Kitaev exchange* (later explained in Section 2.2.4) and *symmetric off-diagonal exchange*, named Γ [11] and Γ' [28] (see Section 4.3.3), to be of importance. Off-diagonal exchange evokes interactions between orthogonal spin directions of neighboring atoms. The Dzyaloshinskii-Moriya interaction is an off-diagonal exchange as well, though an antisymmetric one. In contrast, the Heisenberg interaction only connects same spin-directions between the atoms. This is more

easily comprehended by looking at a general tensor for the different interactions of Heisenberg ($\boldsymbol{J}_{\mathrm{H},ij}$), Dzyaloshinskii-Moriya ($\boldsymbol{J}_{\mathrm{D},ij}$) and symmetric off-diagonal exchange ($\boldsymbol{J}_{\Gamma,ij}$) (only for Γ) . When casting it into the form:

$$\mathcal{H} = \sum_{ij} \boldsymbol{S}_i \cdot \boldsymbol{J}_{ij} \cdot \boldsymbol{S}_j,$$

we get [15]:

$$\boldsymbol{J}_{\mathrm{H},ij} = \begin{pmatrix} J_a & 0 & 0 \\ 0 & J_b & 0 \\ 0 & 0 & J_c \end{pmatrix} \quad \boldsymbol{J}_{\mathrm{D},ij} = \begin{pmatrix} 0 & D^{\mathrm{c}} & -D^{\mathrm{b}} \\ -D^{\mathrm{c}} & 0 & D^{\mathrm{a}} \\ D^{\mathrm{b}} & -D^{\mathrm{a}} & 0 \end{pmatrix} \quad \boldsymbol{J}_{\Gamma,ij} = \begin{pmatrix} 0 & \Gamma^{\mathrm{ab}} & \Gamma^{\mathrm{ac}} \\ \Gamma^{\mathrm{ab}} & 0 & \Gamma^{\mathrm{bc}} \\ \Gamma^{\mathrm{ac}} & \Gamma^{\mathrm{bc}} & 0 \end{pmatrix}.$$

2.2.3 Frustrated magnetism

When we go to more complex systems, new phenomena occur. One large research field focuses on *frustrated magnetism*. Here, the magnetic moments order at lower temperatures than we would expect from the Curie-Weiss temperature or, in the extreme case, do not order at all. Although the system would like to order, it is prevented to do so. There can be different reasons for such a phenomenon.

Geometrical frustration

The most prominent example of geometrical frustration are Ising-type spins (one easy axis) on a triangular lattice that couple antiferromagnetically. When two spins of a triangle have chosen their orientation, the third one does not know how to satisfy the interaction to both spins (Figure 2.5). The same is true for a three-dimensional antiferromagnetically coupled tetrahedron. The spins can only couple antiparallel to one of the two neighbors.
[2, p.166-167]

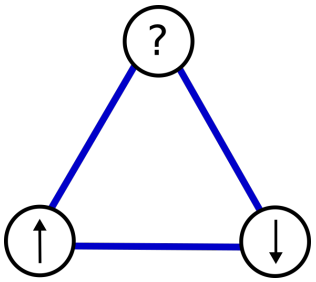

Figure 2.5.: Geometrical frustration of Ising spins on a triangular lattice.

Exchange frustration

When different exchange interactions are competing, it is possible that they contradict each other. This is called exchange frustration. Imagine a square lattice with antiferromagnetic nearest-neighbor interaction J_1 and next-nearest-neighbor interaction J_2 (Figure 2.6). In the weak J_2 limit, the system shows a Néel ordered ground state. When J_2 becomes comparable to J_1, the system cannot satisfy all interactions and we find strong frustration. Another prominent example of such an exchange frustration is the Kitaev interaction, which will be explained in detail in Section 2.2.4. [29]

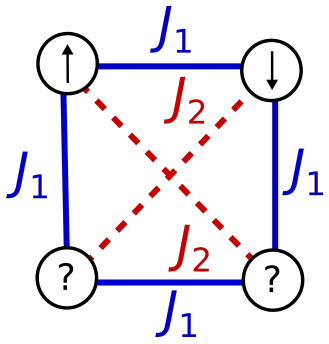

Figure 2.6.: Two competing antiferromagnetic exchange interactions J_1 and J_2 with equal size on a square lattice will lead to strong frustration.

Besides special lattice structures or competing interactions, a disordered system leads to frustration as well. A diluted magnetic system where magnetic ions randomly sit between non-magnetic ions or varying exchange interactions due to randomly distributed bond partners involved in the indirect exchange interaction makes it hard for the moments to order in one certain way. Such a system is called a spin glass. [2, 167-169] At one point in temperature, the magnetic moments of the frustrated systems will either order or freeze in one spin configuration.

Spin liquid

What all types of frustration have in common is the fact that, instead of one ground state, we find many energetically equivalent states in between which the system is fluctuating at low temperatures. Compared to a paramagnet, these fluctuations are strongly correlated. This means that each spin is influenced strongly by its surrounding.
A common measure for the frustration of a material is the frustration factor f:

$$f = \frac{\theta_{\mathrm{W}}}{T_{\mathrm{C,N}}}, \tag{2.7}$$

the ratio between the Weiss temperature θ_{W} and the ordering temperature T_{C} or T_{N}. The phase in the range between these temperatures ($T_{\mathrm{C,N}} < T < \theta_{\mathrm{W}}$) is called

a *spin liquid*. Here, the moments are still fluctuating, but show strong short-range correlations. A spin liquid can be either classical or quantum.

A *classical spin liquid* will have classical fluctuations, which are driven by the thermal energy $k_B T$. If the temperatures are low enough, the fluctuations will vanish and the moments order in one possible ground state. This can be found for systems with large spin S as $Dy_2Ti_2O_7$. Here, the large f-electron spins of Dy are sitting on the corner of two tetrahedra. The easy axis is aligned along the connection of the center of these tetrahedra and is therefore different for each spin in the tetrahedron. Altogether, this leads to a frustrated state called *spin ice*. The name does not stand in contrast to a spin liquid, but rather describes the orientations of the spins in one tetrahedron. Just like in ice, where two hydrogen atoms are far and two are close to the oxygen atom, in spin ice systems two spins point inwards and two outwards (Figure 2.7). The energy for all 6 spin configurations obeying the 'ice rule' in one tetrahedron is equal and the system will fluctuate between these states. Since each spin is integrated in two tetrahedra, the number of degenerate states that minimize the energy is large. When the thermal energy is lower than the energy barrier to flip between different ice-rule configurations, the moments freeze in this state.

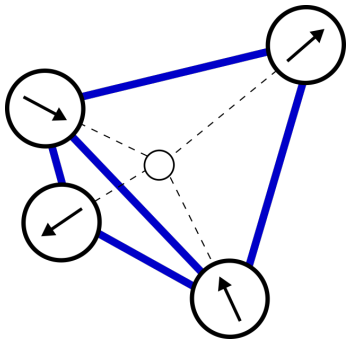

Figure 2.7.: Spin ice: a spin liquid with two spins pointing inwards and two pointing outwards on a tetrahedron.

Even more interesting are *quantum spin liquids* with quantum fluctuations. There is no obvious energy barrier between the possible spin configurations, which is why they persist down to 0 K. The spins are highly entangled and this leads to new exotic phenomena as e.g. fractional quantum numbers. Quantum spin liquids can be found for atomic spins comparable to 1/2, since here the quantum mechanical uncertainty principle produces a zero-point motion of the size of the spin. For example, there can also be a quantum spin ice. Many researchers have tried to achieve a quantum spin liquid. There are trials with artificial lattices for ultracold atoms. Another approach is to search in real materials, which has lead, among other work, to this thesis.

2.2.4 Kitaev honeycomb model

When Kitaev proposed his now called 'Kitaev model' in 2006 [3] , the physics community was excited. It is one of the rare theoretical models that describes very complex and exotic physics and is still analytically solvable. Hence, it is highly desirable to search materials inhibiting the Kitaev interaction. The building blocks for this model are:

1. a 2d honeycomb lattice
2. 1/2-spins sitting on each corner
3. exchange interactions, which couple different spin components with each neighbor

This setting is shown in Figure 2.8. The different exchange interactions are visualized by three different links: x, y, z. The name of the link describes the component

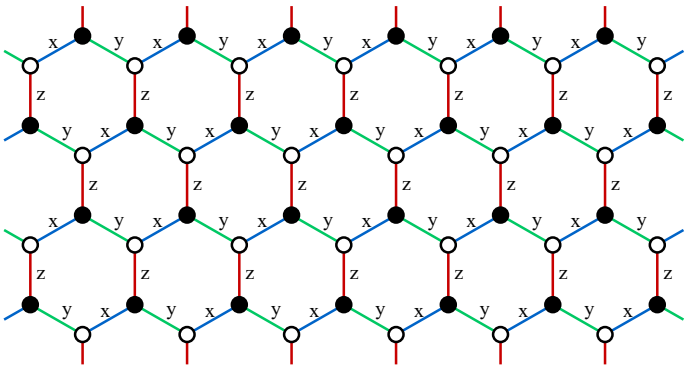

Figure 2.8.: The Kitaev model describes 1/2-spins sitting on the corners of a honeycomb lattice with orthogonal, Ising-like exchange interaction. Each spin has three neighbors, hence three different interactions labeled with x, y and z. Figure adapted from [3].

of the spin, which takes part in the interaction of these bonds. Therefore, the spin of one electron tries to align with each of its three neighbors in three different directions. While the actual direction of the couplings are irrelevant to the problem, it is important that they are orthogonal to each other. The corresponding Hamiltonian can be written as:

$$\mathcal{H} = -J_x \sum_{i,j} \sigma_i^x \sigma_j^x - J_y \sum_{i,j} \sigma_i^y \sigma_j^y - J_z \sum_{i,j} \sigma_i^z \sigma_j^z$$

with σ^{x}, σ^{y} and σ^{z} being the Pauli operators and J_x, J_y, J_z the corresponding coupling constants for each link. Let us assume $J_x = J_y = J_z$. For this case, we will find a highly frustrated system. To solve this problem the spins operators are mapped to four Majorana operators b_i^x, b_i^y, b_i^z, c_i, resulting in a quadratic Hamiltonian that can be exactly diagonalized.
Figure 2.9 shows the solution of the ground state as a phase diagram in dependence of the exchange interactions for $J_x, J_y, J_z \in [0, 1]$ (ferromagnetic interactions).

The ground state is either a gapped (area A) or a gapless (area B) quantum spin liquid, depending on the exchange parameters. In area B a gap opens in a magnetic field. Within these gapped phases, anyonic excitations arise connected to topological order. Kitaev already proposed in 2003 that a two dimensional system with anyonic excitations could be used as a fault-tolerant quantum computer [30]. The fact that the model is analytically solvable as well as the prospect of better quantum computer material opened the race for the search of the Kitaev model materials. [3, 31]

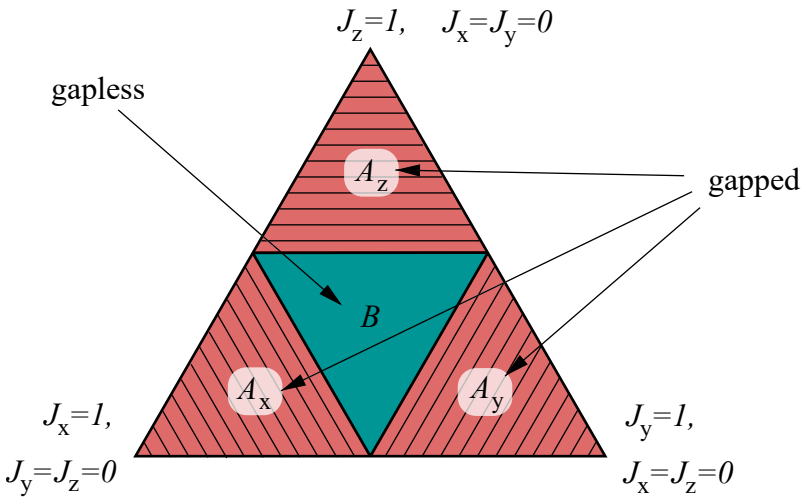

Figure 2.9.: The solution of the Kitaev model is exact using Majorana fermions as excitations and results in a quantum spin liquid ground state, which is either gapped or gapless. Figure adapted from [3].

2.3 *d* transition metal compounds

Since transition metal compounds will be the subject of this thesis, we will take a closer look at which properties influence their electronic structure and, hence, their magnetism. First of all, transition metals (TMs) include all elements of the group 3−12, with either d or f electrons responsible for the magnetic behavior of the material. We will only focus on d transition metals. The ligand atoms (L) form the environment for the TM. Depending on their arrangement around the TM, different atomic orbitals of the TM are energetically favoured. This *crystal field* together with the *Hund's coupling* determine the distribution of the electrons into these orbitals and, henceforth, the size of the quantum numbers S and L. An additional contribution from the *spin-orbit coupling* alters these quantities further by coupling S and L with each other and introduces the total angular momentum J as a new quantum number. The following sections will give a more detailed description of the relevant properties. If not stated differently, the used reference is [2].

2.3.1 Crystal field

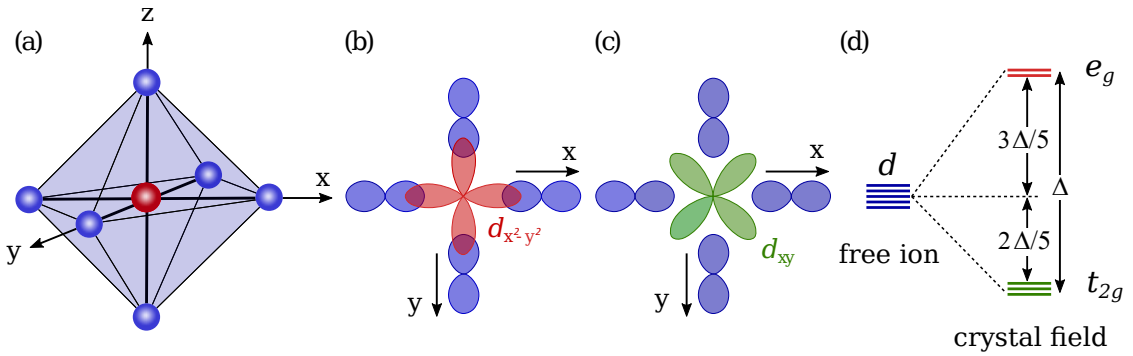

Figure 2.10.: In an octahedral environment (a) with the TM sitting between six L ions the d orbitals with large overlap of the p orbitals (b) are raised in energy, while the energy of the orbitals with smaller overlap (c) is reduced. Thus, the lower three-fold t_{2g} orbitals and the higher e_g orbital form, which are separated by the crystal field splitting Δ (d). Figure adapted from [2], p. 47.

There are five different d orbitals, which look slightly different for $3d$, $4d$ or $5d$ systems. Each of them can hold two electrons, which must differ in their spin orientation. Since the orbitals have an anisotropic form, the environment around

the ion (the position of the ligand atoms) becomes important. For example, d orbitals pointing towards an oxygen p-orbital will rise in energy due to repulsion of the electrons. In contrast, d orbitals which point in between have a lower energy. Hence, the degeneracy of the orbitals of the free metal ion is lifted. In an octahedral environment the crystal field results in three lower orbitals, the so-called t_{2g} orbitals, and two higher e_g states. Δ describes the difference in energy of the two states. An octahedral environment as well as two examples of d orbitals in this surrounding and the resulting crystal field splitting is shown in Figure 2.10.

2.3.2 Spin-orbit coupling

Spin-orbit coupling is a relativistic effect that couples the spin and orbital momentum of an electron, resulting in a change in the electron's energy level. For small atomic numbers this interaction can be taken as a small perturbation, while it becomes increasingly dominant for larger atoms.

In the common and well-known reference frame of an atom, the electron orbits the atomic nucleus. From the electron's point of view, however, the nucleus orbits the electron. The motion of the charged nucleus will create a magnetic flux density $\boldsymbol{B}$ acting on the spin of the electron $\boldsymbol{S}$. This will add the following term in the Hamiltonian:

$$H_{\mathrm{SO}} = -\boldsymbol{m} \cdot \boldsymbol{B}. \tag{2.8}$$

On the one side, the magnetic moment of the electron is given by :

$$\boldsymbol{m} = g\frac{\mu_{\mathrm{B}}}{\hbar}\boldsymbol{S} = g\frac{\mathrm{e}}{2m_{\mathrm{e}}}\boldsymbol{S} \tag{2.9}$$

where g is the Landé g-factor and $\mu_{\mathrm{B}} = \mathrm{e}\hbar/(2m_{\mathrm{e}})$ the Bohr magneton, which is defined by the electron's charge e and mass m_{e}. On the other side, the magnetic field is determined by the electric field $\mathcal{E} = -\boldsymbol{r}/r\, dV(r)/dr$ via the spherical potential energy $V(r)$ and the velocity $\boldsymbol{v}$ of the nucleus and the speed of light c:

$$\boldsymbol{B} = \frac{\mathcal{E} \times \boldsymbol{v}}{\mathrm{c}^2} = -\frac{dV(r)}{dr}\frac{1}{r\mathrm{c}^2}\boldsymbol{r} \times \boldsymbol{v}. \tag{2.10}$$

Inserting equation 2.9 and 2.10 into equation 2.8 results in:

$$\mathcal{H}_{\mathrm{SO}} = \frac{dV(r)}{dr}\frac{g\mathrm{e}}{2m_{\mathrm{e}}r\mathrm{c}^2}\boldsymbol{S}\cdot(\boldsymbol{r}\times\boldsymbol{v}).$$

If we now use the fact that the orbital angular momentum equals $\hbar\boldsymbol{L} = m_{\mathrm{e}}\boldsymbol{r}\times\boldsymbol{v}$, we find the interaction between $\boldsymbol{S}$ and $\boldsymbol{L}$:

$$\mathcal{H}_{\mathrm{SO}} = \frac{dV(r)}{dr}\frac{g\mathrm{e}\hbar}{2m_{\mathrm{e}}^2r\mathrm{c}^2}\boldsymbol{S}\cdot\boldsymbol{L}.$$

For a hydrogen-like atom (a nucleus with atomic number Z and one electron) we can further assume:

$$\frac{1}{r}\frac{dV(r)}{dr} = \frac{Ze}{4\pi\epsilon_0 r^3}$$

as well as:

$$\frac{1}{r^3} = \frac{Z^3}{a_0^3n^3l(l+\frac{1}{2})(l+1)}$$

for the electronic state with quantum numbers l and n using the Bohr radius a_0. In the end, neglecting all constants, the spin-orbit coupling merely depends on the atomic number Z, the quantum numbers l and n as well as the scalar product of $\boldsymbol{S}$ and $\boldsymbol{L}$:

$$\mathcal{H}_{\mathrm{SO}} = \lambda\boldsymbol{S}\cdot\boldsymbol{L} \propto \frac{Z^4}{n^3l(l+\frac{1}{2})(l+1)}\boldsymbol{S}\cdot\boldsymbol{L}.$$

The spin-orbit coupling constant λ gives the strength of the coupling. To obtain the correct equation, a factor of 1/2 (Thomas precession factor) needs to be multiplied to the derived equations, which originates from the relativistic character of the spin-orbit coupling. This is of course a rough approximation, since in non-hydrogen atoms other electrons influence the electric field of the electron as well. Their influence will be smaller, though, due to the smaller charge of the electrons compared to the nucleus. Spin-orbit coupling shifts the energy states, therefore lifting degeneracy and gives rise to anisotropic atomic moments.

2.3.3 Coulomb repulsion

Coulomb's law states that two charges of the same kind will repel each other. Equivalently, this is true for two electrons in the same orbital. The intraorbital Coulomb repulsion U is the energy that has to be overcome in order to put two electrons in the same orbital. Although a metal with itinerant electrons is energetically favorable, a metal to insulator transition occurs, if the energy of the Coulomb repulsion (due to electrons on the same site and orbital) becomes larger than the energy gained from the motion of the electrons.

2.3.4 Hund's rules and Hund's coupling

Hund's rules determine the way the orbitals are filled with electrons in the ground state. The rules are:

1. S must be maximized
2. L must be maximized
3. $J = |L - S|$ if the shell is less than half filled and

   $J = |L + S|$ if the shell is more than half filled

The first and second rule emerge to reduce Coulomb repulsion between the electrons. The third rule arises to minimize spin-orbit energy. Though, one finds many examples where the third rule is violated. According to the first rule, the spin S must be maximized. Therefore, all orbitals are filled first with one spin each, before a second spin is added. These rules only apply if all orbitals have the same energy. If the degeneracy is lifted, for example as a result of the crystal field or spin-orbit coupling, there are two possibilities: The first is called the high-spin configuration, where the first Hund's rule is still valid. Here, the system still saves more energy in separating the spins, although it needs to spend energy to lift some spins in higher states. In the low-spin configuration, the energy for putting spins in higher states exceeds the Coulomb repulsion and the energetically lower orbitals are filled first. Hund's coupling J_{H} is the difference in energy between putting one spin in the higher

empty orbital or to another spin in the lower orbital. It can, therefore, be seen as an intra-atomic exchange. [32]

3 | Experimental Methods

To obtain the results of this thesis a number of experimental techniques have been applied, which will be described in this chapter. One focus has been the crystal growth of Na_2IrO_3 and Li_2IrO_3. Although the systems are similar in structure and chemical composition, different growth techniques are needed to obtain powder as well as crystals for each of them. After synthesis the samples were characterized structurally by X-ray diffraction and chemically by EDX and LA-ICP-M spectroscopy. Hereby, the samples' composition and quality were investigated as well as their crystallographic orientation analyzed. Extensive effort was put into measuring the magnetization, longitudinal and transversal, for the different lattice orientations.

3.1 Growth Techniques

The basic idea of crystal growth is the same for all techniques. The educts are placed into a suitable crucible and protected from air if needed. The educts are heated to a temperature where they experience enough diffusion. The compound is then formed directly or while cooling down. Nevertheless, each technique has its unique advantages (and disadvantages) and typically only a few or even just one technique will produce the desired compound. Depending on the method different phases: solid, liquid or gaseous can be involved. In the following, three methods, relevant to this thesis, are presented shortly. The exact growth procedures will be described later in Chapter 4.

3.1.1 Calcination

Calcination refers to heating a material in order to cause decomposition. The name stems from "burning" limestone ($CaCO_3$) in order to lose CO_2 to produce cement from the resulting CaO. It can be applied for a variety of compounds, for example

to extract Li_2O and Na_2O from its carbonates[33]:

$$Li_2CO_3 \Longrightarrow Li_2O + CO_2 \quad @\ T \gtrsim 720°C$$
$$Na_2CO_3 \Longrightarrow Na_2O + CO_2 \quad @\ T \gtrsim 850°C.$$

3.1.2 Solid state reaction

One of the most important growth methods is by solid state reaction. It is based only on atomic diffusion. Since diffusion rates in solids are low, high temperatures are needed to realize the reaction on reasonable timescales. The starting materials are prepared stoichiometrically and ground thoroughly to increase surface area for reaction. The material is typically kept a long time at high temperatures. Since no additional substances are needed, contamination with undesired elements in a controlled atmosphere is not a problem. Nevertheless, such single crystals typically show significant defects due to small diffusion lengths.[34]

3.1.3 Chemical vapor transport

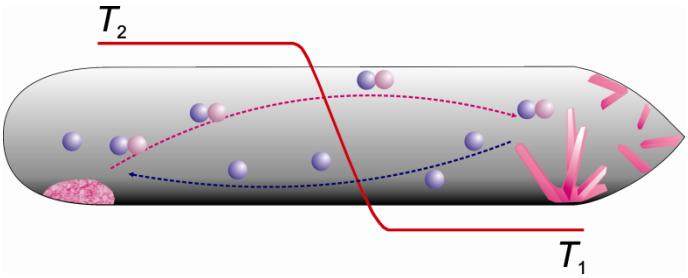

Figure 3.1.: A typical example of a CVT process: Solid material reacts with surrounding gas and is transported to the colder end of the crucible, where crystals grow[35].

A faster growth process is the chemical vapor transport (CVT), explained in detail in [35]. As the name suggests, this method involves the transport of gasses. The solid starting material either sublimates directly or, in the majority of cases, reacts with a surrounding gas, the transport agent, to form a gaseous phase. At a different site with different external conditions (typically a different temperature) the material resublimates under release of the transport agent, forming a crystal. This process is

additionally accompanied with a purification effect, but brings the need of a gradient inside the crucible. A typical growth process is schematically drawn in Figure 3.1.

3.2 X-ray Diffraction

X-ray Diffraction (XRD) is a common tool to characterize the crystallographic structure through the interaction of X-rays with the lattice atoms. It has been used to identify the different crystallographic phases. Apart from showing possible foreign phases, it gives rough insights in the quality of the samples as well as in the presence of certain defects. Furthermore, one can use it to determine the orientation of a crystal. In this thesis two different techniques where used, the *powder diffraction* and the *Laue diffraction*, which will be explained here. Both techniques are based on the idea that X-rays scatter at the atoms, which are arranged periodically in the lattice. At certain incidence angles θ for a certain wavelength λ and distances between atom layers d the waves will interfere constructively after scattering (Figure 3.2). In this case the difference in distance between photons scattering on neighboring layers is precisely a multiple of their wavelength. This is described by Bragg's law:

$$n\lambda = 2d\sin(\theta) \qquad n \in \mathbb{N}. \tag{3.1}$$

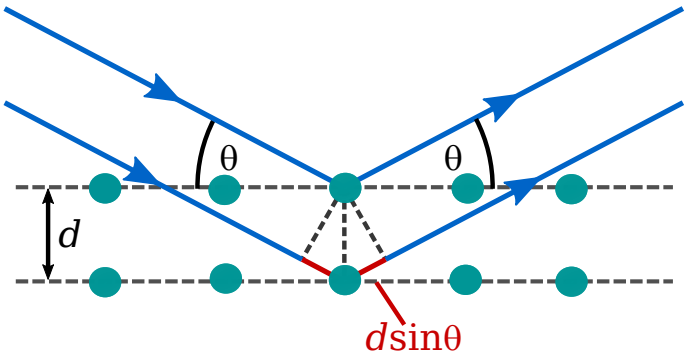

Figure 3.2.: Schematic view of Bragg's law. Two atomic layers show constructive interference for scattered X-rays in the angle θ if the difference of their travel distance $2d\sin(\theta)$ is a multiple of their wavelength λ.

3.2.1 Powder diffraction

For powder diffraction a Rigaku Miniflex 600 was used (Cu-K_α, $\lambda = 1.5406\,\text{Å}$, U=40 keV, A=15 mA). The X-ray source and the detector are located on opposite sides of the device with the sample positioned in between. Since powder will show every orientation of the system simultaneously, a signal is produced for the corresponding pairs of θ and λ in accordance to equation 3.1 for every symmetry plane of the system. To vary the angle θ the sample holder and the detector are rotated during the measurement. To improve statistics the sample is additionally rotated around the axis perpendicular to the sample holder. Such a setup is schematically shown in Figure 3.3. A more detailed description can be found in the manual [36]

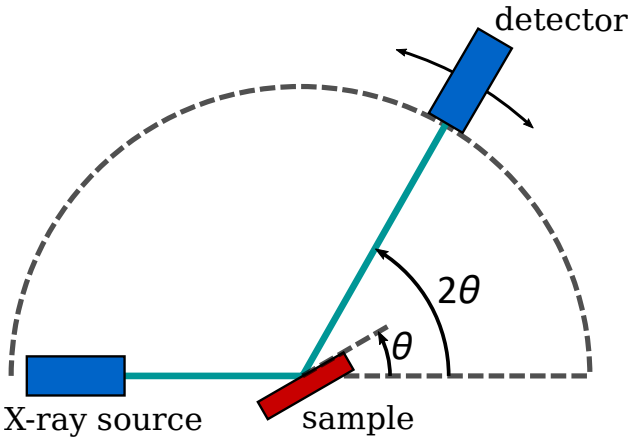

Figure 3.3.: Scheme of the powder diffraction experiment. A monochromatic X-ray beam is scattered at the sample. Sample and detector are rotated around θ and 2θ, respectively, in order to cover a large angular range.

and in [37]. This method gives information about the crystallographic structure and the lattice parameters and uncovers foreign phases. The powder is placed on a sample holder made of a silicon single crystal, oriented in a way to show no signal in the measurement regime. A drop of acetone assures that the powder stays on the holder during rotation.
A powder diffractometer can be used to measure a single crystal as well. Then, only the direction perpendicular to the sample holder is accessible. One has to consider that a single crystal possesses a certain height H, that shifts the angle θ artificially.

This needs to be accounted for by an additional term in Bragg's law[38]

$$n\lambda = 2d\sin(\theta - \frac{H}{R}\cos(\theta)) \tag{3.2}$$

, with R being the diffractometer radius.

3.2.2 Laue diffraction

When investigating single crystals, Laue diffraction is a helpful tool. In this work the images were made by the Laue camera Dual FDI NTX from Photonic Science using a Philips PW 1830 X-ray generator. Typical acceleration voltages range from 10-30 kV,which adjusts the maximal X-ray energy. The current was set to 30 mA for a sufficient intensity. The X-rays move through a hole in the middle of the detector onto the sample and are scattered back to the detector. Therefore, it is also called the Laue backscattering technique. Evidently, only a part of the symmetric planes of the sample are accessible in one measurement, planes orthogonal to the sample-source direction are not. Since the angle range of the detector is rather small, a wide spectrum of X-rays ensures equation 3.1 (Bragg's law) to give results for a wide range of possible d. One point in the detector plane corresponds to one family of parallel planes. Sharp round points are signs of excellent sample quality. Figure 3.4 shows an Na_2IrO_3 sample of good and poorer quality. Twinning and other rotational defects will easily be seen as additional features. Most important for us, though, is the

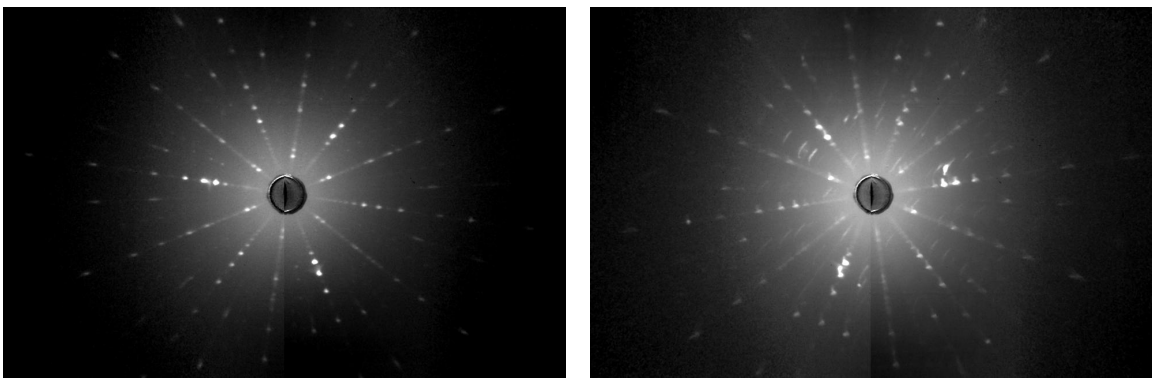

Figure 3.4.: Comparison of Laue patterns of Na_2IrO_3. While the left pattern shows mostly well defined diffraction points, the right one shows smeared points, which implies disorder in the crystallographic structure.

ability to identify the lattice axes for further uses, especially for the measurement

of the transversal magnetization (Section 3.4.2 on page 35).

For the measurement the sample is glued onto a goniometer, which can be rotated along all three axis separately. The angles are adjusted until a point of high symmetry is located in the center of the Laue pattern. The software "Crystal Maker" (version 10.5.5) is then used to clearly identify the orientation of the crystal and the direction of the axes. For more details please read [39].

3.3 Chemical Characterization

3.3.1 X-ray spectroscopy

The chemical characterization was performed by energy-dispersive X-ray spectroscopy (EDXS), implemented into a scanning electron microscope (SEM). Here, a small, focused beam of electrons is directed on the surface of sample, interacting with the atoms up to 1 μm depth. When moving the beam across the sample, the morphology of the surface can be analyzed by detecting backscattered or secondary electrons. A secondary electron is a product of ionization through an interaction of an electron exceeding the ionization energy. The empty state from a freed or excited electron will then be occupied from another electron in an energetically higher state. At the transition a photon is emitted possessing an energy equal to the energy difference of both states. Therefore, these element specific X-rays can be used in the EDX spectroscopy to determine the elements and their ratios. Only very light elements, H to Be cannot be detected and generally heavier elements possess a smaller error in the measurement. The reason is the fact that the lighter an element is the closer the energy levels and, consequently, the energies of the emitted X-rays will be. For elements smaller boron than (like lithium) the levels are simply indistinguishable from the background. Since the samples are placed on a carbon pad, there is always a large C background. [40, 41]

3.3.2 Inductively coupled plasma mass spectroscopy

A second technique to determine the chemical composition is inductively coupled plasma mass spectroscopy, short ICP-MS. It provides very precise results, even for

light elements as lithium and sodium. For this thesis the material was dissolved by laser ablation. The molecules are transported into a very hot plasma of Argon, which is generated by induction of a high-frequency electromagnetic field. This creates ions of all atoms, which are accelerated towards a mass spectrometer. By means of mass and charge each element can be uniquely identified and quantified. A detailed description can be found in [42].
These measurements were performed in the group of Prof. Dr. Wolfgang Bach by Dr. Andreas Klügel from the earth science department, University of Bremen.

3.4 Magnetization Measurement

The magnetic measurements are the central experiments of this work. The magnetization is measured in two different ways – longitudinal and transversal to the applied field direction. In general, the magnetic susceptibility is a 3x3 tensor, whose elements are

$$\chi^{ij} = \frac{\partial M_i}{\partial H_j}$$

with i, j=x,y,z can all be different depending on the crystallographic structure and the underlying magnetism. The longitudinal magnetization is hereby determined by the diagonal terms, while the transversal magnetization is described with the off-diagonal terms. Both methods will be explained in detail here.

3.4.1 Longitudinal magnetization

The longitudinal magnetization includes all susceptibility entries, where the magnetization and field vectors point in the same direction, hence $i = j$.

$$\underline{\chi} = \begin{pmatrix} \chi^{xx} & \chi^{xy} & \chi^{xz} \\ \chi^{yx} & \chi^{yy} & \chi^{yz} \\ \chi^{zx} & \chi^{zy} & \chi^{zz} \end{pmatrix}$$

This is true for most magnetization measurement setups. Our experiments were conducted in an MPMS3 (Magnetic Property Measurement System) from Quantum

Design. This device is able to reach temperatures as low as 1.8 K and as high as 400 K as well as fields up to 7 T[43].

The sample is moved inside the sample chamber, inducing a current in the superconducting pick-up coils (see Figure 3.5). These form a second-order gradiometer, which ideally only induces a current if the second-derivative of the magnetic flux is non-zero, reducing background noise. The actual measurement of the magnetic moment is then performed by a SQUID, a *superconducting quantum interference device*. It is located on the lower end of the device far below sample and magnet. It is capable of detecting smallest magnetic flux changes and needs therefore be shielded from any disturbing magnetic fields.[43, 44]

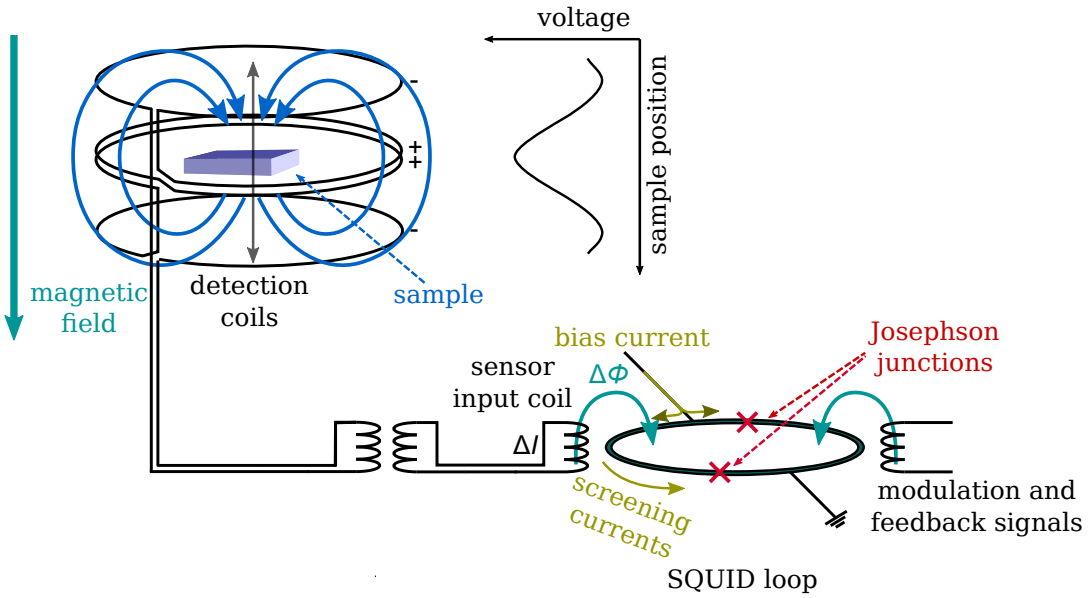

Figure 3.5.: Setup of the superconducting detection coils connected to the DC SQUID. The sample is moved through the coils, inducing a current. The SQUID transforms the current into a voltage signal, which gives a maximum (or minimum depending on the magnetic moment), when the sample is at the center of the coil setup. The respective height correlates to the size of the magnetic moment. The figure is adapted from [43] and [45]. Feedback and amplifying electronics were neglected.

The SQUID works as a current to voltage converter. It consists of a superconducting ring with one or two Josephson junctions. Any superconducting loop will only allow a magnetic flux inside, which is quantized in entities of the flux quantum $\Phi_0 = \frac{h}{2e} \approx 2.07 \cdot 10^{-15}$ Wb (1 Wb/m^2=1 T) with the Planck constant h and the

electronic charge e. If the flux is larger than a multiple n of Φ_0, a superconducting current I_s is induced inside the loop, which compensates the excess of flux until it reaches $n\Phi_0 + \Phi_0/2$. If the flux is increased further, the superconducting ring, instead of compensating, will enhance the flux to the next multiple $n+1$ of Φ_0. In the DC SQUID used here two Josephson junctions are incorporated parallel into a superconducting ring as shown in Figure 3.5. The name stems from the DC bias current $2I_b$ applied to the superconducting ring. The Josephson junctions consist of two superconductors, separated by a thin insulating or normal conducting layer. Each Josephson junction shows a voltage-current characteristic as seen in Figure 3.6. There will be a superconducting state for small currents and a normal state for higher

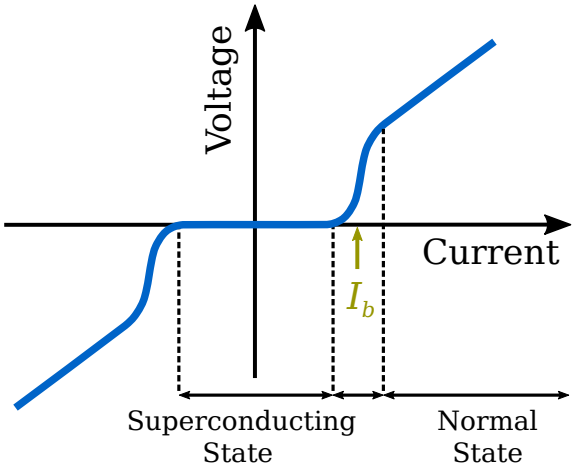

Figure 3.6.: $U - I$ characteristic of a Josephson junction. Within a SQUID the bias current I_b is locked at the steepest part of the curve, thus achieving maximal sensitivity.[45]

currents. In between is a steep $U - I$ dependency, where we find large changes in voltage for small current changes. The bias current I_b will be set there. If a flux, created by the detection coils emerges, a screening current I_s arises, moving in antiparallel directions at the two junctions. The overall flux inside the ring will be given by $\Phi = \Delta\Phi + LI_s$ with the loop inductance L. The feedback loop will lock Φ at a certain value. This means a flux change of $\Delta\Phi$ produces a flux change $-\Delta\Phi$ from the feedback, while producing an output voltage proportional to $\Delta\Phi$. This setup enables the SQUID to detect changes of the fraction of Φ_0, making it the most sensitive device for magnetization measurements nowadays. [44, 45]

The magnetization of a single crystal will typically be measured on a sample holder made of quartz(Figure 3.7(a)). In order to glue the sample onto the holder a small

drop of GE varnish (SCB GbR) is applied and the sample placed on top. Additionally, a drop of ethanol is used to uniformly spread the varnish around the crystal. For plate-like samples (like Na_2IrO_3) this method does not work well for measurements perpendicular to the plate. In this case, the sample would be significantly off-center in the pick-up coils, leading to an altered magnetic moment. This problems are circumvented by using a torlon disk with N Apiezon grease (Cryo-Technics) as adhesive clamped into a straw(Figure 3.7(b),(d)), accepting the enhanced holder background. Powder samples are filled into special powder capsules provided by Quantum Design, which are then inserted into a brass holder(Figure 3.7(c),(e)). All sample holding systems are shown in Figure 3.7). Additionally, a rotator can be used

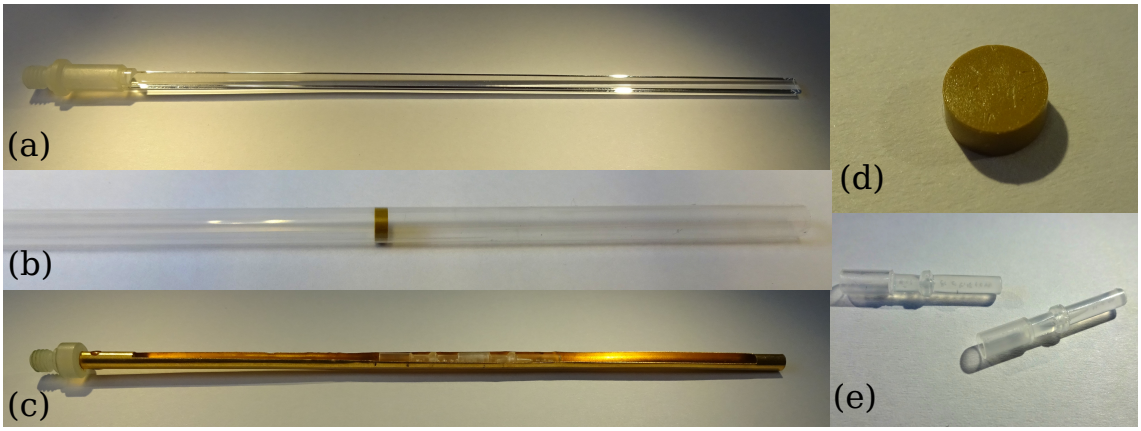

Figure 3.7.: Sample holders for magnetization measurements: (a) quartz rod, (b), torlon disk inside straw, (c) powder capsule inside brass holder, (d) torlon disk and (e) powder capsules

to study angle dependent magnetization. The torlon disk, varnish, the powder capsule and the rotator all have a magnetic moment and therefore show a background that needs to be considered when handling magnetic materials with small magnetic moments. Therefore, the measurements were repeated without the sample and the background data subtracted afterwards. The corrected data are fitted afterwards with the same function used by the MPMS software: [46]:

$$U(z) = X(1) + X(2) \cdot z + X(3) \cdot \{2 \cdot [R^2 + (z + X(4))^2]^{-3/2} - [R^2 + (\Lambda + (z + X(4)))^2]^{-3/2} - [R^2 + (-\Lambda + (z + X(4)))^2]^{-3/2}\}.$$

$R = 0.97$ cm and $\Lambda = 1.519$ cm are geometry constants, while $X(1)$ to $X(4)$ represent the four fitting parameters. The actual magnetic moment μ (in emu) can be

calculated by inserting the obtained value for $X(3)$ into the following equation [46]:

$$\mu = X(3) \cdot \frac{\mathrm{C}}{S}. \tag{3.3}$$

Here, C is a device dependent constant and S the sensitivity factor, which can be calculated by knowing the size of the range and gain (measurement parameters) used during the experiment. All these steps were performed by a python program from Maximilian Seidler [47]. The program, unfortunately, stopped working due to software problems towards the end of this work and could, therefore, not be used for all measurements.

3.4.2 Transversal magnetization

The transversal magnetization refers to all off-diagonal elements of $\underline{\chi}$ ($i \neq j$):

$$\underline{\chi} = \begin{pmatrix} \chi^{xx} & \chi^{xy} & \chi^{xz} \\ \chi^{yx} & \chi^{yy} & \chi^{yz} \\ \chi^{zx} & \chi^{zy} & \chi^{zz} \end{pmatrix}.$$

This means that field and magnetization point in orthogonal directions. To show off-diagonal elements of $\underline{\chi}$ in the paramagnetic regime is not a common feature for materials. It requires certain "exotic" exchange interactions like the Dzyaloshinskii-Moriya interaction or the off-diagonal Γ, Γ' spin exchange (see Section 2.2.2,4.3.3) and the transverse magnetization will typically be of lower magnitude than the longitudinal magnetization.

The transversal option is built into a MPMS 5S, an earlier version of the described MPMS3. The sensitivity is lower and measurement times are longer. Therefore, all longitudinal measurements were performed by the MPMS3. The device is able to cover temperatures between 1.9 K and 400 K up to a magnetic field of 5.5 T. It is equipped with a DC magnetometer using a rf SQUID [48]. Here, only one Josephson junction is used, which is inductively coupled to a radio frequency resonant tank circuit. With varying magnetic flux the frequency of the tank circuit changes, which is technically easier to measure but gives a significantly lower resolution than a DC SQUID [45]. With this additional option the MPMS is able to detect a transversal magnetization pointing in a distinct direction, defined by the coil setup. This means

it measures the projection of the sum of all transversal moments with respect to this direction. Therefore, the MPMS also possesses a rotator, which is able to vary the orientation of the sample in the plane orthogonal to H. By rotating the sample the maximum in the transversal magnetization can be determined, which is the direction in which the transversal moment or the sum of all transversal moments points. For the measurement of the transversal magnetization we use conventional straws with the sample glued to a torlon disk or a quartz holder inside a straw (see Figure 3.7 on page 34).

Compared to longitudinal measurements the determination of transversal magnetization demands a more complicated coil setup shown in Figure 3.8a. The magnetic

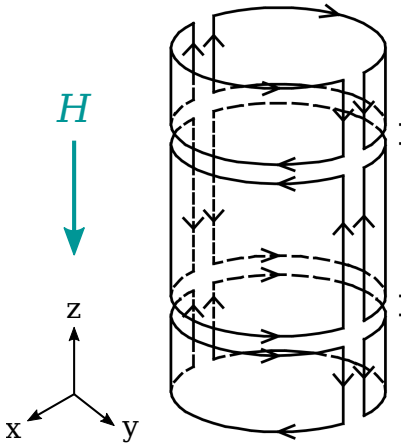

(a) Setup of the transverse pick-up coils, adapted from [49]. While the H and the movement of the sample are directed along z, the measured magnetization lies in the xy-plane.

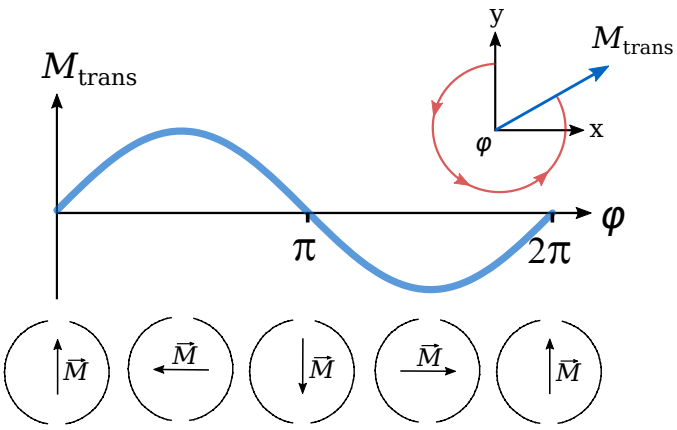

(b) The transversal magnetization M_{trans} shows a sine function in dependence of the angle φ in the xy-plane. At the maximum and minimum the total transversal moment points towards the center of the coils and at the zero crossing in between the gap, illustrated below the graph in top view (Inspired by [49]).

Figure 3.8.

field was chosen to be parallel to the z-axis. Just as for a longitudinal setup, the sample is moved along z during the measurement, although the determined moment lies orthogonal to this direction. The magnetization will show a sine function in dependence of the rotation angle φ (see Figure 3.8b). The maximum of the transversal magnetization will give the angle where the sum of all the moments points directly in the center of one of the pick-up coils (x-direction). The minimum refers to the angle when it points to center of the opposite pick-up coil. In between the coils (along

y-direction) M is always 0. This means we cannot determine the magnetization in dependence of the angle, but rather determine the size of the sum of all transversal moments in the plane at the minimum and maximum position. If the crystallographic orientation of the single crystalline sample is known, the direction of the maximal magnetization relative to the lattice structure can be identified. Of course there are also situations imaginable (e.g. three equally sized moments with 120° angle), where the moments will always cancel out and cannot be detected within this method.
Since only few materials actually show a transversal magnetization, the background magnetization of sample holders is not directly an issue when using this method. But nonetheless there are difficulties to overcome. The main problem is the typically orders of magnitude larger longitudinal magnetization. If the sample is not perfectly aligned in the center of the coils with respect to the xy-plane, the longitudinal moment produces a signal in the transverse coils. Even with a perfect alignment, due to inaccuracies of the coil setup, nearly always a contribution from the longitudinal moment is measured.[49, 50]. Figure 3.9 shows theoretical calcu-

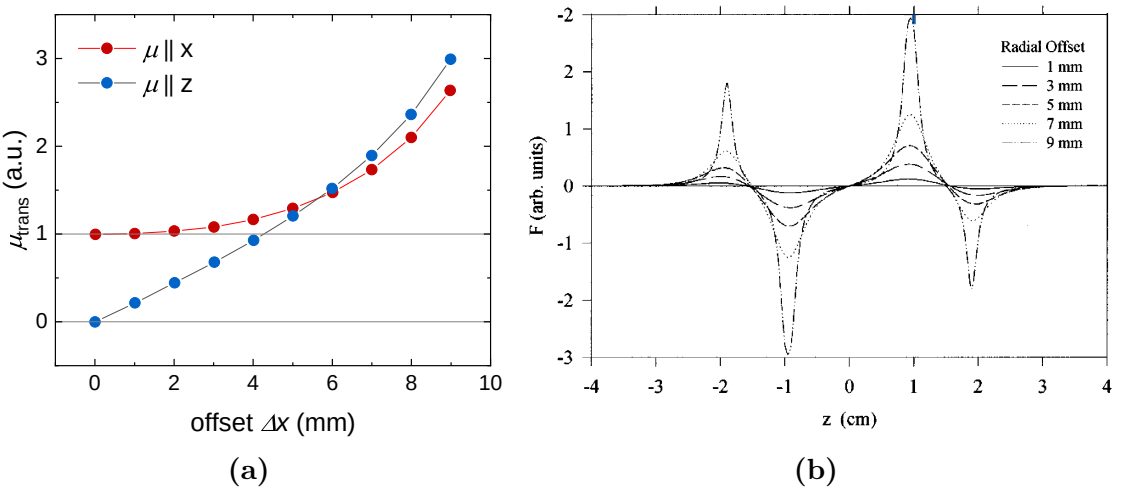

Figure 3.9.: (a) A transverse moment with a radial offset appears larger with increasing Δx. A longitudinal moment ($\mu \parallel z$) with a radial offset induces also a signal in the transverse pickup coils, which strongly increases with increasing Δx. Additionally, for large offsets the contribution from the transverse moment ($\mu \parallel x$) is overestimated as well. (b) shows the measured transverse voltage signal stemming from a longitudinal moment with various offset sizes. The antisymmetric character of the longitudinal contribution is unchanged by an offset. The figures are adapted from [51].

lations of a second derivative pickup coil setup for measurements of a longitudinal

and transverse moment and their dependency on an offset to the center position in the xy-plane. Both, the signal from a longitudinal and a transverse moment in the transverse pickup coils, increase with increasing radial offset. While the effect on the transverse moment is neglectable for $\Delta x \leq 1\,\mathrm{mm}$, the longitudinal contribution is not.

The longitudinal contribution can be easily distinguished from the actual transverse signal through the shape of the voltage signal in dependence of the position inside the sample chamber. Figure 3.10 shows a typical example of a longitudinal signal from a Ni sphere (a), (c) in comparison to a transverse signal from a Cu coil (b), (d) for two angles with 180° difference, respectively. While the transverse moment gives

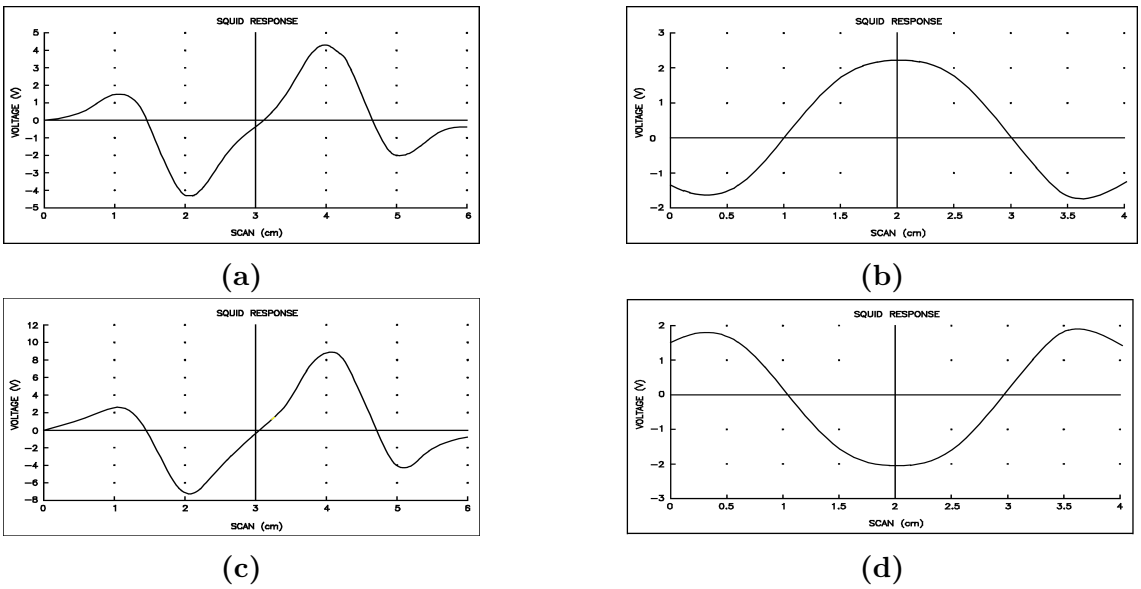

Figure 3.10.: Comparison of the voltage output arising from a longitudinal moment for 0° (a) and 180° (c) to the one from a transversal moment at 0° (b) and 180° (d) [49]. While the former is odd and unchanged by the rotation, the latter shows an even signal and is reversed for 180°.

an even signal, which is reversed for a 180° rotation, the longitudinal one is odd and unaffected by the rotation of the sample. The symmetries of the two different signals can be used to separate them. How this effect is exactly compensated and the raw data analyzed will be described in the results in Section 5.1.1.

4 | Kitaev Model Candidate Materials

Since the proposal of the Kitaev honeycomb model (Section 2.2.4) in 2006 [3], scientists have tried to find a real material on which it could be applicable. Three years later Jackeli and Khaliullin suggested a way to realize the Kitaev interaction. Since then, some materials have been proposed as candidates for the Kitaev model, with Na_2IrO_3, α-Li_2IrO_3 and $RuCl_3$ being the most prominent systems. In this chapter we will first take a closer look at the mechanism put forward by Jackeli and Khaliullin. Afterwards, the realization of the Jackeli-Khaliullin mechanism in real materials is discussed and a short overview over important Kitaev candidates given. Then, reported research about the synthesis as well as about crystallographic and magnetic properties and different attempted doping experiments of the selected Kitaev candidates are reviewed.

4.1 The Jackeli-Khaliullin Mechanism

In 2009 Jackeli and Khaliullin [4] introduced the idea to look for Kitaev interaction in Mott insulators with strong spin-orbit coupling. Here, the spin-orbit coupling is a dominant factor, leading to a highly directional isospin. This is a mandatory condition to be able to establish bond-directional interactions. Since spin-orbit coupling increases quadratically with Z, it is large in the late transition metal ions like Ir, Os, Rh and Ru. Ir^{4+} ions have been found to exhibit a spin-orbit coupling constant λ of approximately 380 meV. Ir possesses five electrons in the $5d$-orbital. An octahedral

environment lifts the degeneracy of the d orbitals into t_{2g} and e_g orbitals. In the low spin configuration only the t_{2g} levels are filled, leaving one hole. Taking spin-orbit coupling into account, one finds the ground state lies in a Kramers doublett, whose isospin states are a combination of four t_{2g} states. Figure 4.1 shows the 'up state' of the isospin and Figure 4.2 the corresponding splittings of the $5d$ orbitals due to crystal field (Section 2.3.1) and spin-orbit-coupling (Section 2.3.2). The resulting

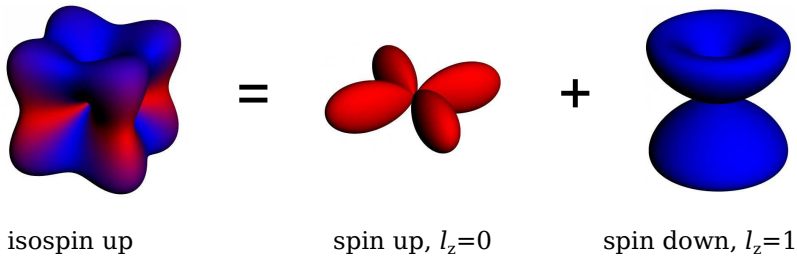

Figure 4.1.: Density profile of a hole in the up state in the $J_{\text{eff}} = \frac{1}{2}$ band. The profile is highly anisotropic, resulting from the superposition of the spin up state of the $l_z = 0$ orbital and the spin down state of the $l_z = 1$ orbital. [4]

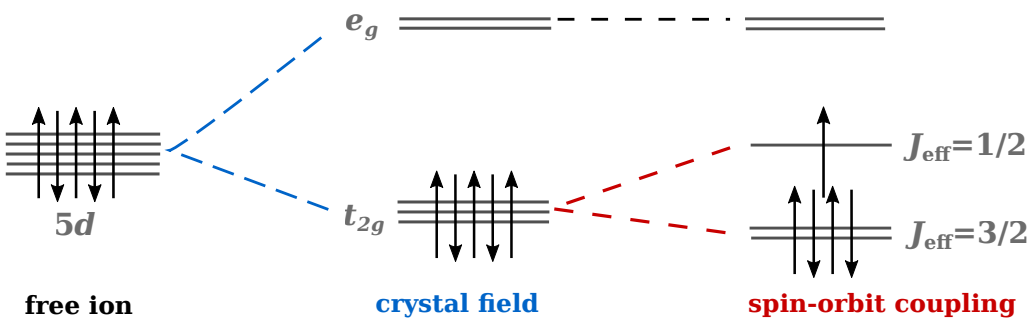

Figure 4.2.: The five $5d$ orbitals of an Ir^{4+} ion are split by an octahedral crystal field into e_g and t_{2g} levels. A large spin-orbit coupling leads to a lower fully occupied $J_{\text{eff}} = \frac{3}{2}$ band and a half filled $J_{\text{eff}} = \frac{1}{2}$ band. Scheme adapted from [52].

band has an effective total angular momentum of $J_{\text{eff}} = 1/2$ and is half filled. In the case of a sufficient Coulomb interaction U the band is split and the system turns into a Mott insulator (Section 2.1). For this case, we find very localized and highly anisotropic spin-1/2 moments. By including the Hund's coupling (Section 2.3.4), they found, for the case of 90° TM-L-TM bonds connecting the magnetic moments and edge-shared ligand octahedra, an bond dependent anisotropic interaction via the ligand atoms, which realizes the Kitaev model.

4.2 Realization in real materials

Chaloupka proposed in 2010 together with Jackeli and Khaliullin A_2IrO_3 (A=Li, Na) as good candidates for a material with Kitaev interaction [5]. A_2IrO_3 not only has the Ir^{4+} ions surrounded by edge-sharing oxygen octahedra, but these also sit on a 2 dimensional honeycomb lattice, whose layers are only weakly coupled to each other. All of these are necessary criteria to establish a Kitaev interaction, according to the authors. Figure 4.3 shows the super-exchange via the two 90° Ir-O-Ir bonds,

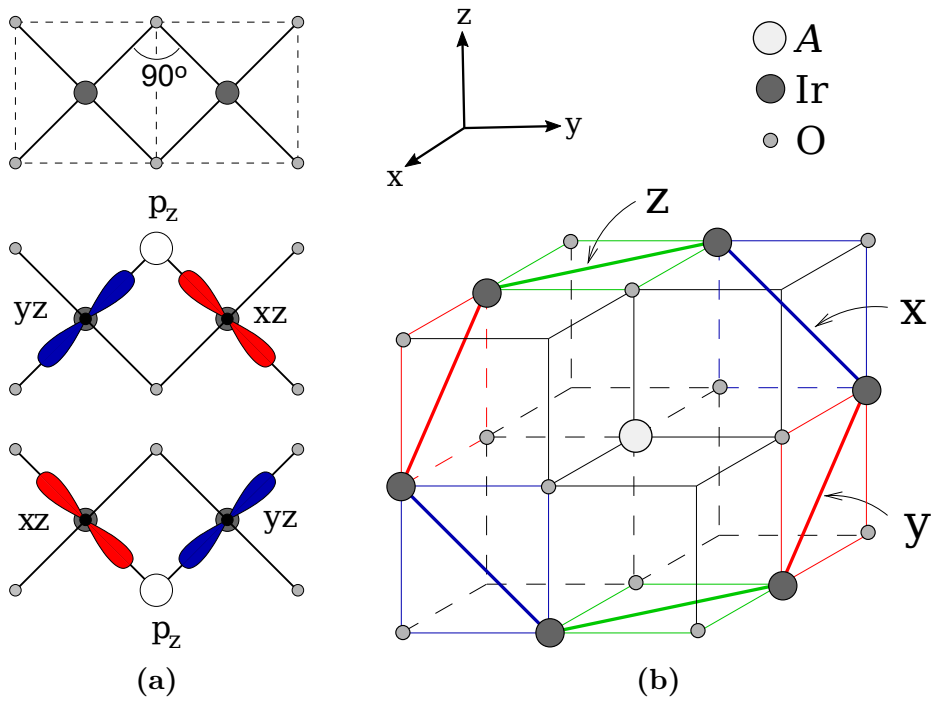

Figure 4.3.: The Jackeli-Khaliullin mechanism in A_2IrO_3: A super-exchange of two Ir ions via the oxygen orbitals. There are two equal Ir-O-Ir paths for each bond (a). All spatial components cancel except for the z component in this example, leading to an interaction between $\boldsymbol{S}_i^z \cdot \boldsymbol{S}_j^z$. The interacting spin components are different for all three Ir bonds with the spins trying to align orthogonal to the plane spanned by the respective bonds. These bonds are named x, y and z bond according to their coupling in respect to the cubic coordinate system. (b) shows their position in the crystal structure of A_2IrO_3. Figures adapted from [4].

resulting in the anisotropic interaction. Each Ir has three Ir neighbors, each coupled by two different O ions. One example is presented in Figure 4.3a. For each bond different d and p orbitals are involved, resulting in a coupling of the two Ir spins orthogonal to the plane spanned by the involved atoms (Figure 4.3b). Three different

types of bonds are established, which are named x-, y- and z-bond according to the direction of the spin coupling. Chaloupka *et al.* introduced the Kitaev-Heisenberg model, trying to predict the magnetic ground states of A_2IrO_3 (A=Li, Na). They use a spin Hamiltonian, taking only nearest neighbor Kitaev (K) and Heisenberg interaction (J) into account:

$$\mathcal{H}_{ij}^{\gamma} = -KS_i^{\gamma}S_j^{\gamma} + J\boldsymbol{S}_i \cdot \boldsymbol{S}_j.$$

γ (=x, y or z) indicates the bond type according to the labels in Figure 4.3b. Since the Jackeli-Khaliullin mechanism only considers the exchange via the Ir-O-Ir bonds, the Heisenberg term accounts for the direct overlap of the Ir ions. However, following experimental measurements neither revealed the predicted Néel AFM, the stripy AFM nor a spin liquid phase for the iridate systems. Instead, zig-zag AFM was found for Na_2IrO_3 [53–55]. The magnetic order of α-Li_2IrO_3 turned out to be an even more complex counter-rotating spiral order [56]. This suggests that even more exchange interactions play an important role. Nevertheless, there is strong evidence that the Kitaev interaction plays a significant role for the magnetism in the Na_2IrO_3 system as well as for Li_2IrO_3. Though, an extension of the Kitaev-Heisenberg model to explain the observed magnetic ordering is required. Over the years several groups have theoretically investigated a model for the iridates, adding the Dzyaloshinskii-Moriya interaction, off-diagonal Γ and Γ' terms (see Section 2.2.2) as well as second- and third-neighbor interactions [10, 11, 15, 18, 28, 57–60]. First experimental evidence for significant influence of the Kitaev term was found in 2015 as a group was able to directly show the bond-directional interaction associated with the Kitaev term for Na_2IrO_3 using diffuse magnetic X-ray scattering [18].

Additionally, to the α phase, two high-temperature phases β and γ of Li_2IrO_3 have soon been found [61, 62]. In comparison to α-Li_2IrO_3, which is the crystallographic equivalent to Na_2IrO_3 both, β and γ phase, consist of a three-dimensional honeycomb structure. Still, they have been expected to exhibit Kitaev interaction as well [61, 63–65] and have found to show the same counter-rotating spiral order as α-Li_2IrO_3 [66, 67]. Although surely these materials would also be an interesting subject to study, they will not be covered in this work.

In 2014 yet another candidate was put forward: α-$RuCl_3$ [6]. The 4*d* Ru system, similar in crystallographic structure to Na_2IrO_3 and α-Li_2IrO_3, exhibits a smaller

λ of 154 meV [68], but was proposed to be closer to the cubic symmetry [6, 59]. Here, a zig-zag magnetic ground state was determined, similar to Na_2IrO_3 [69, 70]. Since than, fingerprints of Majorana fermions associated with the Kitaev exchange could be found for α-$RuCl_3$ [19, 20]. Additionally, there is evidence for a quantum spin-liquid regime for fields around $\sim$8 T, which exhibit oscillations of the thermal conductivity at $T < 2$ K [71] and a half-integer thermal quantum Hall effect slightly below 6 K [72]. Both phenomena can be explained by Majorana excitations, which are expected for a Kitaev quantum spin liquid in proximity of this phase.

It must be noted that there is also another approach to explain the observed behavior. Some physicists question the validity of the localized $J_{\text{eff}} = \frac{1}{2}$ moments for the iridate systems [73–76]. They rather argument that spin-orbit coupling is not the dominating factor, but must compete with equally sized bandwidth and Hubbard and Hund's rule correlation ($U - J_{\text{H}}$). They introduce the model of quasi molecular orbitals (QMO), where the moments are localized for Ir hexagons. This would position Na_2IrO_3 close to an itinerant regime, which contradicts the assumption of $U \gg t$, which is used in the theoretical models mentioned above.

4.3 Na_2IrO_3, α-Li_2IrO_3 and α-$RuCl_3$

The most promising candidates to exhibit Kitaev interaction are Na_2IrO_3, α-Li_2IrO_3 and α-$RuCl_3$. This section gives an overview over research on these compounds, relevant to this work. We will examine the synthesis as well as crystallographic and magnetic properties and evaluate their deviation to the Heisenberg-Kitaev model. An extension of the model is needed to explain the behavior of these real systems. In the end, doping experiments are investigated with the focus on the doping series of $(Na_{1-x}Li_x)_2IrO_3$, which is investigated in this thesis.

4.3.1 Synthesis

Different methods where needed to obtain powder as well as crystals of each compound. All own growth experiments were conducted in a Muffle furnace (model L5/C6H) from the company 'Nabertherm' using corundum (Al_2O_3) crucibles with lids in air. The growth methods were adapted from previous work [77, 78]. Doped

samples of $(Na_{1-x}Li_x)_2IrO_3$ were grown with the same method as their parent compound Na_2IrO_3. The different starting materials are listed in Table A.1 in the appendix.

A_2IrO_3 powder

The powder of Na_2IrO_3 and α-Li_2IrO_3 was synthesized by a combination of calcination and solid state reaction.
The starting materials, Na_2CO_3 or Li_2CO_3 and Ir, were mixed in a mortar in the ratio of A_2CO_3 : Ir = 1.05 : 1 and blended vigorously. The deviation from stoichiometry compensates the loss of the more volatile Na/Li during the growth process. Afterwards everything is filled in the crucible and loosely sealed with a lid. Hence, air can still enter the crucible, but the loss of material during the process is reduced. For every growth step the oven is preheated to 200°C. At 800°C and 700°C for Na_2CO_3 and Li_2CO_3, respectively, the calcination is conducted, decomposing the carbonate. The alkali metal than reacts with the iridium forming the desired compounds:

$$\begin{aligned} Na_2CO_3 + Ir + O_2 &\xrightarrow{@800°C} Na_2IrO_3 + CO_2 \\ Li_2CO_3 + Ir + O_2 &\xrightarrow{@700°C} \alpha\text{-}Li_2IrO_3 + CO_2\ . \end{aligned} \tag{4.1}$$

Typically, the sample will stay at the calcination temperature for 12-24 h. Afterwards the oven is turned off, left to cool down to 200°C and then the sample is

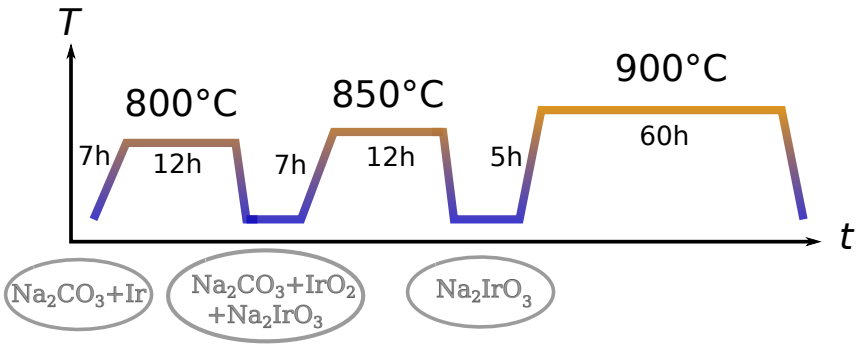

Figure 4.4.: A typical growth process for Na_2IrO_3. For cooling the furnace is turned off. In between heating steps the sample is repeatedly mixed. After the second heating step the formation of Na_2IrO_3 is completed, but the quality is still poor. An annealing at 900°C for 60 h or longer improves the crystal structure.

removed. Most material will have reacted at this point. After a second heating process, 50°C higher, the calcination will be completed, although the crystalline order will still be very poor. Therefore, an annealing at 900°C for at least 3 days is necessary. Such a heating sequence can be seen in Figure 4.4. Repeated mixing in between heating steps helps speed the process of producing well-ordered A_2IrO_3. To obtain $(Na_{1-x}Li_x)_2IrO_3$ samples the same can be done, mixing Li_2CO_3 and Na_2CO_3 in the desired molar ratios.

α-Li_2IrO_3 single crystals

To grow single crystals of α-Li_2IrO_3 has been a big challenge for a long time. Finally, Freund *et al.* [79] succeeded by using a very unusual growth method, which they called separated educt technique. With this method, simultaneously α-Li_2IrO_3 and β-Li_2IrO_3 single crystals grow side by side, some reaching over 1 mm length.

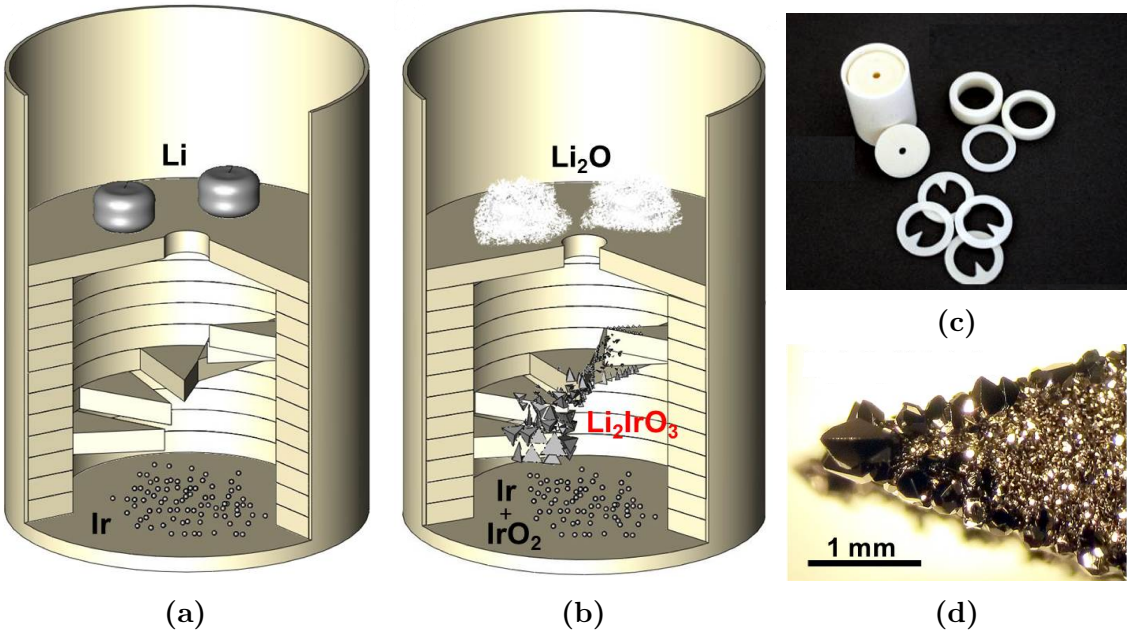

Figure 4.5.: Growth setup for α-Li_2IrO_3 [79]. (a) Ir is placed on the bottom and Li on the top of the crucible. (b) At temperatures roughly between 800°C and 1000°C the crystals grow on spikes in between the educts. (c) The crucible as well as the spacer, rings with spikes and the aperture are made out of aluminum oxide Al_2O_3. (d) Examples of α-Li_2IrO_3 crystals grown on a tip of a spike.

The educts, here pure Ir and Li, are separated from each other and both transformed into a gaseous phase by heating in air. Via chemical vapor transport the

gases meet in the middle and form crystals. Here, a special setup was used (Figure 4.5) to support the growth. Ir lies on the bottom of the corundum crucible, Li on the top. A loose lid provides a hindrance for the substances to exit the crucible, while still leaving air in. The crystals grow on spikes in between at a temperature of 1020°C after a very short heating process. The temperature is held for three days. This crystal growth shows uncommon properties for a chemical vapor transport. Instead of a temperature gradient, a gradient in particle concentration seems to be the driving force. As a consequence a spacial distance enhances growth conditions. Furthermore, several reactions need to take place before Li_2IrO_3 forms. The exact chemical reactions and which intermediate gaseous phases form to finally condense in the end product is still under debate. The from Freund *et al.* proposed chemical reaction involving water as a transport agent for lithium oxide seems unlikely. Theodor Grünwald (Universtity Augsburg, 2021) reports about a successful synthesis of α-Li_2IrO_3 in a controlled oxygen atmosphere without the availability of water during the course of his master thesis, contradicting this hypothesis.

Na_2IrO_3 single crystals

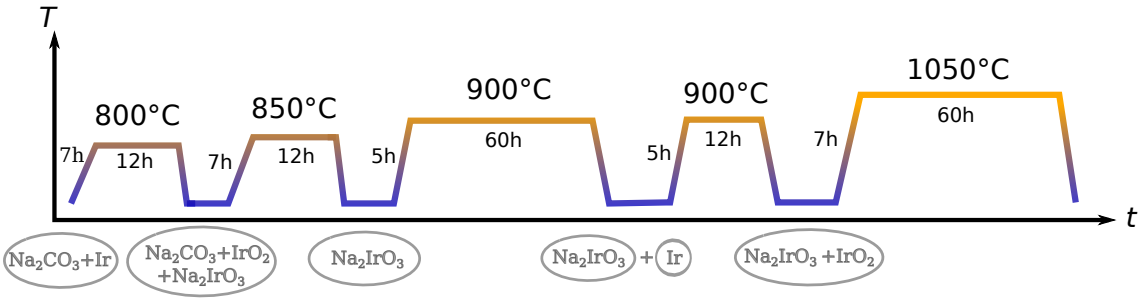

Figure 4.6.: A typical growth process for Na_2IrO_3 single crystals. In between heating steps the sample is repeatedly mixed. The first three heating steps produce high-quality Na_2IrO_3 powder. The fourth step, after adding extra Ir, has empirically been shown to produce larger crystals. During the last step the single crystals grow vertically out of the polycrystalline bed.

For Na_2IrO_3 crystals up to a size of 2 mm x 1 mm x 0.01 mm can directly be grown from powder Na_2IrO_3. For this purpose the powder is annealed at a temperature of 1050°C for three days. It is already known from [77] that adding an extra molar 10% of IrO_2 or Ir (with respect to the molar quantity of Ir already inside the sample) and annealing at 900°C before the actual crystal growth is necessary to obtain such

large crystals. The complete growth process is depicted in Figure 4.6. At 1050°C the single crystals grow vertically out of the polycrystalline bed (see Figure 4.7). This fact and the high growth rate (already after a few hours at $T = 1050$°C can small crystals be seen) suggest a vapor transport might be involved.

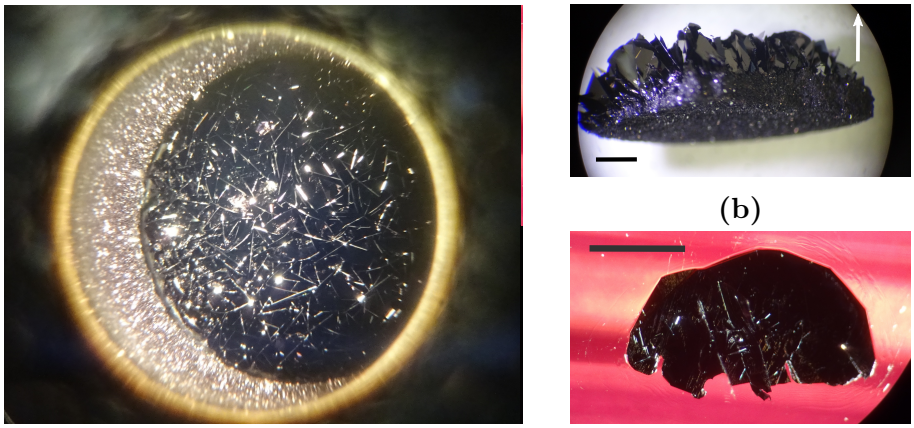

(a) **(b)** **(c)**

Figure 4.7.: Crystal growth of Na_2IrO_3: The crystals grow out of the polycrystalline bed. (a) shows a finished growth from the top and (b) from the side. The crystals are repeatedly intersected and reach sizes up to 2 mm x 1 mm x 0.01 mm like the sample in (c). The bars represent 1 mm length and the arrow in (b) the growth direction.

α-$RuCl_3$ single crystals

α-$RuCl_3$ single crystals can be grown starting from its commercially available $RuCl_3$ using sublimation (CVT). The powder was dried in dynamic vacuum between 10^{-4} and 10^{-5} mbar and at 120°C for 48 hours before the actual growth. Afterwards the sample was loaded into a quartz ampule and sealed in argon atmosphere, protecting it from any unwanted reactions. It was then placed inside a muffle furnace, heated to 970°C slowly cooled down to 700°C at a rate of 1°C/h and at last the furnace turned off. At 970°C the material is completely in the gaseous phase. While cooling it resublimates, forming single crystals at the cold end of the crucible:

$$RuCl_3(s) \rightleftharpoons RuCl_3(g)$$

The small temperature gradient, naturally arising inside the muffle furnace, is enough to achieve a transport to one end, where single crystals of α-$RuCl_3$ form. [80]

The samples where synthesized by Vladimir Tsurkan from the group of Prof. Loidl, University of Augsburg.

4.3.2 Crystal structure

The structure of Na_2IrO_3, α-Li_2IrO_3 and α-$RuCl_3$ realizes almost perfectly the Jackeli-Khaliullin model. Each material crystallize in the monoclinic space group number 12 (C2/m) [54, 69, 70]. They consist of two-dimensional honeycomb layers, which are only weakly coupled. Iridium as well as ruthenium is surrounded by six oxygen/chlorine ions in an octahedral environment (Figure 4.8a). The octahedra are edge-sharing and therefore give rise to the anisotropic exchange interaction for each nearest neighbor atom. Figure 4.8b shows one metal ion and all three neighboring

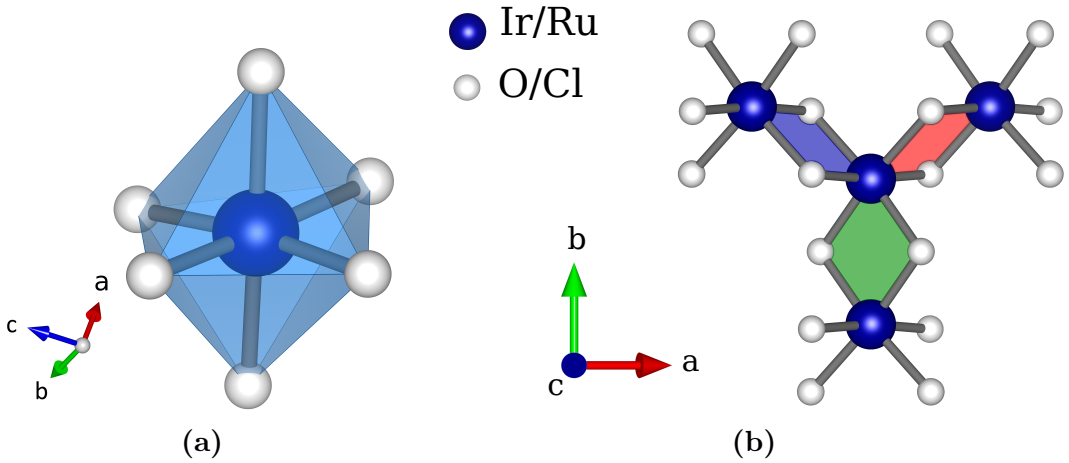

Figure 4.8.: Crystal structure of A_2IrO_3 (A=Li, Na) and α-$RuCl_3$. a) visualizes the octahedral environment of the transition metal. b) shows an Ir/Ru ion with its three nearest neighbors and their O/Cl atoms. The colored areas are spanned between the Ir and O atoms involved in one bond of the Kitaev interaction with the Ir spins interacting via the component perpendicular to that plane. The figures were created with Vesta [81] using the data from Na_2IrO_3 given in [54].

ions as well as the ligand atoms responsible for the exchange in the Jackeli-Khaliullin model. The area in between the involved metal ions and ligand ions are colored differently for each bond, resembling the x, y and z bond from the Kitaev model. The spins will interact with their spacial component orthogonal to that specific plane. For the iridate systems the layers alternate between a layer with iridium ions on

the corners of the honeycombs and a sodium ion in the center (Figure 4.9a) and a layer with only sodium at each site (not shown). In the discussed Jackeli-Khaliullin-

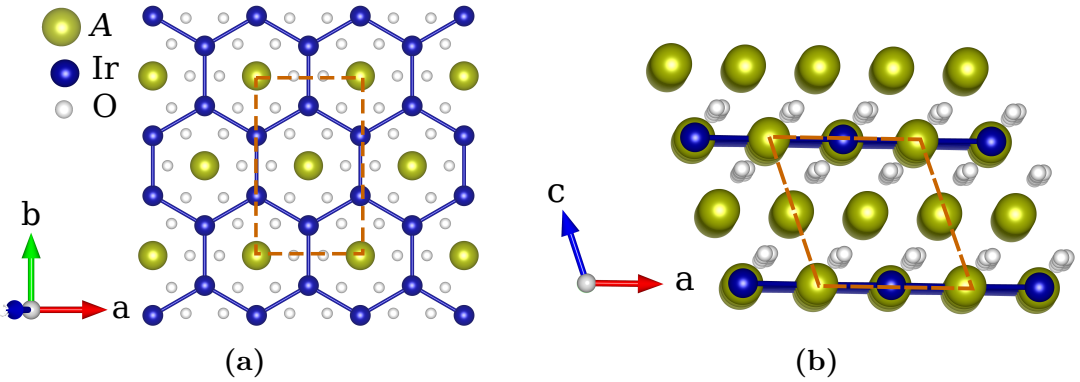

Figure 4.9.: Crystal structure of A_2IrO_3 and α-$RuCl_3$ on the example of Na_2IrO_3 (data from [54]). a) shows the in-plane and b) the out-of-plane perspective. For α-$RuCl_3$ the Ru and Cl sit on the Ir and O sites, respectively, and the additional alkali metal A is missing. The dashed orange line shows the unit cell of Na_2IrO_3. The pictures were created with Vesta [81].

mechanism [4] angles between the metal ions and its ligand ions are assumed to be 90°. This is not perfectly fulfilled in reality. Trigonal distortions (elongation or compression of the honeycomb) change the ideal octahedral environment and henceforth the Ir-O-Ir angle. For Na_2IrO_3 the octahedron is known to be distorted by the large Na^+ ion. As a result, the Ir-Ir distances range in between 3.13 Å to 3.14 Å and the Ir-O-Ir angles in between 98° and 99.4°[54]. The Li^+ ion is smaller and therefore alters the structure less drastically, possessing Ir-Ir distances of 2.98 Å and angles of 94.7° to 95.3°. [82]. α-$RuCl_3$, which lacks the alkali metal, shows bond lengths of 3.43 Å to 3.46 Å and Ru-Cl-Ru angles between 92.6° and 93.9°[69]. The earlier hope, assuming another point group, of nearly undistorted octahedra has not been fulfilled. All three materials have a tendency to form stacking faults, since the interaction between the layers is weak. α-Li_2IrO_3 is also prone to twinning defects, making anisotropic measurements difficult.

Powder degradation

All three material systems are assumed to degrade in air and are, therefore, stored in argon atmosphere. Three groups ([83–85]) have conducted experiments concerning the chemical instability of Na_2IrO_3.

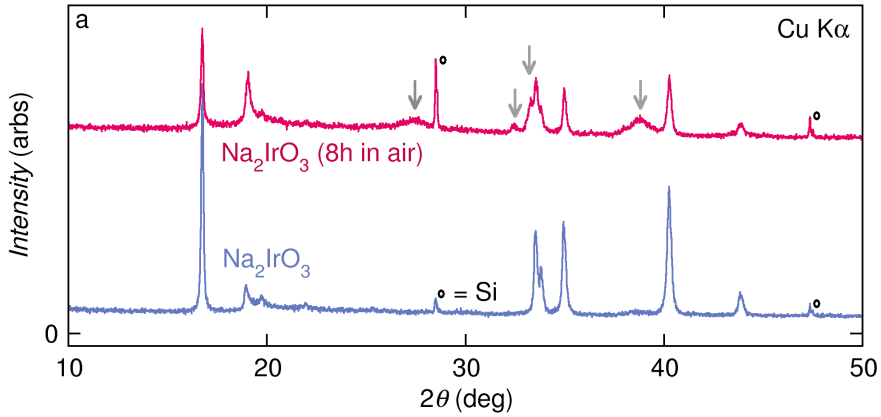

Figure 4.10.: Comparison of the XRD pattern of pristine Na_2IrO_3 powder (blue) to a powder that degraded for eight hours in air (red), taken from [84]. The gray arrows indicate the peaks of the degradation product.

Wallace *et al.* [84] left powder in air for 8 h and compared XRD data as well as

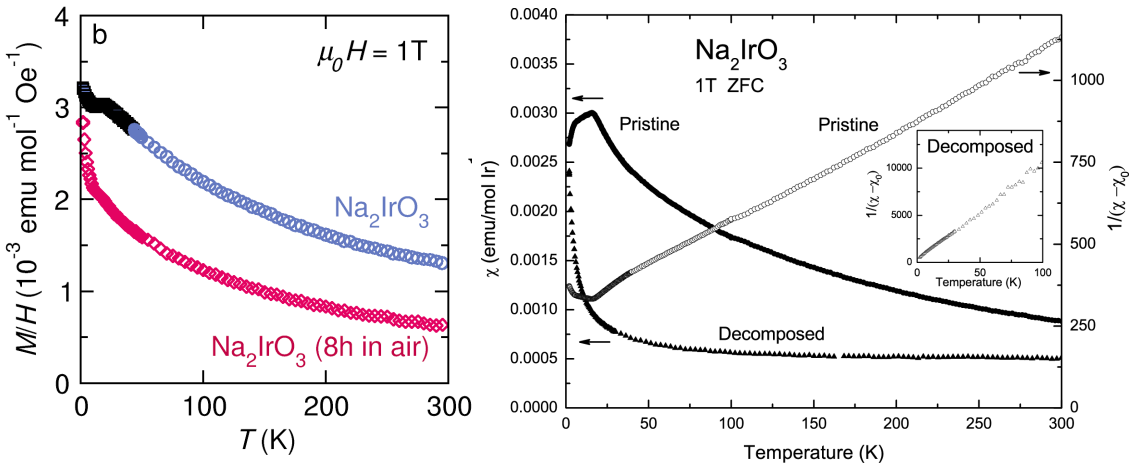

(a) **(b)**

Figure 4.11.: Development of the susceptibility $\chi = M/H$ prior and after exposure to air for (a) 8 h [84] and (b) an "extended period" [83] in a magnetic field of 1 T. After 8 h the magnetic transition can barely be identified and χ reduced. After an even longer time χ has decreased even more and the transition has vanished.

magnetization data prior and after air exposure. Already after these 8 h new reflexes in the XRD data appeared (Figure 4.10), suggesting the degradation of the powder. The magnetization data (Figure 4.11a) showed a smaller signal, an almost vanished signature of the ordering transition as well as a decreased θ_W after the exposure.

Krizan *et al.* [83] found Na_2IrO_3 powder to be decomposed within 24 h in air (Figure 4.12). Degradation was also found for 12 h in wet CO_2, but not for dry CO_2 or wet N_2 and wet O_2. The susceptibility of a sample before and after exposure in

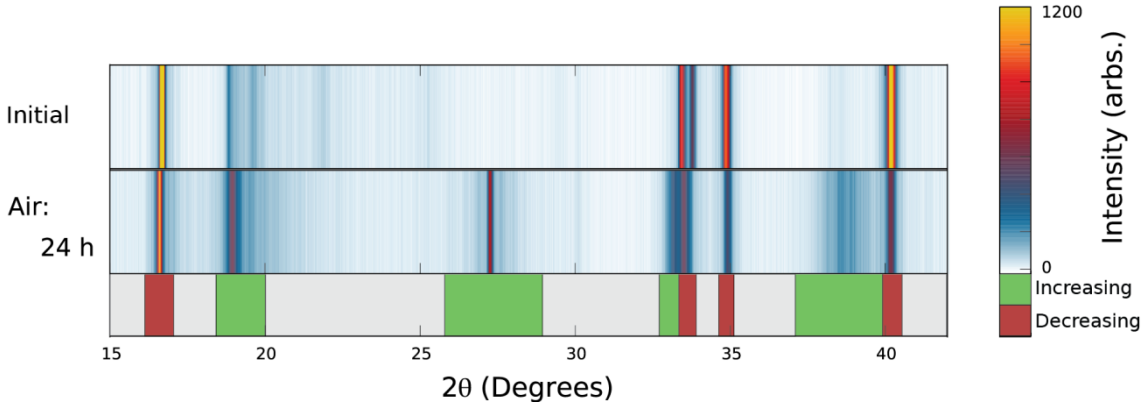

Figure 4.12.: Comparison of the XRD pattern of pristine Na_2IrO_3 (upper part) to the powder after 24 h of degradation in air (middle part), taken from [83]. The intensity is color-coded and the angle ranges which increased (green) or decreased (red) in intensity after degradation are shown in the lower part.

air for an "extended period" shows a drastic effect as well. $\chi(T)$ of the decomposed sample is highly reduced and the magnetic transition has completely vanished (Figure 4.11b). Additionally, Dzuiba *et al.* [85] measured the resistance of a Na_2IrO_3 single crystal as it was grown and after exposure to air, after cleaving in UHV and after exposing this fresh surface air for 13 h, which is shown in Figure 4.13. After the cleavage the resistance was drastically smaller for lower temperatures in comparison to the bulk data and the uncleaved surface. After several hours the resistance increased towards the value prior to the cleavage. This high air-sensitivity leads to the need of storing the samples inside a protected atmosphere and keeping exposure to air as short as possible.

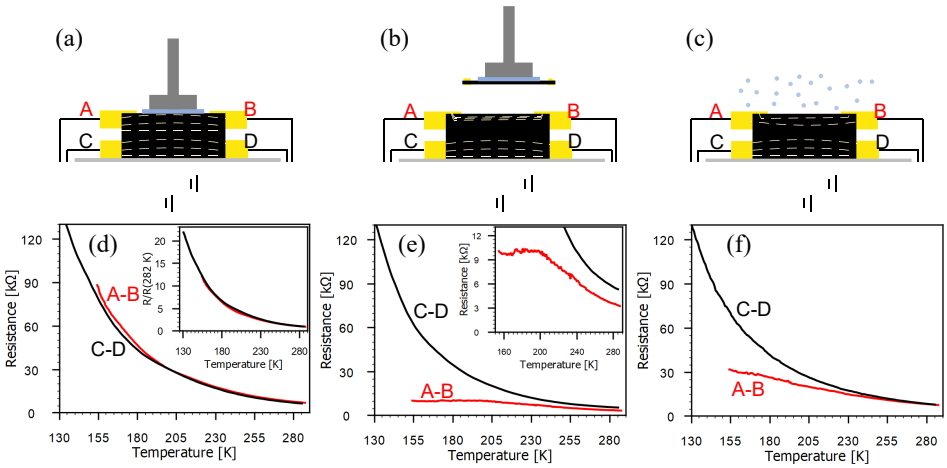

Figure 4.13.: Resistance measurements between the two channels A-B and C-D on a Na_2IrO_3 single crystal. After the measurement in a), the sample was cleaved at the surface connected to A-B in b). The freshly cleaved surface was exposed to air for several hours in c). The respective resistance data are shown in d)-f) below.

4.3.3 Magnetic properties

Magnetic order and theoretical models

Although the crystal structure is similar for all three systems, differences can be found in their magnetic properties. The magnetic moments of Na_2IrO_3 and α-$RuCl_3$ form a zig-zag structure below T_N, coupled antiferromagnetically with each other in-plane as well as out-of-plane (Figure 4.14(a)). The spins are tilted with an angle θ out of the *ab*-plane towards the cubic *c*-axis c^*[1]. For Na_2IrO_3 the angle θ could be determined to 44.3° using diffuse magnetic X-ray scattering [18]. For α-$RuCl_3$ fittings of neutron diffraction and resonant elastic X-ray scattering experiments estimate θ to ∼32° [70, 86]. However, α-Li_2IrO_3 forms a complex counter-rotating spiral magnetic order as shown in Figure 4.14(b). Sears *et al.* [87] reveals the presence of three domains with different directions of the moments and the zig-zag lines for α-$RuCl_3$. These different domains emerge from the proximity to a threefold symmetry of the system. They further showed that applying a field along the direction of the

[1]Due to the monoclinic symmetry the c-axis is not orthogonal to the ab-plane. Hence, all measurements perpendicular to the ab plane are parallel the cubic equivalent c^*.

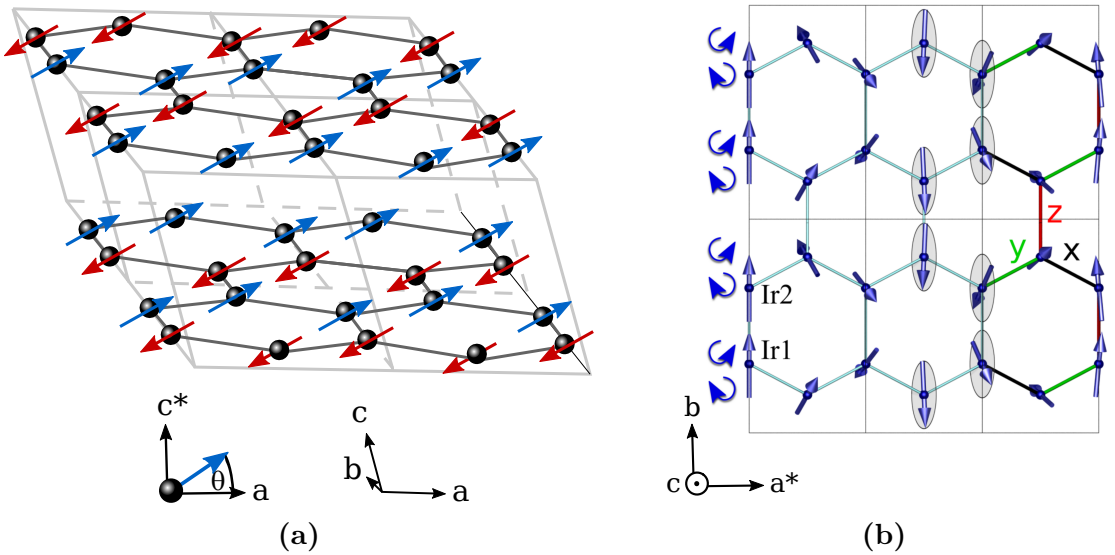

Figure 4.14.: Ordered magnetic structure below T_N. (a) Na_2IrO_3 and α-$RuCl_3$ exhibit a zig-zag order with antiferromagnetic zig-zag chains along the a-axis (figure based on [18]). The spins are tilted out of the ab plane with an angle θ of 44° for Na_2IrO_3 and most likely about 32° for α-$RuCl_3$. In between planes the coupling is antiferromagnetic. (b) α-Li_2IrO_3 shows a more complex counter-rotating spiral order with ferromagnetically coupled planes (picure from [56]).

zig-zag line of one domain leads to the gradual transformation of this domain into the other two domains up to $\mu_0 H$ ~2 T. At roughly 8 T, the magnetic order has been found to completely disappear, when the system enters a disordered quantum state [71, 72, 87].

These types of magnetic order cannot be explained by the Kitaev-Heisenberg model. Therefore, Rau *et al.* [11] introduced the symmetric off-diagonal exchange Γ, claiming it to be generic if both, direct (Heisenberg) and oxygen mediated overlap (Kitaev), are present. Furthermore, they analyze the influence of a trigonal distortion, especially important for Na_2IrO_3, and find it induces another off-diagonal exchange, denoted Γ' [28]. The overall Hamiltonian for the nearest-neighbor HK$\Gamma\Gamma'$ model, combining all four mentioned exchange interactions, is described by [52]:

$$\mathcal{H}_{ij}^{\gamma} = J_{ij}\boldsymbol{S}_i \cdot \boldsymbol{S}_j + K_{ij}S_i^{\gamma}S_j^{\gamma} + \Gamma_{ij}(S_i^{\alpha}S_j^{\beta} + S_i^{\beta}S_j^{\alpha}) \tag{4.2}$$

$$+ \Gamma'_{ij}(S_i^{\gamma}S_j^{\alpha} + S_i^{\alpha}S_j^{\gamma} + S_i^{\gamma}S_j^{\beta} + S_i^{\beta}S_j^{\gamma}) \tag{4.3}$$

where α, β, γ={y,z,x}, {z,x,y} and {x,y,z} for x-, y- and z-bond, respectively. In this

model several phases with zig-zag or spiral order can be found. This model has been varied with interactions up to third-neighbor by different research groups. Additionally, it was found that for C2/m symmetry the Dzyaloshinky-Moriya interaction is permitted for second-neighbor interactions [15]. A list of exchange parameters for Na_2IrO_3 and α-$RuCl_3$ calculated by different groups, is shown in Table 4.1, making no claim for completeness. The indices denote the "order" of interaction, distinguishing first (1), second (2) and third (3) neighbor interactions. α-Li_2IrO_3 is not

material	method	J_1	K_1	Γ_1	Γ_1'	K_2	J_3
Na_2IrO_3	Pert. Theo. [88]	+3.2	**-29.4**	+1.1	-3.5	-0.4	+1.7
	QC (2-site) [12]	+2.7	**-16.9**	+1.0	-	-	-
	ED (6-site) [15]	+0.5	**-16.8**	+1.4	-2.1	-1.4	**+6.7**
α-$RuCl_3$	DFT [16]	-1.8	**-10.6**	**+3.8**	-	-	+1.3
	QC (2-site) [89]	+0.7	**-5.1**	**+1.2**	-	-	-
	ED (6-site) [15]	-1.7	**-6.7**	**+6.6**	-	-	+2.7
	DFT+t/U exp. [17]	-0.3	**-10.9**	**+6.1**	-	-	+0.03
	mod. ab initio [90]	-1.3	**-15.1**	**+10.1**	-0.1	-0.7	+0.1

Table 4.1.: Overview of calculated exchange parameters of Na_2IrO_3 and α-$RuCl_3$ in units of meV (adapted from [52]). In bold are the largest parameters. Different theoretical approaches have been used (abbreviations listed in Section A.1). While for Na_2IrO_3 the Kitaev parameter exceeds all other by far, α-$RuCl_3$ shows additionally a significant Γ_1 factor.

included in this list and will only be covered very shortly below, since it will be less important for the results of this work. Different theoretical approaches have been used (abbreviations listed in the appendix in section A.1), gaining similar results for the sign and order in size of the different interactions. In Na_2IrO_3 a ferromagnetic Kitaev parameter K_1 exceeds all others. Only one study predicted a significantly large J_3 [15]. They argues that the larger Ir-O-Ir angle from the optimal 90° in Na_2IrO_3 is responsible for the smaller contributions of other nearest neighbor interactions, because it enhances the distance between the Ir ions and reduces, therefore, the direct metal-metal hopping. The larger deviation from the Jackeli-Khaliullin is seen as an advantage that pushes the system towards the Kitaev limit. For α-$RuCl_3$

the Kitaev exchange is smaller and ferromagnetic as well. The Γ_1 parameter was calculated to be roughly between a quarter and equal in size compared to K_1. These findings are supported by [86], where the authors claim that the Γ_1 term tilts the ordered moments towards the a-b plane, away from an angle of 50°. For α-$RuCl_3$ ($\sim 32°$), with a significantly smaller angle than for Na_2IrO_3 ($\sim$44°), the Γ_1 term is estimated to be a large fraction or comparable to the Kitaev term. An intensive theoretical study from 2020, developed a model that reproduced experimental magnetic specific heat data as well as inelastic neutron scattering data [90], while most models only captured one of these. They found a strongly enhanced Kitaev term, comparable to Na_2IrO_3.
Extended calculations from [15] for α-Li_2IrO_3 predicted significant contributions from J_1, K_1, Γ_1 as for Na_2IrO_3 and α-$RuCl_3$, but also for K_2, Γ_2, $|D_2|$ and J_3. Here, second and third neighbor interactions seem to play a significantly enhanced role. Additionally, the first neighbor interactions showed considerable differences between the z- and x/y- bonds. Nevertheless, how well these theoretical models agree with the real materials is still under debate and will require further studies.

Janssen *et al.* [91] proposed three scenarios to stabilize a zig-zag ground state in α-$RuCl_3$ and Na_2IrO_3:

- scenario (1): $K_1 > 0$ (AFM) and $J_1 < 0$ (FM)
- scenario (2): $K_1 < 0$ (FM) and sizable $J_3 > 0$ (AFM)
- scenario (3): $K_1 < 0$ (FM), sizable $\Gamma_1 > 0$ and small $J_1 < 0$ (FM)

The third scenario seems to agree with the exchange parameters from literature for α-$RuCl_3$. They therefore predict a finite transversal magnetization for fields not directed parallel or perpendicular to c^*. They point out that a large Γ interaction naturally explains a large anisotropy in magnetization. Since Γ_1' and K_2 seem to play a role for Na_2IrO_3 as well, the system is not easily compatible with these scenarios. The data from [15] suggest a closeness to the second scenario with sizeable J_3. Nevertheless, the off-diagonal interactions Γ_1 and Γ_1' could lead to a detectable transversal moment for Na_2IrO_3 as well. They further predict for both systems an in-plane anisotropy with maximal susceptibility along a Ru-Ru and Ir-Ir bonds.

Experimental magnetization analysis

Field and temperature dependent magnetization have been studied extensively. An overview over important magnetic properties is listed in Table 4.2. The compounds follow Curie-Weiss law at high temperatures. As expected from the theoretical Jackeli-Khalliulin model all three candidates possess an effective moment μ_{eff} close to the value of $1.73\,\mu_{\text{B}}$, which is consistent with the $J_{\text{eff}} = 1/2$ scenario. The magnetic spins of Na_2IrO_3 and α-Li_2IrO_3 both order around 15 K. α-$RuCl_3$ can show two phase transitions at ∼7 K and at ∼14 K. The latter has been found to be attributed to a high density of stacking faults, occurring only in samples with lower quality [52, 70, 92]. The Weiss constants Θ vary significantly between in-plane (Θ_{ab}) and out-of-plane ($\Theta_{\text{c}*}$) components with the anisotropy being reversed for α-Li_2IrO_3 and α-$RuCl_3$ compared to Na_2IrO_3. The large differences between Θ_{W} and T_{N} demonstrate the strong frustration in these systems. The three compounds show large

parameter	Na_2IrO_3	α-Li_2IrO_3	α-$RuCl_3$
μ_{eff} (μ_{B})	∼1.8 [8, 77]	1.8 [8]	2.0 to 2.7 [9, 93–95]
θ_{iso} (K)	∼-125 [8]	-33 to -44 [8, 77, 78]	∼40 [93]
θ_{ab} (K)	-176 [77]	4 [78]	37 to 68 [9, 95]
$\theta_{\text{c}*}$ (K)	-40 [77]	-58 [78]	-145 to -150 [9, 95]
T_{N} (K)	15-18 [55, 77]	∼15 [8, 56]	7 to 14 [70, 95, 96]
order	zig-zag[18, 55]	spiral [56]	zig-zag [69, 70]

Table 4.2.: Overview of the magnetic properties of Na_2IrO_3, α-Li_2IrO_3 and α-$RuCl_3$. Adapted from [15].

anisotropies comparing in- and out-of-plane magnetization. While for α-Li_2IrO_3 and α-$RuCl_3$ the in-plane magnetization is enhanced regarding to the component out-of-plane ($\chi_{\text{ab}} > \chi_{\text{c}*}$), Na_2IrO_3 possesses a reversed anisotropy with $\chi_{\text{c}*} > \chi_{\text{ab}}$ [7, 9, 21, 79, 95, 96].

The magnetization of α-$RuCl_3$ along different directions was investigated intensively by Lampen-Kelley *et al.* [21]. In the following, we will look at their findings in more depth, since the measurements were repeated for α-$RuCl_3$ and for Na_2IrO_3 during the course of this thesis.

Experimental and theoretical magnetization analysis of α-$RuCl_3$[21]

Lampen-Kelley *et al.* performed experiments investigating the in-plane anisotropy and their temperature dependence, comparing it to the out-of-plane susceptibility. They further determined the transversal magnetization, which is related to off-diagonal exchanges like the Γ-exchange. The experimental data was compared to a simple model based on a nearest-neighbor Heisenberg-Kitaev-Γ Hamiltonian, expanded for high temperatures. This model was found to be able to explain the observed behavior and used to extract rough estimates of the exchange constants involved.

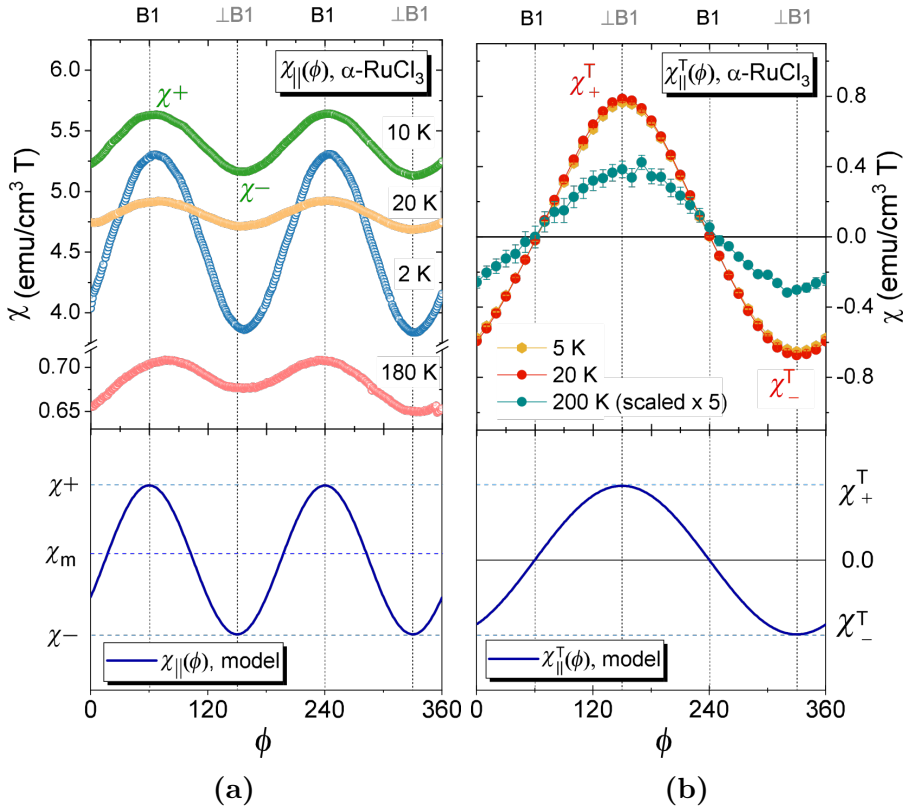

Figure 4.15.: In-plane anisotropy data for different T of the (a) longitudinal and (b) transversal susceptibility in dependence of the angle ϕ for α-$RuCl_3$, measured by [21]: Even above the magnetic transition temperature of $\sim 7\,\mathrm{K}$ $\chi_{||}$ is maximal (minimal) parallel (perpendicular) to one distinct Ru-Ru bond (B1). (b) The transversal susceptibility turns out to be largest for the direction perpendicular to B1. However, due to the measurement setup an angle dependent analysis regarding the transversal in-plane moment cannot be made. The authors developed a theoretical model that is able to describe the observed behavior, shown below the experimental data.

The experimental data of the in-plane susceptibility in dependence of the in-plane angle ϕ are summarized in Figure 4.15. They found an anisotropy in the a-b plane for the longitudinal susceptibility (Figure 4.15a), as predicted by [91]. Even well above the ordering temperature the in-plane susceptibility is maximal (minimal) parallel (perpendicular) to one specific Ru-Ru bond, which they label as B1 (Figure 4.15a). The crystallographic orientation of B1 remains open. Similar measurements for Na_2IrO_3 and α-Li_2IrO_3 could not be found in the literature, most likely due to the absence of high-quality single crystals without twinning defects. Lampen-Kelley *et al.* further verified the transversal magnetization predicted from [91] (although they applied the field along c^*, which was explicitly excluded in [91]). Figure 4.15b shows that the extrema of the transversal magnetization in dependence of the in-plane angle ϕ lie in the direction perpendicular to the B1 bond. This characteristic is persistent up to very high temperatures. The experimental setup to measure a transversal moment (see Section 3.4.2) is not comparable to longitudinal magnetization experiments. Instead of measuring the absolute value of the moments pointing along a certain direction, the experimental setup measures the sum of all transversal moments in the measurement plane. The shape of the susceptibility curve is purely setup dependent, but the direction of the maxima and minima nevertheless represent the direction of the moment (or in the case of several moments the direction of the sum). The authors did not seem to be aware of this fact and have henceforth in some points misinterpreted Figure 4.15b. Another point should be noted that the units for the susceptibility used in the paper [χ]=emu/cm^{3}T are quite unusual. The volume susceptibility is a dimensionless quantity, although one can also find the unit emu/cm^3. Here it must be pointed out that "emu" is not a real unit in the sense that it is defined in different ways. For the maximum and minimum of the in-plane susceptibility χ^+ and χ^-, the out-of-plane susceptibility $\chi_\perp$ and the maximal transversal susceptibility χ_+^T the temperature dependence is shown in Figure 4.16. χ_+^T seems to follow the same temperature dependency as the longitudinal data with the same transition temperature. In fact, it roughly matches the χ^+ data, when multiplied by 6.

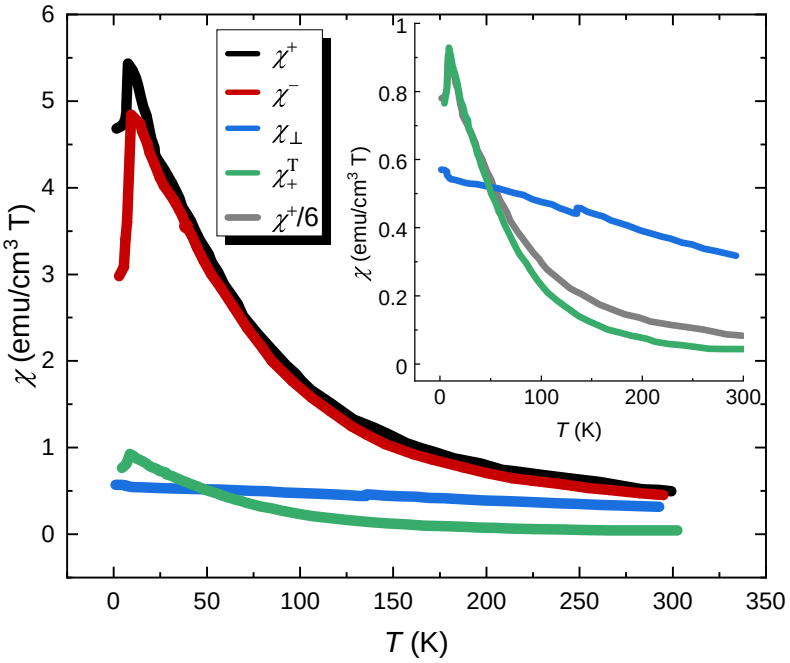

Figure 4.16.: Temperature-dependent susceptibility measurements were performed for $\chi||c^*$ ($\chi_\perp$) as well as for the extrema in-plane (χ^+ and χ^-) and the maximum of transversal susceptibility (χ_+^T). The inset shows a χ_+^T and $\chi_\perp$ enlarged and in comparison to $\chi^+/6$. Data taken from [21].

The authors developed a theoretical model that describes the observed behavior of the susceptibility. For this purpose, they use the nearest-neighbor Kitaev-Heisenberg-Γ model, but are tolerating different exchange parameters for J_1, K_1 and Γ_1 for the B1 bond, marking them J_1', K_1' and Γ_1', compared to the other bonds, called B2$_x$ and B2$_y$ bonds. The overall Hamiltonian is given by the sum of all bond Hamiltonians: $\mathcal{H}_S = \mathcal{H}_{\mathrm{B1}} + \mathcal{H}_{\mathrm{B2}x} + \mathcal{H}_{\mathrm{B2}y}$ with:

$$\mathcal{H}_{\mathrm{B1}} = \sum_{\mathrm{B1\ bonds}<ij>} J_1'\boldsymbol{S}_i \cdot \boldsymbol{S}_j + K_1' S_i^z S_j^z + \Gamma_1'(S_i^x S_j^y + S_i^y S_j^x),$$

$$\mathcal{H}_{\mathrm{B2}x} = \sum_{\mathrm{B2}x\ \mathrm{bonds}<ij>} J_1\boldsymbol{S}_i \cdot \boldsymbol{S}_j + K_1 S_i^x S_j^x + \Gamma_1(S_i^y S_j^z + S_i^z S_j^y) \text{ and}$$

$$\mathcal{H}_{\mathrm{B2}y} = \sum_{\mathrm{B2}y\ \mathrm{bonds}<ij>} J_1\boldsymbol{S}_i \cdot \boldsymbol{S}_j + K_1 S_i^y S_j^y + \Gamma_1(S_i^z S_j^x + S_i^x S_j^z).$$

The coordinate system was chosen in a way that x-, y- and z-direction coincide with the direction of the Kitaev interactions for each bond type, assuming an idealized undistorted octahedral environment. Within this framework a high-temperature expansion of the zero-field susceptibility tensor was performed. The zero-field sus-

ceptibility tensor in the high-temperature regime was calculated up to an order of T^{-2}, thus receiving:

$$\chi^{\mu\mu'} = \frac{\mu_B^2 N}{4k_B T}\begin{pmatrix} g_x & 0 & 0 \\ 0 & g_x & 0 \\ 0 & 0 & g_z \end{pmatrix} - \frac{\mu_B^2 N}{(4k_B T)^2}\begin{pmatrix} g_x^2\tilde{J}_1 & g_x^2\Gamma_1' & g_x g_z \Gamma_1 \\ g_x^2\Gamma_1' & g_x^2\tilde{J}_1 & g_x g_z \Gamma_1 \\ g_x g_z \Gamma_1 & g_x g_z \Gamma_1 & g_z^2\tilde{J}_1' \end{pmatrix}. \quad (4.4)$$

Here, a g-factor anisotropy of $g_x = g_y \neq g_z$ (consistent with [31, 89, 96, 97]) was assumed and $\tilde{J}_1 := 2J_1 + J_1' + K_1$ and $\tilde{J}_1' := 2J_1 + J_1' + K_1'$ defined. The first term is equal to Curie's law with $J = 1/2$. The second term is responsible for deviations of Curie's law at high temperatures by the exchange interactions.
With this equation they are able to explain the observed wave-like curve from the rotation of the longitudinal magnetization by projecting equation 4.4 onto the in-plane direction. The same was done for the transversal magnetization. Within this model (for the high-temperature regime) and assuming an isotropic g-factor, which is close to reality according to [98], the in-plane anisotropy is originated by the difference in exchange parameters of the Kitaev and Γ term:

$$(\chi_+ - \chi_-) \sim T^{-2}[K_1' - K_1 + 2(\Gamma_1' - \Gamma_1)].$$

In contrast, the anisotropy between in-plane and out-of-plane is determined only by the off-diagonal exchange couplings:

$$\frac{\chi_+ + \chi_-}{2} - \chi_\perp \sim T^{-2}(\Gamma_1' + 2\Gamma_1).$$

These T^{-2} dependencies were found in the experimental data, giving strong evidence for the usefulness of the model for α-$RuCl_3$.
Fitting Curie-Weiss behavior to the measured inverse susceptibilities of $\chi_+, \chi_-, \chi_\perp$ and χ_+^T, they find rough estimates of the exchange couplings via the Curie-Weiss constants:

- $\tilde{J}_1 = 14.3\,\text{meV}$
- $\Delta K := K_1 - K_1' = -7.7\,\text{meV}$
- $\Gamma_1 = 29.8\,\text{meV}$
- $\Gamma_1' = 27.9\,\text{meV}$

These constants are far larger than the results obtained from other methods. The authors suggest the small temperature fitting range for the Curie-Weiss fit to be responsible for the discrepancy. Indeed, Kitaev materials have been found to be very

sensitive to the fitting range, even for temperatures several times the Curie-Weiss temperature [78, 99]. Nevertheless, the authors could show good agreement of their theoretical model with their experimental data and showed the importance of the Γ_1-exchange for the in-plane/ out-of-plane anisotropy in α-$RuCl_3$.

4.3.4 Doping experiments

There have been attempts to drive the candidates towards or away from the spin liquid regime by means of chemical doping. In the doping series $(Na_{1-x}Li_x)_2IrO_3$ a topological superconductivity phase for low temperatures has theoretically been proposed [100]. Experiments later showed that the doping of Li into Na_2IrO_3 could only be achieved up to x=0.25, which corresponds to Li sitting inside the Ir honeycombs sandwiched between Na-only layers [101]. For $x > 0.25$ a phase separation takes place. No superconducting phase could be found. Rolfs *et al.* [102] measured magnetization of powder, while Manni *et al.* [101] analyzed lumps of single crystals. Both groups found a reduction of T_N with increasing Li content. Manni *et al.* showed that the Curie-Weiss temperature Θ_W as well as all three lattice parameters are reduced with increasing x. The latter can be easily understood, since the Li ion is smaller than the Na ion. For doping $x \geq 0.1$ Rolfs *et al.* found a glassy spin state and suggest a spiral ordering for the doped samples. Raman experiments showed a polarization-independent broad band that increased in intensity and persisted to higher temperatures for the doped samples [103]. They deduced stronger Kitaev exchange correlations for $x > 0$. Experiments probing the optical conductivity found further evidence that Li doping pushes the system deeper into the Mott-insulating state and closer to the pure Kitaev model [104]. All these pieces of information on the doping series $(Na_{1-x}Li_x)_2IrO_3$ point to an enhanced Kitaev character upon doping, making this material worth studying more closely as it has been done in this thesis.

Na in Na_2IrO_3 can also be substituted by Mg. In [84] the authors found a reduction of the antiferromagnetic coupling (seen in the reduction of Θ_W) with increasing Mg concentration, very similar to $(Na_{1-x}Li_x)_2IrO_3$. This was accompanied by a shortening of the Ir-O-Ir (and Ir-Ir) bonds, moving the angles closer towards the "ideal" 90°.

Furthermore, Na_2IrO_3 and α-Li_2IrO_3 were doped with the non-magnetic Ti^{4+} ion

[105], corresponding to a dilution of the magnetic moments. On the one hand, it clearly shows that for Na_2IrO_3 nearest-neighbor interactions play an important role for the magnetic order, since already small doping concentrations lead to a drastic reduction of the antiferromagnetic coupling (Θ_W). On the other hand, α-Li_2IrO_3 shows no significant change in Θ_W, keeping a stable value up to a doping of 50% Ti atoms. This emphasizes the importance of interactions beyond nearest-neighbor for this compound. These results fit well to the theoretical findings regarding the exchange parameters mentioned in Section 4.3.3. Additionally, for both materials a spin glass phase is found in the doped samples with a freezing temperature inversely proportional to x.
A similar effect can be found for the substitution of Ir by Ru. For the Na_2IrO_3 system small doping values already destroy the antiferromagnetic order and give rise to a disorder-driven spin glass state instead [106]. The same experiment for α-Li_2IrO_3 shows a continuous suppression of T_N below 2 K for x > 0.3.
α-$RuCl_3$ has been studied substituting Cr^{3+} ions with the Ru^{3+}. Here, the anisotropic Ru spin is gradually replaced by the isotropic Cr spin [107–109]. The antiferromagnetic order is already suppressed around $x = 0.05$ and at around $x = 0.1$ a spin-glass state sets in. Interestingly [108] finds a reversal of the in-plane/out-of-plane anisotropy around $x = 0.05$, which is explained by the competition of the isotropic Heisenberg and the anisotropic Γ interactions.

4.3.5 Summary

The Kitaev candidates Na_2IrO_3, α-Li_2IrO_3 and α-$RuCl_3$ realize the Jackeli-Khaliullin mechanism well, but suffer from imperfectness and additional features, not included in the theoretical model. For one, the large extension of the d orbitals leads to direct hopping between the TMs, inducing Heisenberg exchange and Γ-exchange. Further, the crystal structure shows deviations from the perfect honeycomb lattice, leading to the off-diagonal exchange Γ'. The interactions might be relevant even beyond nearest neighbor. These additional interactions are responsible for the zig-zag order for Na_2IrO_3 and α-$RuCl_3$ as well as the counter-rotating spiral order for α-Li_2IrO_3 at low temperatures. Still, in all three materials the Kitaev interaction seems to be the most dominant term. Different groups have found evidence for the strong Kitaev character of the real materials, showing the anisotropic character of the interactions

or hints for Majorana excitations. This induced many experiments trying to push the systems closer to the Kitaev regime by means of doping (intercalation and pressure effects have also been investigated, but will not be of importance here). For the doping series $(Na_{1-x}Li_x)_2IrO_3$ different experiments have suggested an increasing Kitaev character with increasing Li-doping.

5 | Results

Although the result chapter is structured according to the material systems α-$RuCl_3$, Na_2IrO_3 and $(Na_{1-x}Li_x)_2IrO_3$ as well as the applied experimental methods, four different goals were the basis of this work. The results of their research are presented and discussed in this chapter. The first goal was the enhancement of the size of the single crystals of Na_2IrO_3 by modulating the growth process. This is addressed in Section 5.3.1 and the magnetization of samples grown with the old and new method is compared in Section 5.3.3 as well as the influence of the growth time investigated in Section 5.3.2. As a second goal the measurements of the transverse magnetization of [21] on α-$RuCl_3$ were supposed to be repeated (Section 5.2) and further be performed on Na_2IrO_3 (Section 5.3.4). Prior to these experiments, the option to measure transverse magnetization was studied and tested in Section 5.1. To determine the direction of the transverse moment of Na_2IrO_3, Laue-diffraction was performed on a single crystal in section 5.3.2. The last goals concerned the anisotropy of $(Na_{1-x}Li_x)_2IrO_3$ in-plane vs. out-of-plane in dependence of the Li-doping (Section 5.4) as well as the in-plane anisotropy for undoped Na_2IrO_3 (Section 5.3.3). Furthermore, an experiment regarding the degradation of Na_2IrO_3 powder is presented in Section 5.3.2.

5.1 Preparation experiments for the transverse magnetization measurements

Motivated by the results of [21] regarding the transverse magnetization of α-$RuCl_3$ and Na_2IrO_3 was investigated with the transverse option of the MPMS. As it was described in Section 3.4.2, this experimental method is not trivial. Therefore, several experiments have been conducted prior to the measurements of the samples in order to characterize the transverse pick-up coils and analyze the influence of different

essential factors of the measurement. This gave us knowledge about the possibilities and limits of this option. Furthermore, the background of the sample holders were tested. The first section of this part, however, contains a detailed description of the analysis of the raw data, which has been applied to all datasets in order to determine the transverse moment. The introduced coordinate system of Section 3.4.2 will be applied here as well. In this definition the z-axis points parallel to the external field and the measurement takes place in the x-y-plane.

5.1.1 Data analysis

The raw data for the transversal magnetization are put through an elaborate analysis. First, the background of the sample holder needs to be subtracted when measuring samples with a small signal, ideally by the subtraction of the raw data from sample and background. Small in this case means all samples which do not show a transverse moment much larger than the background moment. Secondly, the longitudinal contribution, stemming from the longitudinal moment producing a signal in the transverse pick-up coils due to an inevitable offset to the coil center, needs to be determined and subtracted from the data to gain the transverse signal. In the end, this signal is fit to determine the transverse magnetic moment μ_t. This procedure will be presented in more detail in the following.

Every data point of the magnetic moment $\mu(T, H, \varphi)$ contains of 32, 48 or 64 raw data points for the induced voltage $U(z)$ between $z = 0$ and $z = 4\,\mathrm{cm}$, depending on the properties chosen for the measurement. Since the pick-up coils do not only measure the transverse moment, but also part of the longitudinal moment, the latter can only be subtracted by taking the raw data. Due to the difference in symmetry (see Section 3.4.2), the true transversal moment can be gained by symmetrization around the symmetry point $z_0 = 2\,\mathrm{cm}$. The data $U(z)$ can be split into a symmetric function $U_\mathrm{s}(z)$, corresponding to the transverse moment, and an antisymmetric function $U_\mathrm{a}(z)$, which corresponds to the contribution of the longitudinal moment: $U(z) = U_\mathrm{s}(z) + U_\mathrm{a}(z)$. In order to achieve this, the x values of the data set are shifted by $-2\,\mathrm{cm}$, to move the symmetry point to $0\,\mathrm{cm}$. Then the following equations are applied to the y values of the data set to determine the symmetric and

antisymmetric part of the signal:

$$U_{\mathrm{s}}(z) = \frac{U(z) + U(-z)}{2}$$
$$U_{\mathrm{a}}(z) = \frac{U(z) - U(-z)}{2},$$

which one gets by applying the definitions of the symmetric function and the antisymmetric function: $U_{\mathrm{s}}(z) = U_{\mathrm{s}}(-z)$, $U_{\mathrm{a}}(z) = -U_{\mathrm{a}}(-z)$.

The symmetric part of the function $U_{\mathrm{s}}(z)$ is then fitted to: [110]

$$U_{\mathrm{s}}(z) = -\left[\varphi(2L + d - z) - \varphi(L + d - z)\right] \tag{5.1}$$
$$+\left[\varphi(L_{\mathrm{c}}/2 - z) - \varphi(-L_{\mathrm{c}}/2 - z)\right] \tag{5.2}$$
$$-\left[\varphi(-L - d - z) - \varphi(-2L - d - z)\right] \tag{5.3}$$

with the function φ being defined as:

$$\varphi(x) = \frac{A\pi}{R^2}\left(\frac{4x^3 + 6xR^2 - \sqrt{x^2 + R^2}xR}{\sqrt{x^2 + R^2}(x^2 + R^2)}) - \arctan(x/R)\right).$$

The same equation is used in the software of the MPMS to calculate the magnetic moment. L, L_{c}, R and d are all geometrical constants from the coil setup and the amplitude A is the fitting parameter related to the magnetic moment. To account for a shift in the voltage an additional fitting parameter U_0 is included. Finally, the transverse moment is obtained by applying equation 3.3, via the fitting parameter A ($= X(3)$), a setup-dependent constant and the sensitivity factor. In the MultiVu software, which controls the MPMS, special *.diag* files are saved, logging the *gain* and *range* used for each measurement point. From these parameters the sensitivity can be calculated, which is explained in [46].[1]

For a better understanding Figure 5.1 visualizes the analysis process on the example of three raw data sets with varying proportion of the antisymmetric longitudinal contribution. To analyze the measurements in an effective manner and reasonable times, a program was written in LabTalk, the programming language of OriginLab, that separates the data for each point $\mu(T, H, \varphi)$, performs the symmetrization and calculates the sensitivity from the .diag files. Afterwards, the fitting and calcula-

[1] To be able to compare different raw data of different angles/ temperatures/ fields of one measurement or of different measurements, it is necessary to divide the raw data by its sensitivity.

tion of the transverse magnetic moment was performed manually. The fitting and calculation was proven to be correct by comparing the result of a purely transverse moment (as it will be used in the next section) with the calculated magnetic moment of the MPMS software.

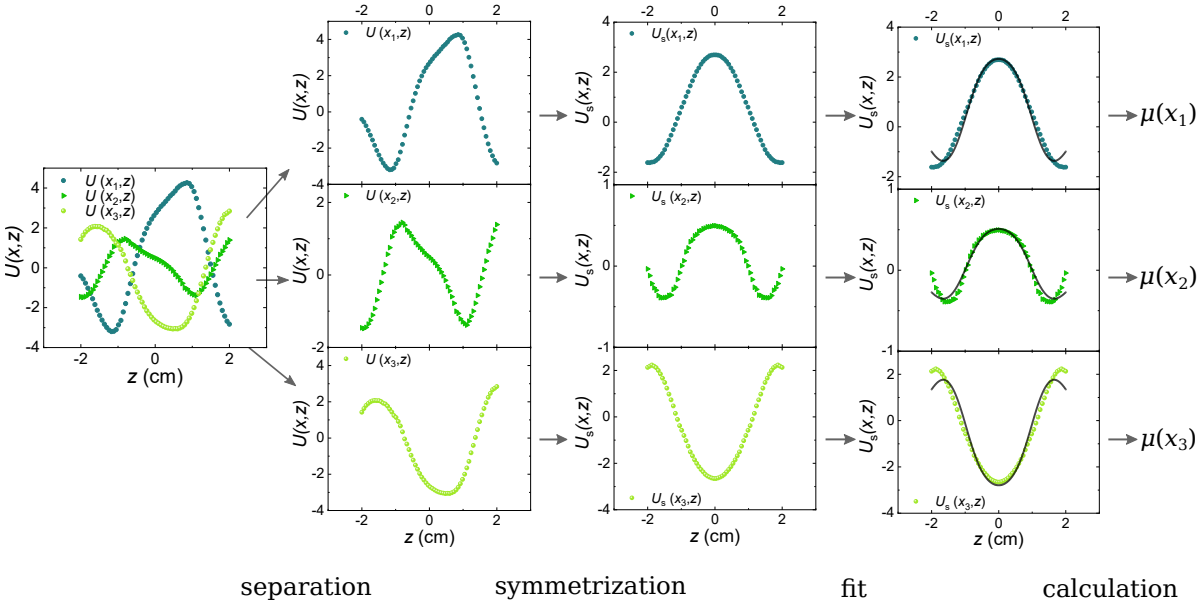

Figure 5.1.: Analysis of the data of the transverse magnetization measurements. The detrended raw voltage is separated for every temperature point x_i, symmetrized around 0, fitted with equation 5.1 and the moment calculated with equation 3.3.

5.1.2 Characterization of the transverse pick-up coils

Before the first samples were measured in the transverse option of the MPMS, a characterization of some elemental features of the system needed to be investigated. For this purpose a small $Nd_2Fe_{14}B$ permanent magnet of the size 1 mm x 1 mm x 1 mm was used. This alloy is known to be a hard magnet with a very large magnetic moment, which is a ideal for our purpose. The magnet was inserted with different orientations of its magnetic moment: parallel and orthogonal to the field direction as well as with an angle of 45° in between these positions (see Figure 5.2). This way we simulate a sample with a) only transverse, b) equally transverse and longitudinal and c) only longitudinal moment. Although the second orientation could in principle be neglected, it serves as a verification of the other two. With these configurations 1) the relative position of the center positions of longitudinal and transverse coils, 2)

the orientation of the pick-up coils, 3) the effect of the longitudinal moment in the transverse coils and 4) the influence of a radial offset on the signal was investigated. The magnet was glued with GE Varnish onto a quartz holder and all measurements were performed at a temperature of 300 K and a magnetic field of 0 T. It must be noted that all alignments were performed by eye, which therefore have a significant error, but are sufficient for our purpose.

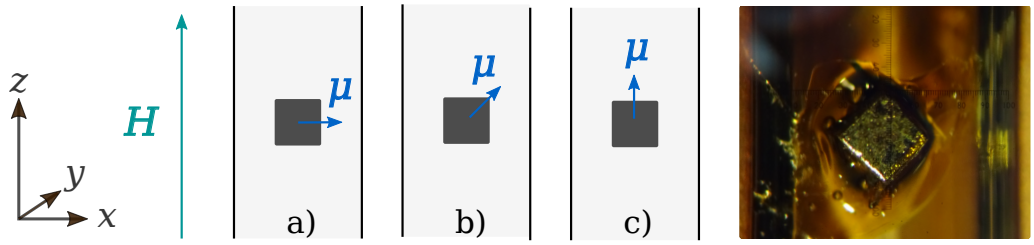

Figure 5.2.: To characterize the transverse pick-up coils a $Nd_2Fe_{14}B$ magnet was oriented with its magnetic moment pointing a) $||$ x ($\mu = \mu_{\text{trans}}$), b) at 45° in the xz plane ($\mu = 1/\sqrt{2}[\mu_{\text{long}} + \mu_{\text{trans}}]$) and c) $||$ z ($\mu = \mu_{\text{long}}$). The picture on the right shows the magnet in position b).

1) Center position

An important detail is the position of the center of the transverse pick-up coils in respect to the longitudinal coils. Ideally, both will be at the same point, enabling to perform the sample centering (before the measurement) via the longitudinal centering process. This has the clear advantage, due to a larger longitudinal moment, of an easier and more precise centering. Since the direction of the transverse moment and its size is unknown before the measurement, it is always possible that it is directed towards or near the gap of the coils, resulting in no or very small measurable transverse moment, if there is one at all.

The $Nd_2Fe_{14}B$ magnet was inserted in position b), enabling a simultaneous measurement of the the longitudinal and transverse magnetic moment. The center is determined by performing a center scan. To reduce errors due to the influence of the longitudinal contribution, the center scans of the transverse moment were only taken at the angle with the maximal amplitude of the transverse signal (here: 0° and 180°) [2]. For the longitudinal measurements, the same angles as well as 90° and 270°

[2]Reminder: The transverse signal shows a sine-like behavior, when rotated in the xy-plane.

were used for center determination. The corresponding values for the center position are listed in Table 5.1. The transverse center is by approximately 1 mm shifted in

angle $\varphi(^\circ)$	center long (cm)	center trans (cm)
0	2.13	2.04
90	2.12	
180	2.14	2.02
270	2.15	

Table 5.1.: Comparison of the center positions of the longitudinal (long) and the transverse signal (trans) of a $Nd_2Fe_{14}B$ in position b).

respect to the longitudinal center. To examine the effect of such a difference in the center positions Δz, raw data (which will be shown in the next section) of position b) and c) were analyzed. The centering was performed using the longitudinal moment and Δz was assumed to be 0.03 cm, 0.06 cm and 0.1 cm. Figure 5.3 shows the 305° data of position b). On the first glance, one would think that the raw signal is

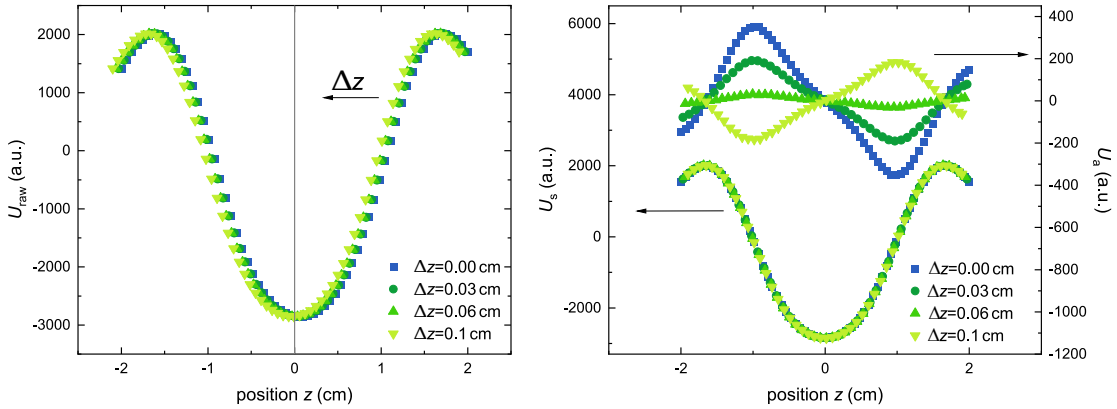

Figure 5.3.: a) Comparison of the raw data in case b) at 305° when the signal is not shifted or shifted by 0.03 cm, 0.06 cm and 0.1 cm. This corresponds to a misalignment of the center in z direction, which is realistic as the previous chapter showed. b) The shift leaves the symmetric part (left axis) almost unchanged, but has an influence of the size and sign on the antisymmetric part (right axis).

simply a symmetric one with a small mismatch in the center position. Changing the center and recalculating the symmetric and antisymmetric part leads to a visible

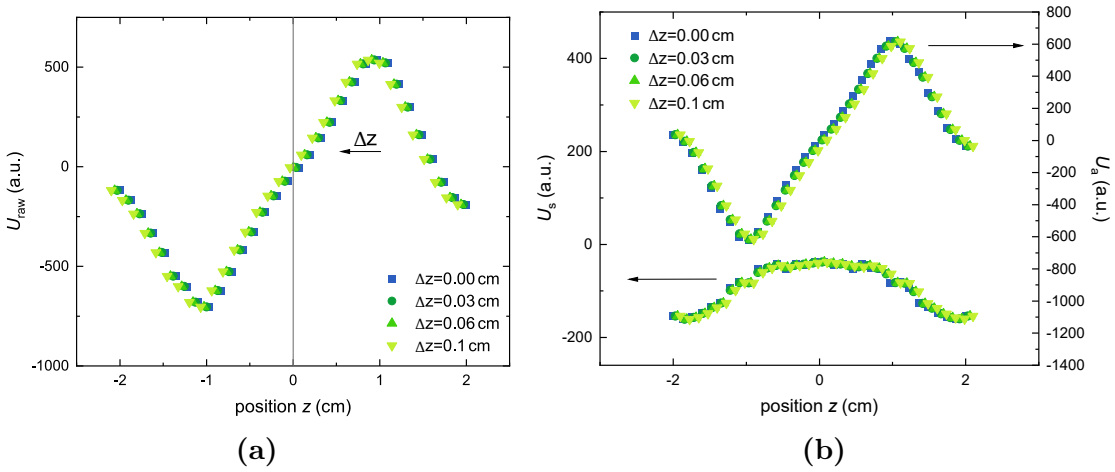

Figure 5.4.: a) Comparison of the raw data in case c) at 0° when the signal is not shifted or shifted by 0.03 cm, 0.06 cm and 0.1 cm. This corresponds to a misalignment of the center in z direction, which is realistic as the previous data showed. b) Both contributions are relatively unaffected by the shift.

change in the antisymmetric voltage signal U_a. Comparing the calculated moments from the symmetric part

- $\Delta z = 0.00\,\mathrm{cm}$: $\mu = -0.495\,\mathrm{emu}$
- $\Delta z = 0.03\,\mathrm{cm}$: $\mu = -0.497\,\mathrm{emu}$
- $\Delta z = 0.06\,\mathrm{cm}$: $\mu = -0.498\,\mathrm{emu}$
- $\Delta z = 0.1\,\mathrm{cm}$: $\mu = -0.497\,\mathrm{emu}$

shows that, although the effect is strong on the antisymmetric part, it scarcely changes the symmetric amplitude. Now the same was repeated for a raw data set of position c) (also shown in the following section). Figure 5.4 analyzes the influence of a center shift of the 0° raw data when the transverse moment is small compared to the longitudinal moment. Even for this case the calculated moments

- $\Delta z = 0.00\,\mathrm{cm}$: $\mu = 0.0116\,\mathrm{emu}$
- $\Delta z = 0.03\,\mathrm{cm}$: $\mu = 0.0114\,\mathrm{emu}$
- $\Delta z = 0.06\,\mathrm{cm}$: $\mu = 0.0113\,\mathrm{emu}$
- $\Delta z = 0.1\,\mathrm{cm}$: $\mu = 0.0113\,\mathrm{emu}$

posses only marginal differences. Due to the broad peak of the transverse signal, this shift leads to a negligible error and the centering of the samples is done using the longitudinal moment.

A second observation can be made from Table 5.1. The longitudinal center seems to change slightly whilst rotating in the xy-plane. To examine this in more detail, a second experiment was conducted, measuring the longitudinal signal for different ro-

tation angles in the xy-plane. Here, the sample was centered (the center position set to 0) before. The result is shown in Figure 5.5. The center position was determined

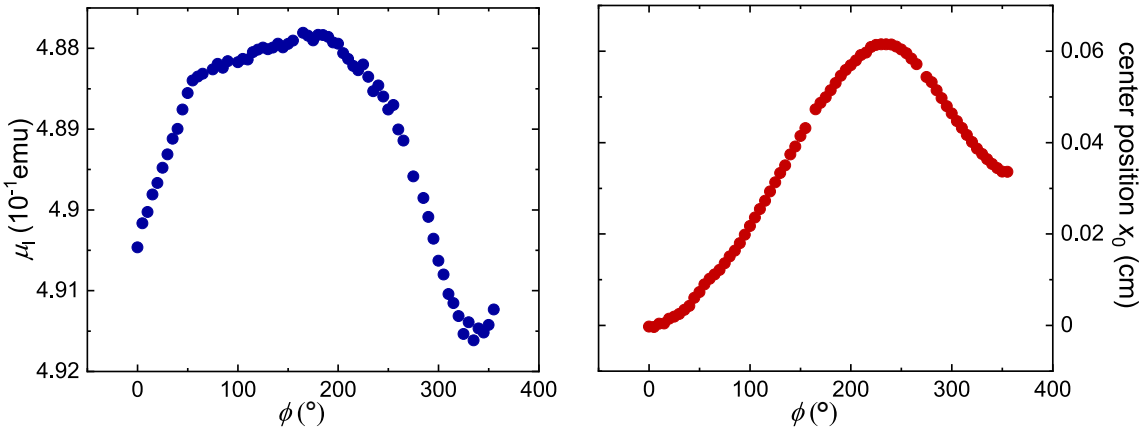

Figure 5.5.: Longitudinal moment (a) and center position (b) during a rotation in the xy-plane.

by fitting a Gaussian function to the raw data. Although one would not expect so, the longitudinal moment μ_l varies about 1% of its absolute value (already neglecting large unreasonable jumps in the data). The center shows a maximal deviation from the starting center position of 0.06 cm. Most likely the sample holder is not perfectly aligned in the pick-up coils. Nevertheless, this deviation is marginal. An open question is still why the data points at the ends of the measurement do not meet. It could be a slight error in the motor of the MPMS, which does not accurately finds the starting position for the measurement. It is possible that during very long measurements this error accumulates and then becomes a problem. Therefore, it is advisable in such a case to check the center positions from time to time.

2) Orientation of the pick-up coils

Important for later analysis is the determination of the gaps and centers of the transverse pick-up coils to be able to match our knowledge of the the crystallographic structure to the direction of the measured magnetic moment. We will find a maximum in the transverse magnetization when the moment points directly towards one of the coil centers. For this purpose the $Nd_2Fe_{14}B$ magnet was inserted in position a) (transverse) and the direction of the moment with respect to the MPMS carefully

recorded. Then, a rotation in the xy-plane was performed and from the extrema (coil centers) and the zero crossings (gaps) the positions extracted. The measurement was performed 4 times to minimize errors due to the orientation by eye. The extracted angles are listed in Table 5.2 and visualized in Figure 5.6. The standard deviation for the mean value from Table 5.2 has been calculated to be $\sigma = 8°$, which is precise enough for our purpose.

	gap1	center1	gap2	center2
ϕ (°)	62	152	242	332

Table 5.2.: Mean value of the measured angles of the transverse pick-up coils in respect to the coordinate system from Figure 5.6. The standard deviation is σ =8°for all angles.

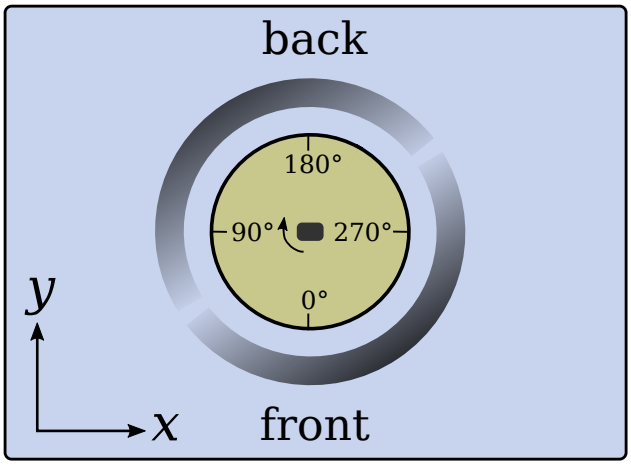

Figure 5.6.: Schematic top view of the MPMS (light grey box), the sample (black rectangle) and the position of the transverse pick-up coils (grey half circles) inside the MPMS.

3) Radial offset and longitudinal contribution

We know that if the sample is not perfectly centered in the xy-plane the transverse signal will show a contribution from the longitudinal moment. The dependence of the radial offset and the longitudinal contribution was theoretically investigated in [51] for a setup very similar to the MPMS used in this project. To get an idea how large this contribution is, the magnet was measured in all three positions a) to c) during a rotation in the xy-plane. Additionally, this experiment can tell us more about how well the symmetrization of the raw signal cleans the data from the

longitudinal contribution. Figure 5.7 shows an overview of the initial raw data, the antisymmetric part and the symmetric part for all three orientations.

To be able to compare the different measurements, the raw voltages where divided by the corresponding sensitivity S. On the first glance, as it is expected, situation a) and b) show the typical shape of the transverse signal in the raw data. We can, hence, notice that for a sufficiently large transverse moment $\mu_{\text{trans}} \geq \mu_{\text{long}}$ (position a,b) the voltage after symmetrization does not differ strongly in the amplitude, which is the important parameter for the transverse moment. To compare the different signals, the size of the largest maxima are compared. The antisymmetric part U_{a} for a) is more than two orders of magnitude smaller than the symmetric part and most likely results from imperfect alignment along z. Multiplying the transverse moment by $1/\sqrt{2}$ and adding an equally large longitudinal moment (situation b) reduces the amplitude of U_{s} as expected by about $1/\sqrt{2}$ as well. The antisymmetric signal U_{a} corresponding to the longitudinal contribution increases to roughly 10% of the transverse signal. This means about 10% of the longitudinal signal is found in the transverse signal before symmetrization. Using the data from [51], the distance to the actual center should be around 0.4 mm. This seems quite reasonable. The magnet is glued to a quartz holder (see Section 3.4.1) and the holder's surface should be at the center in the xy-plane. The magnet itself is 1 mm thick, which gives an offset to the center of the magnet of about 0.5 mm. This is very close to the 0.4 mm estimated from the literature data.

Figure 5.8 compares the transverse moments calculated from the symmetric parts in dependence of the angle ϕ. The real transverse magnetic moment corresponds to the maximum in $\mu(\phi)$. We find $\mu_{\text{trans}} = 0.76\,\text{emu}$ for a) and $\mu_{\text{trans}} = 0.52\,\text{emu}$ ($\sim 0.54 = 0.76/\sqrt{2}$) for b) [3]. The sine-like shape of the data arises from the geometry of the pick-up coils (see Section 3.4.2). If the magnet is measured in the longitudinal orientation (c), the transverse moment ($\mu_{\text{trans}}(\phi_{\text{max}}) = 0.014\,\text{emu}$) is almost two orders of magnitude smaller compared to the case of the full transverse moment (a). This moment most likely results from a small misalignment regarding the longitudinal orientation. Already an error of 1° can account for the observed signal. The same argument can be used for the discrepancy between the expected moment for a) and b). The calculated moment data of the MPMS and the own calculated data overlap nicely for situation a) and b). Only for c), where the longi-

[3] The angles in Figure 5.7 and 5.8 were adjusted for better comparison.

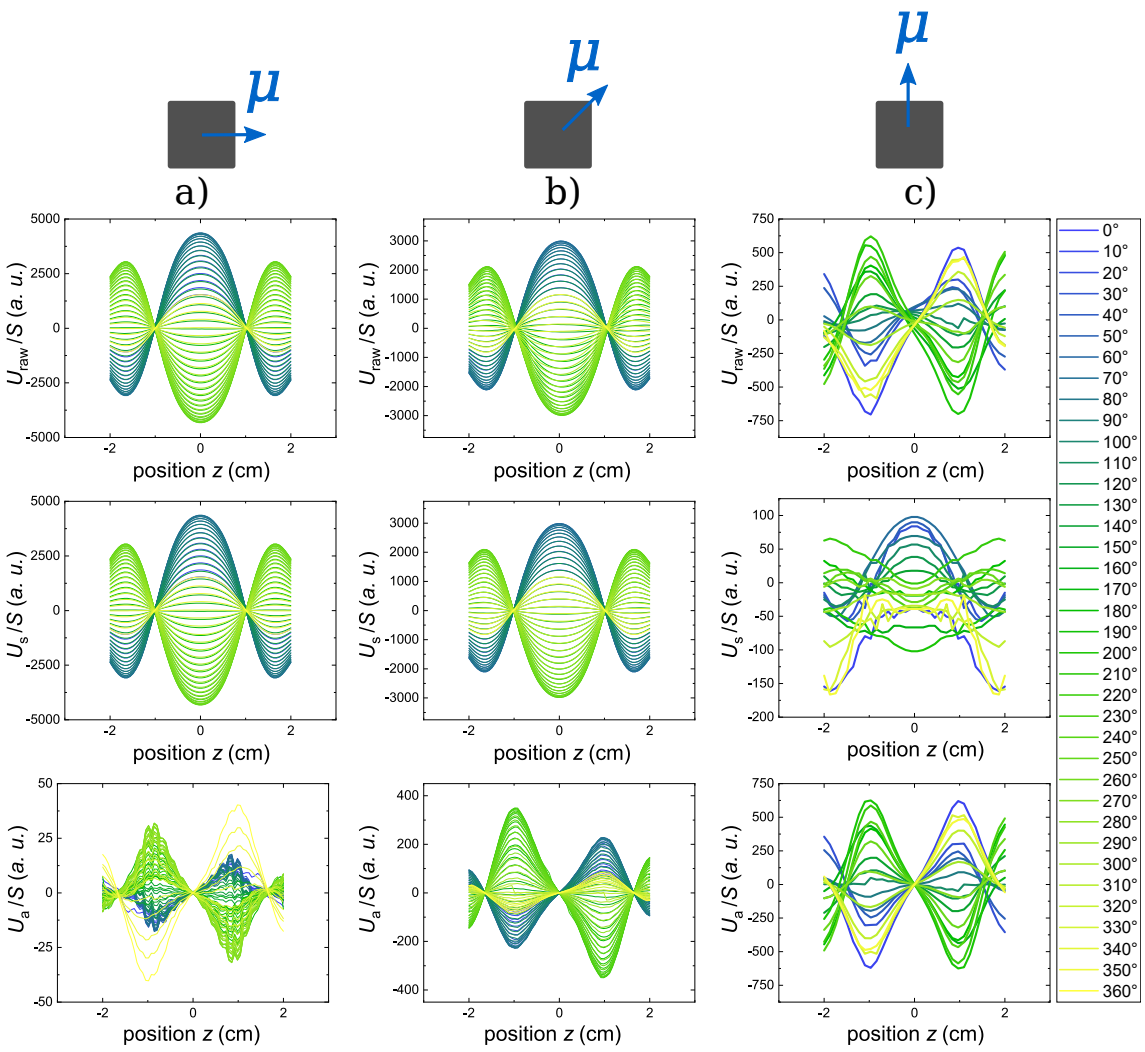

Figure 5.7.: Comparison of unsymmetrized, symmetric and antisymmetric components of the transverse data for the magnet simulating a transverse and a longitudinal moment as well as moment pointing equally longitudinal and transverse. The raw voltages were divided by their sensitivity S. The proportion of the symmetric and antisymmetric part of the signal correlate with the size of the transverse and longitudinal moment, respectively. The maximal symmetric and antisymmetric voltage changes from a) to b) and from b) to c) as we expect from the change of the direction of the magnetic moment. This shows that the symmetrization of the signal works well for subtracting the longitudinal moment.

tudinal contribution dominates the raw data, do both data sets match only poorly. Compared to the noisy data points of the MPMS, the symmetrized data shows a nice sine function as well. This proofs the correctness of the applied data analysis.

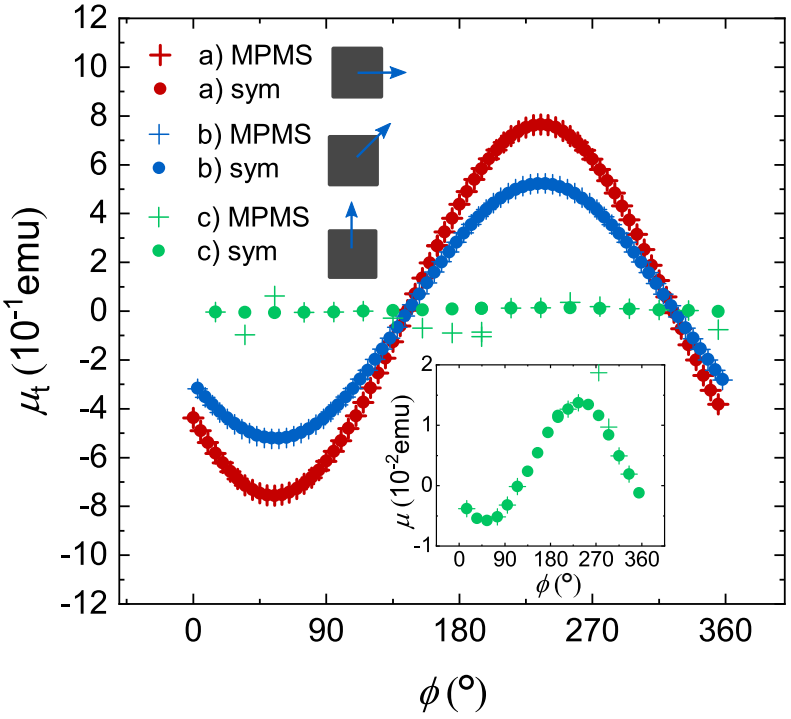

Figure 5.8.: The transverse magnetic moment before (MPMS) and after symmetrization (sym) for situation a), b) and c) during a rotation in the xy-plane. The inset show a zoom of situation c). Although the proportion of the longitudinal contribution increases from a) to c), the transverse moment decreases as theoretically expected. This proofs how well the symmetrization of the raw data works, even when the longitudinal moment dominates. The small signal for c) is most likely due to the imperfect alignment of the $Nd_2Fe_{14}B$ magnet.

Please note the shift of the $\mu(\varphi)$ curve for c) (inset) of roughly $5 \cdot 10^{-3}$ emu. Such a shift in y-direction will encounter us in several cases, always seemingly when the difference of the longitudinal moment and the transverse moment is extremely large. The reason of this offset will be discussed later when more experimental results have been presented. What strikes as odd is the fact that the amplitude of the antisymmetric part U_a in Figure 5.7 changes similar to the symmetric signal. This is contrary to the description in the manual [49], where an unchanging longitudinal contribution during rotation is described. It seems (as it has been suspected in the previous part) that the distance of the sample to the pick-up coils changes during the rotation. Only in the exact center is the longitudinal contribution expected to

be zero. This is in accordance with the explanation that the center of the $Nd_2Fe_{14}B$ magnet is 0.5 mm away from the center of the pick-up coils due to the geometry of the sample holder. When the magnetic moment points more towards the positive coil the longitudinal contribution is maximal and when it points to the negative coil on the other side it will be minimal. When it points to the coil gaps the measured longitudinal contribution should be zero. In the case of the antisymmetric part of b) is the amplitude of one angle not nearly matched by the negative amplitude of another. It seems that in some cases the offset to the center changes during rotation. This means that the sample holder has a kink or is otherwise not aligned perfectly along z. This leads to a rotation with an off-center rotation axis.

All in all we can conclude that the symmetrization works well and the analysis of the data is correct. Even for large longitudinal moments, the calculated transverse moments fulfill our expectations. A small misalignment of the center, as it has been found to occur during the rotation, does not effect the symmetric part significantly. There is strong evidence that the distance to the pick-up coils varies due to the experimental setup and, therefore, changes the antisymmetric part. It must be noted that there is also a second sample holder, including a straw and a torlon disk, which is used for transverse experiments. For the case of plate-like samples as we find for α-$RuCl_3$ and Na_2IrO_3, the centering of the sample in the xy-plane can theoretically be performed perfectly. In reality very complex shapes of the Na_2IrO_3 samples make the centering difficult. Since the subtraction of the longitudinal contribution works well, this should not affect the analysis. Only difficulties occurs if the longitudinal contribution is much larger than the transverse moment. This leads to a worse signal-noise ration for the symmetric data and (at least at constant field and temperature) to a constant offset in the measurement data (for example found for position (c) in Figure 5.8). The origin of this effect is discussed in the following section. In the experiments with the Kitaev model candidates, the ratio of the longitudinal and transverse moment lies somewhere between case (b) and (c).

5.1.3 Background of the sample holder

Important for us is also the background of our sample holder. In principle one would not expect to see any transverse moment, except a possible longitudinal contribution that should vanish by the symmetrization. For the experiments of the transverse

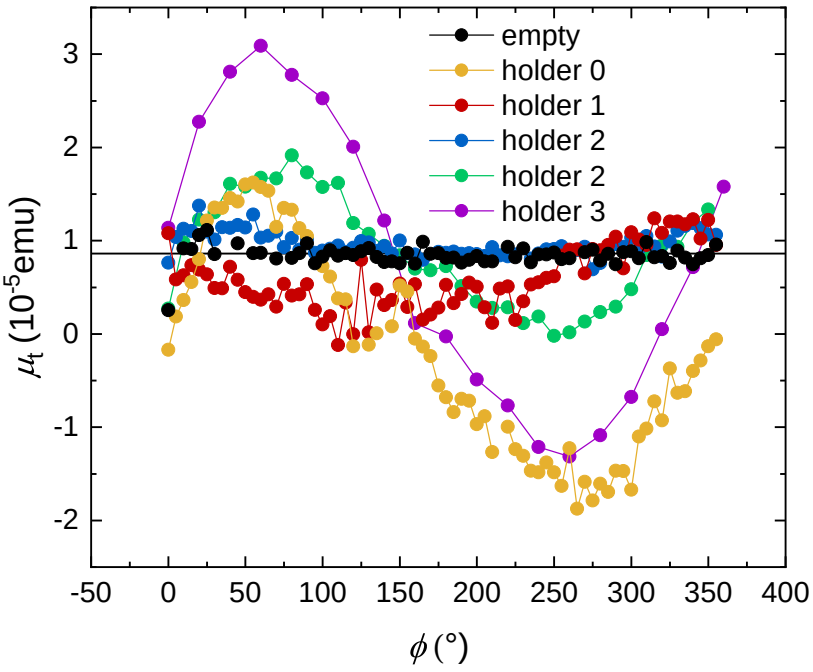

Figure 5.9.: Background measurements of an empty sample chamber as well as of different holders made of a straw wrapped with teflon tape and a torlon disk at 10 K and 5 T. The empty measurements shows noise around $0.84{\cdot}10^{-5}$ emu. This noise is additionally overlapped by a sine-like function in the case of the sample holders.

magnetization, a torlon disk is clamped into a conventional straw. Many layers of teflon tape was wrapped around the straw at two to three spots on the straw. It was taken care that the teflon tape was not too close to the sample to influence the measurement. Since a straw is easy to bend, the tape stabilized it and helped keeping it in the center of the sample chamber. Here, only the torlon disk should possess a small diamagnetic moment along z. Figure 5.9 shows the result of different background data in a magnetic field of 5 T and at a temperature of 10 K. First, the sample chamber was measured empty. The symmetrized and fitted data show a noise around the value of $0.84{\cdot}10^{-5}$ emu (black line). This signal arises from the fact that the drift of the voltage during one measurement is not well described by a linear function as assumed by the MPMS software and it therefore leaves a symmetric part of the voltage change that due to our data analysis is assumed to be a transverse moment. Figure 5.10a shows the raw signal of the empty sample chamber before the subtraction of the drift by the MPMS software[4] and Figure 5.10b the corresponding calculated symmetric part. To reduce distraction, data sets with jumps in the voltage have been omitted. If divided by the sensitivity S (as it has been done in Figure 5.10b), this symmetric signal is roughly the same for all measurement points of this $\mu(\Phi)$-measurement. Unfortunately, the sign of the resulting "transverse moment" is not always the same. While the measurements of holder 1,2 and 3

[4]For all other shown raw signals the drift has already been subtracted

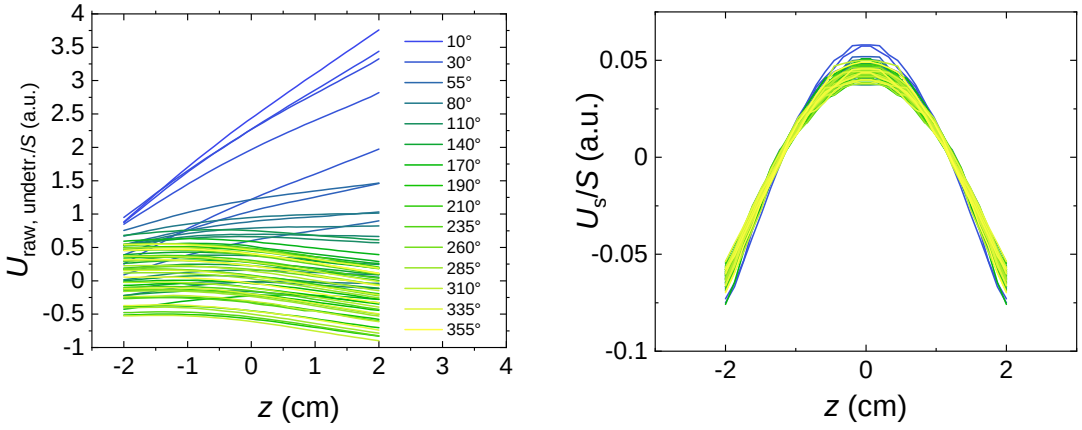

(a) **(b)**

Figure 5.10.: a) The "undetrended" (no subtraction of a linear drift) raw signals of an empty sample chamber in dependence of the in-plane angle. Since the drift of the voltage does not seem to be well described by a linear function as the MPMS program assumes, a small symmetric part remains (b). This leads to the emergence of a constant offset in measurements where the size of the transverse moment is significantly smaller then the longitudinal contribution.

in Figure 5.9 all show an offset around the $0.84{\cdot}10^{-5}$ emu, the offset of holder 0 seems to be around $-0.1{\cdot}10^{-5}$ emu. This is a really small error in the measurement. Nevertheless, in the case of a very small transverse moment in comparison to the overall moment (transverse+longitudinal contribution) it will effect the obtained result. Its influence can be nicely seen by the change of the shape of the symmetric voltage (ideal shape seen in Figure 3.10b in the end of the "Experimental Methods" chapter), which mixes with the shape of from Figure 5.10b.

As soon as a we put a holder into the sample chamber, this noise is superimposed by sine-like oscillation expected for a transverse moment (see Figure 5.9). Offset and amplitude vary from measurement to measurement, even in between measurements of the same sample holder. Nevertheless, the signal of the sample holder is tiny and is not much larger than the intrinsic background of an empty MPMS. A similar picture is found for the temperature dependence of the background. Both sample holder 0 and 3 show only a weak temperature dependence. The absolute value differs due to the angle dependency shown in Figure 5.9. The temperature dependence, though, can be matched by shifting, for example, the data of holder 3. Important for measurements with small magnetic moments is the minimum at a temperature of $\sim$15 K (holder 0) and $\sim$20 K (holder 3). Surprisingly, the measurement of an empty

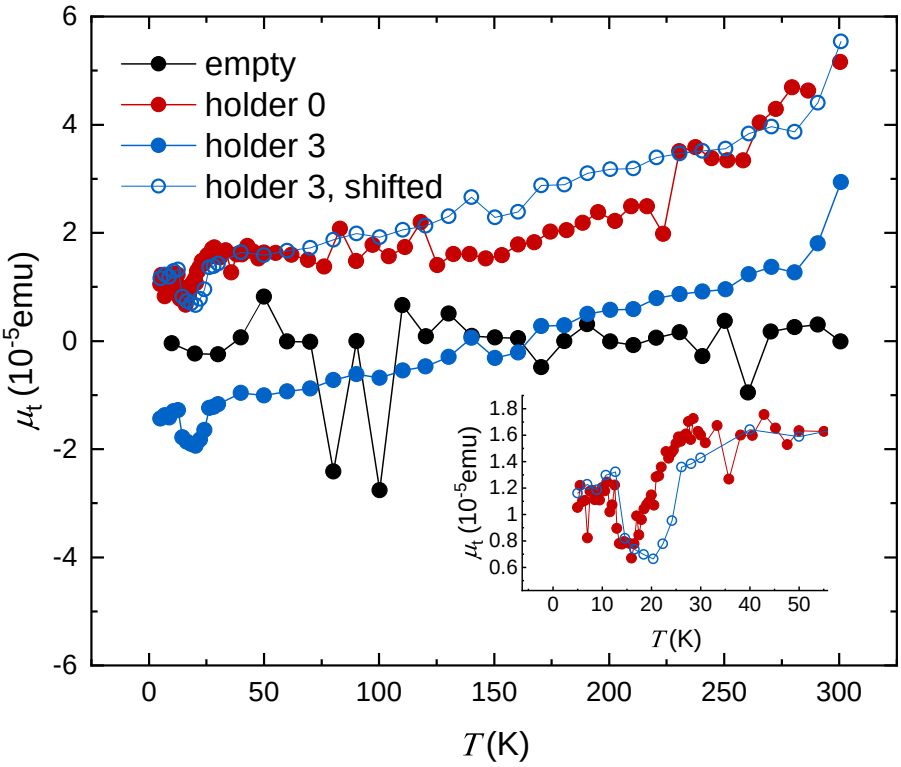

Figure 5.11.: Temperature dependence of the transverse magnetic moment of an empty sample chamber as well as of two different sample holders at $\mu_0 H$ =5 T (filled circles). By adding a constant, holder 3 can be shifted to match the data of holder 0 (empty circles), showing the same temperature dependence as well as a minimum around 15–20 K (see inset).

sample chamber did not show any offset but simply a stochastic variation around 0.

Why the diamagnetic torlon disk shows any transverse moment is unclear so far. A contribution from the longitudinal moment of the disk can be excluded according to Figure 3.9b from Section 3.4.2. It shows that even with an offset the signal is still antisymmetric and is, therefore, This background is scarcely larger than the background noise of our MPMS. Apart from the torlon disk, another sample holder made out of one long piece of quartz glass was used. No background signal is expected for this holder since its moment does not change during the movement through the pick-up coils.

5.1.4 Summary

Let's summarize the insights of these preliminary experiments for the transverse magnetization measurements. The data analysis has been proven to be correct, since it delivers the same results as the program of the MPMS if the transverse moment dominates the raw data. The center position of the longitudinal moment can be used to determine the center position for the transverse magnetization measurement. The position of the pick-up-coils was determined to enable the connection between our knowledge of the crystallographic axes of a sample and the direction of the measured moment. Further, there are three contributions to the measured raw transverse moment:

1. the intrinsic transverse moment
2. the symmetric part of the voltage drift
3. the longitudinal contribution.

The longitudinal contribution (3) is subtracted by a symmetrization of the raw signal. Only a very small part can remain due to a small error in the center position, which is neglectable. The symmetric part of the voltage drift (2) can be neglected as well as long as the raw signal is not overly dominated by the longitudinal contribution, pushing the intrinsic transverse moment in the range of the drift part. This effect can be seen by a constant offset in the resulting $\mu(\phi)$ curves as well as a change of the shape of the symmetric curves.

These information give us a comfortable starting point to begin analyzing real samples. We will see how well this information can be transferred to our samples, which show smaller longitudinal as well as transverse moments.

5.2 α-$RuCl_3$

α-$RuCl_3$ is, to our knowledge, the only one of the three described compounds where data of the transverse magnetization has been published. The authors of [21] applied a field along the c^*-direction and measured transverse magnetization in the ab-plane

as well as longitudinal magnetization parallel and perpendicular to c^*. Their experiments were repeated in this work and additional transverse experiments were conducted. In the end, data for the longitudinal susceptibility $\chi_\mathrm{l}(T)$ as well as the transverse magnetization/susceptibility in dependence of field $\mu_\mathrm{t}(H)$ and of temperature $\chi_\mathrm{t}(T)$ for both directions were collected.

Two samples of α-$RuCl_3$ (m_1: 12.5 mg and m_2: 35.7 mg) have been analyzed. The orientations of the c^*-axis were already analyzed by the group of Prof. Dr. Loidl, which grew the crystal. The large mass of both samples led to large magnetization signals and made a background subtraction unnecessary. For the measurements with $H \perp c^*$ for both samples as well as $H \parallel c^*$ for sample 1 the quartz holder was used. Sample 2 was measured with the torlon disk inside the straw for $H \parallel c^*$. The measurements of the three different quantities ($\chi_\mathrm{l}(T)$, $\mu_\mathrm{t}(H)$, $\chi_\mathrm{t}(T)$) of sample 1 with $H \perp c^*$ were performed by Friedrich Freund. All measurements for the longitudinal magnetization as well as the respective literature data of [21] are compared in Figure 5.12. Both, sample 1 (S1) and sample 2 (S2), show the same temperature dependence with the direction $H \parallel c^*$ showing a strongly reduced susceptibility compared to $H \perp c^*$. The behavior of the literature data is similar, but with an enhanced susceptibility. This difference could be due to an error in the calibration of the used MPMS. Some time after these measurements had been performed, the MPMS was recalibrated, since a mismatch in the absolute value of a reference sample was indeed found. It could also be due to the difference in the applied magnetic fields. While S1 and S2 were measured at 4 T, the sample from [21] was measured at 1 T and 0.1 T. In [69] the magnetization versus magnetic field curves reveal a deviation from a linear behavior for $H \perp c^*$, which is not seen for $H \parallel c^*$. Nevertheless, the data qualitatively follows the literature data. To determine the literature data in units of m^3/mol, the published curves were multiplied by a factor of $4{\cdot}\pi \cdot 10^{-4}{\cdot}207.45/(3.11 \cdot 10^6)$[5] after consultation with the paper's first author.

Additionally, the transverse magnetization in dependence of the magnetic field for different temperatures in and close to the ordered regime was measured. The respective data are presented in Figure 5.13a for fields parallel to c^* and in Figure 5.13b perpendicular to c^*. If the field is applied parallel to c^*, the magnetization follows a linear behavior with the largest magnetization for the magnetic transition temper-

[5] To convert the volume magnetization divided by the magnetic field one needs the molar mass ($M = 207.45$g/mol) and the density ($\rho = 3.11 \cdot 10^6 \mathrm{g/m^3}$ [111]) of α-$RuCl_3$.

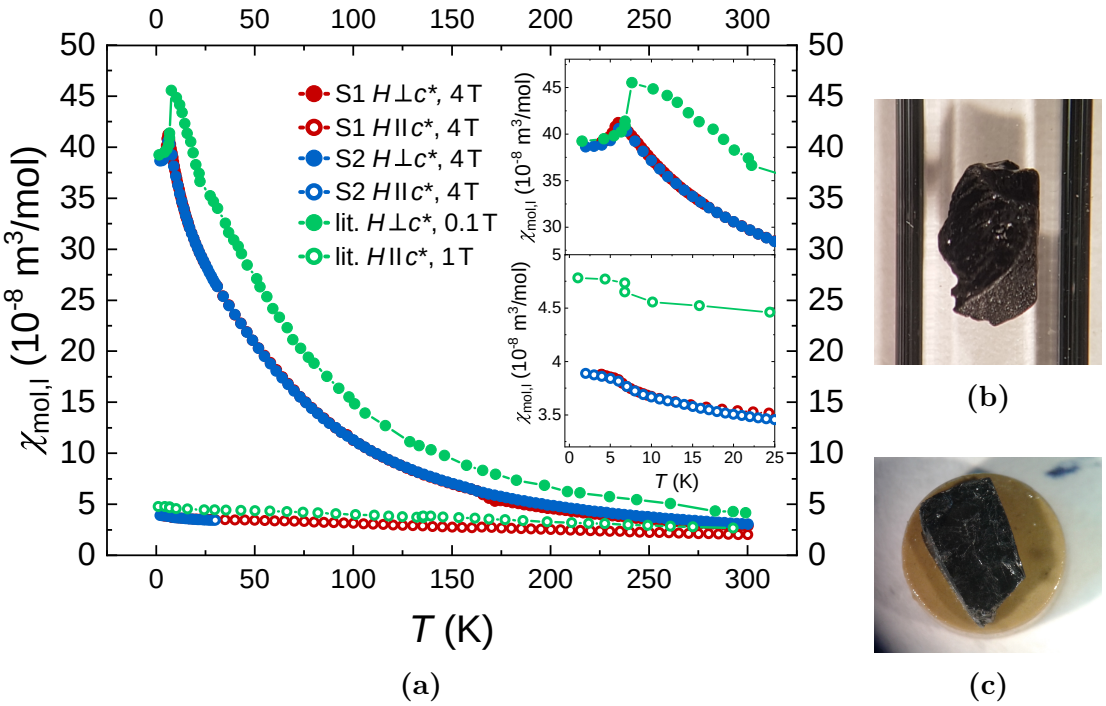

Figure 5.12.: a) Comparison of the longitudinal susceptibility data of α-$RuCl_3$ in dependence of T of sample 1 (S1 (b)) and sample 2 (S2 (c)) as well as the literature data taken from [21]. All samples were measured parallel and perpendicular to the c^*-direction. The insets show a zoom of the low temperature regime for both directions. S1 and S2 nicely match with each other. The literature data is somewhat enhanced, but shows a similar temperature behavior. b) shows S1 on a quartz holder and c) S2 on the torlon disk.

ature at 7 K. A completely different picture can be observed for the data for fields perpendicular to c^*. A linear contribution, similar to Figure 5.13a, is still present. Additionally, there is a contribution showing a maximum. The size of the maximum as well as the field at which the maximum occurs decreases for increasing temperature. Very close to the magnetic transition at 6.5 K is the maximum not visible anymore. From the shape of the curves, it seems that all curves are merging or at least are settling close to the 6.5 K curve at a certain field. It is possible we see a redistribution of the three domains found in [87]. The authors of this paper showed that there are three different types of domains present in α-$RuCl_3$, which differ in a 120° rotation angle in the plane. If a field is aligned parallel to the direction of the moments of one domain [6], this domain gradually disappears with increasing fields,

[6] The moments of α-$RuCl_3$ lie in the $a - c^*$ plane with an angle of ~32° to the a-axis (see Section 4.3.3).

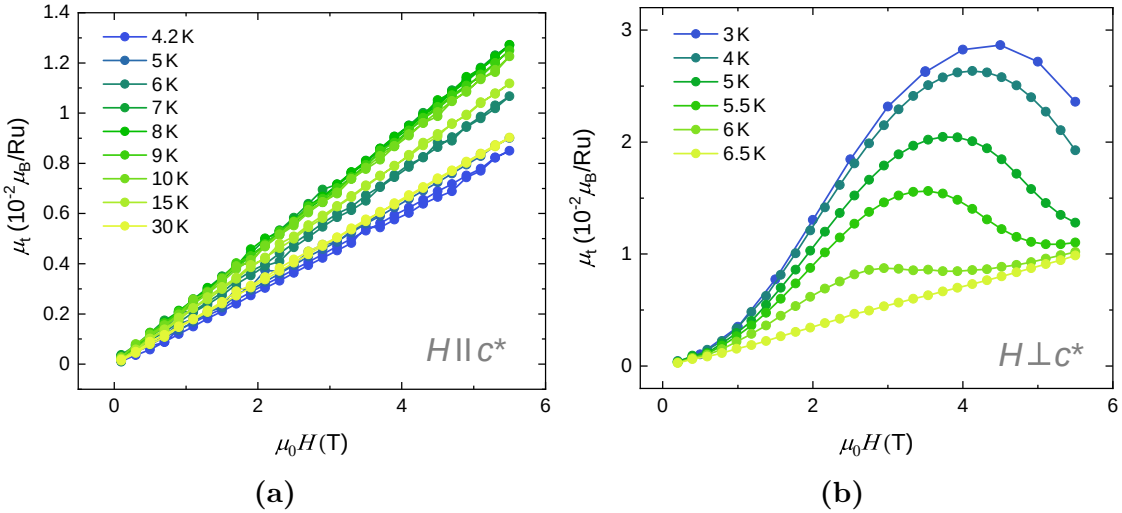

Figure 5.13.: The normalized transverse magnetic moment of α-$RuCl_3$ in dependence of H at temperatures in or close to the ordered phase for a) $H \parallel c^*$ and b) $H \perp c^*$. While the magnetization shows a linear behavior for all temperatures for $H \parallel c^*$, the data for $H \perp c^*$ only becomes linear very close to the transition temperature at 7 K. In the ordered regime there is a maximum in the $\mu_t(H)$ curves that moves to lower fields with increasing temperatures.

according to the findings of [87]. At $T = 2\,\mathrm{K}$ and $\mu_0\tilde{H} = 2\,\mathrm{T}$ (in-plane component of the total field), they found that only two types of domains remained. Applying a field parallel to c^*, the effect on the three domains would be equal. If we apply a field along the a-axis of one of the domains, a similar redistribution of the domains should occur, but only in the ordered phase. It is possible that the maximum is linked to the rearrangement of the domains. It can be excluded that the maximum correlates to the field rotating the moments towards the field axis, since α-$RuCl_3$ was shown not to be saturated for fields up to 60 T at a temperature of $T = 1.3/1.4\,\mathrm{K}$ [69, 96].

Further, Figure 5.14 shows the measurements of the transverse susceptibility in dependence of the temperature T and the in-plane angle ϕ. The $\chi_{\mathrm{mol,t}}(T)$ curves of S1, S2 and the literature data (filled circles) for $H \parallel c^*$ in Figure 5.14a differ in their absolute value, but show the same temperature dependence as an overlap of our data multiplied by a constant (empty circles) with the literature data shows. There is a maximum in χ_t at the transition temperature of 7 K, followed by a drop to lower temperatures. There seems to be a strong sample dependence, possibly due to the amount of certain defects. The measurement of the transverse susceptibility was conducted at roughly the maximum of the susceptibility in dependence of

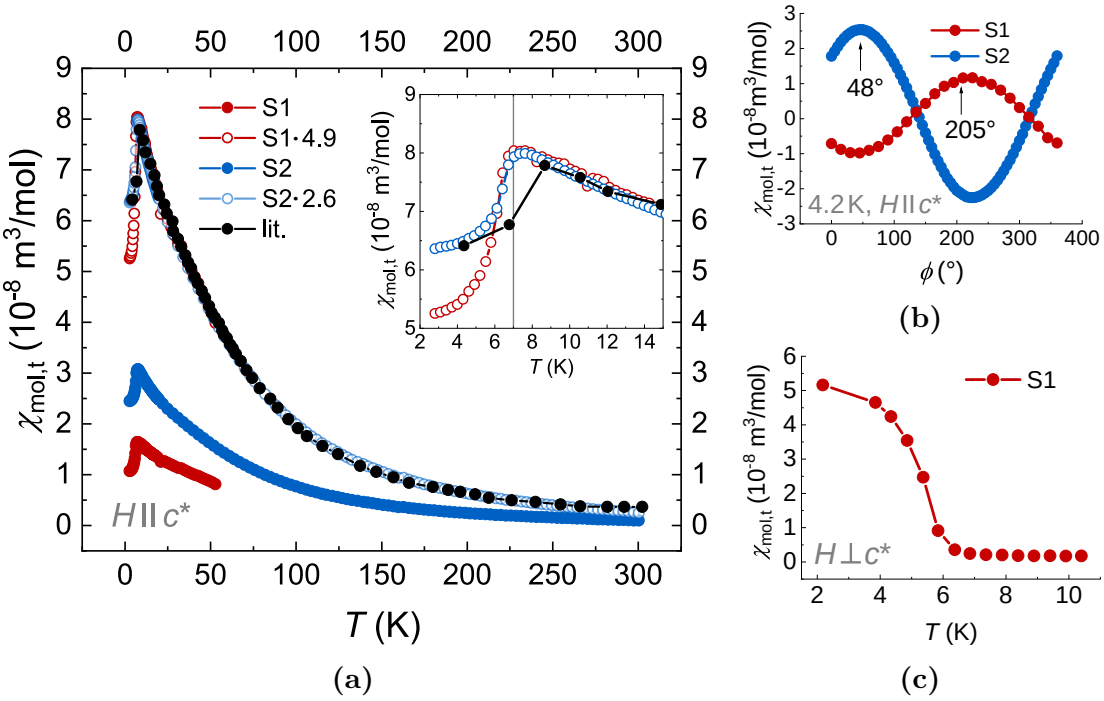

Figure 5.14.: a) The temperature-dependent transverse susceptibility $\chi_t(T)$ of α-$RuCl_3$ of S1 and S2 for $H \parallel c^*$ in comparison to the literature data found in [21]. All curves show the same behavior and can be overlapped by multiplying the data of S1 awith 4.9 and the data of S2 with 2.6. χ shows a maximum at the transition temperature, but the absolute value seems to be very sample dependent. b) The corresponding rotation measurements to find the direction of the moment. The experiments shown in a) were performed at 205° for S1 and at 48° for S2. c) The transverse susceptibility for $H \perp c^*$ at 4 T strongly decreases for increasing T up to the magnetic transition at $T = 7$ K. Above the transition temperature χ_t stays constant in the measurement regime.

the in-plane angle. The respective angles are marked in the measurements in Figure 5.14b. The difference in the absolute value cannot be due to different external fields (S1: 5.5 T, S2: 1 T, lit.: 1 T) since the measurement of the magnetization in dependence of H for fields parallel to c^* has displayed a linear behavior (Figure 5.13a). The transverse susceptibility $\chi(T)$ with $H \perp c^*$, which is seen in Figure 5.14c, shows a completely different temperature dependence. χ_t is very small and constant above the magnetic transition. Below T_N there is a strong increase that weakens at lower temperatures and appears to be close to saturation at $T = 2\,K$. It must be noted that these data do not match the $\mu_t(H)$ curves in Figure 5.13b at 4 T. This might be explained by a different orientation of the crystal regarding the in-plane axes. These experiments were performed by Friedrich Freund and it could, therefore, not

be determined if the sample was oriented in the same manner for both experiments. Nevertheless, the qualitative temperature dependence seems to be very similar. Here again, the rearrangement of the domains mentioned before could be the reason for this behavior. Lampen-Kelley *et al.* [21] found a linear temperature dependence of the inverse transverse susceptibility χ_t^{-1} and, therefore, Curie-Weiss behavior between $175\,\mathrm{K} \leq T \leq 275\,\mathrm{K}$. The larger noise level of the data in this temperature range as well as the deviation from the fit above 275 K is explained by errors due to the separation of the longitudinal and transverse components of the signal, which become of the same order in this regime. No problems of this kind appeared for the measurement data of χ_t^{-1} of S2, shown in Figure 5.15 (gray, left axis), which was measured up to 300 K, but the measurement curve cannot be described with a linear function up to at least 250 K. Why the transverse magnetic moment would not follow Curie-Weiss behavior is not clear. A subtraction of a background as it was found in Figure 5.11 leads to only marginal changes and increases the curvature further. The transverse susceptibility curve is shown in comparison to the longitudinal susceptibilities (right axis) measurements of S1 and S2, which all show the expected linear behavior. The kinks in the longitudinal measurements of S1 at roughly 165 K are related to a known structural transition of α-$RuCl_3$ [9, 21, 112]. Fitting the longitudinal curves above the structural transition with the Curie-Weiss law (equation 2.6) resulted in Weiss temperatures for fields in the plane of $\Theta_{W,S1} = 32\,\mathrm{K}$ and $\Theta_{W,S2} = 35\,\mathrm{K}$ as well as for fields out-of-plane of $\Theta_{W,S1} = -203\,\mathrm{K}$ [7]. The obtained parameter lie very close to the literature data of [21].

To summarize, we have shown the transverse susceptibility data χ_t of two α-$RuCl_3$ samples in dependence of the field and temperature as well as longitudinal susceptibility data χ_l in dependence of temperature for the two orientations $H \parallel c^*$ and $H \perp c^*$. χ_l was found to be in accordance with the literature curves. Field-dependent measurements of χ_t revealed a clear difference of the two field orientations. While for $H \parallel c^*$ the transverse magnetic moment showed a linear behavior, for $H \perp c^*$ it is characterized by a maximum, which shifts to lower fields with increasing temperatures. Close to T_N the curve flattens and turns into a linear behavior. A strong sample dependence was found for the transverse susceptibility

[7] Li *et al.* [113] found that applying a simple Curie-Weiss fit to α-$RuCl_3$ as well as Na_2IrO_3 and α-Li_2IrO_3, as it has been done here, results in false Weiss temperatures θ_W as well as overestimated effective moments μ_{eff}. Since the fitting was done mainly to compare the data with literature data, a fitting with an temperature dependent effective moment $\mu_{eff}(T)$ as suggested in [113] was omitted.

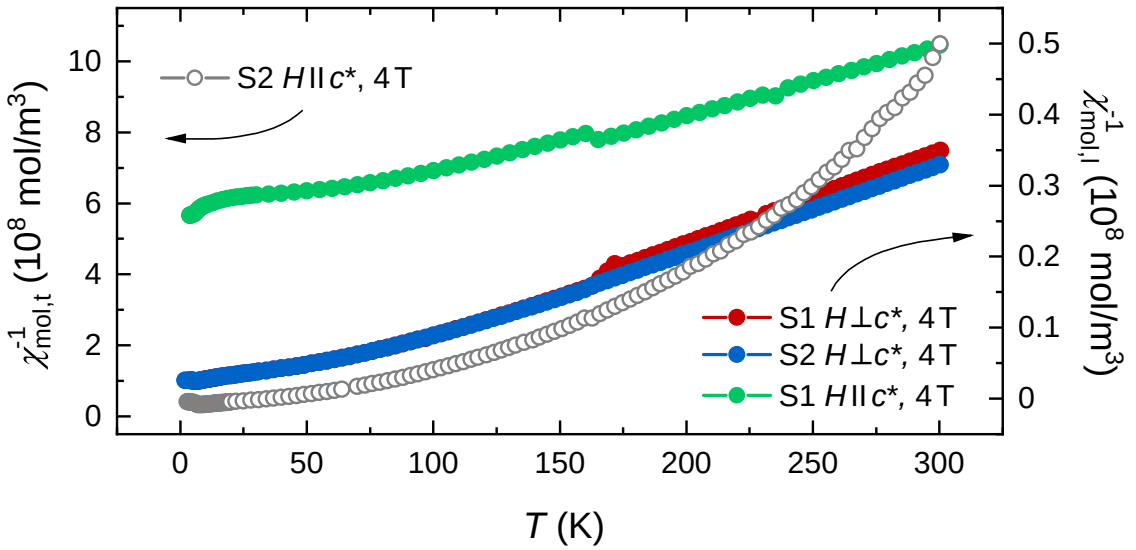

Figure 5.15.: Measurement of the inverse transverse susceptibility $\chi^{-1}_{\mathrm{mol,t}}$ (left axis) and the inverse longitudinal susceptibility $\chi^{-1}_{\mathrm{mol,l}}$ (right axis) in dependence of the temperature T. A linear dependence for $T \gg T_{\mathrm{N}}$, associated with Curie-Weiss behavior, was found for the longitudinal inverse susceptibilities, but not for the transverse.

χ_{t}(T) regarding the absolute value for $H \parallel c^*$, but the qualitative temperature dependence matched nicely with the literature measurement. The curves look similar to the longitudinal measurement along $H \perp c^*$ with a maximum at $T = T_{\mathrm{N}}$. If we measure perpendicular to the c^*-direction, the susceptibility strongly increases above the magnetic transition, almost saturating at 2 K. The behavior of both, the field- and the temperature-dependent magnetization measurements, might be explainable by a rearrangement of the domains.

5.3 Na_2IrO_3

The crystals of Na_2IrO_3 in the beginning of this thesis had a maximal volume of 2x1x0.01mm^3 and typical masses of the largest crystals of about 0.2 mg. These were gained by a growth process used in [7, 77, 78] and explained in Section 4.3.1 and 4.3.1, which will be named the standard growth process (SGP) in the following section. These crystals were not large enough for many experiments as the specific heat or thermal expansion, but even for other measurements a larger sample size leads to an easier handling of the samples. In the past the problem of the sample size was

circumvented by measuring a collection of many samples. To be able to do on one sample many different measurements for different crystallographic directions, the growth procedure needed to be optimized. XRD measurements have further been used to observe structural properties as the size of the *c*-axis, the degradation of Na_2IrO_3 powder with time and the orientation of Na_2IrO_3 crystals for the transversal magnetization experiments. The longitudinal magnetization was investigated comparing single crystals grown with the SGP with single crystals grown with the optimized growth as well as the in-plane anisotropy at different temperatures. In the end, measurements of the temperature-dependent transverse magnetization of three single crystals are analyzed and the orientation of the transverse moment is discussed.

5.3.1 Crystal growth optimization

To approach the goal of larger samples the influence of some factors on the crystal growth was investigated. After a discussion with Marcus Schmidt (Max Planck Institute for Chemical Physics of Solids, Dresden, May 2016) as well as discussions with Anton Jesche (Experimental Physics VI department, Augsburg University), six possible important factors for the crystal growth process were identified. These are collected in Figure 5.16. Of course this list is most likely incomplete and should be extended by following researchers.

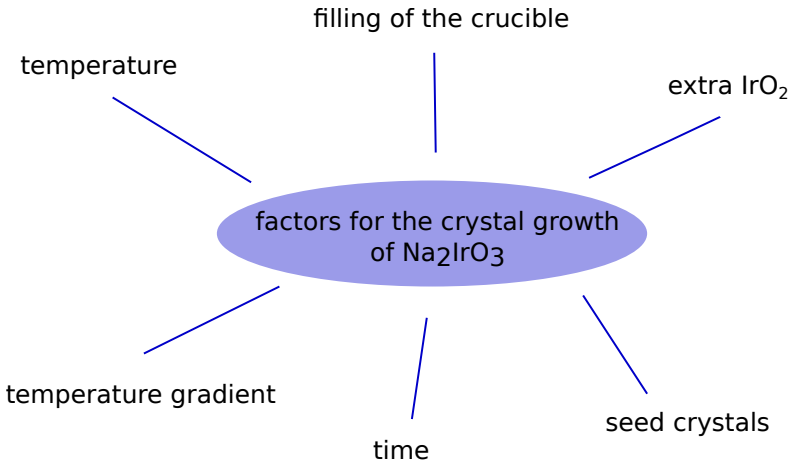

Figure 5.16.: The six identified factors that could play an important role in the crystal growth process of Na_2IrO_3.

The `temperature` is assumed to be already optimized. Singh *et al.* [7] have found that the crystals grow only between 1000°C and 1100°C and have, therefore, determined 1050°C to be the optimal growth temperature.

Soham Manni [77] found that the presence of 10% (atomic) `extra IrO2` enhances the size of the crystals. To identify the kind of crystal growth is not easy. The growth time is presumably too small for a solid state reaction and there is no flux involved for flux growth. The best fit seems to be a chemical vapor transport reaction just as we find for the single crystal growth of Li_2IrO_3. Here, the growth process seems to rely on the presence of IrO_2, which most likely reacts with oxygen to form IrO_3 [35, p. 234]. Nevertheless, the distance the molecules travel are very short, since they grow directly out of the polycrystalline bed. To explore this effect further, experiments have been conducted where the proportion of the extra IrO_2 was increased. In contrast to [77] Ir and not IrO_2 was added. An additional heat treatment at 900°C transforms the Ir into IrO_2. For batch NIOLi4 the prepared Na_2IrO_3 powder was split into four different crucibles (1–3 and 6). In the first crucible roughly 20%, in the second 100%, in the third 250% and in the fourth 370% (atomic) extra Ir was added. It must be noted that the calculation of the atomic percentage of the extra Ir x_{IrO_2} in [77] was based on the sum of Ir atoms in Na_2IrO_3 $N_{Na_2IrO_3}$ and the extra Ir atoms N_{IrO_2} ($x_{IrO_2} = N_{IrO_2}/(N_{IrO_2} + N_{Na_2IrO_3})$). In my calculations it is only based on the amount of Ir atoms in Na_2IrO_3 $N_{Na_2IrO_3}$ ($x_{IrO_2} = N_{IrO_2}/+N_{Na_2IrO_3}$). There were no crystals in crucible 1, 9 large crystals with an area of 0.5x1 mm^2 in crucible 2 and more than 30 crystals of the size 1x1.5 mm^2 in crucible 3. The fourth crucible (6) showed crystals with areas of 1.5x2 mm^2 and larger as well as masses of over 1 mg. This was an important step, since specific heat measurements for example require a

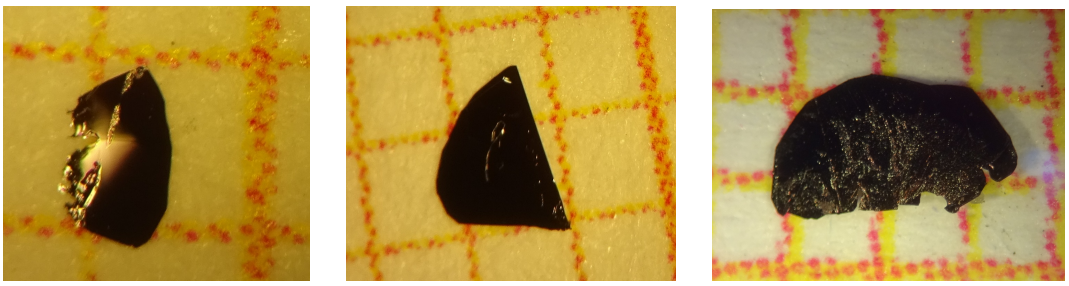

(a) **(b)** **(c)**

Figure 5.17.: A typical sample size of a) NIOLi4_2, b) NIOLi4_3 and c) NIOLi4_6 with an amount of extra Ir of 20%, 100% and 370%, respectively, based on the amount of the existing Ir in the Na_2IrO_3 powder.

mass of at least 1 mg. A comparison of a typical crystal size for crucible 2, 3 and 6 is shown in Figure 5.17. It seemed to be a clear case. Two other batches were made to reproduce this finding: NIOLi5_1 and NIOLi5_2 (again undoped Na_2IrO_3). Here, the first crucible was given about 10% extra Ir and the second 100%. Astonishingly, no clear difference could be observed between the two batches. The largest samples had area sizes of around 2x2 mm^2. It seems that the amount of extra Ir was not the crucial parameter for the observed changes in NIOLi4.

A second growth experiment sheds light on another important factor and most likely the source of the dramatic change in the crystal size for NIOLi4: The `filling height of the crucible`. During the growth, a lot of material is lost which escapes the crucible. To restrict this process a lid is placed on top, but it does not prevent it completely and the material can (and does) still move to the walls and the lid of the crucible. Two different types of alumina crucibles were used in these experiments: the small ones with an inner diameter of 10 mm and a height of 25 mm as well as large ones with 15 mm inner diameter and 25 mm height. Na_2IrO_3 powder of NIOLi3 was divided into 4 crucibles with different fillings of the crucibles. The first two were put into small crucibles an the last two into large ones (extra Ir was not added). Pictures of the samples before and after the crystal growth are collected in Figure 5.18. Only

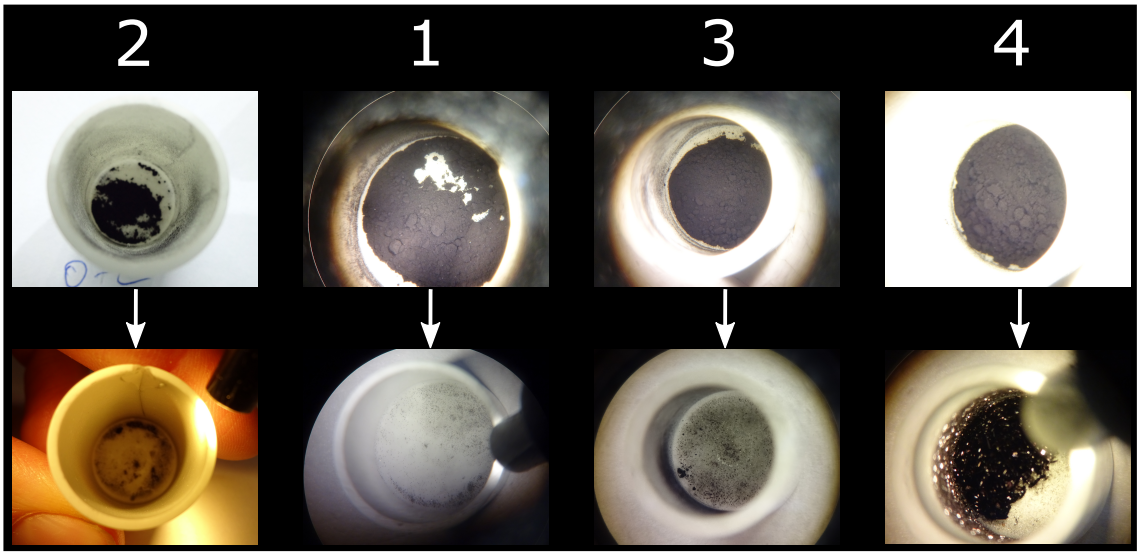

Figure 5.18.: The four batches of NIOLi3 before (top) and after the crystal growth (bottom) starting from the lowest filling (left) to the largest filling (right). Only in the last crucible (4) the amount of Na_2IrO_3 powder was sufficient to produce large Na_2IrO_3 crystals. The small silver crystals are Ir crystals.

in crucible number 4 the filling height was sufficient to produce a larger amount of small Na_2IrO_3 single crystals. The tiny silver crystals, especially well seen in crucible 1, are Ir crystals. If we compare the masses put into the NIOLi3 batches to those of NIOLi4 and NIOLi5, the picture becomes clearer. Table 5.3 compares the three batches in regard of crucible size, sample mass, extra Ir and the outcome of the growth. The first two batches of NIOLi3 are neglected, since they had the smallest fillings and give no additional information.

batch	3_3	4_1	4_2	3_4	4_3	5_1	5_2
crucible size	small	small	small	small	small	large	large
$m_{Na_2IrO_3+IrO_2}$ (g)	0.05	0.07	0.11	0.13	0.17	0.48	0.67
extra Ir (%)	0	20	100	0	250	10	100
Na_2IrO_3 crystals (mm^2)	-	-	≤0.5x1	≤0.3x0.8	1x1.5	2x2	2x2

Table 5.3.: Comparison of crystal growth parameters for the batches of NIOLi3, NIOLi4 and NIOLi5. The filling height of the crucible, which correlates with the mass of the educt, increases from left to right.

We can conclude that the crucible filling height is very important. Additionally, extra Ir seems to increases the size of the samples. The samples of 4_2 were larger than of 3_4, although the filling was slightly less. The main difference was the addition of 0% (3_4) and 100% (4_2) of extra Ir. Nevertheless, at large crucible filling heights as we have for the batches NIOLi5_1 and 5_2 an increase of the amount of extra Ir above 10% does not seem to change the resulting crystal size. Batch NIOLi4_6 with an amount of extra Ir of 370% and a total mass of 1.82 mg has not yielded larger crystals as the batches of NIOLi5. It seems the effect of the crucible height on the crystal size is not increasing above 0.67 g. In the following batches (above NIOLi7) 25% of extra Ir were added and to IrO_2 transformed before the single crystal growth and it was taken care that the masses of the powder was not below 0.67 g.

For a chemical vapor transport a (typically in `temperature`) `gradient` is necessary. This has been proven by putting a prepared powder sample (pre-reacted Na_2IrO_3 and IrO_2) into an furnace with an altered temperature gradient. While by far the most samples of doped and undoped $(Na_{1-x}Li_x)_2IrO_3$ were prepared in one special Muffle furnace (Nab3), where the heating elements are located on the top and the bottom of the furnace, furnaces with heating elements on the sides failed to produce $(Na_{1-x}Li_x)_2IrO_3$ crystals. Another hint is the fact that, when several crucibles are

put together in one furnace, the crystals which are not grown at the center position show a preferred growth side away from the warmer center as it is shown in Figure 5.19. To obtain an idea of the magnitude of the gradient and the real temperatures in the crucible, a heating element was used to compare the temperatures between the bottom and the top (at a height of 25 mm) of a type of crucible which was used frequently. The experiment simulates a crucible standing in the center of the furnace. Figure 5.20 shows the heating step, the holding time at 1050°C as well as the cooling for both positions of the heating element of a typical growth with reduced holding time. The gray curve shows the difference of both temperatures (right axis). Naturally, the difference is largest in the heating process (≈ 20°C) and saturates at around 14°C after 6 hours. Of course the situation in a real crucible might still deviate slightly, since the crucible is (loosely) sealed by a lid during the growth. Assuming the crystals grow during the waiting time at 1050°C, a 14°C difference leads to an estimated temperature gradient of 0.6 °C/mm for the growth of $(Na_{1-x}Li_x)_2IrO_3$.

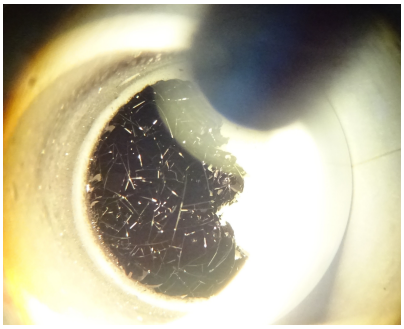

Figure 5.19.: Crucible with $(Na_{1-x}Li_x)_2IrO_3$ crystals, where the crucible was placed off-center in the oven during the growth.

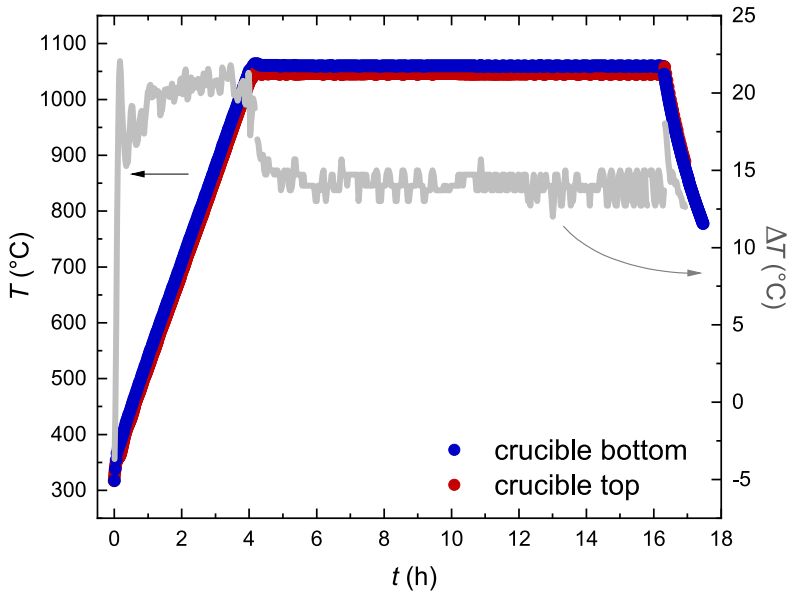

Figure 5.20.: Temperature profile at the center of the furnace at a height of 0 mm (bottom of a crucible) and 25 mm (top of a small crucible). The furnace sequence corresponds to a typical crystal growth process with a shortened holding time.

Especially the filling of the crucible more than any of the other factors seems to determinate the size of the crystals. But there are still two factors which have not been discussed yet: `time` and the presence of `seed crystals`. The most drastic improvement of the crystal size occurred by accident when a crucible of small crystals grown with the SGP, introduced in Section 4.3.1, was added to a growth procedure of a completely different material. Here, the crucible was slowly (0.2°C/min) warmed up from room temperature to 1050°C and kept at this temperature for two weeks[8]. To analyze what made the crucial difference, the slow heating, the long hold time or the presence of seed crystals, another experiment was conducted. Prepared powder of high-quality Na_2IrO_3 and IrO_2 (NIOLi12) was again divided up to 5 different

[8]This batch (NIOLi7) included the largest crystals of Na_2IrO_3. This growth procedure was repeated and always produced large crystals, although never as large as they were found in NIOLi7. The crystals of NIOLi7 were grown over the Christmas holidays. Also a synthesis made by Friedrich Freund of the similar material Li_2IrO_3 produced the largest crystals over the Christmas holidays. Possibly the lack of researchers in the lab and, hence, less vibrations due to walking or a different room climate might have a positive influence on the crystal growth.

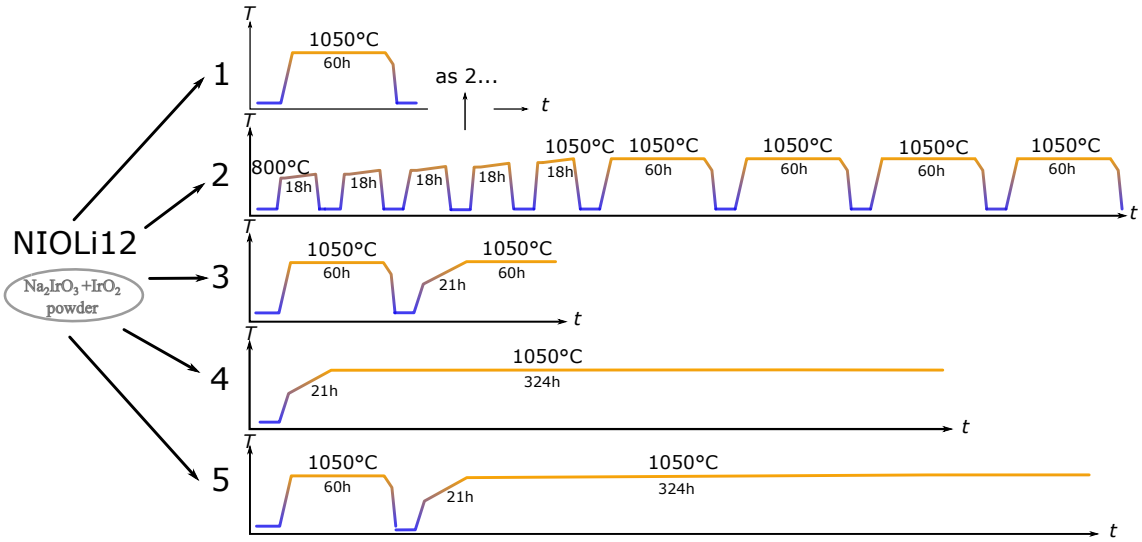

Figure 5.21.: Growth sequence for NIOLi12_1 to NIOLi12_5 to analyze the role of a slow heating time and a large holding time as well as the presence of seed crystals. All batches start with high-quality Na_2IrO_3 powder and prereacted IrO_2 powder. Batch 1 and 2 investigate the role of slow heating with (1) and without (2) seed crystals in different temperature intervals. Afterwards batch 1 and 2 were repeatedly annealed at 1050°C for 60 h to see, if the size of the crystals could be increased further. Batch 3 examines the influence of continuous slow heating with seed crystals. The effect of slow heating and a long holding time is investigated by batch 4 (without seed crystals) and 5 (with seed crystals). Between each heating step pictures of the crucibles were made.

crucibles (1–5) and each batch of crystals grown with a different procedure, which are visualized in Figure 5.21[9]. Crucible 1 and 2 were very slowly heated over night (≈18 h) in 50°C steps starting from 800°C up to 1050°C (first night: 800°C→850°C, second night 850°C→900°C...). In the last heating step, the samples were warmed up to a temperature of 1050°C and kept there for 60 h (3 nights). Crucible 1 was then taken to 1050°C for 60 h again for three times to see if the crystal size would increase. To cool the samples in between the heating steps the furnace was simply turned off. After each heating step the samples were taken out of the furnace and photographed to see, when the crystals would start growing. In contrast to crucible 2, crucible 1 had already been at 1050°C for three days before the heating steps were performed and, therefore, already started with small crystals. The pictures of both samples are presented in Figure 5.22. This way a SGP is simulated, while checking the crystal size frequently. Crucible 2 nicely shows that the crystal growth of the

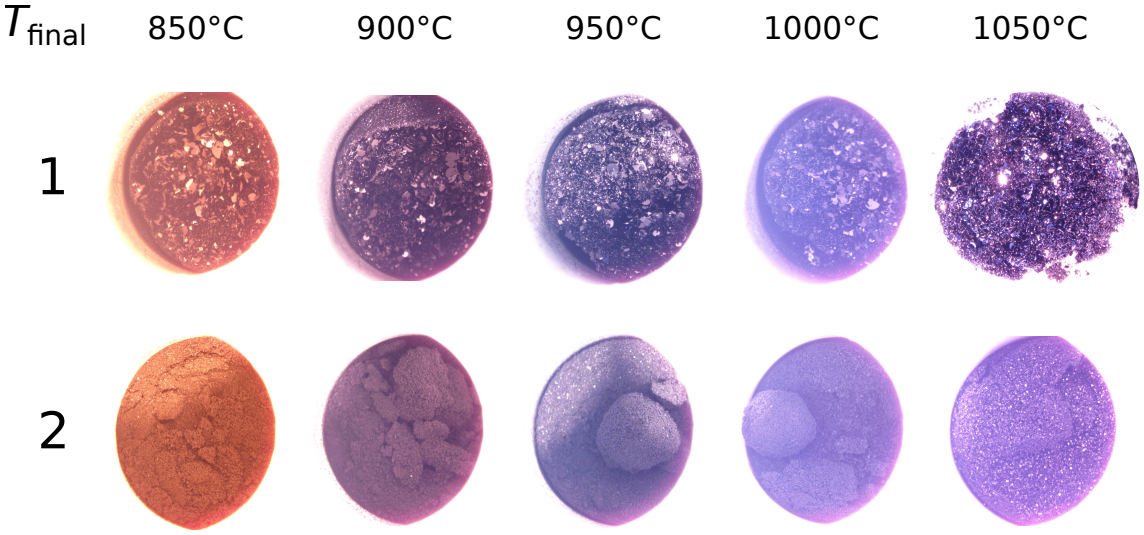

Figure 5.22.: Pictures of crucible 1 and 2 after each short heating step, starting from $T = 800$°C in 50°C-steps up to a final temperature of 1050°C. With seed crystals (crucible 1) as well as without (crucible 2) we see only a significant change in the last step from 1000°C to 1050°C. These growth procedures as well as the pictures were done by Franziska Breitner.

larger crystals does not start before a temperature of 1000°C. After the step with $T_{final} = 1050$°C, we can already see specular reflections of tiny crystals, but their size significantly enhances in the next step, when holding the crystals at 1050°C for 60 h. This can be seen in crucible 1, which had been at 1050°C prior to the

[9]This synthesis was performed and the pictures taken by Franziska Breitner (EPVI, University Augsburg).

heat treatment. There is no sign that the single crystals from crucible 1 change below 1000°C as well. In the last short heating step the crystals seemed to have started transforming. A slow heating up to 1050°C seems, therefore, unnecessary. The crystals grow mainly during the hold at 1050°C. Even with seeds (batch 1), the samples do not significantly increase their size during the slow heating. Similar conclusions can be drawn from crucible 3–5. Batch 3 and 5 have been held at 1050°C for three nights before, batch 4 has not. All three of them were first heated fast up to 800°C (≈ 2.5°/min) and then slowly up to 1050°C (0.2°/min), which we now know was most likely unnecessary. Batch 3 was taken out of the furnace after three days, while batch 4 and 5 were kept at 1050°C for another 11 days. With the help of the pictures of the crucibles after the growth sequence is finished, the sizes of the crystals can be analyzed. Since the size of the crucible is known (10 mm) the length of the crystals could be compared with the crucible diameter, which is also the size of the polycrystalline bed. This is not an exact method, but it is meant as an easy technique to estimate crystal sizes. The results for the largest crystals from batch 1 after each heating step that reached 1050°C are shown in Figure 5.23a. The second growth step which reaches 1050°C for batch 1 stops as soon as the final temperature is approached. Therefore, the time at 1050°C was considered 60 h as for the first step and we find two different measurements for $t = 60$ h. Comparing these two data sets it seems that the crystal growth between below 1050°C is significantly less

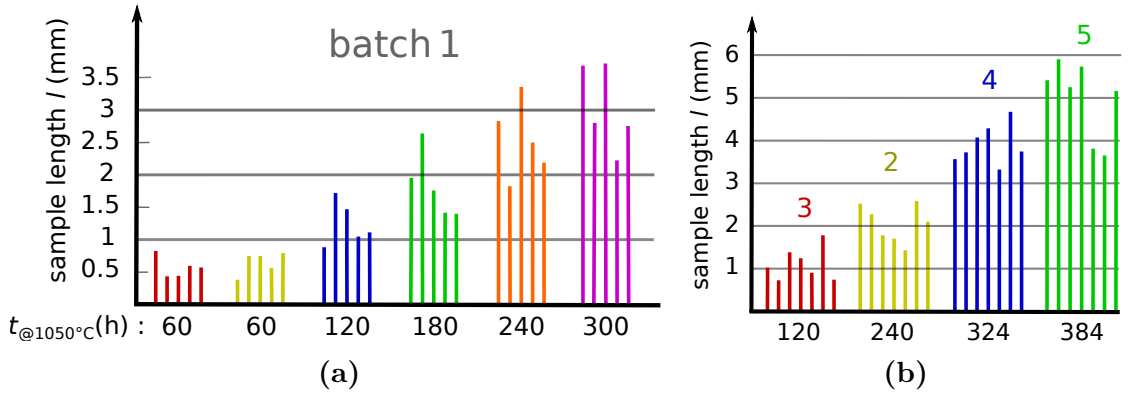

Figure 5.23.: Comparison of the length of the largest crystals of different batches. The length is estimated from pictures of the crucible for a) batch NIOLi12_1 after each growth step that reached 1050°C and b) batches NIOLi12_2–NIOLI12_5 at the end of the growth procedure. It is clearly visible that the size of the crystals increases with the time they have spent at $T = 1050$°C up to the longest duration available.

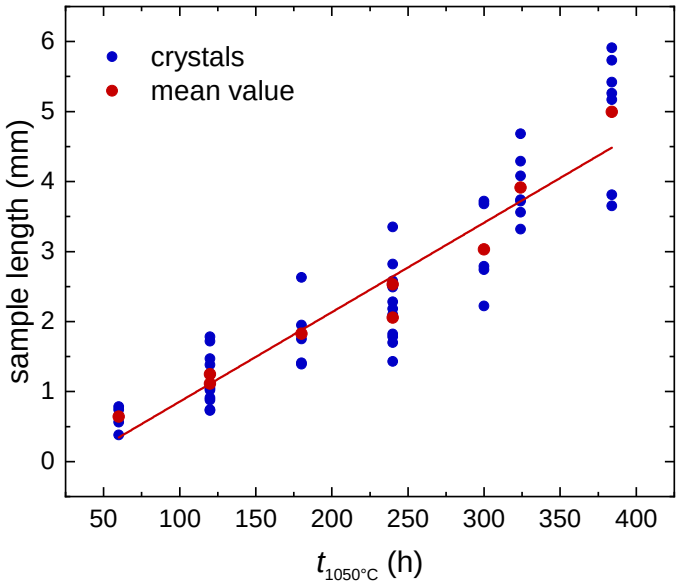

Figure 5.24.: The estimated crystal lengths in dependence of the time at 1050°C (blue points). The calculated mean values (red points) are fitted linearly. The first data set at 60 h correspond to the yellow lines in Figure 5.23a, since the crystal growth below 1050°C would distort the measurement result.

effective. Figure 5.23b compares the crystal lengths of batch 2–5 after the whole growth procedure. The corresponding pictures of the crucibles can be found in the appendix in Section B.1. The measured length typically coincides with the longest crystal edge. Most crystals show in the *ab*-plane a shorter edge, that is roughly $\frac{2}{3}$ of the longer edge, but it can also range from half the length to the same length. Figure 5.24 combines the results of all batches and plots the crystal lengths l in dependence of the time t the crystals have been at 1050°C. The data roughly show a linear behavior, which suggests the irrelevance of the slow heating and the holding time as the dominant factor. This rough estimate finds that the largest crystals grow about 0.3 mm per day. This gives an idea of how long one has to keep the samples at 1050°C to achieve a desired sample size. There is every reason to suspect that, for the case of a large filling and, therefore, a large supply of Na_2IrO_3 powder and IrO_2 powder, the size of the crystals will still increase if the last heating process will be extended. In this case the size of the samples is only limited by the size of the crucible. If the powder supply is exhausted, the crystals seem to decompose again and the materials escape from the crucible and onto the walls and lid. This was seen in an experiment where the holding time for the last step was doubled as well as for a growth of Franziska Breitner (EPVI, University Augsburg)where the last

step was repeated twice. Possibly the crystals are only stable at this temperature in the presence of gaseous IrO_3, which is suspected to also play an important role in the growth process of Li_2IrO_3 single crystals.

The optimal growth process for our purposes is schematically drawn in Figure 5.25. It is preceded by the calcination process described in Section 4.3.1 to produce high-quality Na_2IrO_3 powder from 0.5 g Ir powder and stoichiometrically adjusted Na_2CO_3 powder in a small crucible (10 mm diameter). Afterwards 25% of extra Ir (10% would most likely do the same) was added and transformed to IrO_2 in the first heating step in Figure 5.25 at $T = 900°C$. In the second step, the crucible is held for 17 days at 1050°C to grow the single crystals.

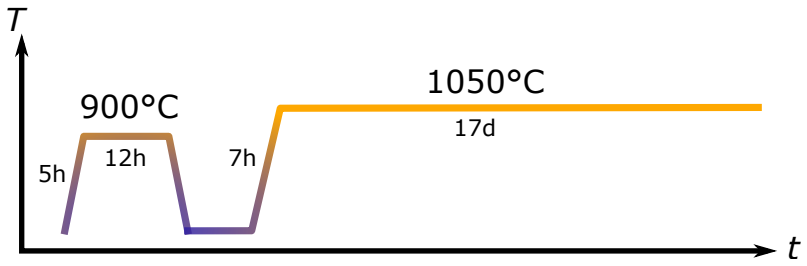

Figure 5.25.: Temperature profile of the optimized growth including the addition of extra Ir and its transformation to IrO_2 as well as a very long holding time at 1050°C. Depending on the desired crystal size the samples can be kept at 1050°C for a shorter or longer times. It only needs to be taken care that enough starting material is present. If a certain threshold is crossed, the crystals will decompose and the material transport out of the crucible.

Figure 5.26.: The largest single crystal of Na_2IrO_3 with smaller crystals sticking out.

The single crystals achieved via this method are larger and thicker as those grown with the SGP. The largest single crystal possessed an in-plane area of 8x5 mm^2 (see Figure 5.26), but also other crystals with 3 mm, 4 mm or 5 mm edge length were regularly found. The masses of the larger crystals have been found to be several milligrams. Now the question of course remains if the larger crystals obtained with optimized growth process yield better or at least crystals of the same quality as the original one. For this purpose, the different batches of NIOLi12 are compared by powder diffraction and samples grown with the old and new growth sequence are compared in their magnetization, among other experiments, in the following sections. If not stated

differently, the magnetization measurements in Section 5.3 are performed on samples grown with the optimized growth, while the samples in Section 5.4 were grown with the SGP.

5.3.2 X-ray diffraction

Powder X-ray diffraction was used to verify the structural quality of Na_2IrO_3 powder. Only for well defined peaks of Na_2IrO_3 the powder was used for growing single crystals. Additionally, the peaks corresponding to the *c*-axis of single crystals were investigated, which are naturally found if the samples are placed with their plane onto the holder of the powder diffractometer. This can give us hints about the influence of the growth procedure on the crystal structure (at least along *c*). An experiment about the degradation of Na_2IrO_3 powder was conducted to learn more about the reactivity of Na_2IrO_3 in air and, therewith, the necessary sample handling requirements for the compound. There will be a short remark on the shape of the diffraction peaks of the single crystals along the *c*-axis. Further, Laue diffraction was used to determine the orientation of single crystals in preparation of the experiments on the transverse magnetization.

Influence of the growth holding time

Evidence for a better crystal quality are narrower peaks and reproducible lattice parameters. When measuring powder diffraction patterns of a single crystal with crystal placed with the *ab*-plane onto the holder, only the $(00l)$ peaks appear. Therefore, the lattice parameter *c* can be analyzed for the different batches of NIOLi12. For each batch three samples where measured by Achouak Hassini (Figure 5.27a) and the results for *c* given in Figure 5.27b. The peaks of the XRD pattern were fit by the equation 3.2, which was introduced in the "Experimental Methods" chapter, to compensate the different thicknesses of the crystals in the calculation of the *c*-parameter. In the XRD pattern in Figure 5.27a the error of the angle θ due to the sample height is already eliminated. Figure 5.27b. All samples showed a length of

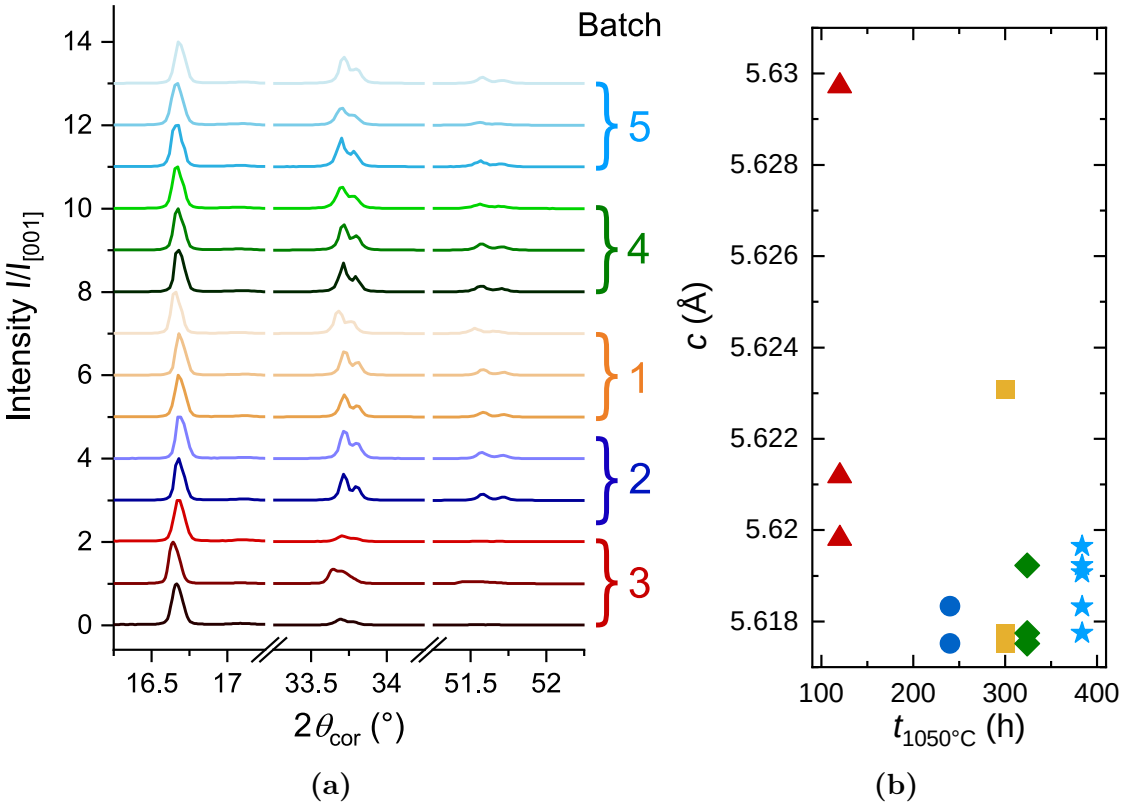

Figure 5.27.: a) XRD pattern and b) calculated length of the c-parameter in dependence of the time spend at $T = 1050°C$ of samples of the five batches of NIOLi12. The experiment was performed by Achouak Hassini [114]. One sample of batch 2 (dark blue) showed too weak intensities and was excluded from the experiment. While samples of batch 1 (orange) and 3 (red) show a broader distribution of the c-parameter as well as a larger deviation from the literature data [54], the c-parameter for the samples of batch 4 (green) and 5 (light blue) are closer to the literature value and to each other.

the c-axis that is slightly larger than the literature value of 5.614 Å [54]. Batch 3, with the smallest time at 1050°C of ∼120 h, seems to possess the worst crystal quality. The samples show by far the worst diffraction pattern and the largest deviation to the literature value as well as the largest variance in between the samples. The c-axes of all other crystals with exception of one in batch 1 (∼300 h) range between 5.617 Å and 5.620 Å. In batch 2 (∼240 h) one sample showed such low intensities that it could not be used for the determination of c. No such problems were found for samples of batch 4 (∼324 h) and 5 (∼384 h). The statistics of batch 5 was greatly improved by the addition of two samples measured by the author (shown only in Figure 5.27b). All samples of batch 4 and 5 showed well-defined $(00l)$ peaks and a

small variance. These results suggest an improved crystal quality for longer holding times in the c-direction.

Powder degradation

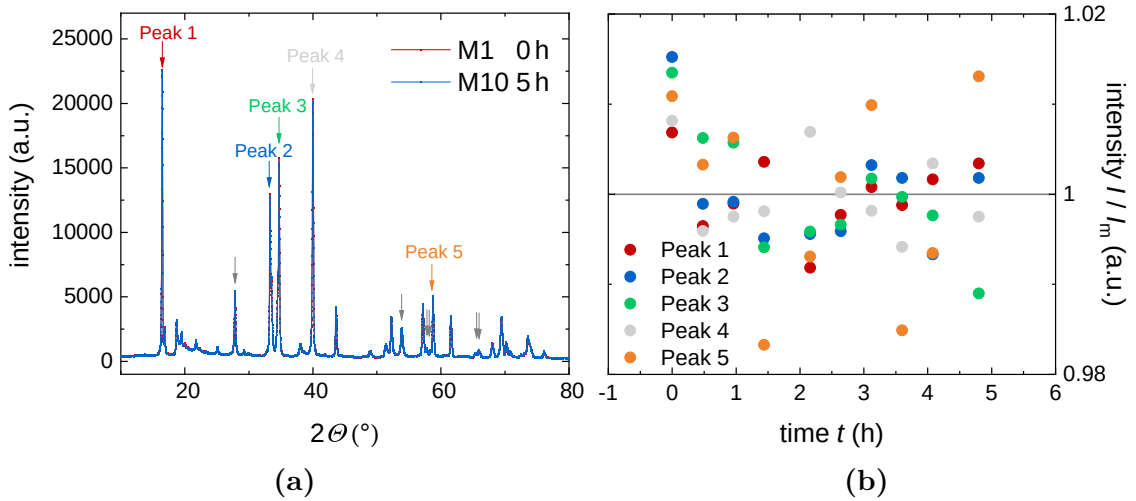

Figure 5.28.: a) Comparison of the XRD pattern after 0 h and 5 h and definition of Peak 1–5 for further analysis. Peak 1 to 4 show a slightly smaller maximal intensity after 5 h, but the rest seems unchanged. Due to the synthesis of Na_2IrO_3 crystals, the powder contains IrO_2 as well (gray arrows). b) Development of the peak intensities (divided by their mean value) with t of all 10 measurements made in the time span of 5 h. Here, it becomes clear that the difference in a) merely stems from a statistical error due to measurement uncertainties. The peak heights vary around the mean value with a deviation of 2%.

A mixture of high-quality powder of Na_2IrO_3 and IrO_2 powder was repeatedly measured with powder X-ray diffraction. During this time, the sample stayed inside the experimental setup in air and was not removed. After 5 h the XRD pattern has not changed strongly (see Figure 5.28a). The peaks corresponding to IrO_2 are marked with gray arrows. To better visualize the degradation process, the five largest peaks of Na_2IrO_3 were chosen (marked in Figure 5.28a) and the evolution of the peak heights with time was analyzed. The results are shown in Figure 5.28b. The peak intensities were normalized by the mean value of all peaks. So far, there is no sign of a true reduction of the peak heights. We see a random distribution of the data around 1 with a statistical error of 2%. This is a reasonable value, since the peaks are narrow and small changes in the measured angles (step size: 0.02°) lead to

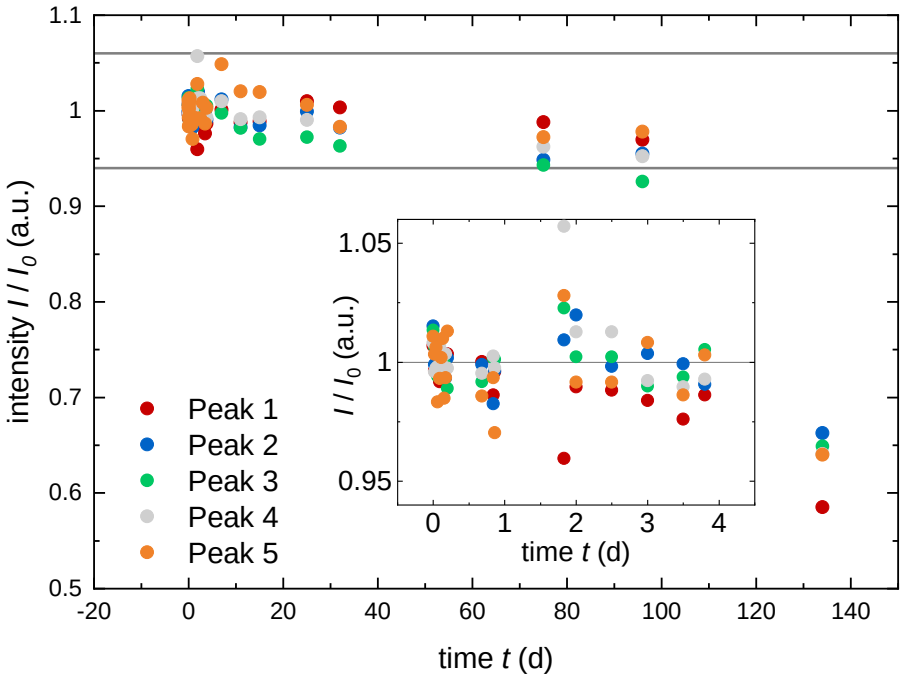

Figure 5.29.: After 4 days in air the maximal peak intensities (divided by the mean value of the first 10 measurements) still show a statistical distribution around 1. b) After about four months (134 d), the peak intensities drop to about 40% of the original value.

changes in the maximal measured peak height. The results suggests that there is no significant degradation in the first 5 hours. After 4 days, shown in the inset of Figure 5.29, the situation is similar. In the end, the powder has been measured up to nearly 4 months (Figure 5.29). Especially the last measurement showed a significant change in the diffraction pattern. The third last measurements could be seen as the starting point of the degradation. Here, the peak heights already start to reduce. Nevertheless, the number of measurements in this time range is too small to make any strong statements. The comparison of the last and first XRD measurement is shown in Figure 5.30. Most Na_2IrO_3 peaks have decreased by approximately 29% to 42% and new peaks belonging to a new phase have emerged. The same peaks have been observed in [83] and [84] after the degradation started. Figure 5.31 shows the development of the XRD patterns between 15° and 45°. Between each measurements roughly one month has passed. The new peaks from the degradation product(s) for the most part appear only in the last measurement on June 7th. This still holds true even when plotting the data on a logarithmic scale. This result is astonishing. As far as we can tell, the Na_2IrO_3 powder did not degrade for three months. This clearly

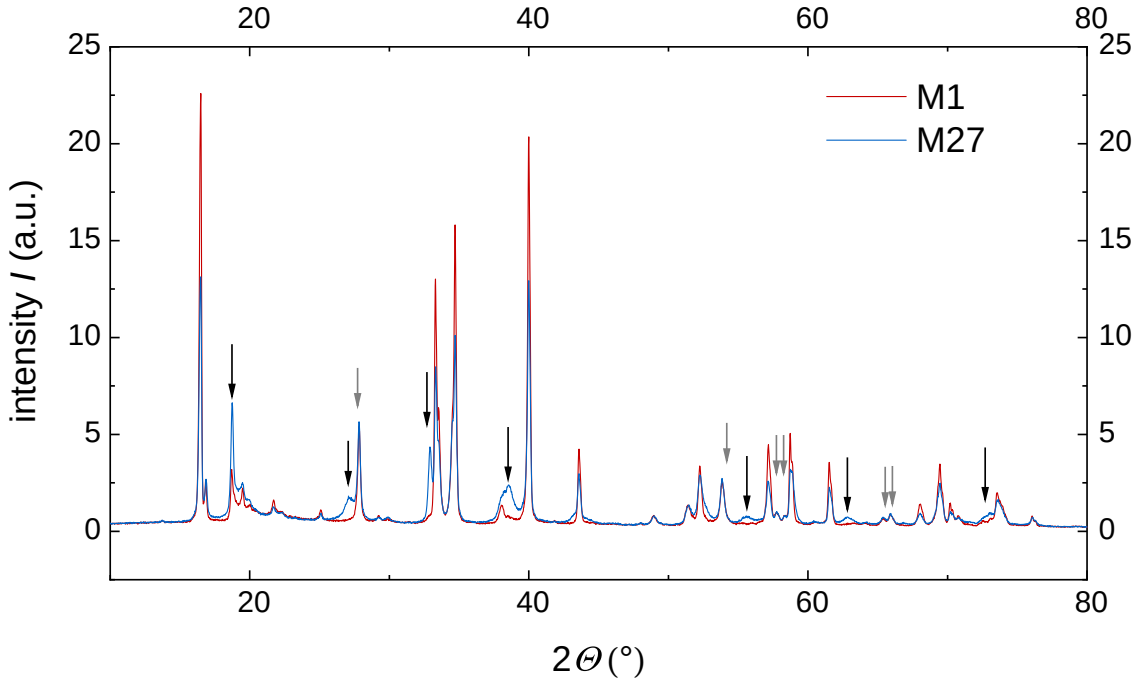

Figure 5.30.: Na_2IrO_3 powder XRD pattern after four months in air M27 compared to the starting pattern M1. Most peaks belonging to Na_2IrO_3 show a reduced intensity, while reflections of a new phase appear (black arrows). The peaks of IrO_2 (gray arrows) are unchanged.

contradicts the findings of other groups presented in Section 4.3.2. Wallace *et al.*[84] found their sample to be degraded to the same degree, as it has been found here, already after 8 h. The reasons for this extreme difference can only be speculated about. The measurements were started in the middle of the winter (February 11th). Krizan *et al.*[83] showed that the reaction needs H_2O as well as CO_2. The significantly drier air, especially inside the lab, might have slowed down the degradation down. Possibly, the experiments of the other groups were performed during summer with a high humidity. Further, the other groups could have carefully ground the powder before the measurement, starting with smaller polycristalline material with a larger surface area. Our crystals could also be of better crystalline quality with fewer surface defects, exposing less target points for degradation.

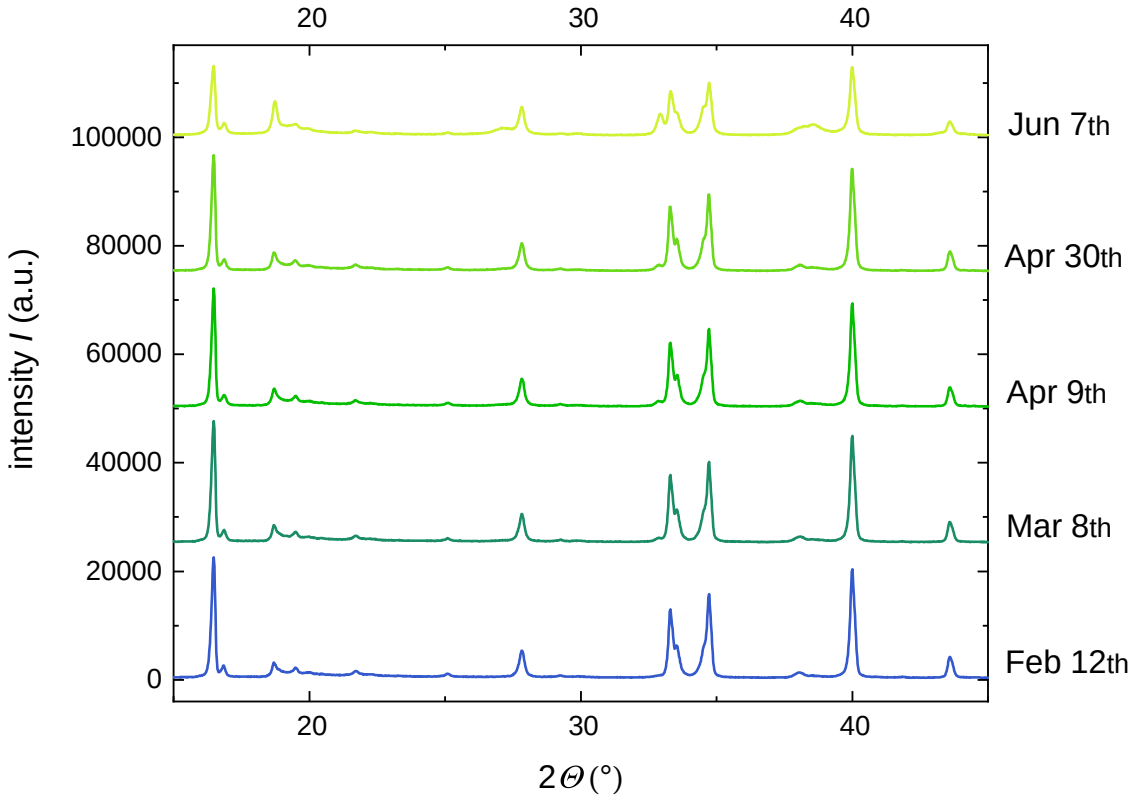

Figure 5.31.: Development of the XRD pattern with time: From February 11th to April 30th, the XRD data show no significant change. On June 7th, after roughly four months in air, the sample shows a reduction of the Na_2IrO_3 peaks and the appearance of new peaks belonging to the degradation product.

[00*l*] diffraction peaks

If one looks closely at diffraction patterns of Na_2IrO_3 single crystals, there is one peak that is not covered by the literature data at 17.1°. After a careful study of all diffraction patterns, it turns out that this peak appears for powder of good crystalline quality as well and can be found in every diffraction pattern of a single crystal. In the experiment shown in Figure 5.32 poorly structured Na_2IrO_3 powder was annealed at 1150°C to achieve good quality powder in a very short amount of time. In the first round the sample was put into the furnace for five minutes, in the second for 10 minutes and in the last round for 15 minutes. After each round the diffraction pattern was checked. The quality improves which is nicely seen in the narrowing of the peaks. Furthermore, we find a reduction of the signal between the [020] peak at 19.0° and the [100] peak at 19.8°, which is is associated with the

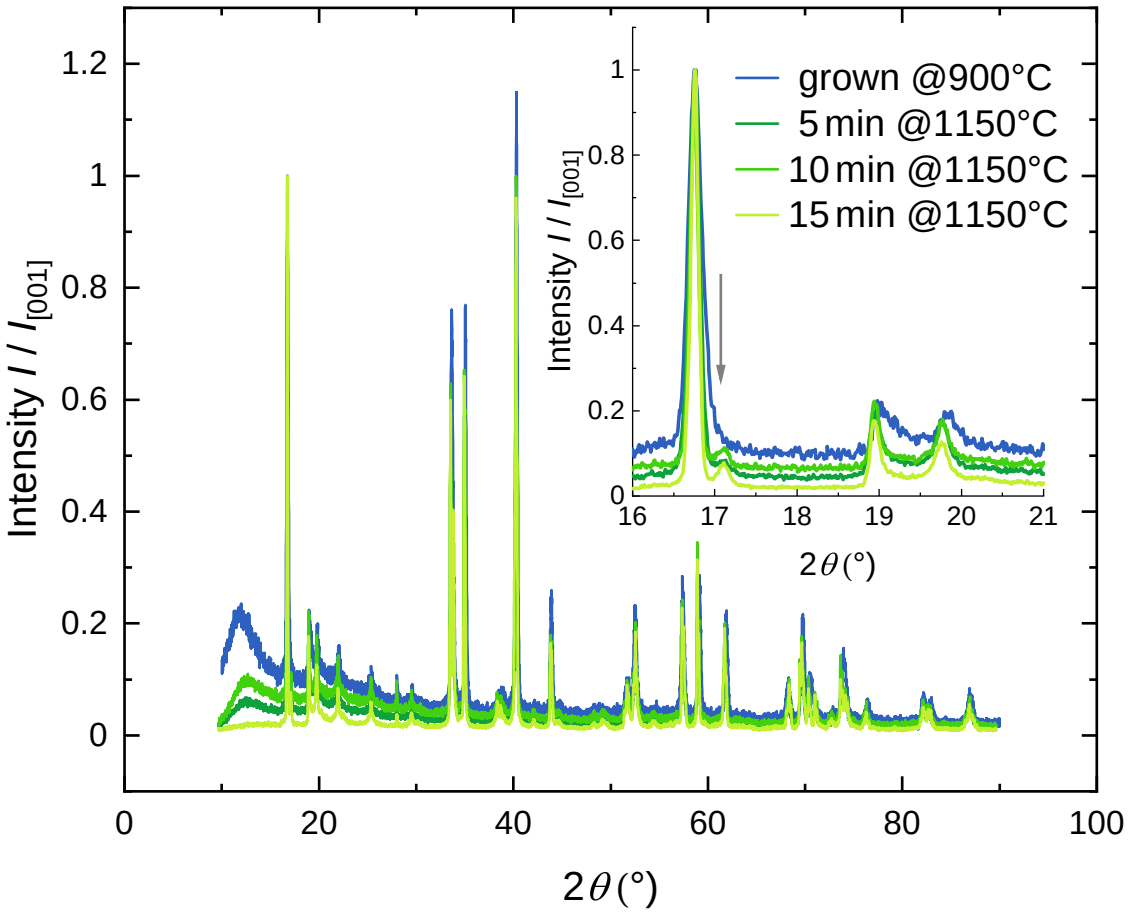

Figure 5.32.: Diffraction patterns of Na_2IrO_3 powder. Starting with poor-quality powder (grown @900°C) and annealing it at 1150°C for 5 min, then for 10 min and finally for 15 min (always the same powder) the quality of the powder clearly improves. Additionally, a new peak emerges at $2\Theta = 17.1°$(gray arrow).

amount of stacking faults in the c-direction [115]. With the first heat treatment the peak at 17.1° appears and increases with further treatments. Other annealing experiments have shown that if the crystal quality does not increase further the size of this peak in relation to the main [001] peak remains unchanged as well. This indicates that the peak might in fact be intrinsic to Na_2IrO_3.

Figure 5.33 shows all single crystal diffraction pattern of NIOLi12 (excluding the obviously poor-quality patterns). For a better comparison the main [001] peaks were shifted on top of each other, since all samples show a slightly different c-parameter. The peaks were further shown in log scale and the x-axis reduced to the angles around the [00l] peaks. If we look at data in the logarithmic scale, we find this peak appearing behind every [00l] peak. We find, additionally, a shoulder on the

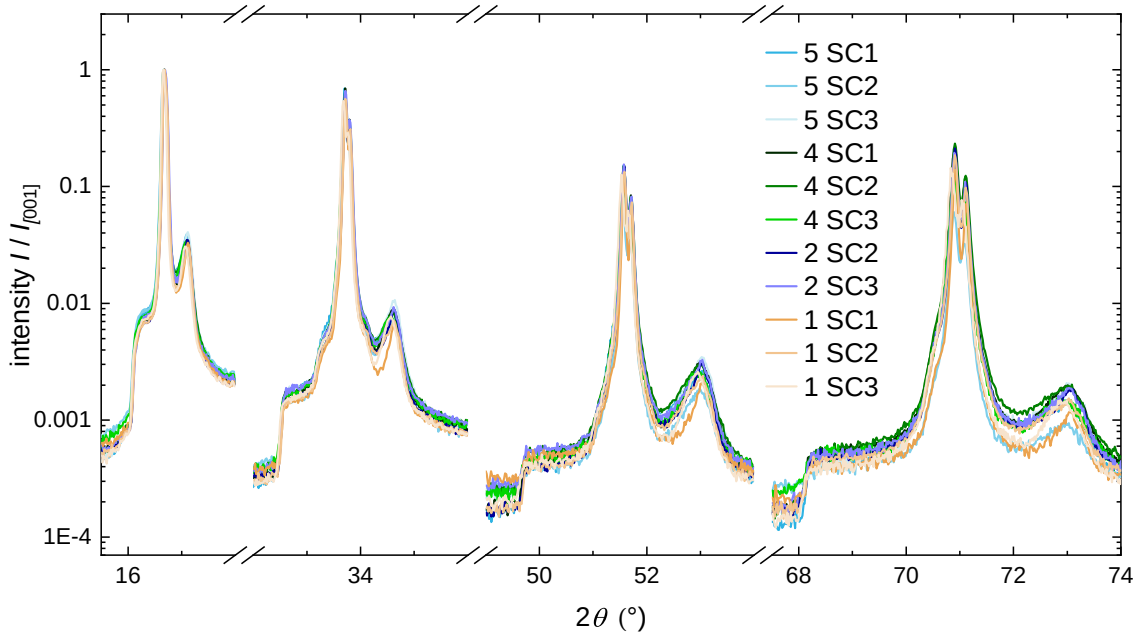

Figure 5.33.: Powder diffraction on Na_2IrO_3 single crystals in c-direction around the [00l]-peaks. All samples show a shoulder on the left and a second peak on the right of the [00l] reflections.

left side of the [00l] peaks, which stems from the nickel filter of the diffractometer [10]. The question might arise if the longer growth might be responsible for a change in the structure. This possibility can be excluded since these features appear in most diffraction patterns of Friedrich Freund on Na_2IrO_3 single crystals (see appendix Section B.2) Figure B.3) as well, who always used the SGP to grow the single crystals.

Now there seems to be only two possible explanations for the extra peak. It can be a foreign phase or it is in fact intrinsic. The fact that the size of the features in relation to the main peak is very similar for all samples seems odd for a foreign phase that are typically found with varying content. Attempts to find a suitable phase that shows a reflection in this region have remained fruitless. The other argument would lead to the assumption that the c-parameter is not equal throughout the crystal. Instead, it is possible that the it is smaller for some parts of the crystal. Lüpke *et. al.* [116] detected with scanning tunneling microscopy, next to the expected surface configurations, a second one that seemed to contain only 1/3 of the Na atoms.

[10] There are also two other peaks that surround the [00l] peaks, for example, at 15.0° and 19.7° for the [001] peak, which were not shown in the figure. But their intensities are even much smaller than the first discovered extra peaks.

Julian Kaiser (EPVI, University Augsburg) found stripes with Na-deficiency on the surface of Na_2IrO_3 single crystals using scanning electron microscopy (SEM) and energy-dispersive X-ray spectroscopy (EDX) as well. It seems reasonable that a smaller Na content could lead to smaller lattice parameter, being able to explain this observation. Nevertheless, one has to keep in mind that this features are very small. The largest one is the peak at 17.1° with a size of 4% in comparison to the [001] peak.

Laue diffraction of Na_2IrO_3 single crystals

Laue diffraction is a helpful technique to find suitable candidates for transverse magnetization experiments. Ideally, a crystal would show only one orientation in the whole sample. The larger the fraction of the crystal with the same orientation is, the larger the magnetic transverse moment should be. The reason is the working principle of the transverse measurement option of the MPMS (see Section 3.4.2). Only the sum of all moments in one plane is measured, compared to the moment along a certain direction like in longitudinal measurements. For different orientations in the sample, the moments will partially cancel each other and weaken the signal. A different in-plane orientation will show a rotated Laue diffraction pattern. The sample is typically scanned on different spots on the sample to ensure a more broad overview over the samples crystalline structure. Many samples showed rotated Laue pattern in an angle range of roughly 5° to 20°. Mostly one, but sometimes even up to three twins were found. Figure 5.34 shows two examples of such defects.

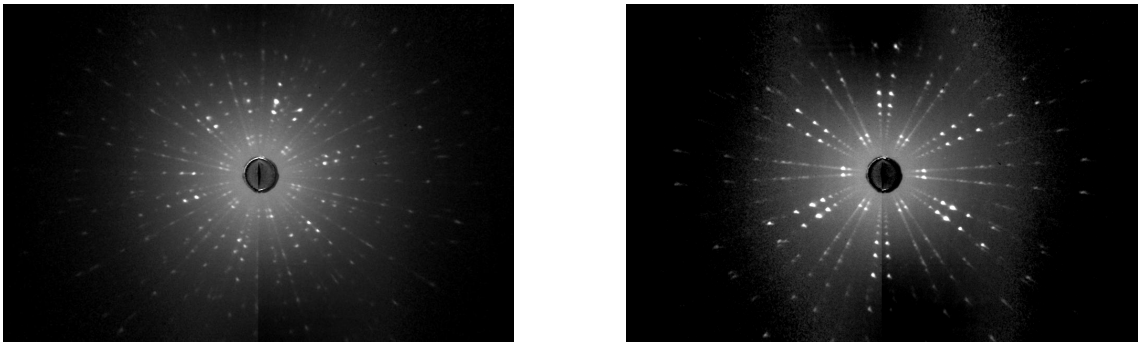

(a) **(b)**

Figure 5.34.: Two examples of diffraction patterns of Na_2IrO_3 single crystals showing different orientations.

Another important step was the determination of the orientation of the crystalline axes via the Laue diffraction pattern. With this information the crystallographic direction of the measured magnetic moment (or the sum of all magnetic moments) could be identified. To achieve this, the diffraction pattern was compared to theoretically modeled diffraction patterns using the combination of the *CrystalMaker* [117] and *SingleCrystal* [118] software. In these programs, the modeled pattern can be directly laid above the measured pattern and, by changing the orientation of the crystal in the model, the modeled pattern is adjusted until it matches the measured data. The theoretical data were taken from [54]. One has to know the orientation of the crystal in the Laue diffractometer and can, herewith, determine the direction of the crystal axes in the single crystal. This process was performed on Na_2IrO_3 sample NIOLi7-SC6.

One important question, before we look at the results, is whether we can observe the whole sample thickness with the Laue experiment. Due to the weak chemical link of the different Na_2IrO_3 layers is the system prone to stacking faults, which might go hand in hand with rotated orientations between different layers. In few Na_2IrO_3 single crystals such a property could even be seen by eye on rotated honeycomb-like structures as the example in Figure 5.35 shows. The mean free path of an X-ray

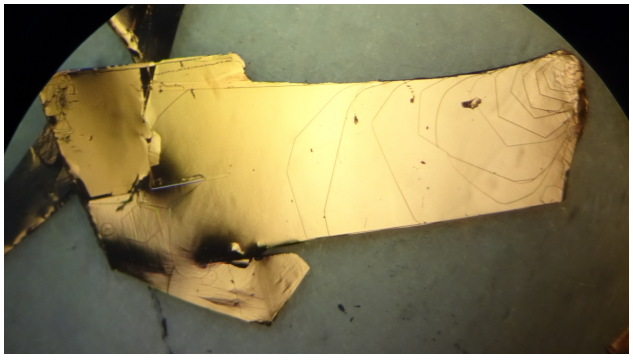

Figure 5.35.: A Na_2IrO_3 single crystal which shows, especially on the right half, different oriented honeycombs or shapes similar to honeycombs. This suggests that in this crystal the orientation rotates for different layers.

in Na_2IrO_3 was calculated with the help of a program of NIST (National Institute of Standard and Technology)[119]. There, one can calculate the linear attenuation coefficient μ, which is the inverse of the mean free path l. The density of Na_2IrO_3 was calculated from the giving literature data in [54] to be $6.4\,\mathrm{g/cm^{-3}}$. The result for the applied energy of 30 kV was an attenuation coefficient of $108\,\frac{1}{\mathrm{cm}}$, giving a

mean free path of 93 µm in Na_2IrO_3. The thickness of most samples ranges between 10 and 100 µm. This result suggests that we can see the whole sample in the Laue backscattering technique for thinner samples. For very large samples, as they have been used for the transverse magnetization measurements, we expect to safely cover the whole sample thickness when measuring the Laue spectra of the front and back side of the crystal.

NIOLi7-SC6 was measured on both sides of the crystal. The first side showed several different orientations in the measurement. The second side was measured on five different spots on the sample. In three patterns two different orientations were present, but one was in all patterns present and in all except one had the dominating reflections. Since the surface of a sample is, due to missing bond partners, prone to show all kinds of defects, the idea came up to polish the surface and repeat the measurement. Therefore, the first side was polished and for three different spot on the crystal the same Laue pattern with the identical orientation was indeed measured. This indicates that, although the X-rays might be able to interact with atoms of the whole sample depth, a large amount of the intensity comes from the first layers. In Figure 5.36 the dominating orientation of the second side is compared

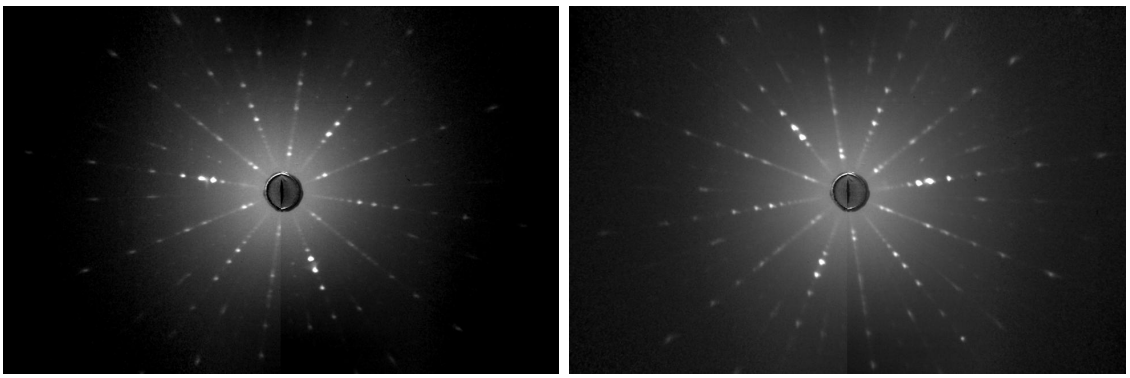

(a) **(b)**

Figure 5.36.: Laue diffraction pattern of a) NIOLi7-SC6 unpolished side 2 and b) NIOLi7-SC6 polished side 1.

to the first polished side. On the first glance, one might notice that the two pattern look like a mirror image of the other with the mirror plane in the paper. For the mounting of the sample for both sides a characteristic edge of the sample was aligned by eye to a line on the sample holder. The sample was turned between these measurements in a way that the X-ray beam fell on an around 180° in-plane rotated back side of the sample. These operations on the oriented pattern of the

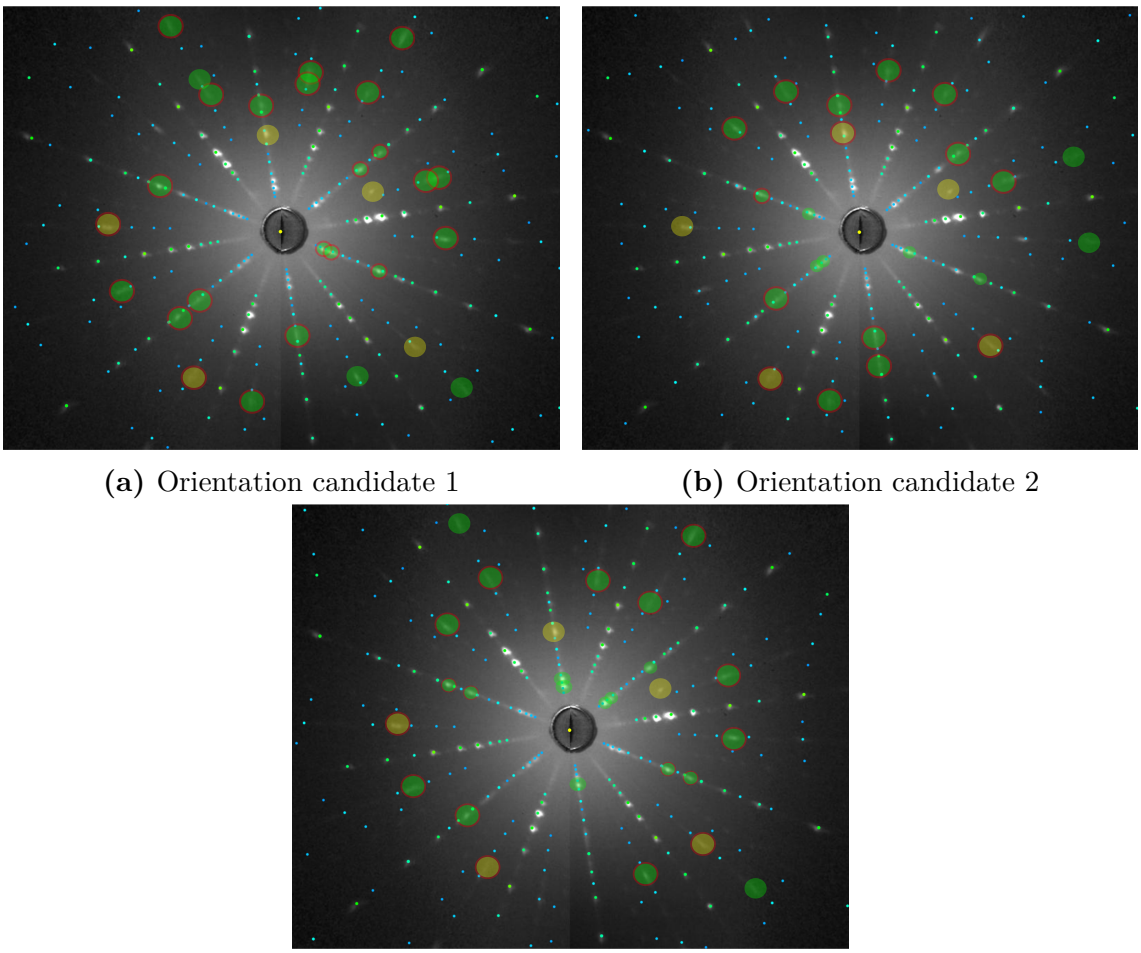

(a) Orientation candidate 1

(b) Orientation candidate 2

(c) Orientation candidate 3

Figure 5.37.: The three possible orientations for the sample 7-SC6. The intensity of the calculated Laue pattern from [54] is color coded from yellow (highest intensity) to dark blue (lowest intensity). There exist many reflections, which are not captured by the literature data (yellow areas) or only by one or two (green areas) of the possible orientations. It seems there is no answer to the right orientation possible, since all of them seem to be present.

unpolished (or polished) side in the *SingleCrystal* software showed to be a very well orientation of the opposite side. We can conclude that the orientation of both sides (at least below the surface) is the same. The polishing of the sample revealed the true structure of the bulk. To identify the orientation of the single crystal is not trivial. The sample is measured with the in-plane orthogonal to the sample–X-ray–source direction. One has to know the size and resolution of the Laue picture (15.5x10.2 cm^2 and 62.9 pixel/cm) as well as the distance to the Laue camera. With this information the Laue pattern can be compared to a modeled Laue pattern.

First, we look at the strongest reflections and can relatively easy identify three different possible configurations with a 120°-rotation between them. This is due to the almost perfect honeycomb structure of Na_2IrO_3. The real challenge is to find the right configuration between those three candidates. For comparison these three candidates are presented in Figure 5.37. The measured reflections are white, while the calculated reflections from [54] are color coded regarding their intensity from yellow (highest intensity) to dark blue (lowest intensity). All reflection points which could not be matched by a literature reflection are covered by large circles. The yellow areas could not be matched for any of the three possible orientations, while the green ones could only be matched in two of the three orientations. There are many spots that fall in the latter category. Since there is always an orientation that explains the reflection point, it seems clear that all of these three orientations must be present. Another sample was analyzed in this manner. All circles with red contours represent points found for this sample as well, which include the majority of reflections. The respective picture can be found in the appendix in Figure B.5. The yellow circles might point to other defects present in the sample.

To look into this in more detail, the pattern using the crystallographic data of [54] was investigated regarding the presence of different orientations. Figure 5.38 shows a comparison of the calculated pattern (Figure 5.38a) with only one orientation present and the pattern when it is overlaid by a 120° rotated pattern (Figure 5.38b). In the red starting pattern the point in the middle is the c*-direction. Since the compound has a layered structure, the c*-direction is easily identified by the samples surface. In the horizontal line from left to right we find the $[0kl]$ reflections, marking the direction of the b-axis, while the $[h0l]$ reflections, related to the a-axis, follow the vertical line from top to bottom. The blue clockwise rotated pattern has been overlapped with the red pattern and the opacity decreased to 50%. Thus, overlapping reflections appear as violets dots. On the first glance, the pattern from Figure 5.38a seems to have a 120° symmetry. This would be expected for a perfect honeycomb without the nonclinical angle β. The overlap of the patterns in Figure 5.38b, though, clearly reveals the imperfect 120° symmetry of the system. The $[h0l]$ reflections as well as all reflections in 60° steps in regard to these stay unchanged upon rotation (violet dots). All other reflections, except for some single points, show a different position. The point is that for $\beta \neq 90°$ there is a difference when rotating the crystal structure from the c*-direction to the [100]-direction compared to the $[\bar{1}00]$-direction. As a result, the reflections with $h \neq 0$ appear at different positions for

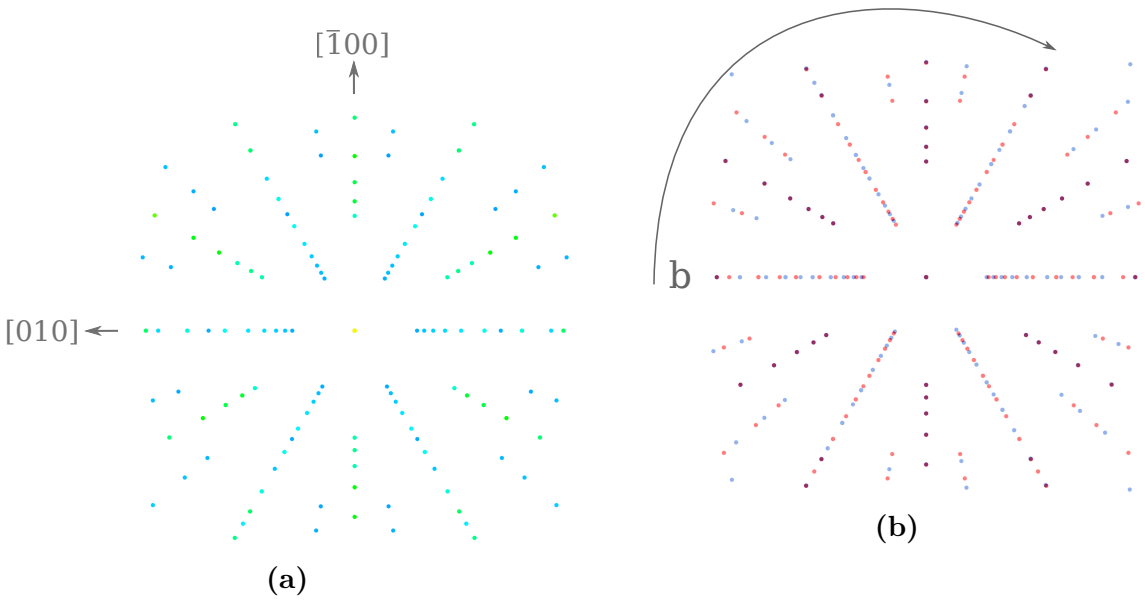

Figure 5.38.: a) Calculated pattern from [54] with the b-axis horizontally and the a-axis vertically oriented. The point of symmetry in the middle of the pattern corresponds to the c^*-direction. The diffraction pattern is color coded according to the intensity of the reflection point from yellow (highest) to dark blue (lowest) b) Overlay of the pattern from a) in red and an around 120° clockwise rotated pattern in blue. The rotated pattern is placed exactly above the original one and its opacity is lowered to show all reflections. Where both patterns overlap the color turns violet.

positive and negative h. This should in principle enable us to determine the exact orientation of one's crystal in the case of a one-domain sample. If we rotate the sample 180° around c^*, the $[0kl]$ reflections will overlap with the $[0\bar{k}l]$] reflections of the unrotated measurement. This can be seen when overlapping both diffraction patterns, indicating the direction of the b-axis. This is discussed in more detail in the appendix in Section B.4. There, also other rotation angles between different orientations are looked at. With this nearly perfect honeycomb structure in-plane a 120° twinning of the crystal seems likely. Figure 5.39a shows us how a diffraction pattern with all three 120° configurations in red, blue and green, respectively, would look like. This can be compared to the measured diffraction pattern of NIOLi7-SC6 in Figure 5.39b, already shown in Figure 5.36b. To make further discussions about the calculated patterns easier I will define the 6 reflection lines with 120° symmetry (violet dots) as *short main reflection lines* since they start farther away from the c* reflection. In contrast, the other 6 main reflection lines, which start closer to the center, will be called *long main reflection lines*. These reflections can be used best

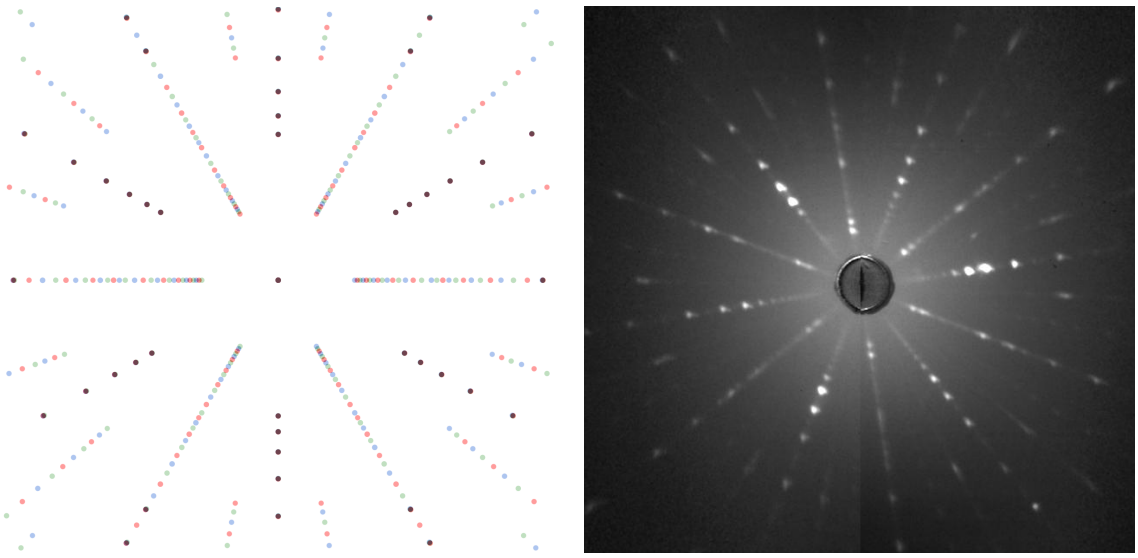

(a) **(b)**

Figure 5.39.: a) Calculated diffraction pattern with all three 120° orientations in red, blue and green present. Where reflections of all three orientations overlap, the color turns brown. b) Measured diffraction pattern of NIOLi7-SC6 in comparison.

to determine the exact orientation. For 120°-twinning the long main reflection lines would smear out, especially close to the center, to a real line, while the reflections on the short main reflection line would be enhanced in intensity due to the same position for all orientations. It seems, although the Laue pattern of NIOLi7-SC6 looked well-defined on the first look, all three possible orientations are present. We clearly see the smearing out of the long main reflection lines, while it is not present for the short main reflection lines apart from the area very close to the center. This phenomenon is found for all measured Na_2IrO_3 single crystals and it can also be seen Figure 5.34 in the beginning of this section for all orientations. An important question is now whether we are able to identify a dominating orientation. An idea is to compare the intensity of the reflections in the colored areas. The diffraction pattern with the smallest overall intensity in these areas could be determined as the dominating orientation. For NIOLi7-SC6 there seems to be no clear difference and, therefore, this idea was not further pursued. All this seems to point to the fact that we cannot determine an in-plane orientation, but must be satisfied by determining the direction of the honeycomb edges. These follow the direction of the three possible b-directions determined from Figure 5.37.

To summarize, in principle, the orientation of a Na_2IrO_3 crystal could easily be

identified by simple rotation and comparison of the Laue picture, if the alignment of the sample has been done accurately. Further, programs for diffraction pattern analysis help identifying the right orientation. Here, it seems helpful to polish the surfaces of the sample to get rid of defects from the first layers of the crystal. In our case the diffraction pattern can only be explained by including at least three orientations, which are rotated by 120° relative to each other. This is a hard finding for the transverse experiment, but it explains the trouble we have been having. Many samples, although the Laue picture looked well, showed no or extremely low signal in the transverse magnetization. Even samples with a relatively large signal barely exceeded the background data. If all three 120°-orientations in equal proportions are present, the expected transverse moment will be zero, since they cancel each other out. Additionally, if we assume the constellation: orientation 1 < orientation 2 < orientation 3, the sum of the resulting moment from the surplus of 2 and 3 can be anywhere and does not have to be restrained to a certain crystallographic axis. The information of the direction of the magnetic moment in respect to the honeycomb might not help us at all. Nevertheless, we can clearly detain the direction of the honeycomb edges for these two crystals. These lie along the directions of the possible b-axes for the three 120°-orientations. These are sketched in Figure 5.40 next two a picture of the sample.

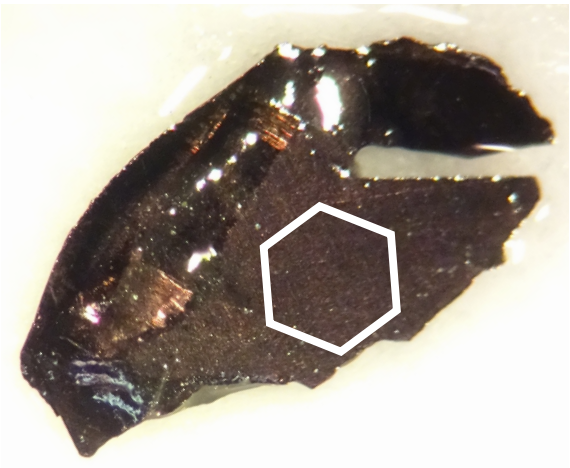

Figure 5.40.: Sketch of the determined honeycomb orientation in NIOLi7-SC6. The long edges of the samples as well as some short ones seem to roughly match the direction of a honeycomb edge.

5.3.3 Longitudinal magnetization

The anisotropy for Na_2IrO_3 of the in-plane vs. out-of-plane direction has been known for a long time. In this section the in-plane anisotropy is presented. Beforehand, the influence of the growth procedure on the longitudinal magnetization is discussed.

Influence of the growth holding time

To approach an answer to the question of the quality of the larger crystals grown via longer holding times, different samples of Na_2IrO_3 were compared in their magnetization in Figure 5.41. The plot shows the molar susceptibility of crystals with the

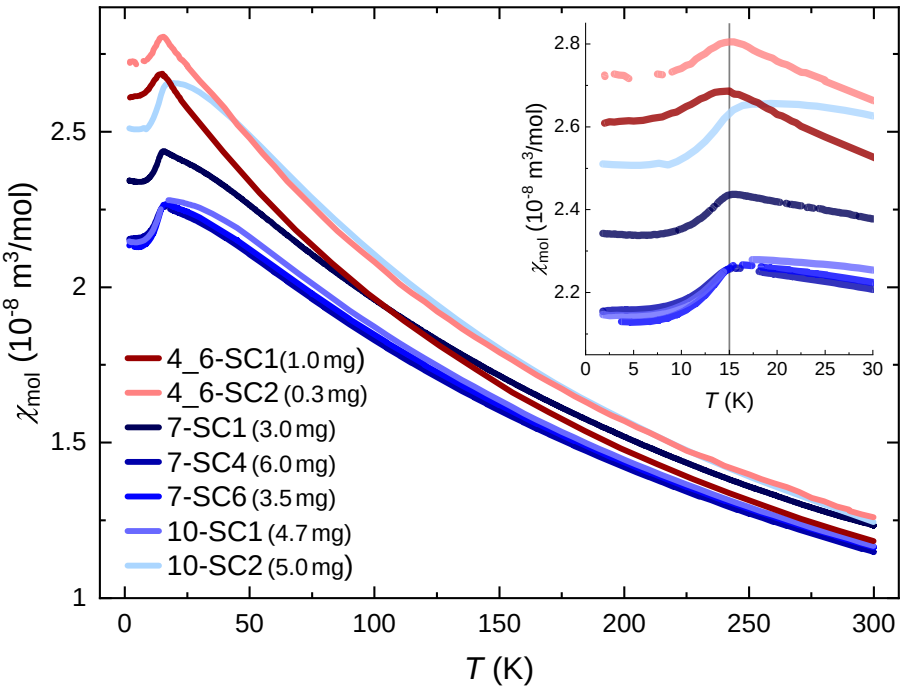

Figure 5.41.: Comparison of the susceptibility $\chi(T)$ of Na_2IrO_3 single crystals grown with a short (red) and a long (blue) holding time, measured with an in-plane field. The curves are very similar and for both groups we see a sample dependence. For temperatures just above the transition temperature the samples with a longer holding time show a flatter decrease than the other curves. Two samples with a long holding time show a slightly larger transition temperature.

field pointing along the *ab*-plane. The red curves correspond to samples grown by the SGP with a holding time of three days at 1050°C, in comparison to the samples

represented by blue curves, which have been 17 days at 1050°C. There is a sample dependence especially at low temperatures for both growth sequences. What differs clearly for all samples grown in short compared to samples grown in long holding times is the shape of the curve above the magnetic transition. While the red curves are almost symmetric around the transition at 15 K, the blue curves all show a flatter decrease towards higher temperatures. It seems the samples with long holding times deviate earlier from Curie's law. This suggests also a (small) difference in the magnetic properties. Nevertheless, one has to admit that the small number of samples, especially on the side of the crystals with short holding times, does not allow a very strong statement. Additionally, the strong decrease towards lower T (which should correlate to the maximum for the red curves at 15 K, associated with T_N) is shifted for NIOLi7-SC6 to 15.7 K and NIOLi10-SC2 to 16.4 K. This could be interpreted as less frustration due to a better crystalline structure. We can also compare the constants of the Curie-Weiss fit for these measurements [11]. The fits were performed between 150 K and 300 K . One has to keep in mind that the fit parameter might show a dependence of the chosen fit temperature range as suggested for the Kitaev-Heisenberg model in [99]. A constant χ_0 contribution was not included in the fit function. The reason for this decision is discussed in the appendix in Section B.5. The results are presented in Table 5.4. The transition temperature T_N, which was

sample	4_6-SC1	4_6-SC2	7-SC1	7-SC4	7-SC6	10-SC1	10-SC2
T_N (K)	14.5(3)	15.3(3)	15.0(3)	15.4(3)	15.7(5)	15.3(15)	16.4(5)
Θ_W (K)	-202.4(6)	-205(1)	-230.3(2)	-227.0(6)	-231.0(7)	-223.9(6)	-184.8(9)
μ_{eff} (μ_B)	1.945(2)	2.012(4)	2.039(4)	1.964(2)	1.983(2)	1.975(2)	1.962(4)

Table 5.4.: Comparison of the magnetic parameters T_N, Θ_W and μ_{eff}. For longer holding times there seems to be a trend towards slightly higher transition temperatures T_N and smaller Weiss temperatures Θ_W. No influence of the growth procedure on the effective moment μ_{eff} is visible.

determined from the maximum of the susceptibility curves for samples with short holding times and as the onset of the steep decrease for samples with long holding times, was included as well. The step size as well as missing points due to artificial

[11] Li *et al.* [113] found that applying a simple Curie-Weiss fit to Na_2IrO_3 results in false Weiss temperatures θ_W as well as overestimated effective moments μ_{eff}. Since the fitting was done mainly to compare the data, a fitting with an temperature dependent effective moment $\mu_{eff}(T)$ as suggested in [113] was omitted.

jumps in the susceptibility contribute to the estimated error of T_N. The errors of the other parameters were taken from the Curie-Weiss fit.

A view on the inverse susceptibility and their fit functions in Figure 5.42 clearly shows a deviation of the samples with longer holding times from the Curie-Weiss behavior at far larger temperatures compared to the other samples. While they loose their linearity at roughly 145 K, samples with short growth times follow their fit down to roughly 75 K. It seems the crystals with longer holding times show a tendency towards slightly higher transition temperatures as well as smaller Weiss temperatures, although the latter most likely results from the too low fitting range.

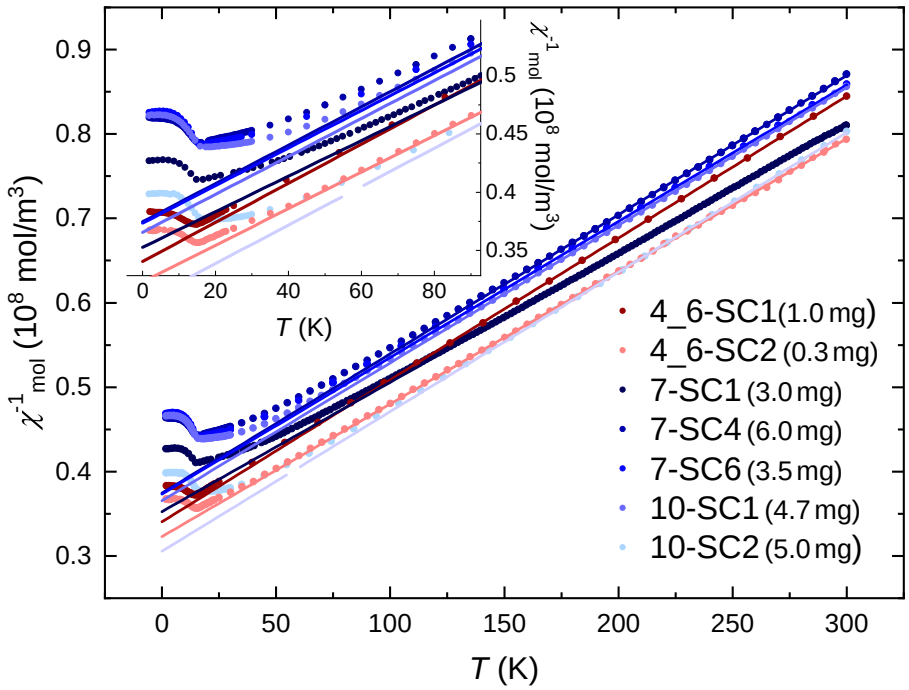

Figure 5.42.: Temperature dependent inverse susceptibility of different Na_2IrO_3 single crystals with short (red) and long (blue) holding times during the growth. The measurements were fit by a Curie-Weiss fit without a constant diamagnetic contribution from 150 K to 300 K. The fit functions were extended over the whole measured temperature range to show the deviation of the data from the fitting function.

In-plane anisotropy

The longitudinal in-plane anisotropy measurements were performed by Achouak Hassini [114]. For this experiment a rotator was inserted into the MPMS3 with the preliminary with Laue diffraction oriented sample NIOLi71. The magnetic background of the setup was measured beforehand. Since the background subtraction program that could subtract the raw data stopped working, only the resulting magnetization values of the background measurement were subtracted. The measurement was performed twice and each angle was measured in a forward and a background rotation. There were remarkably many data points, which showed jumps in the measured raw voltages at a temperature of 10 K and, hence, in the respective magnetization as well. These data points were excluded and, to enhance accuracy, the $\mu(\phi)$ curves were fit by one sine function[12] for the background and by the sum of two sine functions for the measurement of sample and background. The periodicity w was allowed to take values between 80° and 200°, since 90°, 120°and 180° were considered the only reasonable periodicities for sample and background. The

[12]The sine function used here had the form $\mu(\phi) = y_0 + A \cdot \sin(\pi \cdot (\phi - \phi_c)/w)$ with the fitting parameter being the amplitude A, the periodicity w, a shift in the magnetization y_0 as well as a shift in the angle ϕ_c.

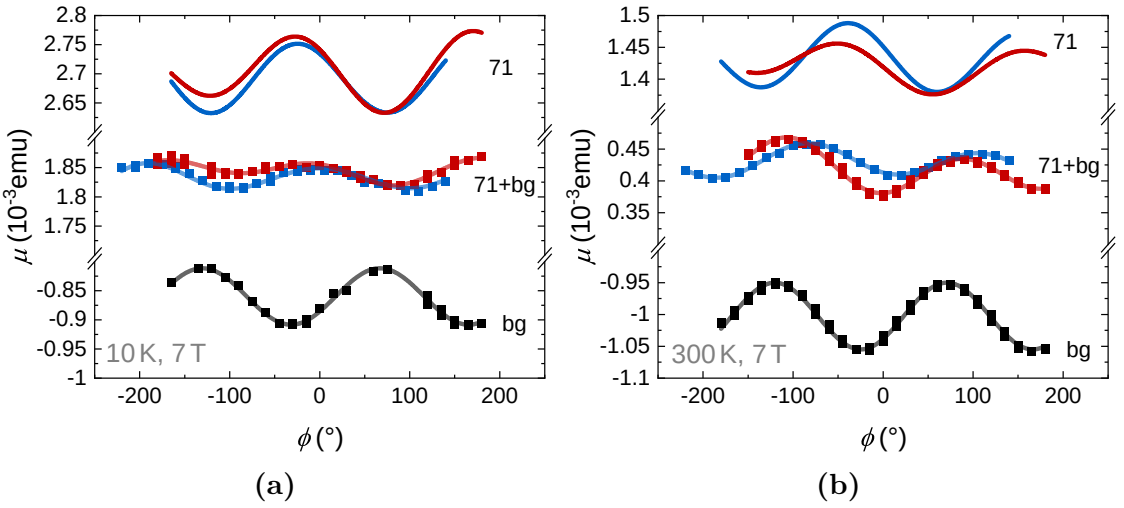

Figure 5.43.: Measurement of the longitudinal magnetic moment μ in dependence of the in-plane angle ϕ of the **rotator background**, **measurement 1** and **measurement 2** of sample and background (symbols). These data were fit by sine functions (transparent lines), which were subtracted from another to receive the pure sample signal (opaque lines) for a) 10 K and b) 300 K.

determined periodicity for sample and background was $w \approx 90°$. Afterwards, both fitting curves were subtracted to receive the pure sample magnetization. Although there were no problems with jumps in the raw voltage data for $T = 300\,\mathrm{K}$, the explained analysis procedure was repeated here to be consistent. The raw data of the magnetic moments $\mu(\phi)$ and the respective fits as well as the calculated sample signal are shown in Figure 5.43a and Figure 5.43b.

Figure 5.44a shows the final results for the susceptibility calculated from the calculated moments for temperatures of 10 K and 300 K, respectively. The sample was inserted in such a way that the 0° angle corresponds to the field being aligned perpendicular to an Ir-Ir bond, shown in Figure 5.44b. At $30° \pm 60° \cdot n$ ($n \in \mathbb{N}$) the magnetization is measured along Ir-Ir bonds (marked by arrows), which correspond to the edges of the honeycomb. The mean value of the susceptibility is around $2.18 \cdot 10^{-8}\mathrm{m}^3/\mathrm{mol}$ at 10 K and $1.15 \cdot 10^{-8}\mathrm{m}^3/\mathrm{mol}$ at 300 K. If we compare the suscep-

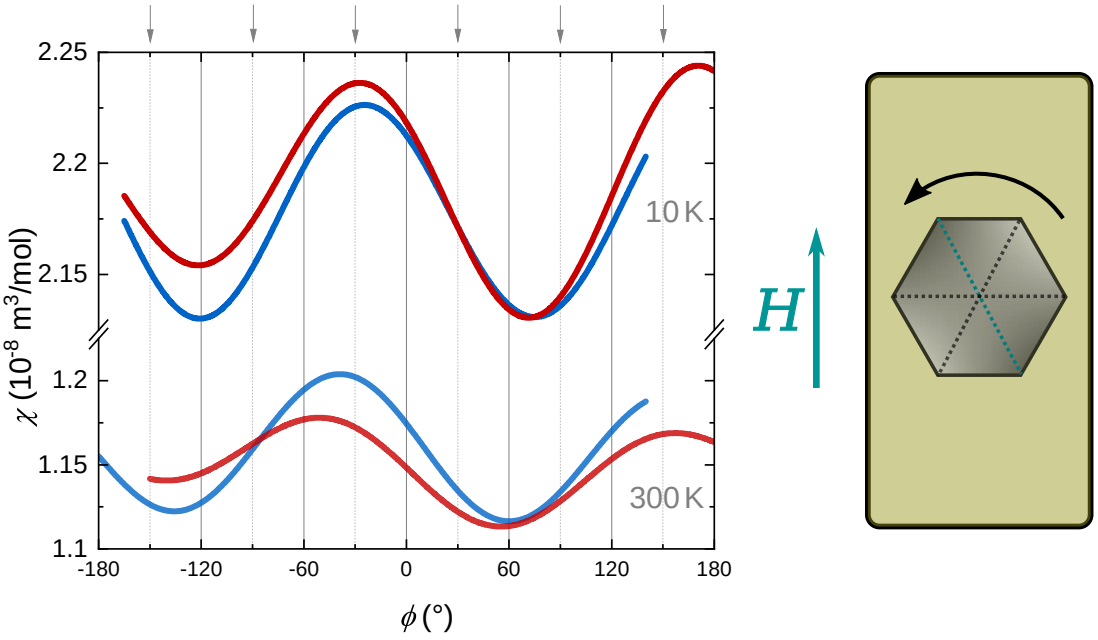

Figure 5.44.: a) Measurement of the in-plane susceptibility in dependence of the in-plane angle for two separate measurements (blue and red) at temperatures of 10 K and 300 K. b) Orientation of the Ir honeycombs at 0°. For $30° \pm 60° \cdot n$ ($n \in \mathbb{N}$) the magnetic moment is directed parallel to an Ir-Ir bond, which lie along the edges of the honeycomb. These angles are marked with arrows in a) and with dotted lines in b).

tibility of other Na_2IrO_3 crystals (Figure 5.41), the values for sample NIOLi71 are slightly smaller, but are located within the same range for both temperatures. The in-plane anisotropy is small with a difference in the susceptibility between easy axis and hard axis of only 4-6% in relation to the mean value. It looks like the easy axis is situated along one special Ir-Ir bond at an angle of ≈-30°/150°, which is colored turquoise in Figure 5.44b. From the findings of the Laue diffraction it is surprising to see any anisotropy at all. Since we find all three 120°-orientations in one crystal, the anisotropy should cancel out. Of course, this cancellation will not be perfect and some orientation is most likely dominating by a small amount, not detectable by the Laue diffraction. The intrinsic value of the in-plane anisotropy should, therefore, be much larger.

5.3.4 Transverse magnetization

Temperature dependence of the transverse moment

For several Na_2IrO_3 crystals the in-plane transverse magnetic moment has been measured. As we have learned from the Laue diffraction experiments (Section 5.3.2), Na_2IrO_3 samples do not only possess one distinct in-plane orientation, but show three orientations, which can be transformed into each other by 120° rotations. This would automatically lead to a vanishing signal in the transverse magnetization if all three orientations were to be found in an equal ratio. This is, fortunately, not always the case, which gave us the opportunity to at least study the quantitative development of the transverse magnetization in dependence of the temperature. The

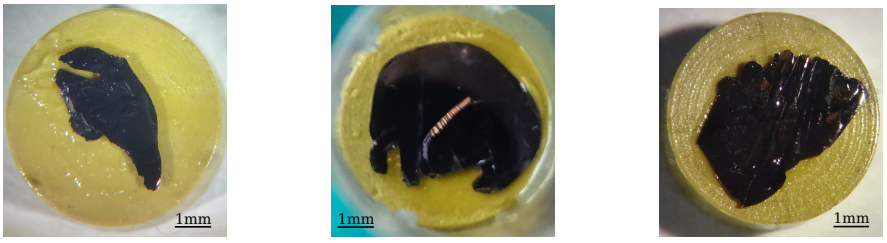

(a) NIOLi7-SC6 **(b)** NIOLi7-SC7 **(c)** NIOLi7-SC9

Figure 5.45.: Pictures of the samples, which were used for the transverse magnetization measurements, on the torlon disk.

in-plane anisotropy experiment (Section 5.3.3) already suggested that an excess of one orientation is possible. Nevertheless, only three out of eight samples showed a signal well above the background and the noise level of the MPMS, whilst showing the expected shape of symmetrized raw data at the same time. The results of these three samples NIOLi7-SC6 (3.54 mg), NIOLi7-SC7 (3.47 mg) and NIOLi7-SC9 (7.5 mg) will be presented here (Figure 5.45). These samples are extremely

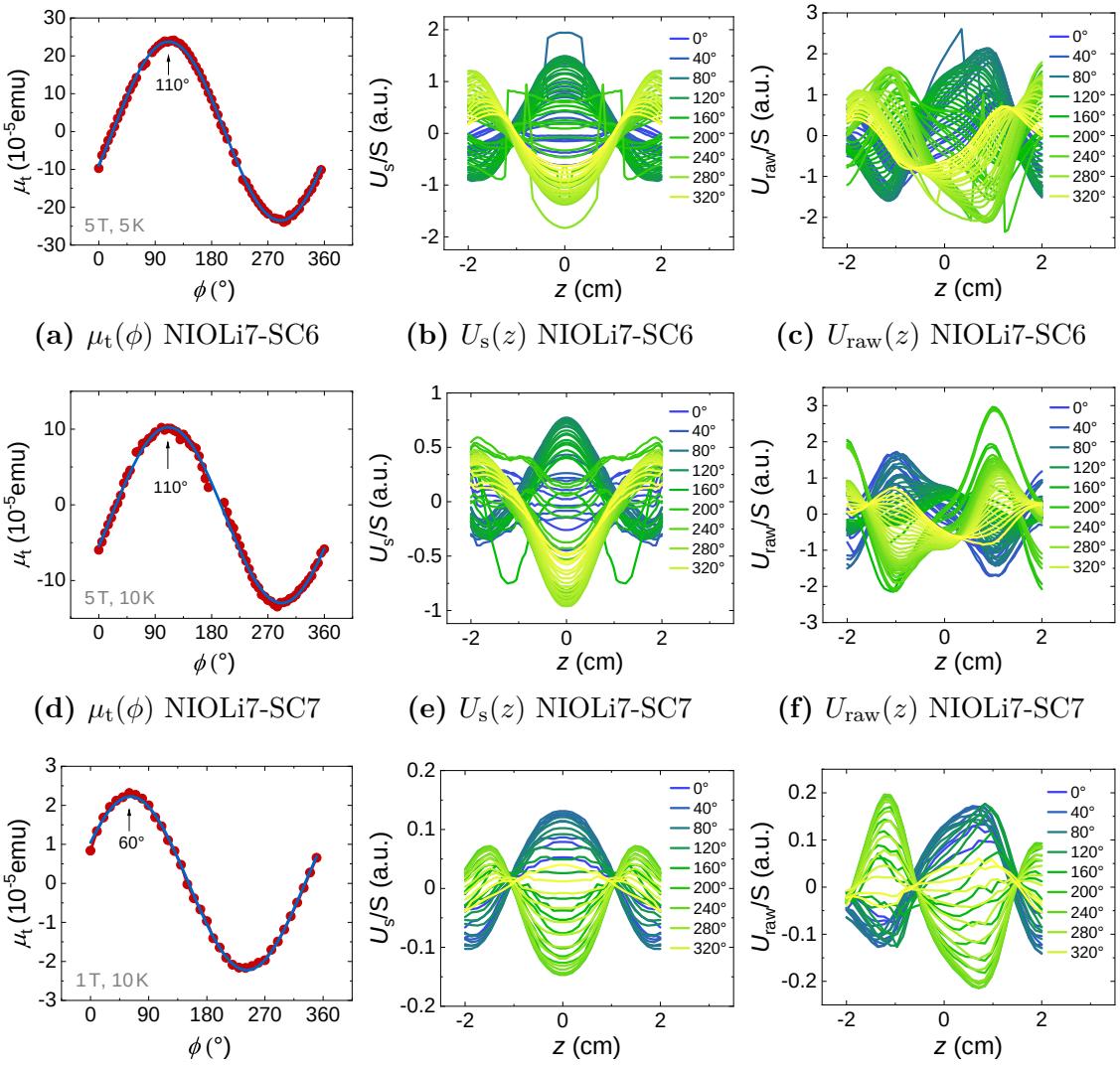

(a) $\mu_t(\phi)$ NIOLi7-SC6 **(b)** $U_s(z)$ NIOLi7-SC6 **(c)** $U_{raw}(z)$ NIOLi7-SC6

(d) $\mu_t(\phi)$ NIOLi7-SC7 **(e)** $U_s(z)$ NIOLi7-SC7 **(f)** $U_{raw}(z)$ NIOLi7-SC7

(g) $\mu_t(\phi)$ NIOLi7-SC9 **(h)** $U_s(z)$ NIOLi7-SC9 **(i)** $U_{raw}(z)$ NIOLi7-SC9

Figure 5.46.: The transverse magnetization in dependence of the in-plane angle for sample NIOLi7-SC6 (a), NIOLi7-SC7 (d) and NIOLi7-SC9 (g) as well as the respective symmetrized (b, e, h) and raw voltages (c, f, i). The marked angles in $\mu_t(\phi)$ correspond to the angles where the temperature dependent measurements were performed.

large crystals grown with the optimized crystal growth procedure presented in Section 5.3.1. The large mass increased the chance of a sufficiently large transverse magnetization signal and was an important criterion for the sample selection.

As a preparation for the transverse magnetization measurements the in-plane angle position of the maximal value corresponding to the transverse moment (called also the maximum angle or $\phi_{\max}$ hereafter) has to be determined. At this position, the full magnetic moment in the plane is captured. Figure 5.46 collects all $\mu_t(\phi)$ measurements and the respective symmetrized and raw voltage curves for the samples. The marked angles have been used for the $\mu_t(T)$ measurements and have been obtained by fitting the data to the sine function: $\mu_t(\phi) = \mu_0 + A \cdot \sin(\pi \cdot (\phi - \phi_c)/180°)$ with an amplitude A, an offset μ_0 and a phase shift ϕ_c. All three samples show an antisymmetric part in the raw data of roughly the same size as the symmetric part. The symmetrized curves show the expected curve shape: a large peak at 0 cm and two smaller ones around -2 cm and 2 cm as well as the intersection of all curves at roughly -1 cm and 1 cm. Two other samples were measured with reasonable large magnetic moment, but with modified shapes of the symmetrized curves. Such data was not trusted and excluded from further analysis. In order to perform temperature dependent experiments, a question that needs to be answered is whether the maximum angle changes with the temperature. For this reason $\mu_t(\phi)$ curves were measured at different T for NIOLi7-SC6. The results, normalized for an easier comparison, are collected in Figure 5.47. The data were fit, again, by the sine function: $\mu_t(\phi) = \mu_0 + A \cdot \sin(\pi \cdot (\phi - \phi_c)/180°)$.The maximum angle of NIOLi7-SC6 for $T \leq 100\,\mathrm{K}$ (the data above were too noisy for a reliable fit) and $\mu_0 H = 1\,\mathrm{T}$ ranges seemingly randomly between 119.5° and 122.5°, while the measurement at 5 T shows a clear difference of roughly 10° in comparison to the 1 T data. The maximum angle for NIOLi7-SC6 prior to the temperature-dependent measurements were pinpointed to 110° from the measurement of Figure 5.46a. Analyzing the data from Figure 5.47, most likely the real value of $\phi_{\max}$ for $\mu_0 H = 1\,\mathrm{T}$ would lie around 121°. The measurement at the smaller field was, therefore, performed at 96% of the maximal value of the magnetic moment. Since the maximum is very broad, we find that such small misalignments of the maximum angle do not change the absolute value strongly and the determination of the maximum angle at one temperature and one field is sufficient.

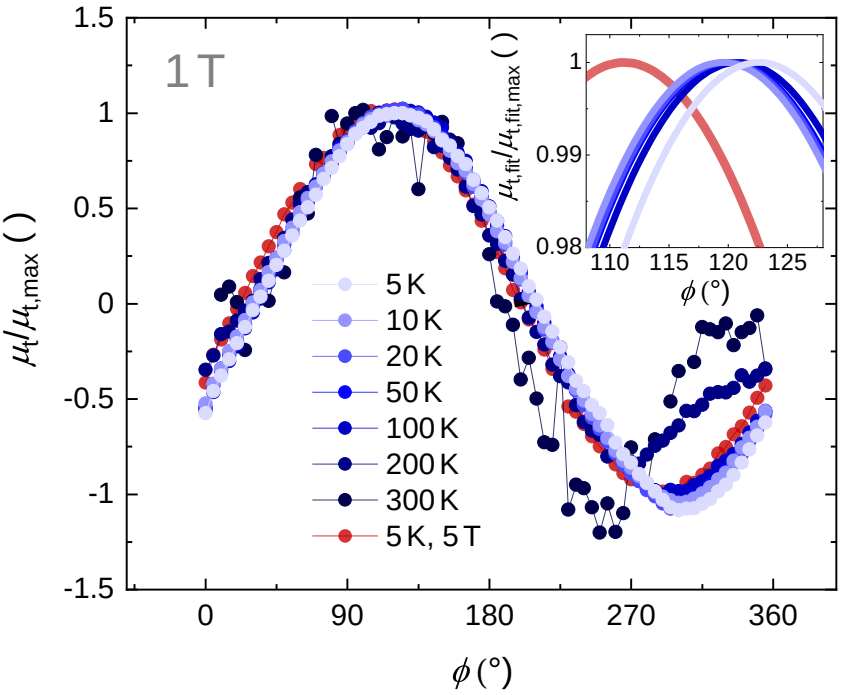

Figure 5.47.: The normalized transverse magnetic moment $\mu_t(\phi)/\mu_{t,\,max}$ at different temperatures of NIOLi7-SC6 at 1 T (blue symbols+thin lines). The measurement from Figure 5.46a at 5 K and a higher field of 5 T was added as well (red symbols+thin lines). The symmetrized transverse data were fit by a sine function and the fit functions (thick solid lines) around the maxima were enlarged in the inset. There seems to be a small effect in dependence of the magnetic field and no significant effect in the temperature dependence.

The temperature dependence of the transverse magnetic moments of NIOLi7-SC6, NIOLi7-SC7 and NIOLi7-SC9 are presented in Figure 5.48 for a field of 1 T. All raw data with jumps in the raw voltage were omitted. All curves were measured at the angle with maximal and/or minimal transverse magnetic moment. For better comparison was the moment multiplied by -1 for measurements at the minimum angle. NIOLi7-SC6 was the first sample measured and the only one, whose feature at low temperatures deviates from a simple maximum at roughly 22 K. Here, we find two maxima at 9 K and 25 K enclosing a minimum at 15.5 K. In the second measurement of NIOLi7-SC6 (m2) nine months later, this feature changed to a simple maximum. In $\chi(T)$ at 5 T one could interpret that the minimum has not vanished, but rather moved to 40 K. It is possible that only very fresh samples show the minimum at 15.5 K. In the 1 T measurement, however, such a feature is not found. Although the mass of NIOLi7-SC9 is more than twice as large as the other two samples, the

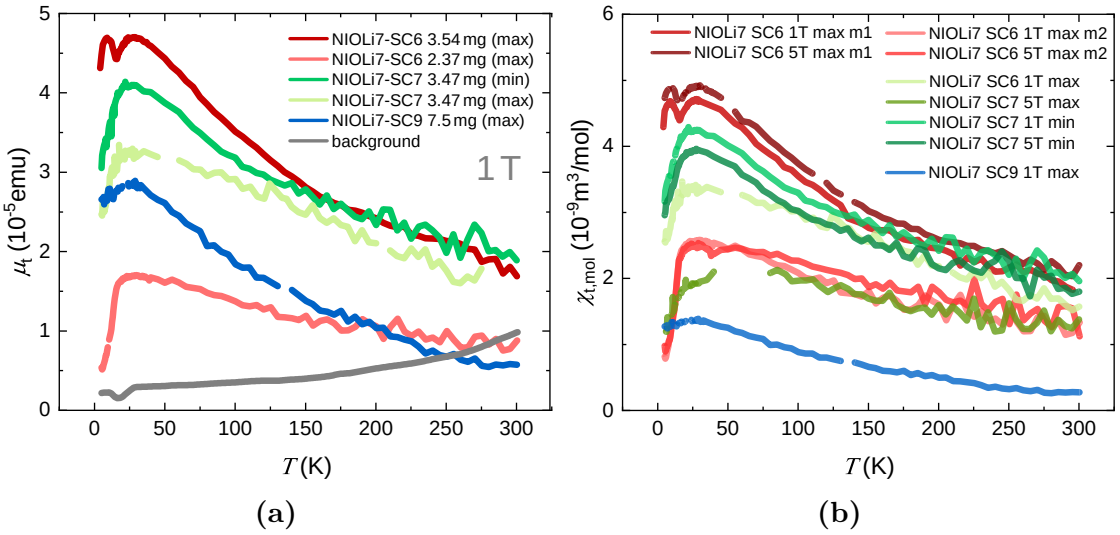

Figure 5.48.: a) Comparison of transverse magnetic moment with temperature for NIOLi7-SC6, NIOLi7-SC7 and NIOLi7-SC9. These measurements still include the background signal. As the gray background curve shows, the background becomes relevant at higher temperatures. NIOLi7-SC6 was measured twice, marked as m1 and m2. The second measurement was conducted nine months after the first one one a piece having 2/3 of the original sample mass. b) The resulting susceptibilities without a background subtraction for 5 T and 1 T.

transverse magnetic moment is significantly smaller. Nevertheless, the temperature dependence looks very similar to NIOLi7-SC6, which already suggests a constant offset due to different backgrounds. The temperature dependence of the transverse magnetic moment of NIOLI7-SC7 shows some similarity to the NIOLi7-SC6 m2. Additionally, in Figure 5.48a we see background data that have been obtained by calculating the average of the background curves of holder 0 and the shifted background curve of holder 3, show in Figure 5.11. It seems, from the two measurements, that the temperature dependence of the background is reproducible, but the absolute value depends on the phase shift of the $\mu(\phi)$ curve of the background (Figure 5.9 in comparison to the $\mu(\phi)$ curve of the sample. It is unclear so far what generates the transverse moment of the background. Further, we find varying maximum values for the different holders. With increasing temperature the ratio of the background moment to the sample moment is increasing. Since the background was only measured at 5 T and a linear behavior with the field was assumed, the data were divided by 5 in Figure 5.48a.

Figure 5.49.: Sample holder used for direct background subtraction.

To be able to analyze the data with a Curie-Weiss fit, the background must be removed. This has been done in two different ways. For the data of NIOLi7-SC6 and -SC9, the absolute values of the measured background from Figure 5.48 were subtracted. Since we now do not know the absolute value of the background for these specific measurements, there is still an unknown shift parameter. The best option would be to measure the sample and subsequently measure the background with the same setup after removing the sample. This method has been tried for NIOLi7-SC7. For this purpose, the background holder had to be changed to ensure an easy removal of the sample while making sure the background stayed unchanged. The new sample holder is shown in Figure 5.49. The straw is cut in two parts at $\sim$1 cm above the Torlon disk. There is a small cut at the lower end of the upper straw part. This way the lower part can be fixed by pushing it into the upper part. The clear disadvantage of this setup is that, although it easily withstands small impacts, strong collisions will lead to the loss of the lower part into the measurement device. Therefore, a careful mounting and dismounting of the sample chamber is strongly recommended. In this context, it seems clear that the measured temperature dependence of SC7 is different compared to the other samples, since the background itself is different. The raw background data were directly subtracted from the raw sample data. The results of both background subtraction methods are presented in Figure 5.50 in magnetic fields of 5 T and 1 T. To account for the unknown shift parameter of the background subtraction for NIOLi7-SC6 and -SC9, the data at 300 K were modified to match the data of NIOLi7-SC7. This, of course, only works if we assume the magnetization due to one (or two) dominating orientations to be similar. To check the background subtraction of NIOLi7-SC7, the resulting raw data were inspected. These are shown in the appendix in Figure B.7-B.9. The expected shape of the transverse raw data curves can be found in Section 5.1. Only the 1 T, min measurement as well as the 5 T, max for $T \leq 200$ K show reasonable curves and can, therefore be assumed to be reliable.

The background-corrected data are shown in Figure 5.50a. All samples start at the same point at 300 K, because we have decided to do this. This by no means must be true, but it is most likely closer to reality than the data prior to the background subtraction. All samples, excluding the first measurement of NIOLi7-SC6, show a

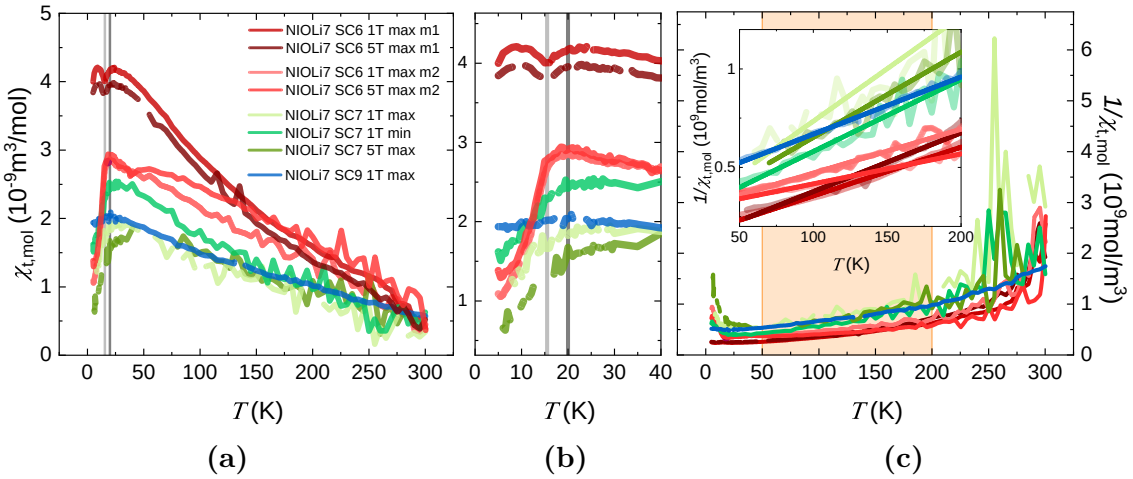

Figure 5.50.: a) The molar susceptibility in dependence of the temperature after the background subtraction. b) Zoom into the low temperature region with the magnetic transition. c) The inverse molar susceptibility and a Curie-Weiss fit of from 50 K to 200 K (inset).

very similar temperature dependence. Why the first experiment of NIOLi7-SC7 differs so strongly compared to the other measurements remains unknown. For most measurements the descent of the susceptibility towards lower T starts at 20 K (dark gray line) and for the second, third and fifth measurement we find a pronounced accelerated decrease at 15.5 K. This temperature corresponds to the magnetic transition found in the longitudinal experiments. The direct background subtraction of NIOLi7-SC7 has introduced an even large noise level at higher temperatures, which otherwise would have been the most trustworthy data due to the exact background measurement. Large jumps in the data have again been omitted. A Curie-Weiss fit (equation 2.6) has been performed between 50 K and 200 K on the inverse susceptibilities in Figure 5.50b. Above 200 K the data strongly deviate from a linear behavior and the noise level drastically increases for all samples. The results of the fitting parameter are collected in Table 5.5.

For further analysis, we neglect the first measurement of NIOLi7-SC7 (1 T, max), which was found to show an altered symmetrized voltage shape as well as the last of NIOLi7-SC6 (5 T, max, m2), which exhibits a kink at roughly 50 K. These measurements also show the most extreme values for C. With the remaining fitting parameters, we find a weighted average molar Curie constant of $\overline{C} = (3.7 \pm 0.2) \cdot 10^{-7}\ \frac{\mathrm{Km}^3}{\mathrm{mol}}$ ($\mu_{\mathrm{eff}} = 0.49\,\mu_{\mathrm{B}}$) and a Weiss temperature of $\overline{\theta_{\mathrm{W}}}$ =(-70±20) K. The results closest to reality should be the measurements of NIOLi7-SC7 at 1T, min and 5 T, max. If we

NIOLi7-SC	$6_{m1,1T}$	$6_{m1,5T}$	$6_{m2,1T}$	$6_{m2,5T}$	$7_{1T,max}$	$7_{1T,min}$	$7_{5T,max}$	9_{1T}
C ($10^{-7}\frac{Km^3}{mol}$)	4.04(4)	3.36(5)	4.49(7)	6.6(1)	1.9(4)	2.7(2)	2.3(3)	3.44(4)
θ_W (K)	-44(2)	-27(3)	-111(4)	-173(5)	-40(30)	-60(20)	-50(20)	-130(3)

Table 5.5.: Collection of all fitting parameters, the molar Curie constant C and the Weiss-temperature θ_W, of all samples. The curves from Figure 5.50c were fit with the Curie-Weiss formula in the temperature interval from 50 K–200 K.

just consider these two measurements the resulting parameter are $C = 2.5 \cdot 10^{-7} \frac{Km^3}{mol}$ ($\mu_{eff} = 0.40\,\mu_B$) and $\theta_W = 55\,K$. Here, the background of the measurement was determined right after the experiment with the same setup and the raw data were subtracted with the raw data of the background. In comparison to the other measurements of SC7, the background subtraction lead to reasonably shaped raw data. Nevertheless, these numbers should not be taken too seriously, but should rather be seen as a rough estimate of these magnetic parameters for Na_2IrO_3.

If we compare the measurements of the transverse magnetization of Na_2IrO_3 and α-$RuCl_3$, the measurements of α-$RuCl_3$ have shown a transverse moment of one order of magnitude larger in comparison to Na_2IrO_3. Although both systems display three different domains, which should weaken the transverse signal to a great extend, the samples of α-$RuCl_3$ had two advantages in comparison to the Na_2IrO_3 samples. One, the crystals for α-$RuCl_3$ showed drastically larger thicknesses along c^*, which resulted in roughly one order of magnitude larger masses and respectively larger moments. Second, the anisotropy of the systems leads for measurements along $H \parallel c^*$ for α-$RuCl_3$ to a smaller longitudinal contribution (H is parallel to the hard axis) and for Na_2IrO_3 to a larger longitudinal contribution (H is parallel to the easy axis). Although the longitudinal contribution is subtracted during the data analysis, it increases the signal-to-noise ratio for Na_2IrO_3 in comparison to α-$RuCl_3$. These reasons made the measurements of α-$RuCl_3$ a priori easier and more precise. Further, the transverse moment and, hence, the respective off-diagonal terms for Na_2IrO_3 might just as the results suggest be smaller than for α-$RuCl_3$. This was proposed by most theoretical models in Section 4.3.3.

Crystallographic orientation of the transverse moment

One major question was the orientation of the transverse moment in the plane of Na_2IrO_3. We can estimate the orientation of the transverse moment from the first measurement of NIOLi7-SC6, which was analyzed by Laue diffraction.

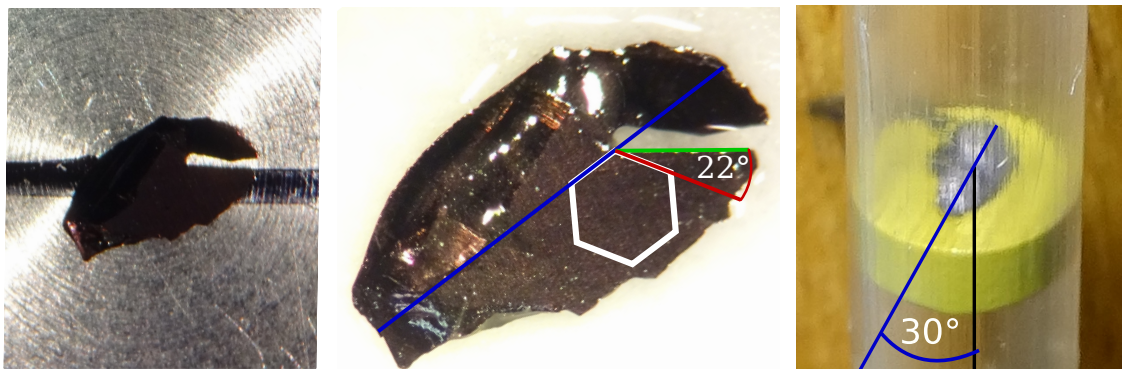

(a) **(b)** **(c)**

Figure 5.51.: Orientation determination of the transverse magnetic moment of NIOLi7-SC6. a) The sample on the Laue holder. The black line marks the horizontal line, aligned on a sharp edge of the sample. b) Orientation of the honeycomb in the sample determined by Laue diffraction. At 22° rotated clockwise starting from the green line (black line in (a)), the first honeycomb edge was identified (red line). c) Orientation of the sample in the MPMS. The blue line marks the same direction as the blue line in b) and the black line corresponds to 90° in the MPMS coordinate system.

Here, the horizontal axis of the Laue goniometer was aligned to a very distinct edge of the sample (black line in Figure 5.51a). Although the measurement found three different orientations to be present, they all share the same orientation of the edges of the honeycomb due to the 120° angle difference between the orientations. The respective Laue measurements revealed an angle between one of the Ir–Ir bonds to the horizontal axis of 22° (back side) and −21°[13] (front side). With a picture of the sample in the sample holder prior to the measurement, the orientation of the sample in the MPMS could be determined (Figure 5.51c). This procedure will give the largest contribution to the error. The blue connection line corresponds to the blue line in (Figure 5.51b), which itself lies along the direction of a honeycomb edge. The black line in Figure 5.51c corresponds to the direction of 90° in the MPMS coordinate system. The blue line is rotated by 30° clockwise in respect to the black

[13]The sample was turned around, therefore the angle must have the opposite sign.

line. Together with the observed maximum in $\mu(\phi)$ at $\sim$121° for $\mu_0 H = 1\,\mathrm{T}$, the picked honeycomb edge direction (blue line) is at an angle of 241°in the MPMS coordinate system. At 242° one of the two gaps of the transverse pick-up coils was identified. This points to the fact that the transverse moment is not directed along an Ir–Ir bond/ honeycomb edge, but rather orthogonal to them.

Including all the errors resulting from the alignment of the sample, especially from the estimation of the sample direction in the MPMS as well as the error from the fit of $\mu(\phi)$, gives an estimated total error of ±7°. If the direction of the magnetic moment really changes with enhanced magnetic fields as it was observed for the 5 T measurement ($\sim$10° difference), has to be determined in further experiments.

5.4 $(Na_{1-x}Li_x)_2IrO_3$

In the last section of this chapter, we will talk about Li-doped Na_2IrO_3. One can substitute up to 25% of Na with Li. Two series of batches with different doping levels were synthesized: NIOLi2b and NIOLi11. The former series was characterized by LA-ICP-MS and this results will be presented first. Additionally, XRD measurements were analyzed to look at the dependence of the lattice parameter on the Li-content. In the end, the magnetization of samples with different doping level were measured in the MPMS in the in-plane as well as the out-of-plane direction.

Chemical characterization

The chemical analysis of $(Na_{1-x}Li_x)_2IrO_3$, especially in regard to the Na/Li ratio, is not trivial. The two standard methods used in our research group, EDX and ICP-MS, cannot be applied. EDX measurements do not detect Li and Na only with a significant error, while no solvent has been found capable of dissolving the compound for the ICP-MS. To obtain the correct doping level of the batches, five samples of each batch were send to the University of Bremen, where they were measured with Laser-ICP-MS. Here, a 35 µm pulsed laser beam with 1 $\mathrm{GW/cm^2}$ power density and a pulse rate of 5 Hz was used to divide the compound into its parts. The ICP worked with a power of 1200 W and high resolution measurements of Li7, Na23 and Ir191 were performed. Undoped samples of Na_2IrO_3 and Li_2IrO_3

served as a reference for the measurement. The results are presented in Figure 5.52. All samples showed a higher Li-content than intended. This is not surprising, since

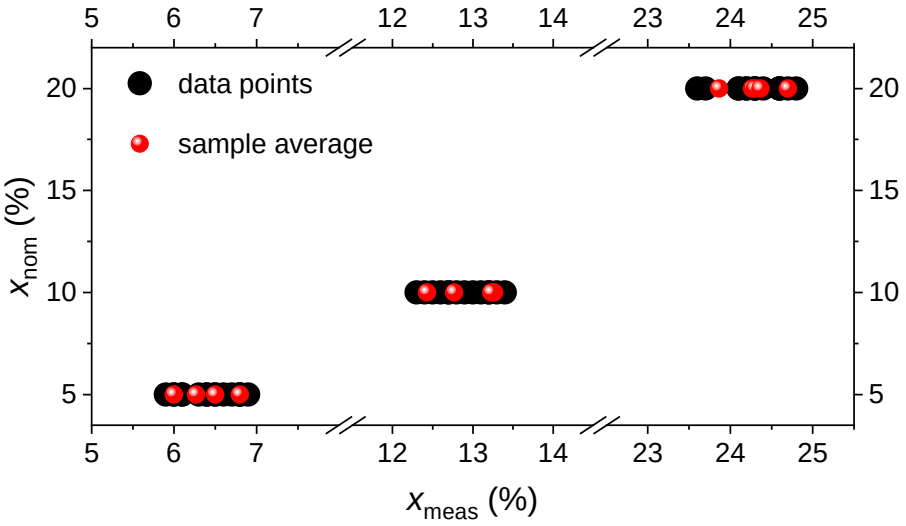

Figure 5.52.: Results of the LA-ICP-MS measurements of NIOLi2b. Each sample was measured three times (black dots) and from these a sample average was calculated (red dots).

the starting material included a 10% Li-excess, while there was no excess of Na. This made no sense and must be attributed to a lack of knowledge in the very beginning of this thesis. Nominal $x = 5\%$ turned out to be around 6.4%, $x = 10\%$ around 12.9% and $x = 20\%$ around 24.3%. It seems the opposite might be reasonable. Since the difference between measured and nominal Li-doping is even larger than the 10% Li-excess, one could consider a small excess of Na. The doping concentration x of the samples of one batch do not vary strongly. The standard deviation between the mean values of the samples of one batch were found to be less than 0.4%. For simplicity, the doping concentrations were rounded in the following to 6%, 13% and 24%.

For the second doping series NIOLi11, no Li-excess was added to the starting material. We assume that the samples have the nominal doping concentration with an estimated error of 2% based on the measurements of NIOLi2b.

Development of the *c*-axis

With doping the lattice parameters change. The length of the *c*-axis can be accessed by powder X-ray diffraction on a single crystal. Here, the height of the sample must be considered using equation 3.2 from the "Experimental Methods" chapter. Figure 5.53 compares the results to the measured *c*-parameter of Manni et al.[101]. The measurement data agree well with the literature data and show the same dependence with Li-doping. The more Li the material contains, the smaller is the *c*-parameter. This is not surprising since the Li ion is smaller than the Na ion. However, the dependence is not very strong.

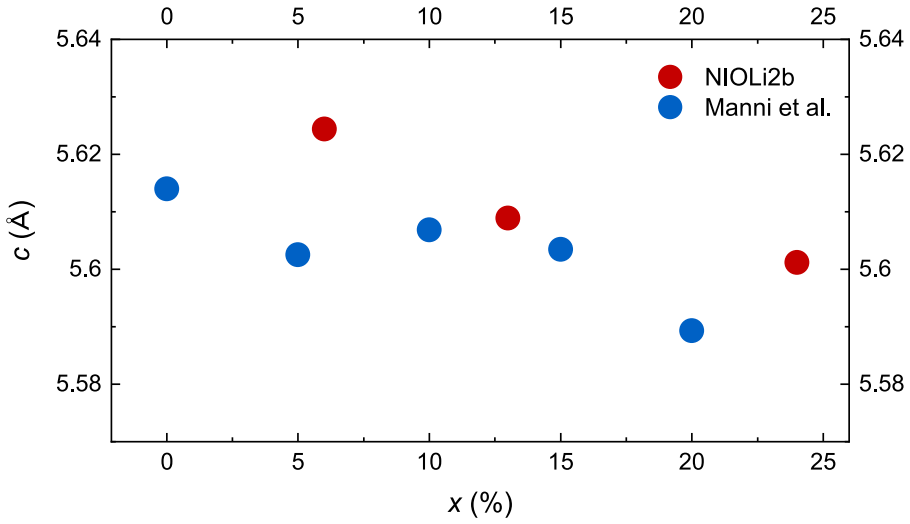

Figure 5.53.: Development of the *c*-parameter of $(Na_{1-x}Li_x)_2IrO_3$ single crystals from the doping series NIOLi2b (red) in dependence of the doping concentration x compared to the literature data in [101] (blue). The more Li is incorporated into the structure, the smaller c becomes. The measured values agree well with the literature data.

In-plane/out-of-plane anisotropy

The in-plane/out-of-plane anisotropy is known to be large for Na_2IrO_3 and α-Li_2IrO_3. What has not been known so far was the development of the magnetic anisotropy with Li-concentration, which is shown in Figure 5.54 in dependence of temperature T for a magnetic field of $\mu_0 H = 7\,\mathrm{T}$. The in-plane orientation of the samples is unknown, but we know from Section 5.3.3 that the in-plane anisotropy

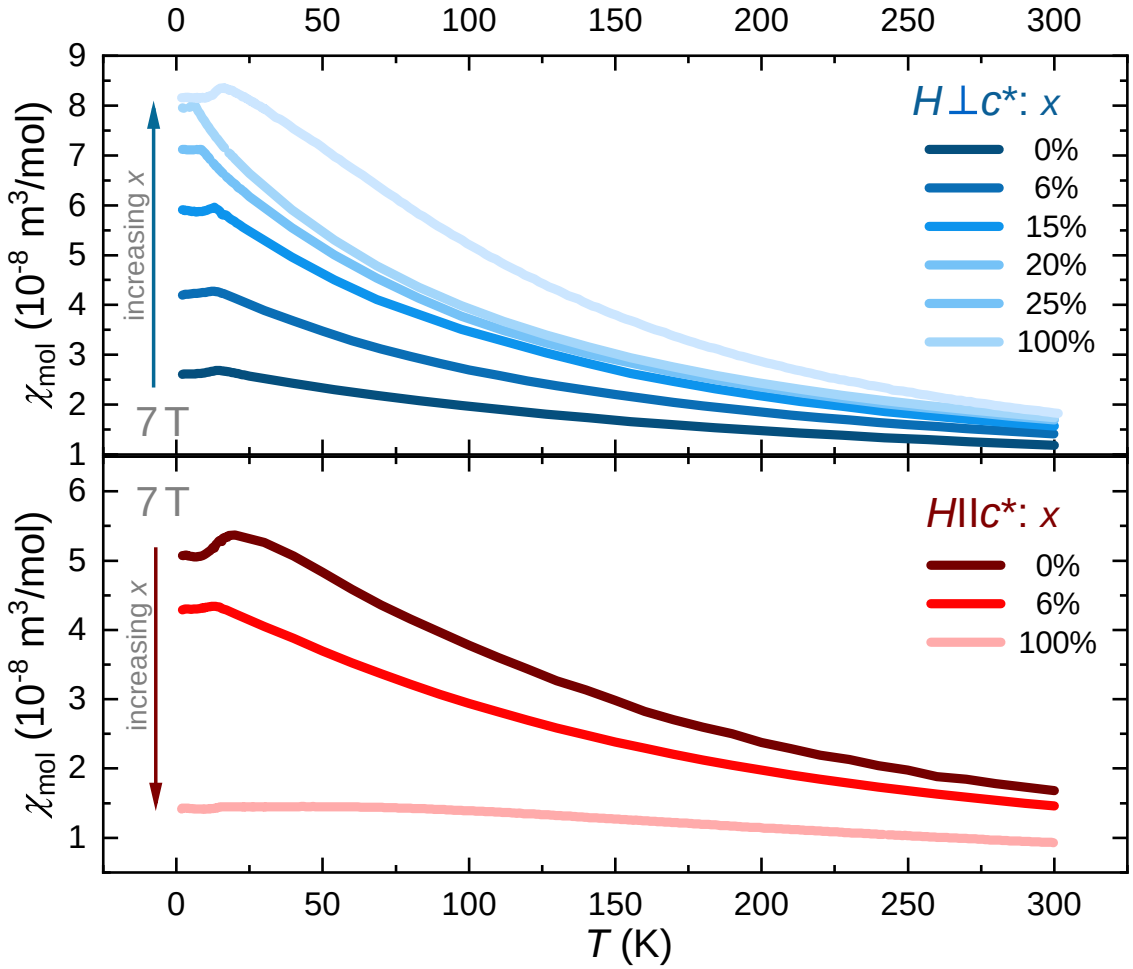

Figure 5.54.: Magnetic susceptibility of $(Na_{1-x}Li_x)_2IrO_3$ single crystals for different doping concentrations in dependence of the temperature, measured with a magnetic field of 7 T applied orthogonal (upper figure) and parallel to c^* (lower figure). The absolute value of $\chi(T)$ increases in the former and decreases in the latter case. The magnetic transition (maximum), additionally, shifts to lower T with increasing doping level, excluding pure Li_2IrO_3. The data for Li_2IrO_3 ($x = 100\%$) were taken from [78].

only gives a small error (assuming it does not change significantly with doping). The transition temperature of $(Na_{1-x}Li_x)_2IrO_3$ decreases with increasing Li-doping for both measurement directions. Furthermore, the anisotropy decreases with doping and already at roughly $x = 6\%$, both measurement directions show very similar magnetization values. For doping levels $x > 6\%$ we expect a reversed anisotropy as it is found for α-Li_2IrO_3. To measure samples in this regime with the field applied parallel to c^* turned out to be challenging. The typical approach to measure these samples was the usage of a quartz holder with some GE Varnish to glue the sample onto the

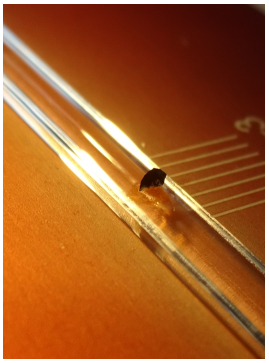

Figure 5.55.: Sample holder and sample for a measurement with $H \parallel c$.

holder. Here, only the glue gave a background signal, significant especially at lowest temperatures. To subtract this background for an easier determination of T_N, the Varnish was measured beforehand and the raw data were subtracted afterwards. For measurements along c^* the sample had to be aligned on the holder on a very thin edge (see Figure 5.55). This worked sufficiently well for samples with $x = 0\%$ and 6%. For samples with higher Li-content the glue could not hold the sample in place anymore. Instead the sample always bend in the direction of the easy plane, delivering a magnetization which contained both directions with an unknown ratio. To achieve the desired results a different setup with a torlon disk in a straw (as it has been used for the transverse magnetization measurements) had been tested. A sample with $x = 25\%$ was measured with this technique. To put the sample on the torlon disk after the background measurement, the disk had to be removed from the straw and, on the right place, reinstalled afterwards. To reproduce the exact same background is difficult. Therefore on the second try with a 15% Li-doped sample, the straw was cut above the torlon disk (as it had been done for the transverse magnetization of NIOLi7-SC7) to simplify the deposition/removal of the sample. The disadvantage of the torlon disk is the significantly larger background. For every measurement the raw data of the background had been subtracted from the sample measurement data. The results are unconvincing. The temperature dependence does not fit well to the rest of the measurements. Of course, the data could still be valid, but an error regarding the background measurement seems more likely. The measurements can be found in the appendix in Section B.7. Nevertheless, the simple fact that the sample turns out of the c^*-direction strongly suggests a reversal of the anisotropy above x=6% as it is found for α-Li_2IrO_3.

The field-dependent magnetization has been measured as well. All measurements showed a linear behavior after the background subtraction. Since they give no further insights, they are omitted here. Examples are shown in the appendix in Section B.7.

The linear part of the magnetic susceptibility above the magnetic transition can be fitted to the Curie-Weiss law (equation 2.6) to extract the Weiss temperatures Θ_W, which are correlated to the temperatures at which the frustrated system would

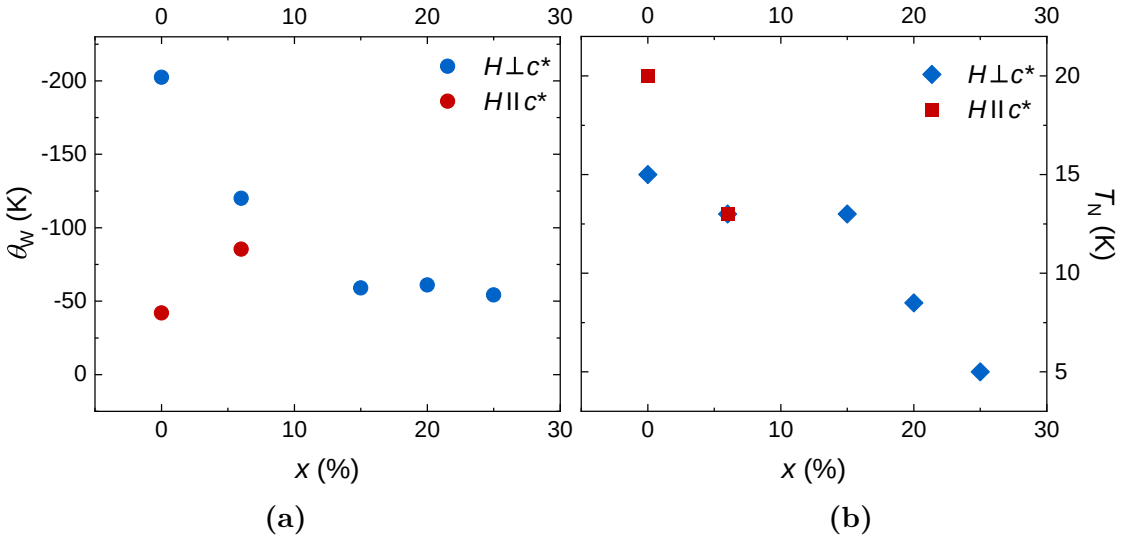

Figure 5.56.: Comparison of the Weiss temperature Θ_W and the actual ordering temperature T_N in dependence of the doping level x. Due to the frustration in $(Na_{1-x}Li_x)_2IrO_3$, we find $|\Theta_W| >> T_N$. For both field directions, T_N decreases with increasing Li-content. The same trend can be found for Θ_W with an in-plane magnetic field, while the data for a field parallel to c^* suggest an opposite development.

like to order. The chosen temperature range is 150 K to 300 K. The development of Θ_W is then compared to the actual ordering temperature T_N in Figure 5.56. T_N was determined from the maximum position of the susceptibility, following the approach described in [101]. Just as for undoped samples in Section 5.3.3 the Curie-Weiss fit was performed with and without a temperature-independent contribution χ_0 and the results without χ_0 found to be more reasonable(a respective explanation is given in Section B.5). The magnetic parameters Θ_W and μ_{eff} obtained from the corresponding fits as well as the determined transition temperatures are collected in Table 5.6. The errors stem from the fitting and my own discretion, respectively. For comparison are the fitting parameters with χ_0 listed in the appendix in Section B.5 and the respective fitting curves for Table 5.6 in Section B.7. While the absolute value of the Weiss temperature is decreasing with increasing x for fields aligned in-plane ($H \perp c^*$), the data for fields orthogonal to the plane ($H \parallel c^*$) suggest an increase of Θ_W. However, the change for doping levels $x \geq 15\%$ is minimal and might as well point to a constant Weiss parameter in this regime. T_N, on the other side, is decreasing with increasing x up to the maximal Li-concentration. Both developments agree well with the measurements of Manni *et al.*[101], where lumps of arbitrary oriented single crystals were measured. It strikes the eye that the transition

x (%)	0	6	15	20	25	0	6
T_N (K)	15(1)	13(2)	13(1)	8.5(5)	5.0(5)	20(2)	13(1)
Θ_W(K)	-202.4(6)	-120(1)	-59(2)	-61(2)	-54.2(5)	-42(2)	-85.4(7)
$\mu_{eff}(\mu_B)$	1.945(2)	1.942(4)	1.890(5)	1.975(5)	1.982(2)	1.911(8)	1.894(4)

Table 5.6.: Magnetic parameters T_N, Θ_W and μ_{eff} of the samples from Figure 5.54 for a magnetic field $H \perp c^*$ (blue) and $H \parallel c^*$ (red).

temperatures for $x = 0\%$ of the two field direction diverge. This results from the fact that the measurements for these two data points stem from two different samples[14], which is not the case for 6%. Many different undoped samples have been measured and the ordering temperature varied between 15 K and 20 K between them. Reasons for this large deviation are unknown and are suspected to lie in the different amount of faults in the structure. The effective moment does not seem to be affected by the exchange of Na and Li. It varies randomly between values of $1.89\mu_B$ and $1.98\mu_B$. All these values lie significantly above the spin-1/2 value of 1.73. This is another clear hint of the deviation of Na_2IrO_3 and $(Na_{1-x}Li_x)_2IrO_3$ from the Kitaev model.

[14]Both samples stem from the same batch.

6 | Summary and Outlook

This thesis has started with four different questions regarding the synthesis of Na_2IrO_3 as well as the magnetic behavior of α-$RuCl_3$, Na_2IrO_3 and $(Na_{1-x}Li_x)_2IrO_3$. The answers found in this work are summarized in the following.

The mass of the Na_2IrO_3 single crystals grown by the optimized growth process have successfully been multiplied by a factor of ten and more compared to the single crystals grown with the previously known growth. Within 17 days the crystals showed 2 mm to 5 mm (or even 8 mm) in length and weights of several mg. A recipe was presented that generally should produce crystals of unlimited sizes. The most important factors have turned out to be the filling factor of the crucible as well as the time at the holding temperature $T = 1050°C$. The longer the prepared Na_2IrO_3 powder is kept at this temperature, the larger single crystals grow. However, they seem to decompose again as soon as the polycrystalline starting material supply is exhausted. The experiments show that the crystals grow roughly 0.3 mm per day. The growth was shown to start above 1000°C, which makes a slow heating below this temperature unnecessary. Additionally, the temperature gradient within the crucible was estimated to be 0.6°C/mm. To enhance the gradient might be a useful tool to speed up the crystal growth process and reach sufficiently large crystals in smaller times. The analysis of powder diffraction measurements on single crystals with different times t at 1050°C suggest smaller deviations within samples of the same t and closer values to the literature value for $t > 300$ h. A comparison of longitudinal magnetization experiments on samples with short and long growth times revealed a difference in the shape of the susceptibility curve above the structural ordering. Single crystals with long growth times deviate at significant higher temperatures from the linear Curie-Weiss behavior of $\chi_\parallel^{-1}(T)$ than single crystals with shorter growth times. Additionally, the longer grown single crystals showed a tendency to

slightly higher transition temperatures T_N. To answer the question whether the crystalline quality is better for the single crystals with long growth times further experiments are needed, but the results presented in this work suggest that the quality is not lowered by the larger size.

Furthermore, the degradation of Na_2IrO_3 powder in air was analyzed and surprisingly, no clear sign of degradation could be found after leaving the sample for three months in air. Only in the last measurement, after roughly four months, a significant reduction of the Na_2IrO_3 peaks and the emergence of new peaks was observed. This is highly contradictory to the measurements of other groups ([83, 84]). Possibly, the degradation process strongly depends on the air humidity. Krizan *et al.* [83] showed that the degradation only takes place in the presence of H_2O. While humidity is low for the winter months, it increases towards summer. The experiments of the other groups might have been performed during the summer time with a high water concentration in the air. Another reason could be a smaller crystal size or a worse quality of the powder measured in [83] and [84].

XRD patterns showed that at 17.1° a peak appeared for single crystals and high-quality powder with a size of roughly 4% in relation to the main [001] peak, which is not described by the literature. It could not be identified with a foreign phase and evolves with the enhancement of the powder quality. The origin could be a part of the crystal with a smaller c-parameter like the areas with Na-deficiency found in [116].

The in-plane anisotropy measurements revealed a small anisotropy of roughly 5% magnetization difference between easy and hard axis in relation to the mean value. Laue experiments revealed that Na_2IrO_3, just as α-$RuCl_3$ [87], shows the three domains, which originate from the almost perfect 120° symmetry of the crystal structure in the plane. Since Na_2IrO_3 at $\mu_0 H = 7\,\mathrm{T}$ is far from saturating, it can be assumed that for the most part, the moments from the different orientations will cancel each other out. It can, therefore, be assumed that the intrinsic anisotropy of Na_2IrO_3 is larger than it has been observed here.

I succeeded in repeating the reported measurements of the longitudinal and transverse temperature-dependent susceptibility of α-$RuCl_3$ with the magnetic field $H \parallel c^*$. An additional measurement of the transverse susceptibility for $H \perp c^*$ as well as measurements of the transverse susceptibility in dependence of the field at differ-

ent temperatures for both measurement directions have been performed. While the longitudinal susceptibility agrees well with the literature data, the transverse susceptibility for $H \parallel c^*$ only follows the literature data qualitatively, showing a sample dependence even between the α-$RuCl_3$ samples studied in this work. The reason is most likely the presence of three different domain types in α-$RuCl_3$ [87], which will be differently distributed for each sample. Hints for the presence of the domains are also found in the field-dependent measurements. When the field is applied parallel to c^*, we find a linear increase of the moment. For fields perpendicular to c^*, the linear contribution is still there, but is superimposed by another contribution showing a maximum in the ordered phase. This maximum might result from the redistribution of the domains as described in [87]. The temperature dependence of χ_t of this measurement direction shows an unexpected strong increase towards lower temperatures below T_N, which emphasizes that something unusual happens in this regime. However, the qualitative behavior of the transverse susceptibility for $H \parallel c^*$ follows the behavior of the longitudinal measurements. Unlike the transverse susceptibility reported in [21], the susceptibility strongly deviates from a linear behavior in dependence of the temperature. It would be interesting to further study the transverse moment with fields aligned in the *ab* plane. If the sample's orientation would be known due to Laue measurements, the influence of different in-plane field directions could be analyzed and further conclusions of the movement of the moments be drawn.

The measurement of the transverse susceptibility of Na_2IrO_3 turned out to far more challenging. Only some of the largest crystals showed a significant signal to be used for further analysis. Although the samples match the α-$RuCl_3$ samples in length in the *ab* plane, the length in c^*-direction is drastically reduced compared to α-$RuCl_3$, which leads to a much smaller transverse signal. Since we also have the presence of the three domains in Na_2IrO_3, the measured moment will be a small fraction of the intrinsic value. Two different ways to subtract the background have been tried, none of them leading to a convincing result. Still, the results point to a reduced transverse susceptibility of Na_2IrO_3 in comparison to α-$RuCl_3$. Since the measurement signals are so low, the background subtraction is an essential part in gaining reasonable data of the transverse moment for Na_2IrO_3 and could be further optimized. Additionally, one could try to enhance the size of the signal by stacking equally oriented samples on top of each other. The determination of the direction of the measured transverse moment was attempted and found to be orthogonal to

one of the honeycomb edges, which corresponds to the a-axis of one domain. Since we do not know if the moment results from the sum of the moment of two different domains, this result should be taken with caution. It would be very interesting to measure the transverse moment of Na_2IrO_3 with a field applied parallel to the plane. Exactly as for α-$RuCl_3$, different field directions could be analyzed to see if the arrangement of the domains of Na_2IrO_3 changes as well.

Interestingly, the anisotropy between in-plane and out-of-plane measurement direction changes quite drastically when we replace Na with Li in $(Na_{1-x}Li_x)_2IrO_3$. While the susceptibility of the for $x = 0$ easy axis direction $H \parallel c^*$ decreases, it increases for $H \perp c^*$. Already at a doping concentration of $x = 6\%$ they possess almost the same size. While the susceptibility for $H \perp c^*$ is continuously increasing up to the highest doping concentration, measurements at higher doping concentrations for $H \parallel c^*$ have not been successful due to rotations of the sample in the field away from this orientation. This observation, however, strengthens the claim that the anisotropy above $x = 6\%$ reverses to the anisotropy found in α-Li_2IrO_3. The change in the anisotropy can also be seen in the opposite development of the Weiss temperature for the two measurement directions. The transition temperature T_N was found to be continuously decreasing with increasing doping concentration x down to 5 K for $x = 25\%$. In further studies, the measurements could be repeated with doped single crystals grown by the optimized growth. Due to larger moments, the problems with the background would be reduced and further measurements, e.g., specific heat experiments could be performed on them.

This work has done its part to expand the knowledge about the Kitaev model candidates α-$RuCl_3$, Na_2IrO_3 and $(Na_{1-x}Li_x)_2IrO_3$. The torch is no passed to future researchers to continue the journey of understanding their magnetism.

A | Additional Information

A.1 List of acronyms

FM ferromagnetism/ferromagnetic

AFM antiferromagnetism/antiferromagnetic

PM paramagnetism/paramagnetic

TM transition metal

L ligand

CVT chemical vapor transport

Pert. Theo. second order perturbation theory

QC quantum chemistry methods

ED exact diagonalization

DFT density functional theory total energy

t/U exp. t/U expansion

mod. ab initio modified ab initio model

SGP standard growth process

maximum angle angle in $\mu_{\mathrm{t}}(\phi)$ measurements, where the transverse moment is maximal

A.2 List of starting materials

material	purity [%]	company	type
Na_2CO_3	99.998	Alfa Aesar	powder
Li_2CO_3	99.998	Alfa Aesar	powder
Ir	99.95	ChemPUR	powder
Li	99	Alfa Aesar	granules
$RuCl_3$	unknown	Alfa Aesar	powder

Table A.1.: Used starting materials for the synthesis.

B | Additional Data and Measurements

B.1 Crystal sizes of NIOLi12 batch 1–5

The sizes of selected crystals were measured via pictures taken from the crucibles after the growth steps. It was aimed for the largest crystals visible. Figure B.1 shows the pictures of batch 1 after the first step at T =1050°C for 60 h, after the last small

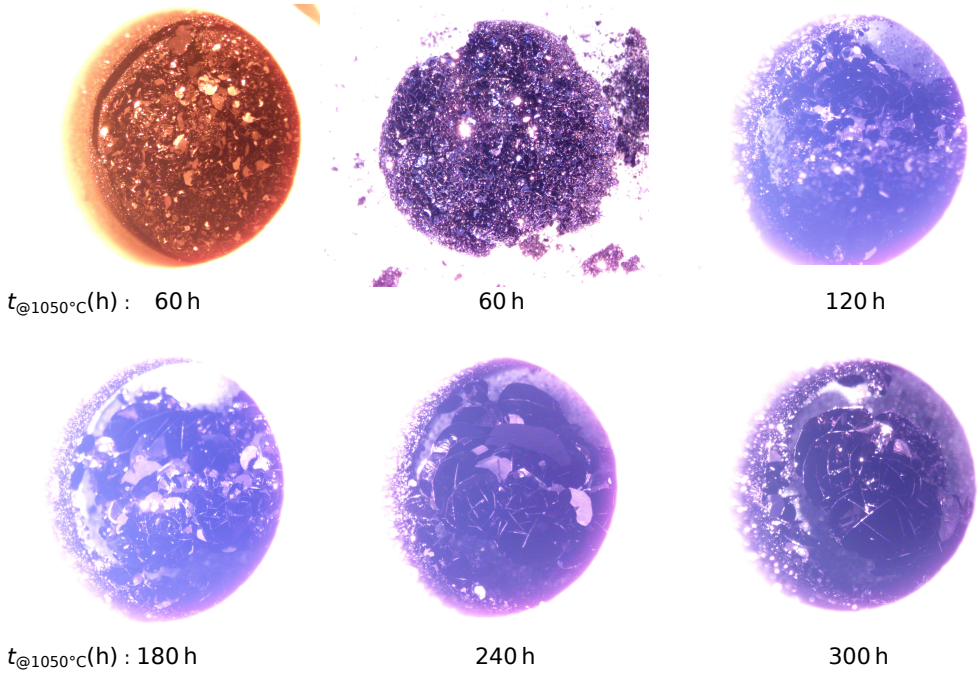

Figure B.1.: Pictures taken from Franziska Breitner of NIOLi12_1 after several growth steps, which had been used to analyze the development of the crystals size with the time, which the crucible was kept at $T = 1050$°C.

heating from 1000°C to 1050°C (which was also counted as 60 h at 1050°C) and after each following heating step at 1050°C, which were all used for the analysis in Figure 5.23a. The respective pictures for the analysis of Figure 5.23b from the end of the growth process of batch 2–5 are shown in Figure B.2.

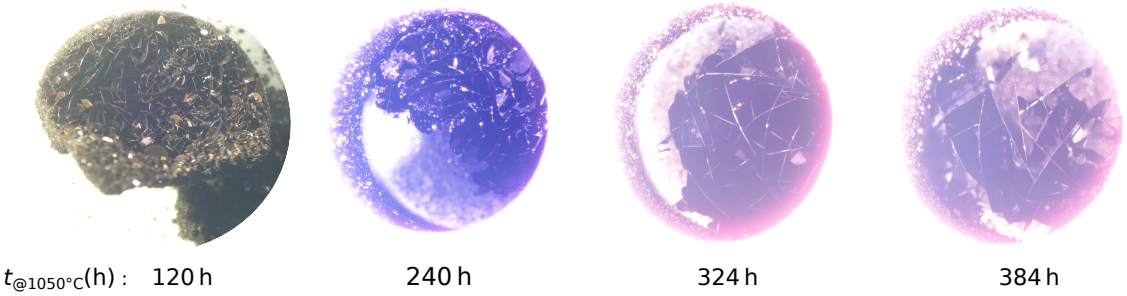

Figure B.2.: Pictures taken from Franziska Breitner of NIOLi12 batch 2–5 after the growth process, which had been used to analyze the development of the crystals size with the time, which the crucible was kept at $T = 1050°C$.

B.2 XRD patterns of Na_2IrO_3 single crystals from Friedrich Freund

The in section 5.3.2 discussed peak shape of the $[00l]$ peaks of Na_2IrO_3 single crystals can be seen in diffraction patterns of Friedrich Freund (formerly EP VI, University Augsburg) as well. Figure B.3 shows 6 different measurements of single crystals in the powder diffractometer, zoomed on the $[00l]$ peaks.

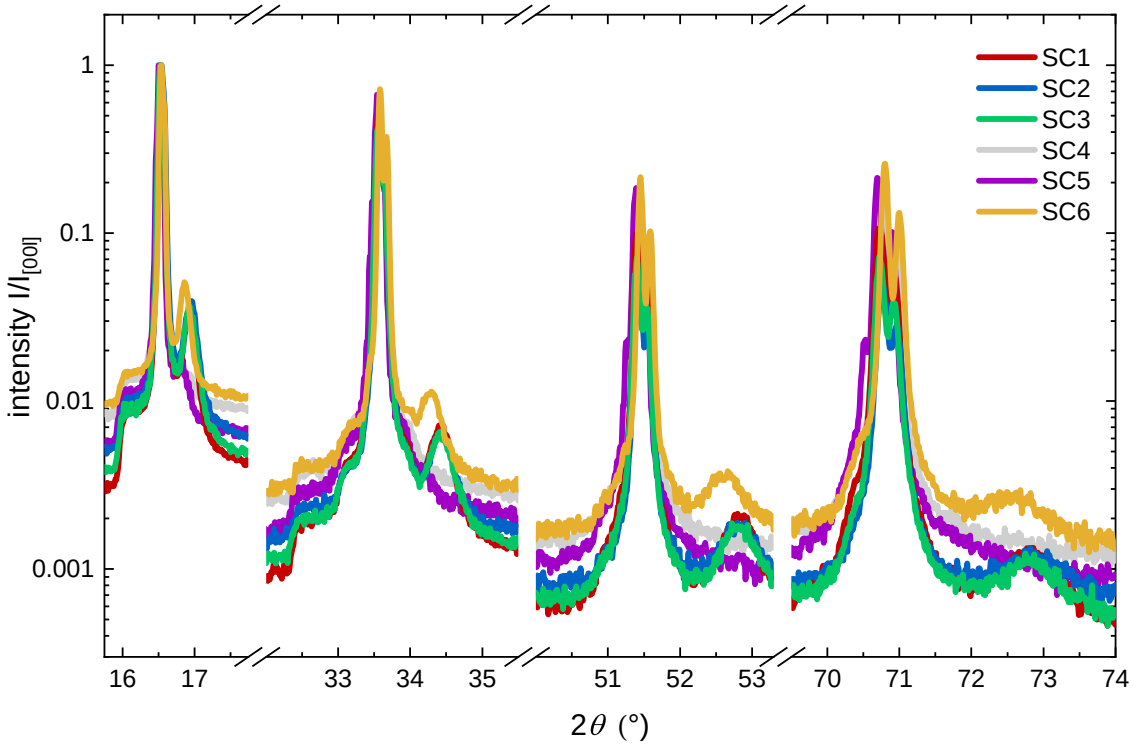

Figure B.3.: Diffraction patterns of Na_2IrO_3 single crystals grown and measured by Friedrich Freund. Four out of six samples show the described extra peaks on the right side of the $[00l]$ peak.

B.3 Laue diffraction patterns of Na_2IrO_3 single crystals

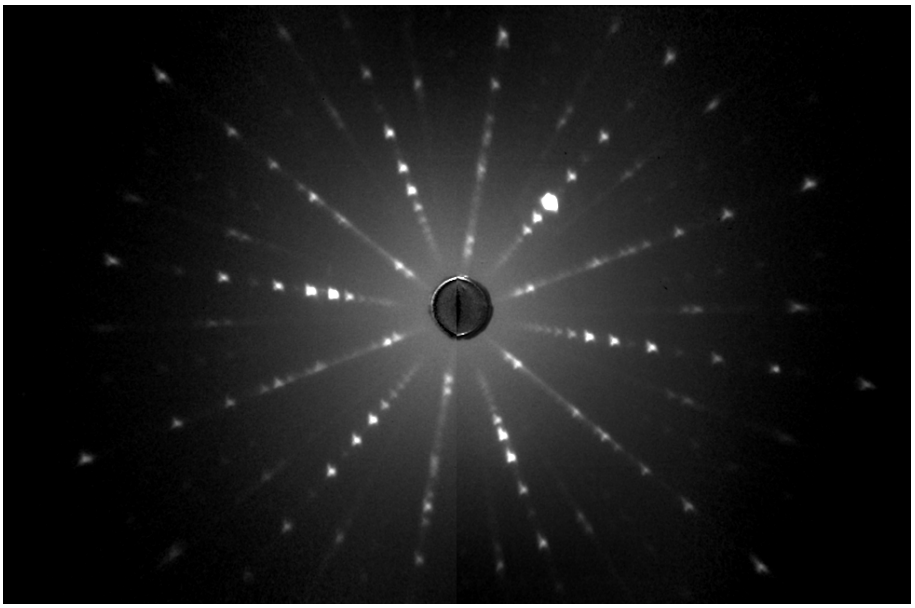

Figure B.4.: Laue diffraction pattern of NIOLi72.

Laue diffraction was also performed on many Na_2IrO_3 single crystals. Achouak Hassini measured NIOLi72 (Figure B.4)in the course of her bachelor thesis [114]. This diffraction pattern was analyzed in the same manner as the pattern for NIOLi7-SC6 in the main text of this thesis. Figure B.5 shows the three possible orientations of the crystal after a first alignment to the calculated diffraction pattern. Most reflections points that are not covered by the calculated pattern have been found for sample NIOLi7-SC6 as well (circles with red contours) and most are also covered by at least one of the possible orientations (green circles). This gives the impression that all three orientations are present.

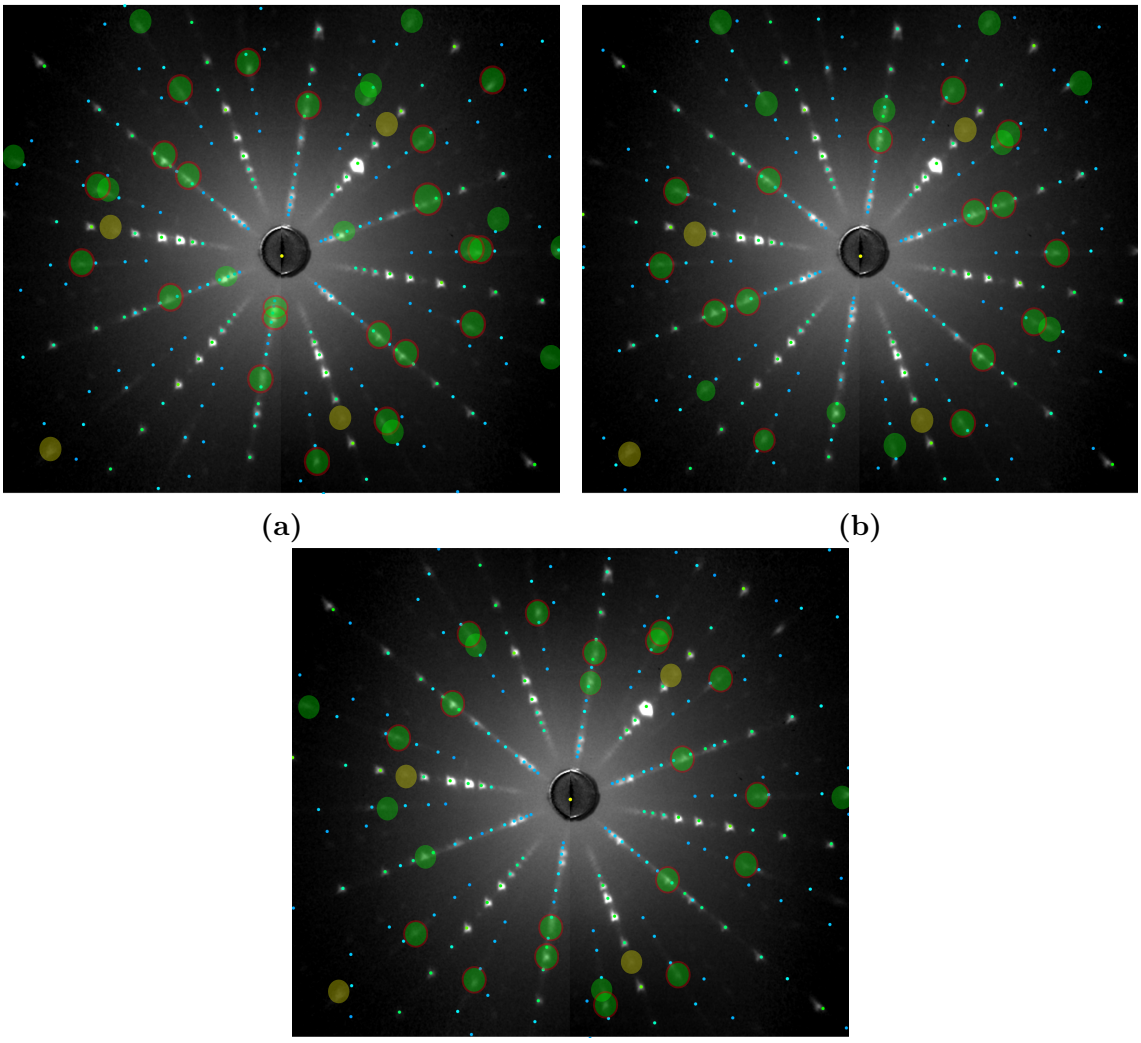

(a) **(b)**

(c)

Figure B.5.: The three possible orientations for the sample 72. The literature Laue pattern is intensity coded from red (highest intensity) to dark blue (lowest intensity). All reflections, which were not captured by the literature pattern were colored. Green colored reflections were matched by the literature pattern by at least one candidate, while yellow colored reflections were not. For all candidates many points are not covered. Nevertheless, most of them are covered by at least one candidate, which gives the impression that all three orientations are present here. Circles with red contours have been found for sample NIOLi7-SC6 as well.

B.4 Easy determination of a one-domain Na_2IrO_3 single crystal with Laue diffraction

In Figure B.6 a comparison of a rotation of 60°, 90° and 180° to the starting pattern is shown. The red starting pattern is overlapped with the blue rotated pattern. Where the reflections of both orientations overlap, the color turns violet. The red pattern is oriented in the same way as in Figure 5.38a in Section 5.3.2. Due to the symmetry of the system, we find a rotation angle of 60° as well as of 180° leads to one distinct crystallographic direction showing a complete overlap of the reflections, making this direction easy to detect. In the case of a 180° rotation, this coincides with the direction of the b-axis. This offers an interesting way to a fast and easy determination the b-axis of a Na_2IrO_3 single crystal without having to use a special program. One would measure the crystal in an arbitrary in-plane orientation and repeat the measurement after a 180° rotation around c^*. These diffraction pattern can later be overlapped to identify the orientation. A requirement for this method would be a very good adjustment of the c^* direction in the middle of the diffraction pattern.

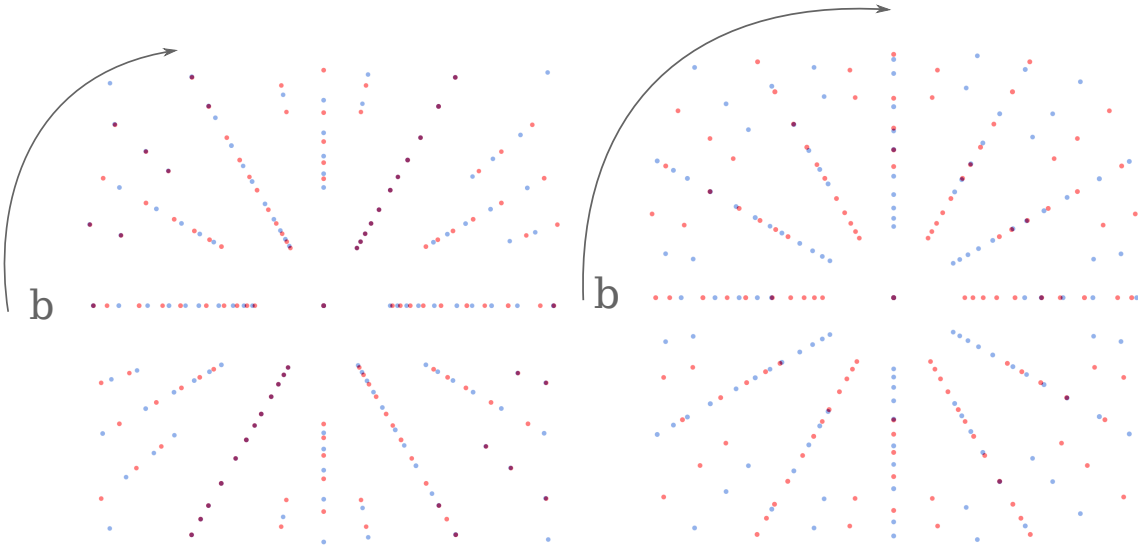

(a) 60° rotation **(b)** 90° rotation

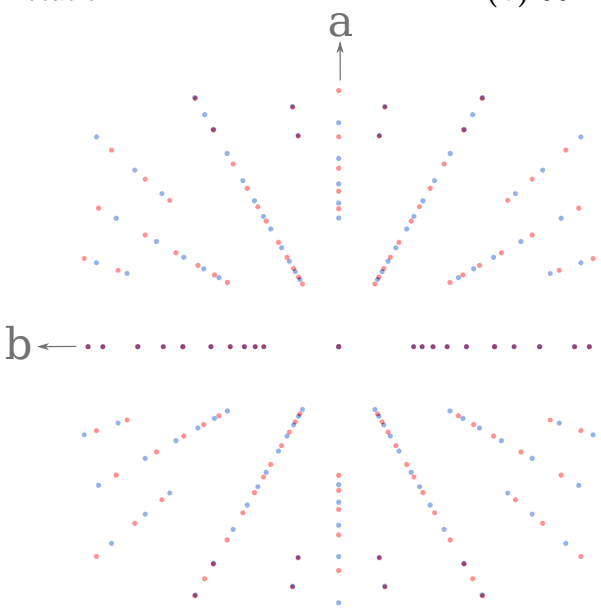

(c) 180° rotation

Figure B.6.: The red pattern calculated from [54] is compared to the same pattern in blue rotated clockwise around a) 60°, b) 90° and c) 180°. Where the reflections of both patterns overlap turns the color of the reflections to violet. The pictures where created by the combination of the software programs CrystalMaker and SingleCrystal.

B.5 Longitudinal magnetization of $(Na_{1-x}Li_x)_2IrO_3$

When fitting Curie-Weiss behavior, typically a temperature independent factor χ_0 is added to account for a negative diamagnetic contribution (of the sample or the background) or a positive van Vleck term due to excitations into higher energy states [2, p.30]. This method has the potential danger that part of the paramagnetic behavior is attributed to χ_0, which changes the other magnetic parameter like the Weiss temperature θ_W and the effective moment μ_{eff}. It was found that for the Curie-Weiss fits on samples of doped and undoped $(Na_{1-x}Li_x)_2IrO_3$ χ_0 varied between $-8 \cdot 10^{-9}$ and $1{\cdot}10^{-9}$ and the other magnetic parameter between the samples varied strongly as well. Fitting curves without χ_0 showed a more consistent picture for doped and undoped samples and these were, therefore, included in the main part of the thesis. This section presents the respective fitting parameter with inclusion of a temperature independent term in Table B.1 for Na_2IrO_3 and in Table B.2 for $(Na_{1-x}Li_x)_2IrO_3$. Compared to the fit without a temperature independent

sample	4_6-SC1	4_6-SC2	7-SC1	7-SC4	7-SC6	10-SC1	10-SC2
Θ_W (K)	-204(6)	-204(20)	-227(2)	-287(2)	-267(4)	-256(4)	-216(6)
μ_{eff} (μ_B)	1.95(3)	2.01(5)	2.02(1)	2.227(9)	2.14(2)	2.12 (2)	2.11(3)
χ_0 (10^{-10} $\frac{m^3}{mol}$)	-1(2)	10(40)	1.0(5)	-17.9(6)	-11(2)	-10(2)	-11(2)

Table B.1.: Comparison of the magnetic parameters Θ_W and μ_{eff} of different Na_2IrO_3 samples with inclusion of a temperature independent contribution χ_0.

contribution χ_0 (Table 5.4), the parameters vary more drastically, although the overall trend for θ_W is similar.

x (%)	0	6	15	20	25	0	6
Θ_W (K)	-204(6)	-98(4)	-47(7)	-70(10)	-58(3)	-60(20)	-104(3)
μ_{eff} (μ_B)	1.95(3)	1.82(3)	1.81 (5)	2.03(7)	2.01(2)	2.0(1)	2.01(2)
χ_0 (10^{-10} $\frac{m^3}{mol}$)	-1(2)	11(2)	8(5)	-6(8)	-3(3)	-10(20)	-11(2)

Table B.2.: Magnetic parameters Θ_W, μ_{eff} and χ_0 of the samples from Figure 5.54 for a magnetic field $H \perp c^*$ (blue) and $H \parallel c^*$ (red). The values were obtained via a Curie-Weiss fit including the temperature independent contribution χ_0.

B.6 Additional transverse magnetization measurements

Raw data of NIOLi7-SC7 before and after the background subtraction

To obtain the correct transverse magnetic moment of NIOLi7-SC7 the sample holder was measured with and without sample and both measurements subtracted from each other. To ensure that the setup is inserted unchanged after the removal of the sample, the sample holder setup was changed and a larger background accepted. If the background subtraction was successful, the shape of the symmetrized sample voltage signal is expected to show a shape as found for example for the symmetrized data in Figure 5.7. To prove this, the symmetrized voltage curves of all measurements of NIOLi7-SC7 are shown in Figure B.7–B.9 before and after background subtraction. The measurement at the minimum of the $\mu_t(\phi)$ curve at 1 T as well as the measurement at the maximum at 5 T for $T \leq 200$ K fulfill this criterion. Here, one can assume the obtained data to be reliable.

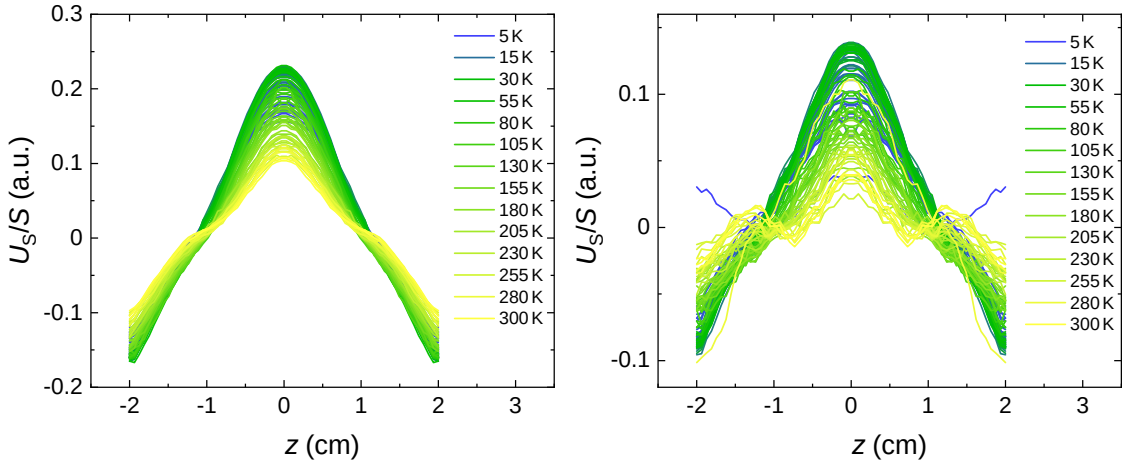

Figure B.7.: Symmetrized voltage data of NIOLi7-SC7 at the maximum in $\mu_t(\phi)$ and at $H = 1$ T a) before background subtraction and b) after background subtraction.

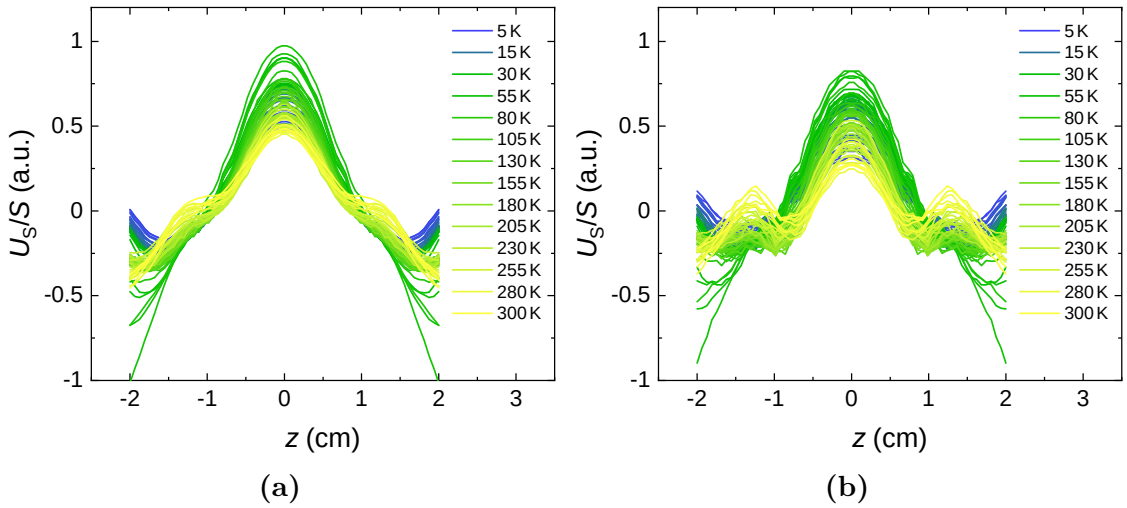

Figure B.8.: Symmetrized voltage data of NIOLi7-SC7 at the maximum in $\mu_t(\phi)$ and at $H = 5\,\mathrm{T}$ a) before background subtraction and b) after background subtraction.

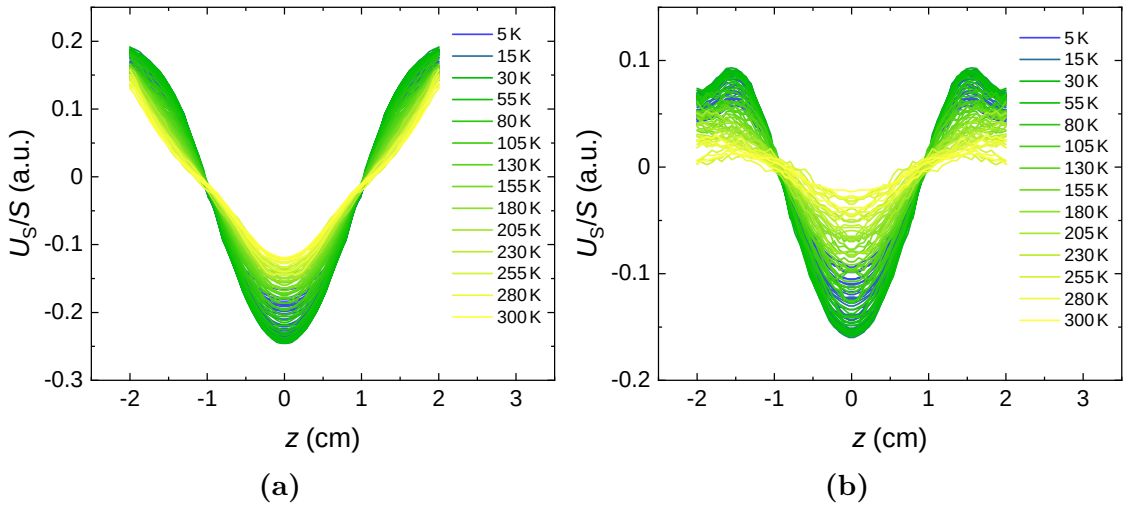

Figure B.9.: Symmetrized voltage data of NIOLi7-SC7 at the minimum in $\mu_t(\phi)$ and at $H = 1\,\mathrm{T}$ a) before background subtraction and b) after background subtraction.

B.7 Doping series $(Na_{1-x}Li_x)_2IrO_3$

Temperature-dependence of the susceptibility

To measure the temperature dependence of the susceptibility of $(Na_{1-x}Li_x)_2IrO_3$ single crystals for $H \parallel c^*$ and $x > 6\%$ has turned out to be challenging. Figure B.10 compares the measurements of the different doping levels for this field direction.

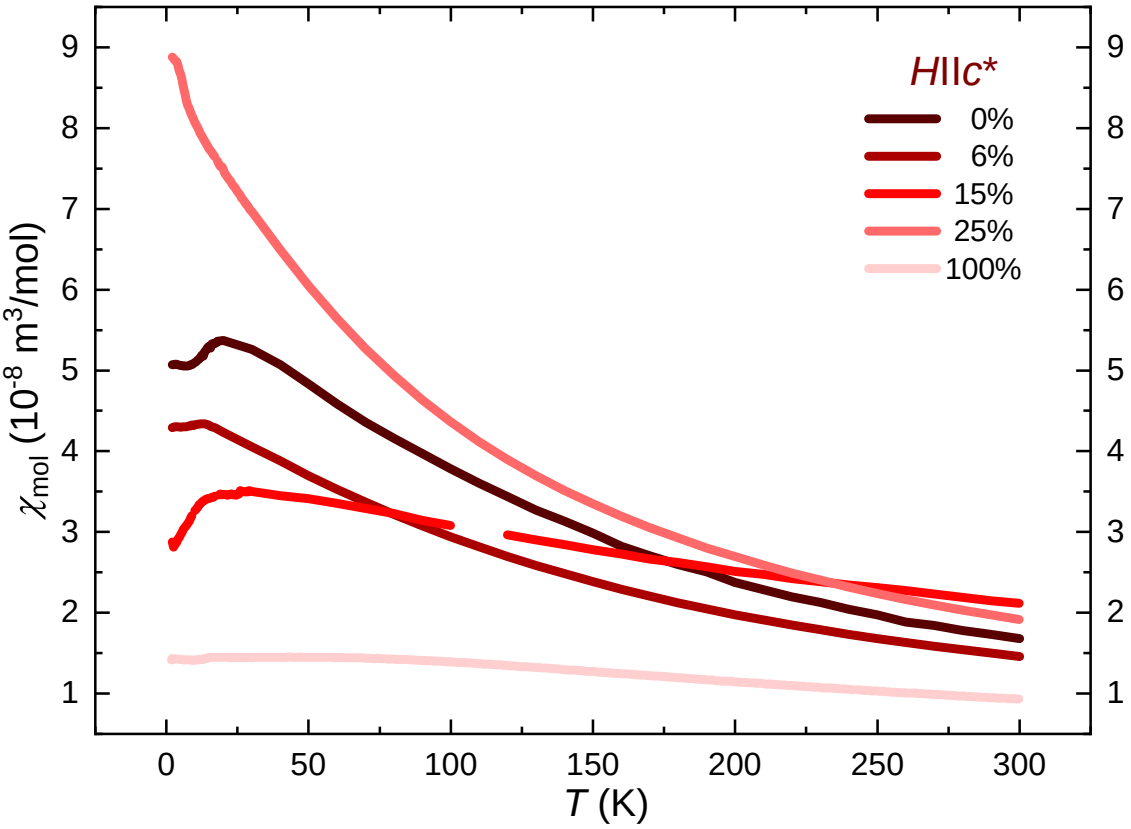

Figure B.10.: The susceptibility in dependence of temperature for doped $(Na_{1-x}Li_x)_2IrO_3$ crystals with the magnetic field parallel to the c^*-axis. While 0%, 6% and 100% were measured with a quartz rod and GE Varnish with a very small background, 15% and 25% were measured with a Torlon disk in a straw. For all measurements the raw background data were subtracted from the raw data of sample and background. It strikes the eye that the latter measurements do not fit well to the rest of the data. This points to an insufficient background subtraction.

The inverse susceptibility and the Curie-Weiss fits

Figure B.11 shows the curves and fits resulting in the fitting parameter from Table 5.6 in Section 5.4.

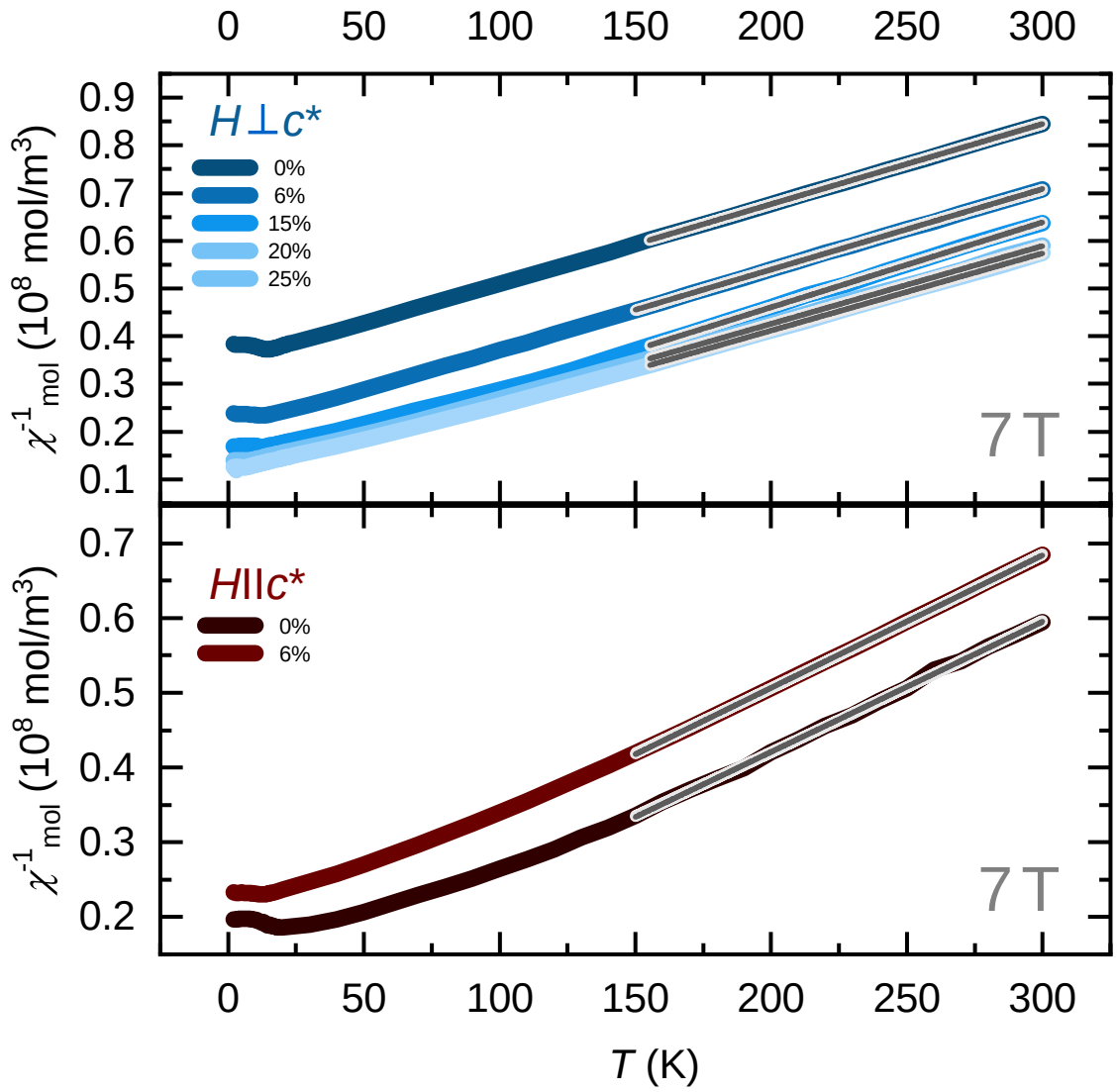

Figure B.11.: The inverse susceptibility in dependence of the temperature for different doping levels and field directions. All curves were fit with (light, thick line) and without (dark, thin line) a constant diamagnetic contribution between 150 K and 300 K.

Magnetization vs. field

The dependence of the magnetic moment of $(Na_{1-x}Li_x)_2IrO_3$ single crystals on the magnetic field for different doping concentrations and measurement directions is presented in Figure B.12

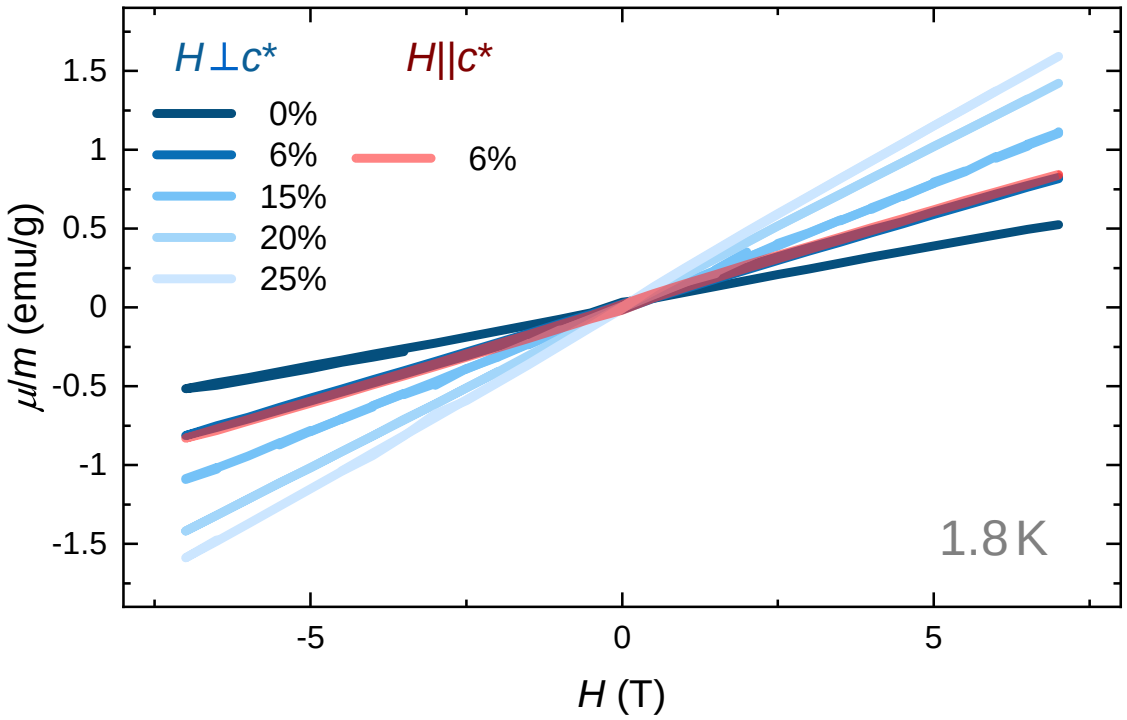

Figure B.12.: Magnetization per gram in dependence of the external magnetic field at 1.8 K. All data sets show a linear dependence with H. With increasing Li-doping the absolute value decreases in the ab-plane. At $x = 6\%$ lie the magnetization curve in-plane and out-of-plane almost on top of each other.

Bibliography

[1] Pliny the Elder. *Chapter 25 - The Magnet: Three Remedies*, volume 6. London: Henry G. Bohn, 1855. translated by John Bostock and H.T. Riley.

[2] S. Blundell. *Magnetism in Condensed Matter*. Oxford University Press, 2014. ISBN 978-0-19-850591-4.

[3] A. Kitaev. Anyons in an exactly solved model and beyond. *Ann. Phys. (N. Y.)*, 321:2–111, Jan 2006. doi:10.1016/j.aop.2005.10.005.

[4] G. Jackeli and G. Khaliullin. Mott Insulators in the Strong Spin-Orbit Coupling Limit: From Heisenberg to a Quantum Compass and Kitaev Models. *Phys. Rev. Lett.*, 102:017205, Jan 2009. doi:10.1103/PhysRevLett.102.017205.

[5] J. Chaloupka, G. Jackeli, and G. Khaliullin. Kitaev-Heisenberg Model on a Honeycomb Lattice: Possible Exotic Phases in Iridium Oxides A_2IrO_3. *Phys. Rev. Lett.*, 105(2), Jul 2010. ISSN 1079-7114. doi:10.1103/physrevlett.105.027204.

[6] K. W. Plumb, J. P. Clancy, L. J. Sandilands, V. Vijay Shankar, Y. F. Hu, K. S. Burch, H.-Y. Kee, and Y.-J. Kim. $\alpha - RuCl_3$: A spin-orbit assisted Mott insulator on a honeycomb lattice. *Phys. Rev. B*, 90:041112, Jul 2014. doi:10.1103/PhysRevB.90.041112.

[7] Y. Singh and P. Gegenwart. Antiferromagnetic Mott insulating state in single crystals of the honeycomb lattice material Na_2IrO_3. *Phys. Rev. B*, 82:064412, Aug 2010. doi:10.1103/PhysRevB.82.064412.

[8] Y. Singh, S. Manni, J. Reuther, T. Berlijn, R. Thomale, W. Ku, S. Trebst, and P. Gegenwart. Relevance of the Heisenberg-Kitaev Model for the Hon-

eycomb Lattice Iridates A_2IrO_3. *Phys. Rev. Lett.*, 108:127203, Mar 2012. doi:10.1103/PhysRevLett.108.127203.

[9] J. A. Sears, M. Songvilay, K. W. Plumb, J. P. Clancy, Y. Qiu, Y. Zhao, D. Parshall, and Y.-J. Kim. Magnetic order in $\alpha - RuCl_3$: A honeycomb-lattice quantum magnet with strong spin-orbit coupling. *Phys. Rev. B*, 91: 144420, Apr 2015. doi:10.1103/PhysRevB.91.144420.

[10] I. Kimchi and Y.-Z. You. Kitaev-Heisenberg-J_2-J_3 model for the iridates A_2IrO_3. *Phys. Rev. B*, 84:180407, Nov 2011. doi:10.1103/PhysRevB.84.180407.

[11] J. G. Rau, E. K.-H. Lee, and H.-Y. Kee. Generic Spin Model for the Honeycomb Iridates beyond the Kitaev Limit. *Phys. Rev. Lett.*, 112:077204, Feb 2014. doi:10.1103/PhysRevLett.112.077204.

[12] V. M. Katukuri, S. Nishimoto, V. Yushankhai, A. Stoyanova, H. Kandpal, S. Choi, R. Coldea, I. Rousochatzakis, L. Hozoi, and J. van den Brink. Kitaev interactions between J =1/2 moments in honeycomb Na_2IrO_3 are large and ferromagnetic: insights from ab initio quantum chemistry calculations. *New Journal of Physics*, 16(1):013056, Jan 2014. doi:10.1088/1367-2630/16/1/013056.

[13] J. Reuther, R. Thomale, and S. Rachel. Spiral order in the honeycomb iridate Li_2IrO_3. *Phys. Rev. B*, 90:100405, Sep 2014. doi:10.1103/PhysRevB.90.100405.

[14] I. Kimchi, R. Coldea, and A. Vishwanath. Unified theory of spiral magnetism in the harmonic-honeycomb iridates α, β, and $\gamma\, Li_2IrO_3$. *Phys. Rev. B*, 91: 245134, Jun 2015. doi:10.1103/PhysRevB.91.245134.

[15] S. M. Winter, Y. Li, H. O. Jeschke, and R. Valentí. Challenges in design of Kitaev materials: Magnetic interactions from competing energy scales. *Phys. Rev. B*, 93:214431, Jun 2016. doi:10.1103/PhysRevB.93.214431.

[16] Y. S. Hou, H. J. Xiang, and X. G. Gong. Unveiling magnetic interactions of ruthenium trichloride via constraining direction of orbital moments: Potential routes to realize a quantum spin liquid. *Phys. Rev. B*, 96:054410, Aug 2017. doi:10.1103/PhysRevB.96.054410.

[17] W. Wang, Z.-Y. Dong, S.-L. Yu, and J.-X. Li. Theoretical investigation of magnetic dynamics in $\alpha - RuCl_3$. *Phys. Rev. B*, 96:115103, Sep 2017. doi:10.1103/PhysRevB.96.115103.

[18] S. Hwan Chun, J. W. Kim, J. Kim, H. Zheng, C. C. Stoumpos, C. D. Malliakas, J. F. Mitchell, K. Mehlawat, Yogesh Singh, Y. Choi, T. Gog, A. Al-Zein, M. Moretti Sala, M. Krisch, J. Chaloupka, G. Jackeli, G. Khaliullin, and B. J. Kim. Direct evidence for dominant bond-directional interactions in a honeycomb lattice iridate Na_2IrO_3. *Nature Phys.*, 11, Jun 2015. doi:10.1038/nphys3322.

[19] A. Banerjee, J. Yan, J. Knolle, C. A. Bridges, M. B. Stone, M. D. Lumsden, D. G. Mandrus, D. A. Tennant, R. Moessner, and S. E. Nagler. Neutron scattering in the proximate quantum spin liquid Terahertz excitations in $\alpha-RuCl_3$. *Sci.*, 356(6342):1055–1059, 2017. doi:10.1126/science.aah6015.

[20] S. Reschke, V. Tsurkan, S.-H. Do, K.-Y. Choi, P. Lunkenheimer, Z. Wang, and A. Loidl. Terahertz excitations in $\alpha-RuCl_3$: Majorana fermions and rigid-plane shear and compression modes. *Phys. Rev. B*, 100:100403, Sep 2019. doi:10.1103/PhysRevB.100.100403.

[21] P. Lampen-Kelley, S. Rachel, J. Reuther, J.-Q. Yan, A. Banerjee, C. A. Bridges, H. B. Cao, S. E. Nagler, and D. Mandrus. Anisotropic susceptibilities in the honeycomb Kitaev system $\alpha - RuCl_3$. *Phys. Rev. B*, 98:100403, Sep 2018. doi:10.1103/PhysRevB.98.100403.

[22] E. Dagotto. Complexity in Strongly Correlated Electronic Systems. *Sci.*, 309 (5732):257–262, 2005. doi:10.1126/science.1107559.

[23] D. Vollhart. Korrelierte Elektronen im Festkörper. *Physik Journal*, 9(8/9), Aug 2010. URL `https://www.pro-physik.de/restricted-files/100136`.

[24] R. Schaffer, E. K.-H. Lee, B.-J Yang, and Y.B . Kim. Recent progress on correlated electron systems with strong spin–orbit coupling. *Rep. Prog. Phys.*, 79(9):094504, Aug 2016. doi:10.1088/0034-4885/79/9/094504.

[25] B. J. Kim, Hosub Jin, S. J. Moon, J.-Y. Kim, B.-G. Park, C. S. Leem, Jaejun Yu, T. W. Noh, C. Kim, S.-J. Oh, J.-H. Park, V. Durairaj, G. Cao, and E. Rotenberg. Novel $J_{\text{eff}} = 1/2$ Mott State Induced by Relativistic

Spin-Orbit Coupling in Sr_2IrO_4. *Phys. Rev. Lett.*, 101:076402, Aug 2008. doi:10.1103/PhysRevLett.101.076402.

[26] S. Hunklinger. *Festkörperphysik*, volume 3. Oldenbourg Wissenschaftsverlag GmbH, 2011. ISBN 978-3-486-70547-8.

[27] L. Balents. Spin liquids in frustrated magnets. *Nature*, 464:199–208, Mar 2010. doi:10.1038/nature08917.

[28] J. G. Rau and H.-Y. Kee. Trigonal distortion in the honeycomb iridates: Proximity of zigzag and spiral phases in Na_2IrO_3, 2014.

[29] G. Mendonça, R. Lapa, J. R. de Sousa, M. A. Neto, K. Majumdar, and T. Datta. The ground state phase diagram of the quantum $J_1 - J_2$ spin-1/2 Heisenberg antiferromagnet on an anisotropic square lattice. *J. Stat. Mech.*, P06022, Jun 2010.

[30] A. Y. Kitaev. Fault-tolerant quantum computation by anyons. *Ann. Phys. (N. Y.)*, 303(1):2–30, Jan 2003. ISSN 0003-4916. doi:https://doi.org/10.1016/S0003-4916(02)00018-0.

[31] S. M. Winter, K. Riedl, D. Kaib, R. Coldea, and R. Valentí. Probing $\alpha-RuCl_3$ Beyond Magnetic Order: Effects of Temperature and Magnetic Field. *Phys. Rev. Lett.*, 120:077203, Feb 2018. doi:10.1103/PhysRevLett.120.077203.

[32] A. Georges, L. de' Medici, and J. Mravlje. Strong Correlations from Hund's Coupling. *Ann. Rev. Condens. Matter Phys.*, 4(1):137–178, Jan 2013. doi:10.1146/annurev-conmatphys-020911-125045.

[33] J. Kim. Thermal and carbothermic decomposition of Na_2CO_3 and Li_2CO_3. *Metall. Mater. Trans. B*, 32:17–24, Feb 2001.

[34] Alsfasser, R. and Riedel, E. *Moderne Anorganische Chemie*. De Gruyter, 2007. ISBN 9783110190601.

[35] P. Schmidt, M. Binnewies, R. Glaum, and M. Schmidt. Chemical Vapor Transport Reactions-Methods, Materials, Modeling. In *Advanced Topics on Crystal Growth*. IntechOpen, 2013. doi:10.5772/46151.

[36] Rigaku. *MiniFlex600: Benchtop X-ray Diffractometer Instruction Manual*, 1. edition, 2012.

[37] A. A. Bunaciu, E.G. Udriştioiu, and H.Y. Aboul-Enein. X-Ray Diffraction: Instrumentation and Applications. *Crit. Rev. Anal. Chem.*, 45(4):289–299, May 2015. doi:10.1080/10408347.2014.949616. PMID: 25831472.

[38] A. Jesche, M. Fix, A. Kreyssig, W. R. Meier, and P. C. Canfield. X-ray diffraction on large single crystals using a powder diffractometer. *Philos. Mag.*, 96(20):2115–2124, 2016. doi:10.1080/14786435.2016.1192725.

[39] Neef, C. Advanced Labcourse F69-Laue X-ray diffraction, May 2015. URL `https://www.physi.uni-heidelberg.de/Einrichtungen/FP/anleitungen/F69.pdf`.

[40] Wassilkowska, A. and Czaplicka-Kotas, A. and Bielski, A. and Zielina, M. An Analysis of the elemental composition of Micro-Samples using EDS Technique. *Czas. Tech.* , 18:133–148, Feb 2014. doi:10.4467/2353737XCT.14.283.3371.

[41] Gnedel, M. and Hartwig, A. supervisors of the REM, AMU, Augsburg University, email, Jul 2020.

[42] Durrant, S. F. Laser ablation inductively coupled plasma mass spectrometry: achievements, problems, prospects. *J. Anal. At. Spektrom.*, 14:1385–1403, 1999. doi:10.1039/A901765H.

[43] Quantum Design. *Magnetic Property Measurement System: MPMS 3 User's Manual*, 15. edition, 2016.

[44] J. Clarke and A. I. Braginski. *The SQUID Handbook*, volume 1. WILEY-VCH, Weinheim, Germany, 2004. ISBN 3-527-40229-2.

[45] R. L. Fagaly. Superconducting quantum interference device instruments and applications. *Rev. Sci. Instrum.*, 77:101101, 2006. doi:10.1063/1.2354545.

[46] Quantum Design. *MPMS Application Note 1014-213: Subtracting the Sample Holder Background from Dilute Samples*, 2002.

[47] M. Seidler. Optimierung der Messwertanalyse bei SQUID Magnetometrie. Master's thesis, Universität Augsburg, 2018. bachelor thesis.

[48] Quantum Design. *Magnetic Property Measurement System: Hardware Reference Manual*, 1996.

[49] Quantum Design. *MPMS Application Note 1014-202: Transverse Detection System*, 2000.

[50] L. L. Miller. The response of longitudinal and transverse pickup coils to a misaligned magnetic dipole. *Rev. Sci. Instrum.*, 67:3201, 1996. doi:10.1063/1.1147493.

[51] L. L. Miller. The response of longitudinal and transverse pickup coils to a misaligned magnetic dipole. *Rev. Sci. Instrum.*, 67(9):3201–3207, 1996. doi:10.1063/1.1147493.

[52] S. M. Winter, A. A. Tsirlin, M. Daghofer, J. van den Brink, Y. Singh, P. Gegenwart, and R. Valentí. Models and materials for generalized Kitaev magnetism. *J. Phys. Condens. Matter*, 29(49):493002, Nov 2017. doi:10.1088/1361-648x/aa8cf5.

[53] X. Liu, T. Berlijn, W.-G. Yin, W. Ku, A. Tsvelik, Y.-J. Kim, H. Gretarsson, Y. Singh, P. Gegenwart, and J. P. Hill. Long-range magnetic ordering in Na_2IrO_3. *Phys. Rev. B*, 83:220403, Jun 2011. doi:10.1103/PhysRevB.83.220403.

[54] S. K. Choi, R. Coldea, A. N. Kolmogorov, T. Lancaster, I. I. Mazin, S. J. Blundell, P. G. Radaelli, Y. Singh, P. Gegenwart, K. R. Choi, S.-W. Cheong, P. J. Baker, C. Stock, and J. Taylor. Spin Waves and Revised Crystal Structure of Honeycomb Iridate Na_2IrO_3. *Phys. Rev. Lett.*, 108:127204, Mar 2012. doi:10.1103/PhysRevLett.108.127204.

[55] F. Ye, S. Chi, H. Cao, B. C. Chakoumakos, J. A. Fernandez-Baca, R. Custelcean, T. F. Qi, O. B. Korneta, and G. Cao. Direct evidence of a zigzag spin-chain structure in the honeycomb lattice: A neutron and x-ray diffraction investigation of single-crystal Na_2IrO_3. *Phys. Rev. B*, 85:180403, May 2012. doi:10.1103/PhysRevB.85.180403.

[56] S. C. Williams, R. D. Johnson, F. Freund, S. Choi, A. Jesche, I. Kimchi, S. Manni, A. Bombardi, P. Manuel, P. Gegenwart, and R. Coldea. Incommensurate counterrotating magnetic order stabilized by Kitaev interactions in the layered honeycomb $\alpha-Li_2IrO_3$. *Phys. Rev. B*, 93:195158, May 2016. doi:10.1103/PhysRevB.93.195158.

[57] Y. Sizyuk, C. Price, P. Wölfle, and N. B. Perkins. Importance of anisotropic exchange interactions in honeycomb iridates: Minimal model for zigzag antiferromagnetic order in Na_2IrO_3. *Phys. Rev. B*, 90:155126, Oct 2014. doi:10.1103/PhysRevB.90.155126.

[58] J. Chaloupka and G. Khaliullin. Hidden symmetries of the extended Kitaev-Heisenberg model: Implications for the honeycomb-lattice iridates A_2IrO_3. *Phys. Rev. B*, 92:024413, Jul 2015. doi:10.1103/PhysRevB.92.024413.

[59] H.-S. Kim, Vijay S. V., A. Catuneanu, and H.-Y. Kee. Kitaev magnetism in honeycomb $RuCl_3$ with intermediate spin-orbit coupling. *Phys. Rev. B*, 91: 241110, Jun 2015. doi:10.1103/PhysRevB.91.241110.

[60] I. Rousochatzakis, J. Reuther, R. Thomale, S. Rachel, and N. B. Perkins. Phase Diagram and Quantum Order by Disorder in the Kitaev $K_1 - K_2$ Honeycomb Magnet. *Phys. Rev. X*, 5:041035, Dec 2015. doi:10.1103/PhysRevX.5.041035.

[61] T. Takayama, A. Kato, R. Dinnebier, J. Nuss, H. Kono, L. S. I. Veiga, G. Fabbris, D. Haskel, and H. Takagi. Hyperhoneycomb Iridate $\beta-Li_2IrO_3$ as a Platform for Kitaev Magnetism. *Phys. Rev. Lett.*, 114:077202, Feb 2015. doi:10.1103/PhysRevLett.114.077202.

[62] K. Modic, T. Smidt, I. Kimchi, N. P. Breznay, A. Biffin, S. Choi, R. D. Johnson, R. Coldea, P. Watkins-Curry, G. T. McCandless, J. Y. Chan, F. Gandara, Z. Islam, A. Vishwanath, A. Shekhter, R. D. McDonald, and J. G. Analytis. Realization of a three-dimensional spin–anisotropic harmonic honeycomb iridate. *Nat. Commun.*, 5:4203, Jun 2014. doi:10.1038/ncomms5203.

[63] S. Mandal and N. Surendran. Exactly solvable Kitaev model in three dimensions. *Phys. Rev. B*, 79:024426, Jan 2009. doi:10.1103/PhysRevB.79.024426.

[64] J. Nasu, T. Kaji, K. Matsuura, M. Udagawa, and Y. Motome. Finite-Temperature Phase Transition to a Quantum Spin Liquid in a Three-Dimensional Kitaev Model on a Hyperhoneycomb Lattice. *Phys. Rev. B*, 89, 09 2013. doi:10.1103/PhysRevB.89.115125.

[65] E. K.-H. Lee, R. Schaffer, S. Bhattacharjee, and Y. B. Kim. Heisenberg-Kitaev model on the hyperhoneycomb lattice. *Phys. Rev. B*, 89(4), Jan 2014. doi:10.1103/physrevb.89.045117.

[66] A. Biffin, R. D. Johnson, S. Choi, F. Freund, S. Manni, A. Bombardi, P. Manuel, P. Gegenwart, and R. Coldea. Unconventional magnetic order on the hyperhoneycomb Kitaev lattice in $\beta-Li_2IrO_3$: Full solution via magnetic resonant x-ray diffraction. *Phys. Rev. B*, 90:205116, Nov 2014. doi:10.1103/PhysRevB.90.205116.

[67] A. Biffin, R. D. Johnson, I. Kimchi, R. Morris, A. Bombardi, J. G. Analytis, A. Vishwanath, and R. Coldea. Noncoplanar and Counterrotating Incommensurate Magnetic Order Stabilized by Kitaev Interactions in $\gamma-Li_2IrO_3$. *Phys. Rev. Lett.*, 113:197201, Nov 2014. doi:10.1103/PhysRevLett.113.197201.

[68] B. W. Lebert, S. Kim, V. Bisogni, I. Jarrige, A. M. Barbour, and Y.-J. Kim. Resonant inelastic X-ray scattering study of $\alpha-RuCl_3$: a progress report. *J. Phys. Condens. Matter*, 32(14):144001, Jan 2020. doi:10.1088/1361-648x/ab5595.

[69] R. D. Johnson, S. C. Williams, A. A. Haghighirad, J. Singleton, V. Zapf, P. Manuel, I. I. Mazin, Y. Li, H. O. Jeschke, R. Valentí, and R. Coldea. Monoclinic crystal structure of $\alpha - RuCl_3$ and the zigzag antiferromagnetic ground state. *Phys. Rev. B*, 92:235119, Dec 2015. doi:10.1103/PhysRevB.92.235119.

[70] H. B. Cao, A. Banerjee, J.-Q. Yan, C. A. Bridges, M. D. Lumsden, D. G. Mandrus, D. A. Tennant, B. C. Chakoumakos, and S. E. Nagler. Low-temperature crystal and magnetic structure of $\alpha - RuCl_3$. *Phys. Rev. B*, 93:134423, Apr 2016. doi:10.1103/PhysRevB.93.134423.

[71] P. Czajka, T. Gao, M. Hirschberger, P. Lampen-Kelley, A. Banerjee, J. Yan, D. G. Mandrus, S. E. Nagler, and N. P. Ong. Oscillations of the thermal conductivity in the spin-liquid state of $\alpha-RuCl_3$. *Nat. Phys.*, pages 1745–2481, May 2021. doi:10.1038/s41567-021-01243-x.

[72] Y. Kasahara, T. Ohnishi, Y. Mizukami, O. Tanaka, S. Ma, K. Sugii, N. Kurita, H. Tanaka, J. NAsu, Y. Motome, T. Shibauchi, and Y. Matsuda. Majorana quantization and half-integer thermal quantum Hall effect in a Kitaev spin liquid. *Nature*, 559:227–231, Jul 2018. doi:10.1038/s41586-018-0274-0.

[73] I. I. Mazin, Harald O. Jeschke, K. Foyevtsova, R. Valentí, and D. I. Khomskii. Na_2IrO_3 as a Molecular Orbital Crystal. *Phys. Rev. Lett.*, 109:197201, Nov 2012. doi:10.1103/PhysRevLett.109.197201.

[74] K. Foyevtsova, Harald O. Jeschke, I. I. Mazin, D. I. Khomskii, and R. Valentí. Ab initio analysis of the tight-binding parameters and magnetic interactions in Na_2IrO_3. *Phys. Rev. B*, 88:035107, Jul 2013. doi:10.1103/PhysRevB.88.035107.

[75] I. I. Mazin, S. Manni, K. Foyevtsova, Harald O. Jeschke, P. Gegenwart, and R. Valentí. Origin of the insulating state in honeycomb iridates and rhodates. *Phys. Rev. B*, 88:035115, Jul 2013. doi:10.1103/PhysRevB.88.035115.

[76] Y. Li, K. Foyevtsova, Harald O. Jeschke, and R. Valentí. Analysis of the optical conductivity for $A_2IrO_3 (A = \mathrm{Na}, \mathrm{Li})$ from first principles. *Phys. Rev. B*, 91:161101, Apr 2015. doi:10.1103/PhysRevB.91.161101.

[77] S. Manni. *Synthesis and investigation of frustrated Honeycomb lattice iridates and rhodates*. PhD thesis, Georg-August-Universität Göttingen, 2014.

[78] F. Freund. *Synthese und physikalische Untersuchungen von Kitaev-Honigwabeniridaten*. PhD thesis, Universität Augsburg, 2019.

[79] F. Freund, S. Williams, R. Johnson, et al. Single crystal growth from separated educts and its application to lithium transition-metal oxides. *Sci. Rep.*, 6: 35362, Oct 2016. doi:10.1038/srep35362.

[80] Tsurkan, V. email, 2021. Experimental Physics V, University of Augsburg.

[81] K. Momma and F. Izumi. VESTA3 for three-dimensional visualization of crystal, volumetric and morphology data. *J. Appl. Crystallogr.*, 44(6):1272–1276, Dec 2011. doi:10.1107/S0021889811038970.

[82] M. J. O'Malley, H. Verweij, and P. M. Woodward. Structure and properties of ordered Li_2IrO_3 and Li_2PtO_3. *J. Solid State Chem.*, 181(8):1803–1809, 2008. ISSN 0022-4596. doi:https://doi.org/10.1016/j.jssc.2008.04.005.

[83] J.W Krizan, J.H. Roudebush, G.M. Fox, and R.J. Cava. The chemical instability of Na_2IrO_3 in air. *Mater. Res. Bull.*, 52:162 – 166, 2014. ISSN 0025-5408. doi:10.1016/j.materresbull.2014.01.021.

[84] D. C. Wallace, C. M. Brown, and T. M. McQueen. Evolution of magnetism in the $Na_{3-\delta}(Na_{1-x}Mg_x)_2Ir_2O_6$ series of honeycomb iridates. *J. Solid State Chem.*, 224:28–35, 2015. ISSN 0022-4596. doi:https://doi.org/10.1016/j.jssc.2014.03.013.

[85] T. Dziuba, I.-M. Pietsch, M. Stark, G. A. Traeger, P. Gegenwart, and M. Wenderoth. Surface Conductivity of the Honeycomb Spin–Orbit Mott Insulator Na_2IrO_3. *Phys. Status Solidi B*, 258:2000421, 2020. ISSN 0025-5408. doi:10.1002/pssb.202000421.

[86] J.A. Sears, L.E. Chern, S. Kim, P. J. Bereciartua, S. Francoual, Y. B. Kim, and Y.-J. Kim. Ferromagnetic Kitaev interaction and the origin of large magnetic anisotropy in $\alpha - RuCl_3$. *Nat. Phys.*, 16, Aug 2016. doi:10.1038/s41567-020-0874-0.

[87] J. A. Sears, Y. Zhao, Z. Xu, J. W. Lynn, and Y.-J. Kim. Phase diagram of $\alpha - rucl_3$ in an in-plane magnetic field. *Phys. Rev. B*, 95:180411, May 2017. doi:10.1103/PhysRevB.95.180411.

[88] Y. Yamaji, Y. Nomura, M. Kurita, R. Arita, and M. Imada. First-Principles Study of the Honeycomb-Lattice Iridates Na_2IrO_3 in the Presence of Strong Spin-Orbit Interaction and Electron Correlations. *Phys. Rev. Lett.*, 113: 107201, Sep 2014. doi:10.1103/PhysRevLett.113.107201.

[89] R. Yadav, N. A. Bogdanov, V. M. Katukuri, S. Nishimoto, J. van den Brink, and L. Hozoi. Kitaev exchange and field-induced quantum spin-liquid states in honeycomb $\alpha - RuCl_3$. *Sci. Rep.*, 6:37925, 2016. doi:10.1038/srep37925.

[90] P. Laurell and S. Okamoto. Dynamical and thermal magnetic properties of the Kitaev spin liquid candidate $\alpha-RuCl_3$. *npj Quantum Mater.*, 5:2397–4648, Jan 2020. doi:10.1038/s41535-019-0203-y.

[91] L. Janssen, E. C. Andrade, and M. Vojta. Magnetization processes of zigzag states on the honeycomb lattice: Identifying spin models for $\alpha-RuCl_3$ and Na_2IrO_3. *Phys. Rev. B*, 96:064430, Aug 2017. doi:10.1103/PhysRevB.96.064430.

[92] A. Banerjee, C. Bridges, J.-Q. Yan, A. A. Aczel, L. Li, M. B. Stone, G. E. Granroth, M. D. Lumsden, Y. Yiu, J. Knolle, S. Bhattacharjee, D. L. Kovrizhin, R. Moessner, D. A. Tennant, D. G. Mandrus, and S. E. Nagler. Proximate Kitaev quantum spin liquid behaviour in a honeycomb magnet. *Nature Mater.*, 15:733, Jul 2016. doi:10.1038/nmat4604.

[93] J. Fletcher, W. Garnder, E. Hooper, et al. Anhydrous Ruthenium Chlorides. *Nature*, 199:1089–1090, Sep 1963. doi:10.1038/1991089a0.

[94] C. Epstein and N. Elliot. Magnetic Susceptibility of K_3MoCl_6 and $RuCl_3$. *J. Chem. Phys.*, 22(4):634–635, 1954. doi:10.1063/1.1740138.

[95] M. Majumder, M. Schmidt, H. Rosner, A. A. Tsirlin, H. Yasuoka, and M. Baenitz. Anisotropic $Ru^{3+}4d^5$ magnetism in the $\alpha - RuCl_3$ honeycomb system: Susceptibility, specific heat, and zero-field NMR. *Phys. Rev. B*, 91: 180401, May 2015. doi:10.1103/PhysRevB.91.180401.

[96] Y. Kubota, H. Tanaka, T. Ono, Y. Narumi, and K. Kindo. Successive magnetic phase transitions in $\alpha - RuCl_3$: XY-like frustrated magnet on the honeycomb lattice. *Phys. Rev. B*, 91:094422, Mar 2015. doi:10.1103/PhysRevB.91.094422.

[97] P. A. Maksimov and A. L. Chernyshev. Rethinking $\alpha-RuCl_3$. *Phys. Rev. Research*, 2:033011, Jul 2020. doi:10.1103/PhysRevResearch.2.033011.

[98] S. Agrestini, C.-Y. Kuo, K.-T. Ko, Z. Hu, D. Kasinathan, H. B. Vasili, J. Herrero-Martin, S. M. Valvidares, E. Pellegrin, L.-Y. Jang, A. Henschel, M. Schmidt, A. Tanaka, and L. H. Tjeng. Electronically highly cubic conditions for Ru in $\alpha - RuCl_3$. *Phys. Rev. B*, 96:161107, Oct 2017. doi:10.1103/PhysRevB.96.161107.

[99] R. R. P. Singh and J. Oitmaa. High-temperature thermodynamics of the honeycomb-lattice Kitaev-Heisenberg model: A high-temperature series expansion study. *Phys. Rev. B*, 96:144414, Oct 2017. doi:10.1103/PhysRevB.96.144414.

[100] Y.-Z. You, I. Kimchi, and A. Vishwanath. Doping a spin-orbit Mott insulator: Topological superconductivity from the Kitaev-Heisenberg model and possible application to $(Na_2/Li_2)IrO_3$. *Phys. Rev. B*, 86:085145, Aug 2012. doi:10.1103/PhysRevB.86.085145.

[101] S. Manni, S. Choi, I. I. Mazin, R. Coldea, M. Altmeyer, Harald O. Jeschke, R. Valentí, and P. Gegenwart. Effect of isoelectronic doping on the honeycomb-lattice iridate A_2IrO_3. *Phys. Rev. B*, 89:245113, Jun 2014. doi:10.1103/PhysRevB.89.245113.

[102] K. Rolfs, S. Toth, E. Pomjakushina, D. Sheptyakov, J. Taylor, and K. Conder. Spiral magnetic phase in Li-doped Na_2IrO_3. *Phys. Rev. B*, 91:180406, May 2015. doi:10.1103/PhysRevB.91.180406.

[103] S. N. Gupta, P. V. Sriluckshmy, K. Mehlawat, A. Balodhi, D. K. Mishra, S. R. Hassan, T. V. Ramakrishnan, D. V. S. Muthu, Y. Singh, and A. K Sood. Raman signatures of strong Kitaev exchange correlations in $(Na_{1-x}Li_x)_2IrO_3$: Experiments and theory. *EPL*, 114(4):47004, May 2016. doi:10.1209/0295-5075/114/47004.

[104] V. Hermann, J. Ebad-Allah, F. Freund, I. M. Pietsch, A. Jesche, A. A. Tsirlin, J. Deisenhofer, M. Hanfland, P. Gegenwart, and C. A. Kuntscher. High-pressure versus isoelectronic doping effect on the honeycomb iridate Na_2IrO_3. *Phys. Rev. B*, 96:195137, Nov 2017. doi:10.1103/PhysRevB.96.195137.

[105] S. Manni, Y. Tokiwa, and P. Gegenwart. Effect of nonmagnetic dilution in the honeycomb-lattice iridates Na_2IrO_3 and Li_2IrO_3. *Phys. Rev. B*, 89:241102, Jun 2014. doi:10.1103/PhysRevB.89.241102.

[106] K. Mehlawat, G. Sharma, and Y. Singh. Fragile magnetic order in the honeycomb lattice Iridate Na_2IrO_3 revealed by magnetic impurity doping. *Phys. Rev. B*, 92:134412, Oct 2015. doi:10.1103/PhysRevB.92.134412.

[107] M. Roslova, J. Hunger, G. Bastien, D. Pohl, H. M. Haghighi, A. U. B. Wolter, A. Isaeva, U. Schwarz, B. Rellinghaus, K. Nielsch, B. Büchner, and T. Doert. Detuning the Honeycomb of the $\alpha - RuCl_3$ Kitaev Lattice: A Case of Cr3+ Dopant. *Inorg. Chem.*, 58(10):6659–6668, 2019. doi:10.1021/acs.inorgchem.8b03545.

[108] G. Bastien, M. Roslova, M. H. Haghighi, K. Mehlawat, J. Hunger, A. Isaeva, T. Doert, M. Vojta, B. Büchner, and A. U. B. Wolter. Spin-glass state and reversed magnetic anisotropy induced by Cr doping in the Kitaev magnet $\alpha-RuCl_3$. *Phys. Rev. B*, 99:214410, Jun 2019. doi:10.1103/PhysRevB.99.214410.

[109] Y.-J. Yuan, C.-H. Li, S.-J. Tian, H.-C. Lei, and X. Zhang. Tuning of Magnetic Properties of $\alpha - RuCl_3$ Single Crystal by Cr Doping. *Chin. Phys. Lett*, 37(6), 2020. doi:10.1088/0256-307X/37/6/067501.

[110] Stefan Riessner, LOT-QuantumDesign. Email, Jul 2018.

[111] Carl Roth. *Safety data sheet: Ruthenium(III)-chlorid, wasserfrei*, 2016.

[112] J.-C. Zheng, Y. Cui, T.-R. Li, K.-J. Ran, J. Wen, and W. Yu. Dielectric evidence for possible type-II multiferroicity in α-$RuCl_3$. *Sci. China Phys., Mech.*, 61(5), Feb 2018. doi:10.1007/s11433-017-9166-1.

[113] Y. Li, S. M. Winter, D. A. S. Kaib, K. Riedl, and R. Valentí. Modified Curie-Weiss law for j_{eff} magnets. *Phys. Rev. B*, 103:L220408, Jun 2021. doi:10.1103/PhysRevB.103.L220408.

[114] A. Hassini. Röntgenographische Charakterisierung und magnetische Eigenschaften von Na_2IrO_3. Master's thesis, Universität Augsburg, 2021. bachelor thesis.

[115] T. Grünwald. Metathesereaktionen in Honigwaben - Ruthenaten und Iridaten. master thesis, Universität Augsburg, 2018.

[116] F. Lüpke, S. Manni, S. C. Erwin, I. I. Mazin, P. Gegenwart, and M. Wenderoth. Highly unconventional surface reconstruction of Na_2IrO_3 with persistent energy gap. *Phys. Rev. B*, 91:041405, Jan 2015. doi:10.1103/PhysRevB.91.041405.

[117] *CrystalMaker software*. CrystalMaker Software Ltd, Oxford, England, . A crystal and molecular structures program for Mac and Windows.

[118] *SingleCrystal software*. CrystalMaker Software Ltd, Oxford, England, . A single-crystal diffraction program for Mac and Windows.

[119] National Institute of Standards and Technology, Feb 2021. URL `https://www.physics.nist.gov/PhysRefData/FFast/html/form.html`.

Danksagung

Es ist tatsächlich geschafft. Nach mehr als sechs Jahren, zwei Kindern und drei Corona-Jahren habe ich die Doktorarbeit abgegeben. Dass dieser Tag gekommen ist, liegt allein daran, dass mich viele Menschen mit helfende Hände, offene Ohren, mit Nachsicht und Anfeuerungen begleitet haben. Es ist an der Zeit diesen Menschen zu danken.

Vielen Dank an meinen Betreuer Philipp Gegenwart, dafür dass du mir die Gelegenheit für diese Arbeit gegeben hast. Danke, dass du ohne Murren Geburten und Elternzeiten mitgemacht hast und, dass du mir trotz meiner naiven, realitätsfernen Vorstellung vom Elternsein einen 20-Stunden-Vertrag aufgedrückt hast. Ich war hinterher sehr froh darüber. Vielen Dank an Manfred Albrecht für das Lesen meiner Arbeit als Zweitgutachter. Am meisten gelernt habe ich von Anton Jesche, der mich während meiner Arbeit beratend begleitet hat und mich in viele Methoden und Geräte eingeführt hat. Deine Tür war immer offen und keine Frage zu dumm, um sie zu beantworten, vielen Dank dafür, Anton. Falls mal wieder ein technisches Problem bestand, war Alexander Herrnberger die Rettung, sowie die unersetzliche Informationsquelle bei der Suche nach Ersatzteilen oder anderem Bestand aller Art. Danke auch an Christine Schäfer, die sich für uns im Sekretariat durch den Bürokratiedschungel gekämpft hat.

Doch erst das soziale Miteinander gibt Freude während der Arbeit. Deshalb danke ich allen Mitarbeiter des Lehrstuhls für ihre warme Aufnahme in all diesen Jahren. Besonders wertvolle Wegbegleiter für mich waren hierbei Jannis Maiwald, Friedrich Freund, Theodor Grünwald, Sebastian Bacchus sowie die Mitglieder der Hanabi-Spielgruppe Vera Bader, Franziska Breitner, Franziska Grußler und Robert Gruhl.

Mindestens genauso wichtig waren für mich die Eltern und Erzieher der Spatzengruppe, welche mit mir die ganze Zeit über mitgefiebert und mich angefeuert haben.

Um eine Doktorarbeit mit zwei kleinen Kindern, vor allem in der Coronazeit, in der jede Woche die Öffnungszeiten der Kitas und der Gesundheitszustand aller Familienmitglieder ungewiss ist, braucht es sehr viel Zeit, Geduld und ein Heer an Unterstützern. Für mich waren das vor allem meine Schwiegereltern, Onkel und Tante der Kinder sowie meine Mutter. Vielen Dank für euren unermüdlichen Einsatz, obwohl das Leben jedes Einzelnen in dieser Zeit nicht weniger turbulent war. Vielen Dank auch an meinen ehemaligen Bürokollegen, besten Freund, Partner und Vater meiner Kinder, Manuel Fix. In was hatten wir uns da nur reingeritten? Wir haben viel geflucht, gestritten, geweint (also ich) und sind immer wieder an unsere Grenzen gestoßen. Doch irgendwie haben wir es geschafft und können uns immer noch liebevoll in die Augen schauen. Ohne dich hätte ich es auf jeden Fall nicht geschafft, ich bin froh dich an meiner Seite zu haben. Auch meine Mutter ist jetzt, seit ihrem Tod letztes Jahr, jeden Tag an meiner Seite. Sie hat mich zu dem Menschen gemacht der ich bin und war und ist mein Fels in der Brandung. Ich bin dankbar für jede Stunde, dir wir miteinander verbringen konnten.